

TECHNISCHE UNIVERSITÄT MÜNCHEN

Physik-Department
Lehrstuhl für Funktionelle Materialien

Novel Structuring Routines for Organic Photovoltaics

Robert P. Meier

Vollständiger Abdruck der von der Fakultät für Physik der Technischen Universität München zur Erlangung des akademischen Grades eines

Doktors der Naturwissenschaften (Dr. rer. nat.)

genehmigten Dissertation.

Vorsitzender: Univ.-Prof. Dr. Martin Zacharias

Prüfer der Dissertation:

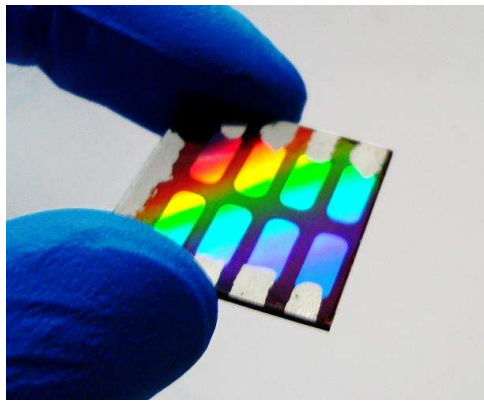
1. Univ.-Prof. Dr. Peter Müller-Buschbaum
2. Univ.-Prof. Dr. Martin S. Brandt

Die Dissertation wurde am 23.01.2012 bei der Technischen Universität München eingereicht und durch die Fakultät für Physik am 14.02.2012 angenommen.

Abstract

Organic photovoltaic devices are promising candidates for a future energy production at low-costs. In the framework of this thesis, fundamental aspects of organic solar cells based on different blend systems were investigated. X-ray scattering revealed a strong dependency of the inner film morphology of such devices on the layer thickness and the film composition. Applying optical methods, an enhanced photochemical degradation of blend films upon UV-irradiation was observed if compared to pure homopolymer samples. Furthermore, novel imprinting routines have been developed for the fabrication of structured polymer films with feature dimensions on the micro- and nanoscale. Making use of such textured films in organic photovoltaic devices, the power conversion efficiency was improved due to an diffraction-induced increase in optical absorption.

Die organische Photovoltaik hat sich zu einem aufstrebenden Feld für die zukünftige Stromerzeugung entwickelt. Im Rahmen dieser Doktorarbeit wurden diverse Messmethoden angewandt, um grundlegende Eigenschaften von organischen Solarzellen basierend auf leitfähigen Polymeren zu untersuchen. Mithilfe von Röntgenstreuung konnte ein starker Einfluss der Schichtdicke und der Zusammensetzung auf die Filmmorphologie nachgewiesen werden. Optische Verfahren haben gezeigt, dass der Einfluss von ultraviolettem Licht auf die photochemische Alterung der angewandten Materialien in Mischungsfilmen stark erhöht ist. Desweiteren wurden neuartige Strukturierungsmethoden für die Herstellung von texturierten, leitfähigen Polymerfilmen entwickelt. Anhand der Implementierung derartiger Filme in organische Solarzellen konnte der Wirkungsgrad aufgrund erhöhter Absorptionseigenschaften gesteigert werden.



In 1820, J. von Fraunhofer was the first to use diffraction gratings based on thin wires for the formation of light spectra.

In this thesis, the same idea is transferred to organic solar cells.

Contents

1	Introduction	1
2	Basic Principles and Theory	5
2.1	Fundamentals of organic solar cells	5
2.1.1	Exciton generation	6
2.1.2	Exciton transport and dissociation	9
2.1.3	Charge carrier pair dissociation	12
2.1.4	Charge carrier transport	13
2.2	Phase separation in polymer blend films	16
2.2.1	Classic Flory-Huggins approach	16
2.2.2	Crystalline ordering in polymer blend films	20
2.2.3	Rodlike: flexible polymer blend	22
2.2.4	Dynamic mean field approach	23
2.3	Structuring of polymer films	25
2.3.1	Solution based texturing	26
2.3.2	Temperature and pressure induced processability	28
2.4	X-ray techniques	30
2.4.1	Basic principles	31
2.4.2	Specular scattering	33
2.4.3	Diffuse scattering close to total reflection	36
2.4.4	Ewald sphere - scattering on three-dimensional lattice structures	41
2.4.5	X-ray absorption	42
3	Experimental Methods	45
3.1	Optical microscopy	46
3.2	Atomic force microscopy	47
3.3	Current-voltage characterization	49
3.4	UV/Vis spectroscopy	50

3.5	Optical ellipsometry	52
3.6	X-ray reflectivity	54
3.7	Grazing incidence (ultra-)small angle X-ray scattering	55
3.8	Near edge X-ray absorption fine structure spectroscopy	58
3.9	Scanning transmission X-ray microscopy	59
4	Materials and Thin Film Preparation	61
4.1	Photoactive conducting polymers	61
4.1.1	Hole conducting polymers	61
4.1.2	Electron conducting materials	64
4.1.3	PEDOT:PSS	66
4.2	Mold materials	68
4.3	Thin film preparation	69
4.3.1	Polymer solution	70
4.3.2	Substrate preparation	70
4.3.3	Spin coating	71
5	Self Organized Structuring in Polymer Blend Films	75
5.1	Phase separation tuning in polymer blend films	76
5.1.1	Sample preparation	76
5.1.2	Film composition	78
5.1.3	Lateral film morphology	79
5.1.4	Vertical film composition	82
5.1.5	Overall film morphology	84
5.1.6	Evolution of film morphology during spin-coating	87
5.2	Photochemical degradation in blend systems	90
5.2.1	Sample preparation	90
5.2.2	Film composition dependent optical absorption	91
5.2.3	Film composition dependent film morphology	92
5.2.4	Polymer degradation upon UV exposure	97
5.3	Residual solvent depending on polymer phase separation	102
5.3.1	Background	102
5.3.2	Absolute solvent content in homopolymer films	103
5.3.3	Solvent content depending on film thickness	105
5.3.4	Compositional mapping of polymer blend films	107
5.3.5	Lateral solvent distribution in polymer blend films	111
5.3.6	Impact on organic solar cells	113

5.4	Conclusions - polymer blend films	115
6	Supplemental Structuring Routines for Conducting Polymer Films and Their Application	117
6.1	Thermal annealing of structured polymer films	118
6.1.1	Fabrication routine	118
6.1.2	Structure tuning via film thickness	121
6.1.3	GISAXS on structured F8BT films	124
6.1.4	Thermal treatment of surface structures	125
6.2	Film thickness controllable wet embossing	133
6.2.1	Structuring routine	134
6.2.2	PC master molds	137
6.2.3	Structured PEDOT:PSS films	138
6.2.4	P3HT:F8BT films on wet embossed PEDOT:PSS	141
6.2.5	OSCs based on wet embossed PEDOT:PSS films	143
6.3	Efficiency improved structured organic solar cells	149
6.3.1	Structuring routine	149
6.3.2	Surface morphology control via plasticizer content	152
6.3.3	Optical properties of PASE-structured PEDOT:PSS gratings	158
6.3.4	Coated PASE-structured PEDOT:PSS films	159
6.3.5	Solar cells based on PASE-structured PEDOT:PSS electrodes	162
6.3.6	Improved charge carrier collection model	168
6.4	Conclusions - structured polymer films	170
7	Conclusions	171
8	Outlook	175
A	Appendix	177
A.1	Supplementary AFM data	177
A.2	Additional polymer blend system	178
A.3	Supplementary information: PASE-structured solar cells	181
A.4	Design and implementation of thermal evaporation set-up	183
	Bibliography	187
	List of publications	211
	Acknowledgements	217

Chapter 1

Introduction

Historic milestone 1839: Alexandre Edmond Becquerel and his father Antoine César were the first to observe the photoelectrical effect.[1]

Following the first law of thermodynamics, which actually goes back to first studies by the French physicist Carnot in 1824 [2], any kind of human activity requires energy input. In the last 50 years alone, worldwide primary energy use increased from around 100 to over 500 EJ (10^{18} J) per year.[3] Up to now, around 80 % of the world's total energy supply has been provided by fossil fuels like oil, gas, and coal.[4] As these energy sources are finite and the global demand for energy continues to grow (typical annual growth rates of around 2 % [5]), high expectations are being placed on alternative and environmentally friendly future energy sources - the so-called *new renewables*: geothermal, wind, biomass, and solar energy.

Since the sun is the largest carbon-neutral energy source available on earth with 89,000 TW of sunlight reaching the earth's surface, energy production via concentration solar power or photovoltaic technologies is very promising. Up to now, different photovoltaic technologies based on inorganic semiconductors have been established on the energy market, which have power conversion efficiencies of up to 20 % as in the case of commercially available monocrystalline silicon solar cells. However, all these different approaches are mechanically rigid and have high manufacturing costs due to energy-intensive fabrication processes. In consequence, after the discovery of the semiconducting properties of polymers [6] the worldwide research community has put a lot of effort into the development of efficient organic solar cells (OSC). Such devices have the great perspective of being cheap, if produced on a large scale, and still allow for a flexible design. Thus, in recent years OSCs have started to attract the interest of the industrial sector as well. In figure 1.1 the

officially reported best research-cell efficiencies of the novel organic devices (dark symbols) are compared to the values of single crystal silicon cells (light symbols). For improved clarity of presentation, the development of the efficiencies of both solar cell types starts from the first reported value (for silicon cells: 1972 and for OSCs: 2001). Although OSCs still lack the high efficiencies of the inorganic counterparts, the organic devices are characterized by a tremendous increase in power conversion efficiency. Taking into account

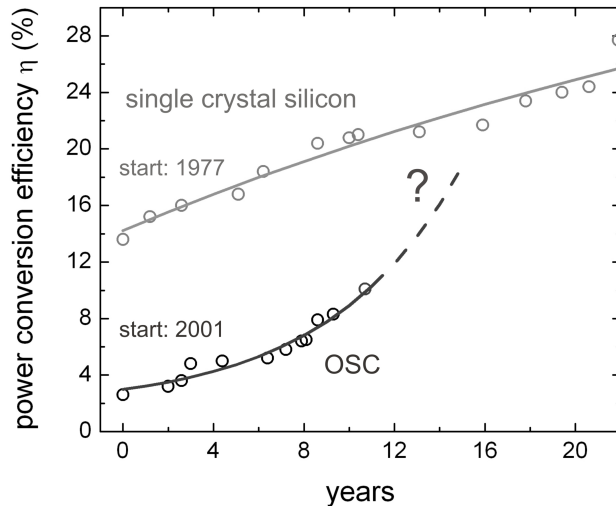


Figure 1.1: Best research-cell efficiencies of organic solar cells (dark symbols) compared to the performance of single crystal silicon devices (light symbols). For clarity, the timescale starts for both cell types at the year of the first officially reported performance value. The exponential fits (solid lines) highlight the future potential of OSCs. The data are provided by the National Renewable Energy Laboratory (NREL).[7] The most recent OSC efficiency is taken from reference [8].

the progress in cell efficiency of OSCs over the last ten years an exponential increase in performance fits the development best (indicated by solid and dashed lines). This clearly indicates the potential of this technology which is mainly a result of the huge chemical variety of the applicable polymeric materials. However, it must be noted that different theoretical studies have been published which limit the maximum attainable efficiencies of OSCs to 10 - 15 %.[9, 10] Since these calculations are based on the characteristics of the known materials, further improvements as results of novel synthesized materials will push this theoretical limit further - such as the introduction of low-band gap polymers to OSCs in 2006.[11]

In general, organic solar cells are based on thin photoactive films, sandwiched between two electrodes, and convert the impinging sunlight directly into electricity. In comparison to conventional silicon based solar cells, in which the generated charge carriers are separated at p-n-junctions due to doping of the silicon, in efficient OSCs this process occurs at the interface between two components.[12] The power conversion efficiencies of the first devices based on pure photoactive polymers were very low ($< 10^{-2}$ % [12, 13]). Therefore, Sariciftci et al. came up with the idea of bilayer devices, which already showed improved characteristics.[14] However, only after the invention of the so-called *bulk heterojunction* (BHJ) solar cell architecture in 1995 by the group of Heeger [12], photoactive organic

materials started to attract serious interest also for photovoltaic applications. In the BHJ approach the two materials are intermixed which leads to the formation of a interdigitated polymer:polymer network. Hence, the interfacial area between the two components is drastically increased, which again favors an efficient charge carrier separation.

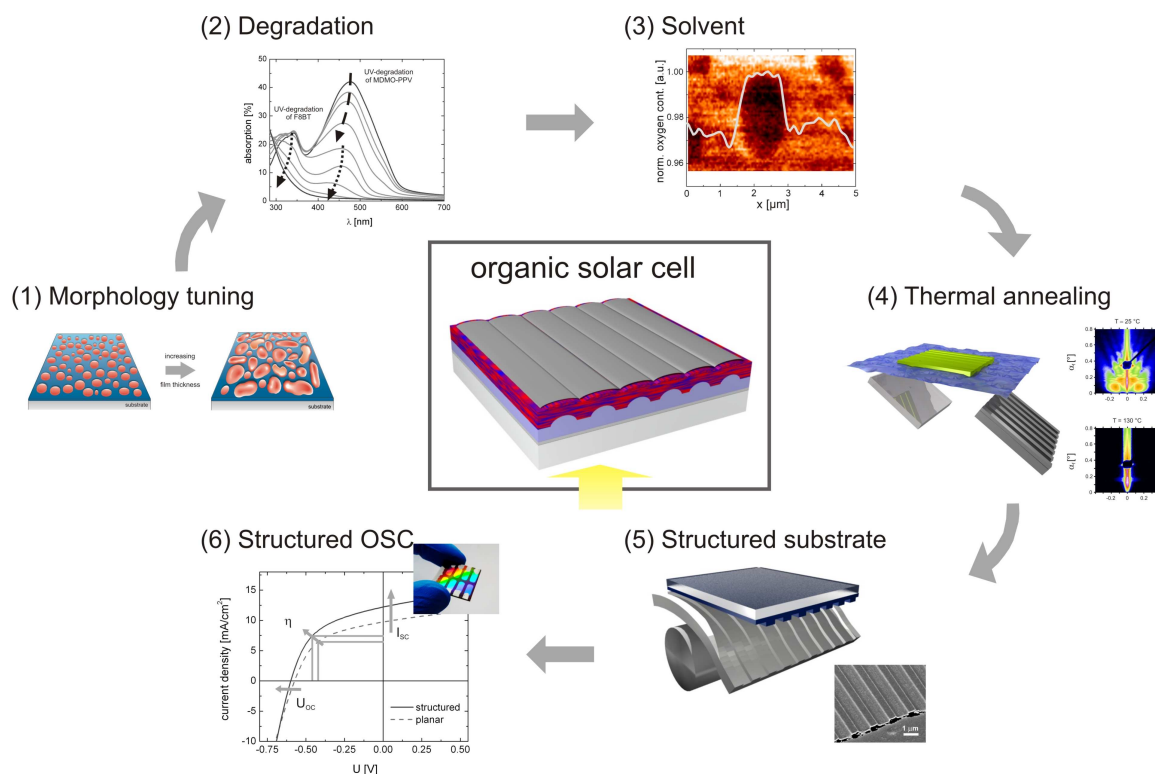


Figure 1.2: In the center part a schematic illustration of an organic solar cell based on a blend system is shown. It is surrounded by the different aspects which have been investigated within the framework of this thesis. More details on the different topics (1) to (6) are given in the text.

In the center part of figure 1.2 a schematic illustration of an organic solar cell is given based on a BHJ photoactive layer (indicated by mixed blue-red layer), which is sandwiched between a transparent bottom and a light reflecting top electrode.

Within the framework of this thesis different fundamental aspects of such OSCs based on blend systems are discussed, which in principal address two main questions: How can the film morphology in conducting polymer blend thin films be controlled and what are its impacts? And second, what is the influence of structured substrates on the performance of OSCs?

The investigated aspects are also included in figure 1.2 as topics (1) to (6) in the same chronological order as they will appear in more detail in this thesis. Since the film morphology of the photoactive blend layer is of utmost importance for an efficient charge carrier separation in an OSC, the question of how variations in film thickness can in-

fluence the polymer:polymer networks in conducting BHJ films is answered in the first topic (see topic (1) in figure 1.2). However, in addition to the total film thickness, the film composition might also have a strong influence on the film morphology (topic (2)). Approaching higher efficiencies, the longtime performance of OSCs is still one of the key issues which limits a future commercialization of such devices. Addressing this point, it is crucial to know how the photochemical stabilities of the applied materials change in blend films instead of simple homopolymer films (also topic (2)). Especially oxygen in combination with high intensity illumination is known to accelerate the aging of photoactive materials. Since the applied solvents, which are used for the fabrication of the thin active layers, often contain oxygen, it is important to know how many of the oxygenic solvent molecules are retained within the conducting polymer blend films (topic (3) in figure 1.2). After discussing these fundamental aspects, the topics (4) to (6) are related to the more application oriented influence of additional polymer structures on the performance of OSCs. Since during the fabrication of OSCs an annealing step at elevated temperatures is crucial, the thermal stability of the fabricated polymer structures might minimize the application possibilities for organic solar cells (topic (4) in figure 1.2). In order to avoid this difficulty, a more efficient texturing of OSCs might be possible, which does not address the active layer itself but rather the transparent electrodes. However, as a result ways of how to structure the transparent electrodes have to be found first (topic (5) in figure 1.2). And finally, the main question, whether an increase in power conversion efficiency is at all possible due to the introduction of artificial polymer structures, needs to be answered (topic (6) in figure 1.2).

The thesis has the following structure: After this introduction, the theoretical aspects of the single processes within OSCs and the basic principles of the applied characterization techniques are illustrated in chapter 2. Subsequently, chapter 3 focuses on the experimental aspects of the used measurement methods. The applied materials are discussed in detail in chapter 4. The first result chapter 5 addresses the different topics related to the film morphology in polymer blend systems (see topics (1) to (3)), whereas the second main chapter 6 puts the influence of artificial surface structures on the performance of OSCs into focus (topics (4) to (6)). Finally, the thesis is concluded with a short summary of the obtained results (chapter 7) and a brief outlook is given in chapter 8.

Chapter 2

Basic Principles and Theory

Historic milestone 1877: The first selenium solar cell was fabricated based on the experimental findings by W. Smith, W. G. Adams, and R. E. Day.[15]

In this work, the application possibilities of structured substrates in the field of organic photovoltaics are investigated. The following chapter presents the fundamental theoretical aspects of the investigated samples and the applied measurement techniques.

The chapter begins with a theoretical explanation of the fundamental processes occurring in an organic photovoltaic device - starting from light absorption and ending in photocurrent extraction. Since all investigated solar cells are based on blend systems, the subsequent section introduces the theoretical background of phase separation in blend films with a special focus on novel conducting multi-component systems. In general, the applied polymers have the big advantage of being easily structured through imprinting processes in solution or under thermal annealing. For an improved understanding of the different imprinting processes, their theoretical background is presented as well. Mainly X-ray methods were applied to investigate the polymer blend films and the artificially structured samples. Therefore, the theoretical background of these techniques is discussed in the final part of the present theory chapter.

2.1 Fundamentals of organic solar cells

In comparison to standard polymers (e.g. polystyrene or polyethylene), whose carbon atoms in the polymer backbone are typically linked via single bonds (sp^3 -hybridized), conducting polymers are built up of alternating single and double bonds. This is possible

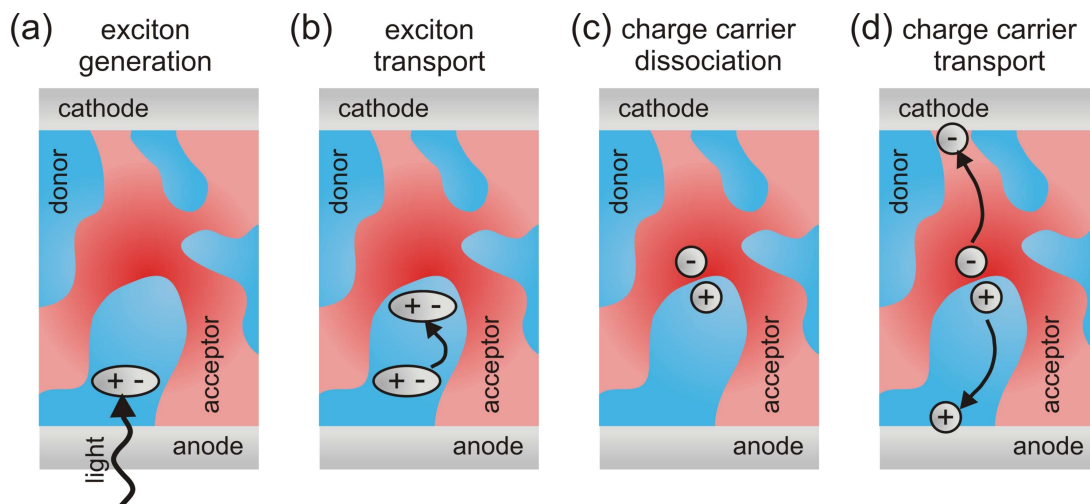


Figure 2.1: Fundamental processes in organic solar cells: (a) exciton generation due to light absorption, (b) exciton diffusion, (c) charge carrier separation, and (d) charge carrier transport.

through sp^2 -hybridization of the carbon atoms, which means that each carbon atom forms three σ - and one π -orbital. It is already important to note here that the π -electrons are fairly delocalized along the polymer chain. The delocalization leads to the conducting properties of this polymer class, which is addressed in more depth in section 2.1.4.

The alternating single and double bonds are characteristic for the so-called conjugated polymers and they are crucial for the general application possibilities of polymers in organic solar cells (OSC). The general working principle of OSCs is described in the following section: The light absorption (exciton generation, figure 2.1(a) and section 2.1.1), the exciton transport to the interface (figure 2.1(b) and section 2.1.2), the charge carrier separation (figure 2.1(c) and section 2.1.3), and the charge carrier transport processes (figure 2.1(d) and section 2.1.4) are individually addressed, always focusing on the application of photoactive polymers.

2.1.1 Exciton generation

Figure 2.2(a) shows the strong optical absorption of an only 42 nm thin film of poly[(1-methoxy)-4-(2-ethylhexyloxy)-p-phenylene-vinylene] (MEH-PPV), which covers a broad spectrum of the visible wavelength regime. In order to explain the observed optical excitations, a closer look to the chemical structure of the polymer is necessary (inset of figure 2.2). The double bonds of the polymer chains consist of one bond set up by two σ -electrons and a second bond, which is formed by overlapping π -orbitals. According to the LCAO (Linear Combination of Atomic Orbitals) theory, two p_z -orbitals of two neighboring

carbon atoms overlap, which leads to the formation of a molecular π -orbital. This π -orbital is characterized by two energetic states, a bonding and an antibonding state, and two delocalized π -electron states. In case of MEH-PPV, the π -states are occupied by eight π -electrons from the phenylene vinylene unit. As it is valid for all multi-electron systems, the different spins of the eight π -electrons compensate in the ground state. In general, the bonding state has a lower energy level than the antibonding one. For conjugated polymers the bonding combination of two π -atomic orbitals leads to the highest occupied molecular orbital (HOMO) and the antibonding combination to the lowest unoccupied molecular orbital (LUMO).[16] As it is derived from the Peierls' theorem [17], the formation of the energetically differing HOMO and LUMO is determined by the bond length alternation (BLA, the bond length difference between the single and double bonds).[18] According to this theory, a one-dimensional polymer chain with one electron per site is unstable and therefore bond length alternations due to chain distortion are induced. As a consequence, the band gap opens up (lowered energy of the ground state). In the case of standard conjugated polymers, the band gap energy is in the range of 1.5 to 3 eV. The chosen example polymer MEH-PPV has a HOMO energy level of -5.3 eV and the LUMO is located at -2.9 eV (see chapter 4 for additional information).

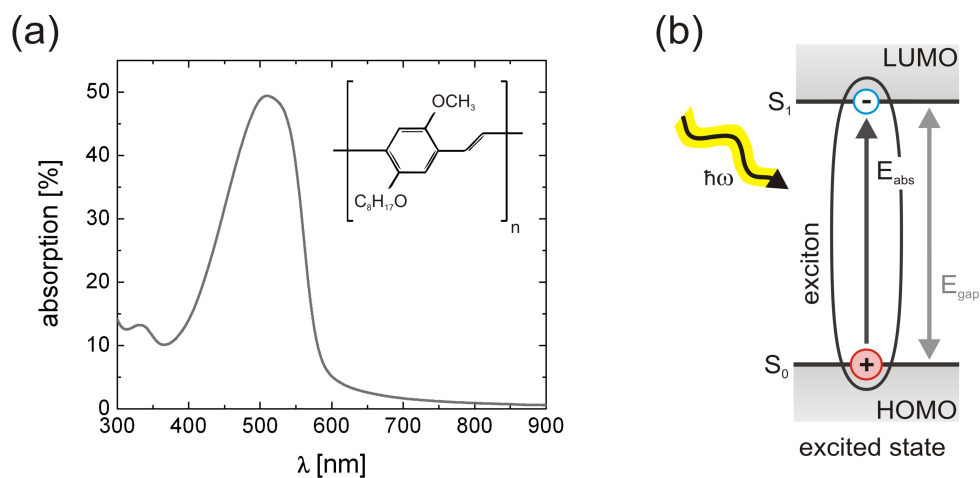


Figure 2.2: (a) The optical absorption spectrum of a MEH-PPV film with a thickness of only 42 nm reveals a strong absorption between 300 and 650 nm. In the inset the chemical structure of MEH-PPV is shown. (b) An electron-hole pair is generated by light absorption as it is represented by the S_0 - S_1 -transition (absorption energy $E_{abs} < E_{gap}$). However, due to the weak screening in organic semiconductors, these electron-hole pairs are strongly bound and are therefore called singlet excitons.

The optical absorption spectrum in figure 2.2(a) is explained by the transfer of an electron from the HOMO level to the next energetically higher level due to the absorption of one photon with an appropriate energy (see figure 2.2(b)). In more detail, this higher level is not directly the LUMO level. Moreover, by lifting an electron from the HOMO level,

an additional positive charge is induced, which exerts an additional attractive Coulomb force on the electron. This superimposing force leads to a shift of the energy level of the HOMO. The combination of the positive charge left on the HOMO level and the implemented negative charge from the lifted electron corresponds to a strongly bound electron-hole pair, which is also called singlet exciton (primary photoexcitation).[19] As a result of the present attractive forces, the excitons have different energy states within the band gap (trap states). In comparison to standard inorganic semiconductors, the strong bonding of the excitons is due to the weak screening of charges in organic semiconductors, which is expressed by their low dielectric permittivity.[20]

However, this simple absorption process still only explains sharp defined peaks in the optical spectrum. The polymer-typical broad absorption in figure 2.2 results from additional mechanical excitations, which are provoked in the polymer besides the electronic excitation. Such excitations are only possible for slight changes in molecular structure. From a quantum mechanical point, the broad absorption maximum is explained by the Franck-Condon principle.[21] Since electronic transitions happen on a much faster timescale than actual motions of the molecular skeleton, they are per se only possible at defined positions in the polymer.

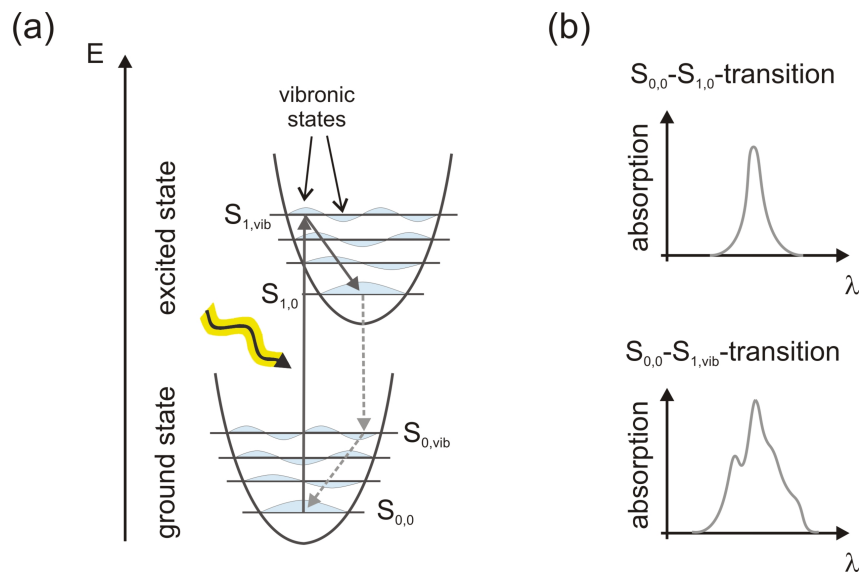


Figure 2.3: (a) Energy profile for effective, harmonic molecule vibrations according to the Franck-Condon principle. The electron is lifted from the ground state $S_{0,0}$ to a higher vibrational band in the excited state $S_{1,vib}$. The relaxation processes (dashed arrows) are only included in order to complete the cycle. In (b) two exemplary absorption spectra are shown for a minimum $S_{0,0}$ - $S_{1,0}$ -transition (upper case) and for a more complex $S_{0,0}$ - $S_{1,vib}$ -transition including the different vibronic bands, which result in additional spectral features.

Figure 2.3(a) shows exemplary exciton band profiles, which include the effective harmonic molecule vibrations according to the Franck-Condon principle. For the simplest absorp-

tion process the electron is lifted from the vibrational ground state of the electronic ground state ($S_{0,0}$) to the vibrational ground state of the excited electronic state ($S_{1,0}$). Only if the molecular structure of the polymer is not influenced by any possible excitation does the transition indeed end in the vibrational ground state of the excited state. Similar to figure 2.2(b), this process would lead to a strong single absorption peak in the wavelength spectrum, as it is also depicted in the upper sketch of figure 2.3(b). However, this simplified absorption process is only rarely observed for photoactive polymers. In general, the electron transfer is accompanied by a shift of the equilibrium value, which leads to an excitation of the vibrational mode. Therefore, it is much more probable that the electron transition ends in an excited vibrational state ($S_{1,vib}$) as depicted in figure 2.3(a). Depending on the structural changes, transitions to different higher and lower vibrational levels are possible as well. Taking into account these different excitation processes, broad absorption spectra can be explained, which consist of multiple peaks with or without additional shoulder features (see lower graph of figure 2.3(b)).

Since the electron is further away from the nucleus in the excited electronic state than in the ground state, the different energy levels in the excited state are more weakly bound. Therefore, the probability of an optical transition into a higher vibrational state is increased. Such transitions are always accompanied by fast relaxations to the lowest vibrational level (e.g. $S_{1,0}$ or $S_{0,0}$) which are also referred to as internal conversions.[22] Nevertheless, the nature and the speed of the vibrational relaxations in conjugated polymers are still under debate in the literature.[23, 24, 25] Since excessive vibrational energy in the excited state might assist photoionization, it is especially interesting for photoactive applications. In such devices the primary photoexcitation is normally a non-relaxed excitation with an electron that stays in higher vibrational modes. Hence, a deepened knowledge about the possible relaxation pathways is necessary to fully understand the optical, as well as the electrical performance of the final device, if applicable.[26]

2.1.2 Exciton transport and dissociation

After the theoretical background of how excitons are generated in conducting polymers by optical absorption, it has to be addressed how they are transported (figure 2.1(b)). For this transport, the interaction between π -electrons of neighboring monomers along the polymer chain plays an important role. In general, excitons, which are created at one monomer by light absorption, propagate along the polymer chain and are not stationary. From an external point of view they appear neutral. Their motion can be described by two different phenomena: (i) *energy transfer*, which describes the transfer of energy between donor and acceptor material and (ii) *energy migration*, which involves multiple energy transfer processes.

For all processes the lifetime of the excitons is a limiting factor, which designates the time before the excitons recombine under photoluminescence. In organic semiconductors the lifetime of singlet excitons is around 1 ns.[27] Since in organic materials the exciton binding energy is much larger than the thermal energy provided by the environment, an additional driving force is needed to dissociate the excitons. Therefore, they have to diffuse to an externally induced interface with an additional material, which has a different energetic band structure. In solution processed films of conjugated poly[3-hexylthiophene] (P3HT) mean diffusion lengths of 4 nm were determined [28], whereas for polyphenylenevinylene values of 12 nm have been observed.[29] Hence, in conjugated polymers the exciton diffusion length is always much smaller than the optical absorption length. Therefore, the concept of bulk heterojunction (BHJ) devices is favored which typically have the shortest donor-acceptor distances. By approaching the interface between host and acceptor material, the exciton is influenced by an altered chemical environment (if compared to excitons in pure bulk material). The resulting modified charge carrier pair is then called exciplex (*excited complex*).[30]

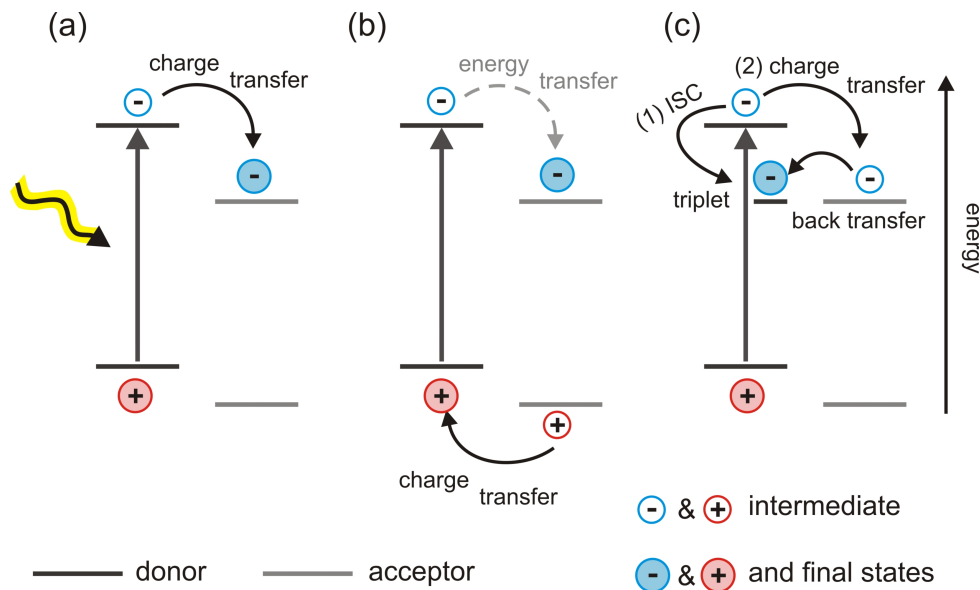


Figure 2.4: (a) Singlet exciton in the donor is dissociated by an electron transfer to the acceptor. For (a) to (c) the final state is given by the filled charge carrier symbols. In (b) the Förster energy transfer is shown: the energy transfer of the exciton from donor to acceptor is accompanied by a hole transfer from acceptor to donor. In (c) the loss processes of triplet excitons are illustrated: (1) if the intersystem crossing (ISC) is faster than the charge transfer, the singlet exciton is converted to a triplet state. In (2) the electron-hole pair from the charge transfer is not separated and it is therefore transferred back to a triplet exciton level. For both cases no free charges are generated.

It must always be taken into account that excitons can only diffuse within their mean diffusion length. However, once an exciton has reached the interface to the acceptor material, a charge is transferred. In figure 2.4(a) the charge transfer of a singlet exciton

electron from the donor to the acceptor material is illustrated. This process has been widely investigated for many polymer blend systems, e.g. polyphenylenevinylene blends [31] or polymer:fullerene systems.[32] Ultrafast spectroscopic measurements have shown that this transfer happens on a timescale in the order of tens of femtoseconds.[33] Besides this straightforward process, also the so-called *Förster transfer* is involved in the charge carrier generation.[34] The principles of this charge transfer process are depicted in figure 2.4(b). As this process is very important for actual devices, it is explained in more detail: After an exciton is generated in the donor material, energy is transferred to the acceptor, which again results in a hole transfer back to the donor. The intermediate step is ascribed to a Förster resonant energy transfer, which transports the whole excitation energy from donor to acceptor.[34] Förster et al. have already proven that the resonance energy transfer rate w_{ETR} from an excited donor to an acceptor is given by [35]

$$w_{ETR}(r) = \frac{1}{\tau_D} \left(\frac{R_{F,0}}{r_{DA}} \right)^6, \quad (2.1)$$

where r_{DA} is the distance between the materials, τ_D the donor lifetime, and $R_{F,0}$ the critical Förster radius. $R_{F,0}$ describes the distance at which the energy transfer balances the natural deactivation of the excited donor. In general, this transfer process requires overlapping absorption and fluorescence spectra of the acceptor and the donor material and very small distances between both materials. In more detail, the critical Förster radius is given by

$$R_{F,0}^6 = \frac{9000(\ln 10)\kappa^2\phi_{f,D}}{128\pi^2 N_A n^4} \int_0^\infty F_D(\lambda)\epsilon_A(\lambda)\lambda^4 d\lambda. \quad (2.2)$$

In equation (2.2) the integral includes the overlap of the emission spectrum $F_D(\lambda)$ of the donor and the absorption spectrum $\epsilon_A(\lambda)$ of the acceptor. In addition, the critical Förster radius depends on the fluorescence quantum yield $\phi_{f,D}$ of the donor, the refractive index n at the spectral overlap, and the Avogadro's number N_A . The orientation factor κ^2 is given by the angle between the transition dipole moments of the donor and acceptor θ_{DA} , and the angles between each of these dipoles and the vector connecting their centers θ_D and θ_A

$$\kappa^2 = (\cos \theta_{DA} - 3 \cos \theta_D \cos \theta_A). \quad (2.3)$$

From a practical point of view $\langle \kappa^2 \rangle$ is averaged over the probabilities of all orientations. Therefore, $\langle \kappa^2 \rangle$ -values of $2/3$ are used for particles which undergo rotational motions faster than the fluorescence lifetime and 0.476 for randomly oriented dipoles.[36, 37] Since the Förster resonant energy transfer strongly depends on the distance between donor and

acceptor, it is also a good measure to investigate the phase separation in bulk heterojunction films.[38]

In figure 2.4 not only the possible exciton dissociation processes are illustrated (see (a) and (b)), but in (c) also the loss processes of triplet excitons are depicted, which are discussed in more detail in the following section.

2.1.3 Charge carrier pair dissociation

After a singlet exciton has been dissociated at the donor-acceptor interface, the electron and the hole remain on the acceptor and the donor material, respectively. Although spatially separated, they are still bound by Coulomb forces [20] and therefore have to be separated in order to gain free charges (figure 2.1(c)). Such bound charges are also called polaron pair. In general, a polaron describes a charge, e.g. an electron or a hole, which is associated with a distortion of the charge's surrounding. This combination is only observed for disordered organic materials which have deformed molecular structures if an additional charge is put on a certain molecular site.

From a theoretical point of view this process is commonly described in context of the Onsager model, which is suited for the dissociation of excitons and polaron pairs (more details in section 2.1.4).[39] Braun further specified this model to also account for the finite lifetimes of the bound states.[40] As a consequence, the final model can be applied to describe the dissociation of charge transfer states in donor-acceptor systems, as well. According to this model different evolution steps are possible for such polaron pairs: (i) They recombine to the ground state at a constant rate, which is defined by its inverse lifetime $k_f = \tau_{pp}^{-1}$, where τ_{pp} is the polaron pair lifetime. (ii) They dissociate to free charges at a rate k_d . However, after dissociation, the resulting free charges have a probability k_r to again generate bound polaron pairs.

Based on a balance between recombination and dissociation, Onsager used the recombination rate k_r to calculate the corresponding dissociation rate k_d . As a result, the dissociation probability $P(F_{dis})$ is derived in dependence on the electric field F_{dis}

$$P(F_{dis}) = \frac{k_d(F_{dis})}{k_d(F_{dis}) + k_f}, \quad (2.4)$$

where the dissociation rate $k_d(F_{dis})$ is given by

$$k_d(F_{dis}) = \frac{3\gamma}{4\pi r_{pp}^3} \exp\left(-\frac{E_b}{kT}\right) \frac{J_1(2\sqrt{-2b_{dis}})}{\sqrt{-2b_{dis}}}. \quad (2.5)$$

In the upper equation $\gamma = e\mu/\epsilon\epsilon_0$ is the Langevin recombination factor, which depends on the sum of electron and hole charge carrier mobility μ , the electric constant ϵ_0 , the

permittivity of the material ϵ , and the elementary charge e . The initial polaron pair radius is denoted by r_{pp} . $E_b = e^2/(4\pi\epsilon\epsilon_0 r_{pp})$ corresponds to the Coulomb binding energy, kT to the thermal energy, J_1 to the Bessel function of order one, and b_{dis} is given by $e^3 F_{dis}/((\pi\epsilon\epsilon_0 k^2 T^2))$. Equation (2.4) reveals a linear dependency of the polaron pair dissociation probability on the mobility μ and the polaron pair combination rate k_f . For organic solar cells the Braun-Onsager model is the most common one to describe charge carrier dissociation.[41] However, the Braun-Onsager theory does not account for hopping transport and energetic or spatial disorder. Therefore, also variations in dissociation yield are found, when comparing results from Monte Carlo simulations with predictions by the Onsager-Braun models.[42]

As it is shown in figure 2.4(c), polaron pairs which are not dissociated can recombine via an electron back transfer from the acceptor to a triplet exciton state. This loss mechanism is only possible for triplet energies which are beneficial for the acceptor electron. In addition, charge carrier extraction can also occur at the wrong electrode. Since polaron pairs dissociate under the influence of mutual Coulomb forces, they can diffuse jointly if the in-built electric field is not much higher than the influence of energetic disorder. For a dielectric constant ϵ of e.g. 3 the Coulomb radius at room temperature is 18 nm. For standard polythiophene:fullerene blends it was found that the polaron density depends exponentially on the Gibbs free energy ΔG , which corresponds to the difference between singlet exciton energy and the energy of the polaron pair.[43] This observation implies that excess energy after exciton dissociation results in so-called hot polaron pairs, which have an additional kinetic energy. This energy excess supports the polaron pair dissociation due to a larger initial spatial separation.

2.1.4 Charge carrier transport

Finally, the dissociated charges have to be transported to the corresponding electrodes as depicted in figure 2.1(d). Already in 1980, Su, Schrieffer, and Heeger proposed a soliton model to describe the electrical conductivity in polymers.[6] In comparison to polarons, which are induced by additional charges, solitons are due to defects in single and double bond alteration. Hence, they can also appear neutral and are stabilized by the neighboring lattice sites. They move along the polymer backbone at a constant velocity without structural and energetic modifications. However, for the investigated semiconducting polymers the photoinduced polarons dominate the conductivity processes.

In comparison to a band transport, which is typically found in non-polymer semiconductors, for solution processed thin films of organic semiconductors the electrical transport is governed by hopping processes. This different mechanism is mainly due to a missing long-range order in the entangled polymer networks. In case of bulk heterojunction solar

cells the donor material is mainly hole conducting and the acceptor material favors an electron transport. In solution processed conducting homopolymer films the degree of disorder of the polymer chains depends on the crystallinity of the material. If the corresponding wavefunctions of electron orbitals from neighboring carbon atoms do not overlap strongly, the localized charge carries can only be transported via slow hopping processes. In general, the electron hopping transport is given by the tunneling probability from one atom to the neighboring one and thereby is a thermally activated process. Marcus derived a hopping rate ν_{ij} , which depends on the transfer integral I_{ij} between the corresponding wave functions of two sites i and j [44, 45]

$$\nu_{ij} = \frac{|I_{ij}|^2}{\hbar} \sqrt{\frac{\pi}{E_\lambda kT}} \exp\left(-\frac{(\Delta E_{ij} + E_\lambda)^2}{4E_\lambda kT}\right). \quad (2.6)$$

Here, kT is the thermal energy, E_λ the reorganization energy, and ΔE_{ij} is an energetic contribution given by the energy difference between the two sites i and j , which is commonly given by a Gaussian distribution. Hence, in equation (2.6) the distortion of the polymer chains due to a charge as well as the energetic disorder are taken into account. An additional approach was developed by Miller and Abrahams [46]

$$\nu_{ij} = \nu_0 \exp(-\gamma r_{ij}) \begin{cases} \exp\left(-\frac{\Delta E_{ij}}{kT}\right) & , \Delta E_{ij} > 0 \text{ (uphop)} , \\ 1 & , \Delta E_{ij} < 0 \text{ (downhop)} . \end{cases} \quad (2.7)$$

In the upper equation ν_0 is the maximum hopping rate, γ the inverse localization radius, and r_{ij} the distance between the two sites i and j . Similar to the Marcus-idea, in equation (2.7) the tunnelling contribution is included by the first exponent. However, in the approach by Miller and Abrahams the hopping process is divided into a direction upwards in energy, which is described by an additional Boltzmann term, and downwards in energy, which is just governed by the tunneling mechanism.

It has to be denoted that also in disordered systems, high conductivity values, and hence high hopping rates, are measured on a mesoscopic scale, e.g. for a charge transport along a polymer chain. In case of organic devices, for which the macroscopic conductivity is more important, the real hopping values strongly differ from the intrinsic values due to structural defects or trap states. Nevertheless, the mesoscopic hopping values, which are actually the ones discussed in the framework of the Marcus- and the Miller-Abrahams-approach [44, 46], have been used for Monte Carlo simulations [47] and introduced to hopping master equations.[48] Both ideas were also successfully applied not only to single materials [47], but also to simulate the charge carrier conductivity in donor-acceptor bilayers [48] and bulk heterojunctions.[49] Bässler's work in particular should be mentioned, as he introduced a Gaussian disorder model to describe the charge transport in a

Gaussian density of states. According to his results the charge carrier mobility μ depends dominantly on the temperature T and the internal field F_{int}

$$\mu = \mu_{\infty} \exp \left(- \left(\frac{2\sigma_{dis}}{3kT} \right)^2 + C_{bas} \left(\left(\frac{\sigma_{dis}}{kT} \right)^2 - \Omega_{spa} \right) F_{int}^{1/2} \right). \quad (2.8)$$

Hence, the mobility is given by a distribution with an energetic width σ_{dis} and a spatial disorder, which is included by Ω_{spa} . C_{bas} is added as scaling factor and kT is again the thermal energy. A material-specific pre-factor mobility is included by μ_{∞} . Up to now, this parametric model has been widely applied and adapted to specific systems, e.g. by introducing a correlation between spatial and energetic disorder.[50]

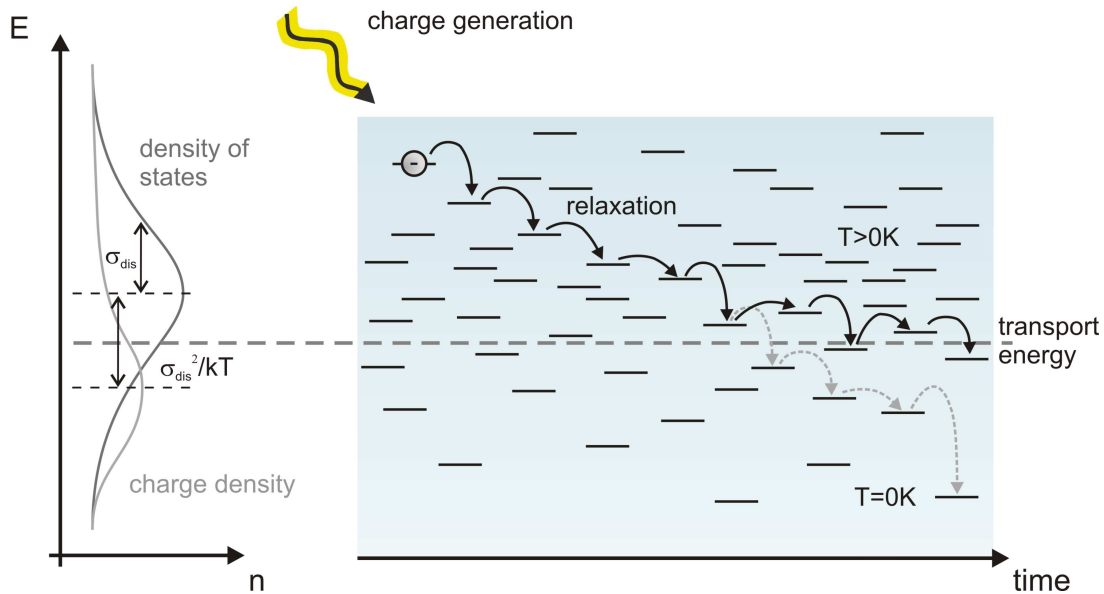


Figure 2.5: The density of states in an organic semiconductor given by a Gaussian distribution with an energetic width σ_{dis} . The center of the charge distribution is shifted by σ_{dis}^2/kT in comparison to the maximum of the density of states. After the photogeneration of the charge carriers and possible relaxation steps the steady-state charge transport occurs around the effective transport energy. At 0 K temperature, the charge carriers are trapped at the deepest states.

After it was found that in organic semiconductors the charge carrier mobility depends on the carrier concentration [51], a modified Gaussian disorder model was invented.[52] This approach includes the presence of charge traps, which are simplified as lower energy states of the Gaussian distribution of the density states. These trap states result in a mobility that depends on the charge concentration. As a consequence, the so-called transport energy plays an important role.[53] This value takes into account that in disordered organic systems the mean charge density thermalizes to $-\sigma_{dis}^2/kT$ below the maximum of the density of states distribution at a known temperature. As already mentioned, conducting

organic materials have typically a Gaussian distribution for the density of states with a width σ_{dis} . In figure 2.5 the charge transport via hopping processes around the transport energy is sketched. Since charge carriers with energies below the threshold of the transport energy are immobile, they do not result in higher conductivities. The Gaussian shape of the density of states leads to an increasing number of available charge carriers for higher transport energies due to an increased thermal energy (see figure 2.5). The absolute amount of charge carriers is therefore given by the sum of the mobile charges, which contribute to the conductivity, and the immobile charges, which are trapped in the tail of the distribution.

However, it has to be denoted that the local charge transport in organic semiconductors is often much faster than the transport on a macroscopic scale.[54] Although many different theoretical approaches have been conducted, a complete multiscale model for the charge transport still does not exist for conjugated polymers. Such a model would be of utmost interest to fully describe highly functional multi-component systems.

2.2 Phase separation in polymer blend films

In order to guarantee an efficient charge carrier separation in BHJ solar cells between donor and acceptor material, a high interfacial area is crucial (see figure 2.1(c)). But on the contrary, also an efficient transport of the generated charge carriers to the corresponding electrodes is necessary along separated percolation paths (see figure 2.1(d)). Therefore, a distinct control of the phase separation in bulk heterojunction films is highly desired.

The following section focuses on the theoretical aspects of the phase separation mechanisms in polymer blend systems. After the classic Flory-Huggins approach is discussed, three specialized models are introduced, which are suited for conducting polymer blends. These models are modified in order to take into account the rodlike behavior of the polymer chains and the tendency to crystallize.

2.2.1 Classic Flory-Huggins approach

Flory and Huggins were the first to establish a theoretical routine to describe the mixing properties of a pair of polymers.[55, 56, 57, 58] In order to find out whether mixing occurs for two components A and B , they investigated the change in the corresponding Gibbs free energy ΔG_{mix}

$$\Delta G_{mix} = G_{AB} - (G_A - G_B) , \quad (2.9)$$

where G_A and G_B are the Gibbs free energies of the two separate compounds and G_{AB} of the mixed state. In the Flory-Huggins approach ΔG_{mix} is given as the sum of an increasing translational entropy ΔS_t and a change of the local interactions of the monomers ΔG_{loc} for a given temperature T

$$\Delta G_{mix} = -T\Delta S_t + \Delta G_{loc} . \quad (2.10)$$

The decrease in Gibbs free energy $-T\Delta S_t$ always favors mixing, whereas the influence of ΔG_{loc} depends on the monomer-monomer pair interactions. However, van der Waals forces, which are common in polymer systems, are often stronger between equal monomers than for unlike pairs. Therefore, typically ΔG_{loc} is positive and hence opposes mixing. Based on a simple lattice model, the mixing entropy can be derived statistically. For the calculations, all lattice sites must always be occupied, but no double entries are possible, and no inter-particle interactions are taken into account either. In general, the entropy S is given by the number of the possible lattice configurations Ω through $S = k \ln \Omega$. In figure 2.6 the stepwise evolution of the lattice model is shown starting from (a) a mixture of two monomers, (b) to a polymer-solution, and (c) a polymer-polymer blend system.

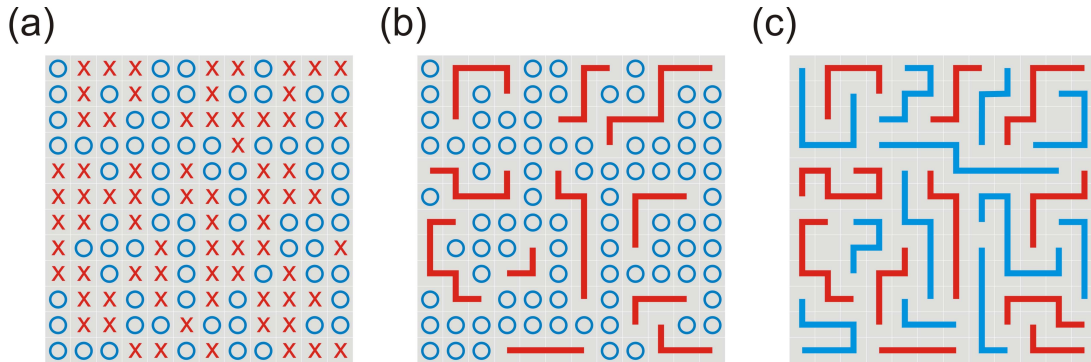


Figure 2.6: Evolution of the lattice model applied for the statistical derivation of the Gibbs free energy. In (a) the model for a monomer-monomer, in (b) for a polymer-solution, and in (c) for a polymer-polymer blend system are shown.

Based on the results for the entropy of the monomer-monomer and the polymer solution systems (figure 2.6(a) and (b)), the complete disorder entropy S_{P-P} for the polymer blend system (figure 2.6(c)) is derived using the Stirling equation

$$S_{P-P} = -R \left(\frac{\Phi_A}{N_A} \ln \Phi_A + \frac{\Phi_B}{N_B} \ln \Phi_B \right) , \quad (2.11)$$

where $R = N_A k$ depicts the ideal gas constant and $\Phi_{A,B} = n_{A,B}^{ls} / (n_A^{ls} + n_B^{ls})$ are the corresponding volume ratios of the two compounds ($n_{A,B}^{ls}$ is the number of lattice sites occupied by compound A and B , respectively). The degree of polymerization is given

by $N_{A,B}^{pol}$. The entropy is decreased as compared to polymer solutions due to the reduced degree of freedom. However, for a correct description the interaction between the two polymers has to be added. By considering only the interaction between two directly neighboring lattice sites, the change in enthalpy is derived as

$$\Delta E = (n_A^{ls} + n_B^{ls})kT\delta_{int}\Phi_A\Phi_B. \quad (2.12)$$

In the upper equation $\delta_{int} = ((z_{cn} - 2)\Delta w_{int})/kT$ is given by the coordination number z_{cn} , which corresponds to the number of possible interaction partners, and the molecular interaction parameter Δw_{int} , which depends on the chemical properties of the compounds. The molecular interaction parameter can be determined via melting point depression [59] and it is crucial for a correct prediction of phase diagrams.[60]

On the basis of the results from above, the free enthalpy of a polymer blend is calculated as

$$\Delta G_{mix} = RT \left(\frac{\Phi_A}{N_A^{pol}} \ln \Phi_A + \frac{\Phi_B}{N_B^{pol}} \ln \Phi_B + \chi \Phi_A \Phi_B \right). \quad (2.13)$$

In this equation $\chi = (a/k_B T) + b$ is the polymer-polymer interaction parameter (also called Flory-Huggins parameter), which depends on an enthalpic ($a/k_B T$) and an entropic (b) part. However, it must be noted that the derived results cannot directly be applied to the phase separation processes in polymer thin films. For such films Binder has shown that the additional substrate- and air-interface play an important role.[61] Besides a phenomenological discussion, Binder has also developed a mean-field approach, which combines the Flory-Huggins free energy [62] with a gradient-square approximation [63] taking into account also the influence of additional surface terms.[64] The influence of the surfaces leads to inhomogeneities $\Gamma(z)$ in film composition along the sample normal (denoted here as z -direction and with a total film thickness D). Therefore, the excess free energy ΔF_{blend} of the blend is given by [65]

$$\frac{\Delta F_{blend}}{k_B T} = \frac{1}{b_{ls}} \int_0^D dz \left(f(\Gamma(z)) + \kappa(\Gamma) \left(\frac{d\Gamma(z)}{dz} \right)^2 \right) + f_s^{bare}(\Gamma_0) + f_s^{bare}(\Gamma_D). \quad (2.14)$$

In equation (2.14) the f_s^{bare} -terms correspond to interfacial contributions to the free energy density and are discussed later. The effective lattice spacing is included by b_{ls} and $\kappa(\Gamma)$ is the gradient energy. Exemplary, for a symmetric blend (equal chain lengths $N_A^{pol} = N_B^{pol} = N^{pol}$) the gradient energy is derived as

$$\kappa(\Phi) = b^2 / (39\Gamma(z)(1 - \Gamma(z))) . \quad (2.15)$$

According to the simple Flory-Huggins approach the free energy density $f(\Phi)$ is calculated as

$$f(\Phi) = \frac{1}{N^{pol}} \left(\frac{\Phi_A}{N_A^{pol}} \ln \Phi_A + \frac{\Phi_B}{N_B^{pol}} \ln \Phi_B \right) + \chi \Phi_A \Phi_B - \Delta\mu , \quad (2.16)$$

where $\Delta\mu$ is the normalized chemical potential difference between both components.[61] In equation (2.14) the contributions of the interfaces to the free energy are included by the terms $f_s^{bare}(\Gamma_0)$ (substrate-polymer) and $f_s^{bare}(\Gamma_D)$ (polymer-air).

The influence of the substrate contributions is also seen in a qualitative phase diagram of a symmetric polymer blend (figure 2.7). The phase transition from homogeneous mixing to two-phase regions depends on the volume ratio $\Phi = \Phi_A/\Phi_B$ and the interaction parameter χ . In figure 2.7 the phase boundary lines and the two-phase regions are plotted for a semi-finite (blue, $D \rightarrow \infty$) and a finite thin film geometry (red). The χ - ϕ pairs, which result in homogeneous mixing, are depicted in gray.

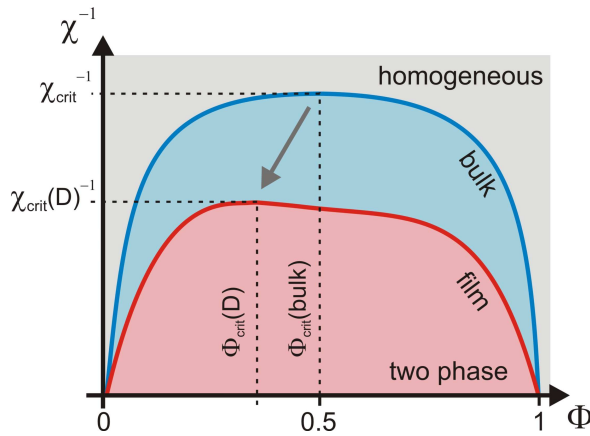


Figure 2.7: Qualitative phase diagram of a symmetric blend in thin film (red) and in semi-finite geometry (blue): The gray area illustrates the homogeneous phase, the blue area the two-phase region for the bulk case, and the red area for the thin film geometry. The arrow depicts the shift of the critical volume fraction.

For a symmetric polymer blend the critical volume fraction is $\Phi_{crit} = 1/2$. It describes the polymer ratio at which phase separation first sets in. Along a phase boundary line the polymer-polymer interaction parameter is always smaller than its critical value.[65] For polymer blend films, which consist of components with different surface attractions, the critical volume fraction is shifted. In the case of a preferential wall attraction of component B the symmetry from the bulk case is lost, and the critical volume fraction and the critical inverse interaction parameter χ_{crit}^{-1} are shifted to smaller values, respectively. For a stronger attraction of component A to the polymer-substrate interface, a similar shift to larger volume fractions Φ_A is observable. Nevertheless, in both cases χ_{crit}^{-1} is depressed, which favors a better miscibility of the polymer-polymer blend.[61]

2.2.2 Crystalline ordering in polymer blend films

In comparison to standard coiled polymers, conducting polymers have a more rodlike chain conformation because of their conjugated backbone. As a consequence, the conducting materials have a reduced degree of freedom at the bonds along the polymer backbone (see also figure 2.6(b) and (c)) which favors a crystalline ordering. Therefore, a modified theoretical approach based on the Flory-Huggins (FH) lattice model is necessary. One approach, which was already successfully applied to polymer:liquid crystal blends, appears to be appropriate for conducting polymer blends as well, since it already accounts for nematic polymer orientations in the crystalline phase.[66] Therefore, the nematic phase, in which the rodlike polymer chains are aligned parallel, was described according to the Maier-Saupe (MS) approximation.[67, 68] In this modified FH/MS theory the free energy G for polymer blends with a crystalline component is given by the sum of the aforementioned Gibbs free energy of mixing G_{mix} (see equation (2.13)) and an additional term for nematic ordering G_{cry} [69]

$$G = G_{mix} + G_{cry} . \quad (2.17)$$

The contribution of the crystalline ordering in the nematic phase is given by the Maier-Saupe mean field approach, which includes the concentration of the crystalline compound B [66]

$$G_{cry,B} = RT\Phi_B \left(\int_0^1 f_{or}(\theta_{cry}) \ln [4\pi f_{or}(\theta_{cry})] d(\cos \theta_{cry}) - \frac{1}{2} \nu_{int} \Phi_B s_{or}^2 \right) . \quad (2.18)$$

In equation (2.18) θ_{cry} depicts the orientational angle between a reference axis and the direction of the crystalline molecule, $f_{or}(\theta)$ the corresponding distribution function, ν_{int} the interaction parameter according to de Gennes [70] (more information is given below along with equation (2.24)), and s_{or} is the orientational order parameter. The latter is given by

$$s_{or} = \frac{1}{2} (3 \langle \cos^2 \theta_{cry} \rangle - 1) . \quad (2.19)$$

It includes the averaged orientational angle, which is, e.g. for a symmetric distribution around the reference axis, calculated as

$$\langle \cos^2 \theta_{cry} \rangle = \int_0^1 \cos^2 \theta_{cry} f_{or}(\theta_{cry}) d(\cos \theta_{cry}) . \quad (2.20)$$

Assuming a Gibbs ensemble, the orientation distribution function $f_{or}(\theta_{cry})$ of rodlike polymer chains with a crystalline ordering is deduced as [71]

$$f_{or}(\theta_{cry}) = \frac{1}{Z} \exp\left(-\frac{u(\theta_{cry})}{kT}\right). \quad (2.21)$$

The corresponding partition function Z is given by

$$Z = \int \exp\left(-\frac{u(\theta_{cry})}{kT}\right) d(\cos \theta_{cry}). \quad (2.22)$$

$u(\theta_{cry})$ is a pseudopotential, which is used as an approximation to simplify the ordering orientation. Shen and Kyu used the following description [66]

$$\frac{u(\theta_{cry})}{kT} = -\frac{1}{2}m_{pf}(3 \cos^2 \theta_{cry} - 1). \quad (2.23)$$

As it was also introduced by de Gennes [70], the mean field parameter m_{pf} describes the strength of the potential field. In more detail, the interaction parameter ν_{int} from equation (2.18) is the Maier-Saupe interaction parameter, which shows an inverse temperature dependence

$$\nu_{int} = C_{MS} \frac{T_{NI}}{T}. \quad (2.24)$$

C_{MS} is a material depending constant and T_{NI} corresponds to the nematic-isotropic transition temperature.

In a similar, but more compressed notation, Mucha derived the total Gibbs free energy as follows [69]

$$G = RT \left(\frac{\Phi_A}{N_A^{pol}} \ln \Phi_A + \frac{\Phi_B}{N_B^{pol}} \ln \Phi_B + \chi \Phi_A \Phi_B - \Phi_B \sum S - \frac{1}{2} \nu \Phi^2 S^2 \right), \quad (2.25)$$

where $-\Phi_B \sum S$ is the general decrease of entropy due to alignment of the crystalline compound B . This additional negative contribution results in an overall reduced free energy for crystalline polymers, which furthermore leads to a reduced miscibility of the two components. However, for polymer blends with an intensified crystalline ordering, strong interfacial effects are also likely if the phase separation is investigated in thin film geometry (see section 2.2.1).

Nevertheless, it must be noted that the illustrated FH/MS approach was in a first instance derived for polymer:liquid crystal blends. Although such systems generally behave similarly to conducting polymer blends, which also tend to crystallize, this method does not fully take into account the rodlike chain conformations.

2.2.3 Rodlike:flexible polymer blend

The previous section showed how a crystalline orientation factor is introduced to the standard Flory-Huggins model. However, if this idea is applied to conducting polymers with a rodlike chain conformation, the elongation of the polymer needs to be taken into account as well. Therefore, in order to describe the miscibility of a crystalline and a flexible chain polymer, Lee et al. came up with the idea to add a degree of disorder for the crystalline component.[72]

Figure 2.8: Schematic illustration of a partial Flory-Huggins lattice model occupied with a flexible (red line) and a rodlike polymer (blue line).

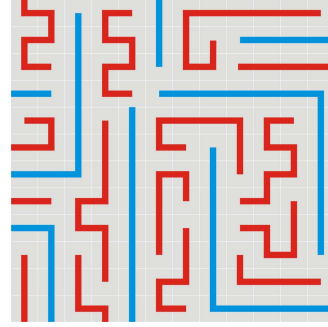


Figure 2.8 shows a schematic illustration of the Flory-Huggins lattice model discussed above (see figure 2.6), which is now occupied with a binary rodlike:flexible polymer blend system. The flexible polymer A is illustrated by red and the crystalline component B by blue lines. For the following calculations the crystalline polymer is simplified as a freely jointed chain with m rodlike chain sections of equal length. Under the assumption of a completely ordered structure, the configurational partition function Z_M depends on the mole numbers $n_A = \Phi_A/N_A^{pol}$ and $n_B = \Phi_B/N_B^{pol}$ as follows

$$Z_M = \frac{(n_B x_B + y m n_A)! y^{2m n_A} z_B^{n_B}}{n_A! n_B! (n_A m x_A + n_B x_B)^{n_A(m y - 1) + n_B(x_B - 1)}} . \quad (2.26)$$

In this equation $y = \sin \theta_{cry}$ denotes again the disorientation in dependence on the angle of the domain axis of the crystalline compound θ_{cry} (see equation (2.18)). In the case of a completely ordered structure, y is equal to one. The $m - 1$ freely rotating joints are further described by x_A , which denotes the axial ratio of each of the m rods, and x_B , which is the contour length of the flexible polymer chain. The corresponding internal configurational partition function is included via z_B . [73] Based on the Stirling approximation, these results are used to derive the Gibbs free energy of mixing as

$$\Delta G_{mix} = RT (n_A \ln \Phi_A + n_B \ln \Phi_B + \chi \Phi_A \Phi_B (x_A m n_A + x_B n_B) + \Delta G_{cry}) , \quad (2.27)$$

with

$$\begin{aligned} \Delta G_{cry} = & n_A m y_p \ln \frac{y_p}{x_A} - (x_B n_B + m_b y_b n_A) \ln \frac{(x_B n_B + m_b y_b n_A)}{x_A m_b n_A + x_B n_B} \\ & + n_A (m \ln y_p^2 - m y_p + 1) - n_A (m_b \ln y_b^2 - m_b y_b + 1). \end{aligned} \quad (2.28)$$

In equation (2.28) y_p is the orientation factor of the pure crystalline component and y_b of the blend phase. In the blend films the number of freely jointed chains m_b is reduced in comparison to the pure state. This equation also shows that the contribution of the crystalline ordering is divided in a combinatorial and an orientational part. If a perfect order of the crystalline component is assumed, y_p and m simplify to one, whereas if a completely disordered structure is implied (e.g. $y_p = y_b = x_A$), the orientational contribution becomes zero. As a result, equation (2.27) is reduced to the already discussed Flory-Huggins equation (see equation (2.13)) in the case of complete disorder.

On the contrary to the model from section 2.2.2, the recent approach explicitly considers the rodlike polymer chain character. In principle, this model is also suited to describing the standard crystallization of rodlike polymers. Strobl and coworkers have not only shown that polymers typically crystallize via the formation and growth of lamellar crystallites, but they have also found a kinetic behavior for the polymer crystallization.[74] Hence, the thermodynamic approach from above cannot be used to fully describe the phase separation in conducting polymer blends.

2.2.4 Dynamic mean field approach

Since phase separation in polymer blends is mainly a diffusion driven process that already starts in solution and evolves during coating, Liu and Fredrickson developed an approach based on the dynamic mean field theory.[75] Their statistical approach is based on translational diffusion coefficients of the flexible component and on rotational diffusion coefficients of the rodlike component of the blend. Both are combined via thermodynamic forces, which are given by the derivatives of the corresponding free energy functionals. Therefore, they calculated the response functions of interacting polymer blends according to the random phase approximation.[76] As possible interactions between the two components, direct chemical interactions are included by the polymer-polymer interaction parameter χ , anisotropic interactions among the rodlike polymer chains are considered in the Maier-Saupe parameter w_{MS} , and a total chemical potential μ is also taken into account. Liu and Fredrickson assumed that the volume fractions of both components Φ_A and Φ_B slightly change within a weak external chemical potential field $h_{A,B}^{eff}(\vec{q}\omega)$, which is given by the wavevector \vec{q}_w and the frequency ω

$$\begin{aligned}
\Phi_A(\vec{q}_w, \omega) &= r_A(\vec{q}_w, \omega) h_A^{eff}(\vec{q}_w, \omega) , \\
\Phi_B(\vec{q}_w, \omega) &= r_B(\vec{q}_w, \omega) h_B^{eff}(\vec{q}_w, \omega) + r_S(\vec{q}_w, \omega) \mathbf{U}_S^{eff}(\vec{q}_w, \omega) .
\end{aligned} \tag{2.29}$$

In the upper equations \mathbf{U}_S^{eff} is a tensor, which is necessary for the symmetric properties of the rodlike polymer chains. r_A and r_B , respectively, are the linear response functions of the flexible (A) and the rodlike (B) component. For standard coiled polymers it is given by

$$r_A = \frac{q_w^2 D_A \Phi_A N_A^{pol}}{-i\omega + D_B q_w^2} \tag{2.30}$$

and for rigid rodlike components by

$$r_B = \frac{q_w^2 D_t \Phi_B N_B^{pol}}{-i\omega + D_t q_w^2} . \tag{2.31}$$

In equation (2.30) q_w^2 denotes the quadratic length of the wavevector \vec{q}_w and $D_{A,B}$ illustrate the center-of-mass diffusion coefficients. In the case of rodlike chains (equation (2.31)) D_t is subdivided into a parallel and a perpendicular translational diffusion

$$D_t = \frac{1}{3} D_{\parallel} + \frac{2}{3} D_{\perp} . \tag{2.32}$$

In equation (2.29) the external effects are included in the chemical potential field by

$$h_{A,B}^{eff} = h_{A,B} + \mu - \chi \Phi_{A,B} , \tag{2.33}$$

where again μ is the chemical potential and χ the interaction parameter. Taking into account all response functions of the interacting mixture (see also reference [75]) the Onsager coefficients, which in general describe the reciprocal relation between simultaneous processes in a thermodynamic system, can be calculated.[77] Under the assumption of a stable isotropic state of the blend, the resulting complex free energy functional is reduced to a more simple linearized approximation

$$\begin{aligned}
G = & \frac{RT}{2V_{tot}} \sum_{\vec{q}_w} \left(\frac{1}{N_A^{pol} \Phi_A} + \frac{1}{N_B^{pol} \Phi_B} - 2\chi + \frac{1}{36} \left(\frac{4}{\Phi_A} + \frac{N_B^{pol}}{\Phi_B} \right) q_w^2 \right) |\Phi_B(\vec{q}_w)|^2 + \\
& \left(\frac{15}{2} \frac{1}{\Phi_B N_B^{pol}} - w + \frac{5}{56} \frac{N_B^{pol}}{\Phi_B} q_w^2 \right) S_1(\vec{q}_w) S_1(-\vec{q}_w) + \\
& \frac{5}{14} \frac{N_B^{pol}}{\Phi_B} q_{w,A} q_{w,B} S_2(\vec{q}_w) S_3(-\vec{q}_w) - \frac{1}{6} \frac{N_B^{pol}}{\Phi_B} q_{w,A} q_{w,B} S_1(-\vec{q}_w) . \tag{2.34}
\end{aligned}$$

In equation (2.34) $S_{1,2,3}$ denote different decoupled nematic orientation densities of rod-like segments, V_{tot} the total system volume, and $q_{w,A/B}$ the wavevector length for both components.

Although this dynamic mean field theory approach is rather complex, it yields insight into the role of molecular ordering on the phase separation. Liu and Fredrickson have shown that due to the presence of orientational order the phase separation can differ strongly for binary polymer blends.[75] A key advantage of this model is the time resolved mapping of the phase separation process. However, due to its multiple variables, this method is only applicable to simple polymer systems with known physical properties.

Reconsidering the illustrated theoretical models for the phase separation in conducting polymer blends, the models in section 2.2.2 and 2.2.3 imply a less favored polymer intermixing due to the rodlike polymer configurations and the polymer crystallization. However, no single model can fully combine both phenomena. It should also be pointed out that the models are in principle only suited to describing the bulk phase separation. In thin film geometry the presence of additional interfaces also has a strong impact on the phase separation. On the basis of these theoretical results, different conducting polymer blend films are investigated concerning phase separation in chapter 5 of this thesis.

2.3 Structuring of polymer films

Plastic deformability of polymeric materials allows the introduction of secondary artificial physical properties to polymer thin films due to an additional surface structuring. In this section the theoretical aspects of two widely applied structuring routines are discussed. The first method is based on a polymer structuring during solution casting, whereas the second approach is temperature and pressure induced.

2.3.1 Solution based texturing

In 1995 Kim et al. established a general solution based structuring routine, which is suitable for polymeric microstructures: micromolding in capillaries (MIMIC).[78, 79] The basic concept of MIMIC is that the polymer solution fills the structures in the master mold due to capillary forces. In general, the capillary forces result from inter-molecular attractive forces between the polymer solution and the surrounding solid surfaces. Therefore, the surface tension of the solution and the adhesion forces are crucial for successful imprinting. The corresponding surface pressure difference ΔP of the solution on the surface is described by the Young-Laplace equation

$$\Delta P = \gamma_{sur} \left(\frac{1}{R_x} + \frac{1}{R_y} \right), \quad (2.35)$$

where R_x and R_y are the curvature radii in both axes parallel to the sample surface and γ_{sur} is the surface tension (equivalent to surface free energy). The surface adhesion is also well described by the contact angles between solution and substrate at the intersection. As a model system for the MIMIC approach, the interfacial free energies for solution, which moves from a spherical drop into a square hollow tube, are discussed. A schematic illustration with the important geometric properties is presented in figure 2.9(a).[80, 81]

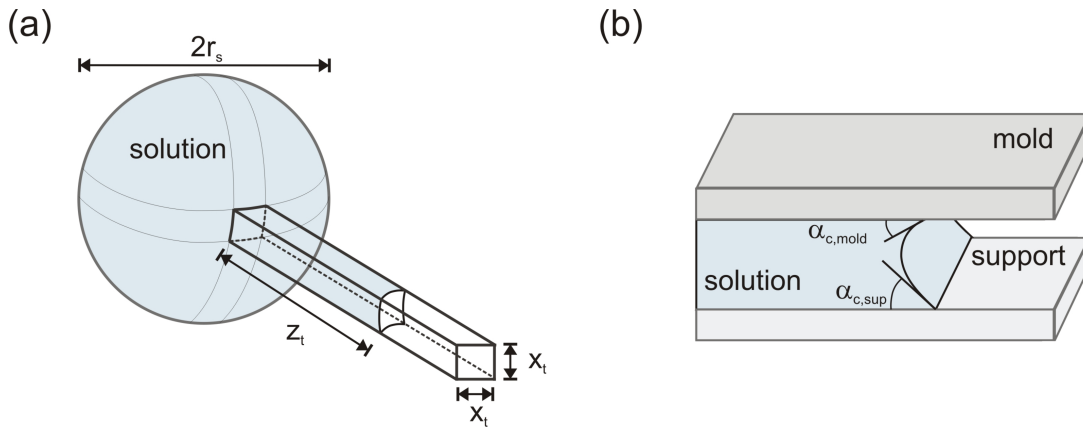


Figure 2.9: Models for capillary micromolding: In (a) a drop of solution moving in a hollow tube is shown and in (b) the contact angles of solution sandwiched between two different surfaces are illustrated.

If the surface properties of the hollow tube are assumed to be equal, the total change in interfacial free energy ΔF_i depends on the changes in interfacial surface area of the solution

$$\Delta F_i = \gamma_{lv} \Delta A_{sphere} - f(\gamma_{s1l}, \gamma_{s2l}) \Delta A_{channel}. \quad (2.36)$$

In the upper equation, γ_{lv} represents the liquid-vapor and γ_{sl} the solid-liquid interfacial

free energy.[79] Since in real application the sidewalls of the channels are not equal, the possible influence of two different surface properties is already taken into account in $f(\gamma_{s_1l}, \gamma_{s_2l})$. The interfacial free energies γ_{s_1l} and γ_{s_2l} correspond to modified surfaces, e.g. substrate and mold material. Including the mathematical expression for the changes in surface area, the interfacial free energy is modified to [78]

$$\Delta F_i = \frac{x_t^2 \Delta z_t \gamma_{lv}}{r_s} - (3x_t \Delta z_t (\gamma_{s_1v} - \gamma_{s_1l}) + x_t \Delta z_t (\gamma_{s_2v} - \gamma_{s_2l})) , \quad (2.37)$$

where γ_{sv} is the solid-vapor interfacial free energy. For small channels ($r \gg x$) the first term in equation (2.37), which is due to the polymer solution, can be neglected and the free energy simplifies to

$$\Delta F_i \approx - (3x_t \Delta z_t (\gamma_{s_1v} - \gamma_{s_1l}) + x_t \Delta z_t (\gamma_{s_2v} - \gamma_{s_2l})) . \quad (2.38)$$

As a result, the filling of the channels is mainly dominated by the free energies of the solid-vapor and the solid-liquid interfaces. Since the capillary is only filled for a negative change in interfacial free energy ($\Delta F_i < 0$), negative values for $(\gamma_{s_1v} - \gamma_{s_1l})$ and $(\gamma_{s_2v} - \gamma_{s_2l})$ have to be avoided in the experiment.

Figure 2.9(b) depicts a side-cut view of polymer solution, which is sandwiched between substrate and mold material, as it is also found in the channel of figure 2.9(a). Including the different contact angles between solution and support $\alpha_{c,sup}$ and solution and mold $\alpha_{c,mold}$, the interfacial free energy changes to

$$\Delta F_i \approx x_t \Delta z_t \gamma_{lv} (3 \cos \alpha_{c,sup} + \cos \alpha_{c,mold}) . \quad (2.39)$$

As a consequence, for any contact angle values of $\alpha_{c,sup}$ and $\alpha_{c,mold}$ between 0 and 90° the solution completely fills the capillary due to the good wetting properties at the different side walls.

In addition, these results also allow the calculation of the solution flow rate dz/dt within the capillary [79]

$$\frac{dz}{dt} = \frac{R_{hyd} \gamma_{lv} \cos \alpha_{c,mold}}{4\eta_{sol} z_t} = \frac{R_{hyd} (\gamma_{sv} - \gamma_{sl})}{4\eta_{sol} z_t} , \quad (2.40)$$

where R_{hyd} is the hydraulic radius (ratio between volume of solution in tube and area of solid and liquid interface) and η_{sol} is the viscosity of the solution. For a decreasing dimension of the channel the hydraulic radius is reduced as well. Hence, also the filling velocity is reduced for smaller mold structures. Since during the molding process the channels are typically placed horizontally, the gravitational force $F_g = x_t^2 h_{sol} \rho_{sol} g$ is neglected in equation (2.40) (h_{sol} depicts the height of solution in channel, ρ_{sol} the mass density, and

g the gravitational constant).

2.3.2 Temperature and pressure induced processability

Nanoimprint lithography (NIL) is a very promising and already commonly applied technology for the fabrication of micro- and nanostructured polymer films.[82] During NIL the polymer film is heated above its glass transition temperature T_g and the mold structures are transferred to the polymer by an external pressure. This method has already been used to successfully fabricate polymer structures with sub-10 nm dimensions.[83] In figure 2.10 a polymer flow during NIL is shown as it is typical for a master mold with channel features. The structure transfer is often accompanied by the formation of a prominent dual peak structure.

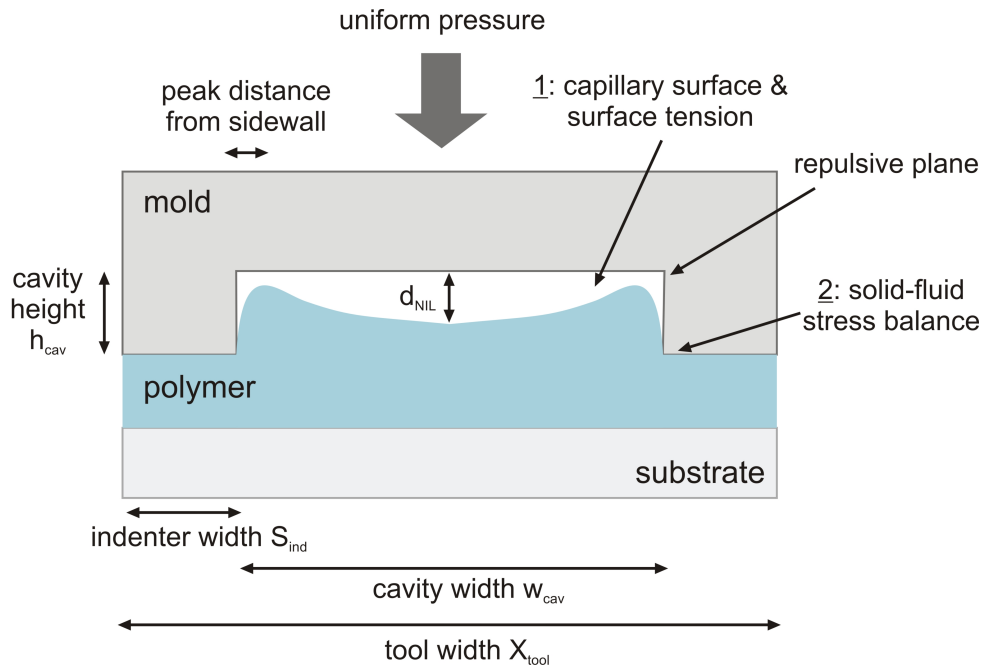


Figure 2.10: Nanoimprint lithography: The characteristic double peak deformation of a polymer film is shown for one master cavity. The important geometric variables and the different boundary conditions are illustrated as well.

In order to fully describe the nanoimprint process, the necessary geometric values and the boundary conditions are included in figure 2.10. In general, three parameters are most important for the polymer deformation: the cavity width w_{cav} to the initial polymer thickness d ratio, the polymer supply ratio, and the capillary number.[84] However, in order to understand the polymer flow, a detailed knowledge about the different physical processes in the polymer film and at the polymer-mold interfaces is crucial. According to Newton's second law, which implies the conservation of momentum, the polymer flow is

described by the Navier-Stokes equations

$$Re \left(\frac{\partial \vec{v}_{flow}}{\partial t} + \vec{v}_{flow} \nabla \vec{v}_{flow} \right) = -\nabla P + \nabla \mathbf{\Gamma} + \vec{\Upsilon}. \quad (2.41)$$

In the upper equation, \vec{v}_{flow} corresponds to the flow velocity, Re to the Reynolds number of the solution, ∇ to the three-dimensional del-operator, P to the pressure, $\mathbf{\Gamma}$ to the liquid stress tensor, and $\vec{\Upsilon}$ represents the body forces acting on the liquid polymer. However, for the heated polymer films, which can be treated as incompressible liquids, the pressure gradient component $-\nabla P$ and the other body forces $\vec{\Upsilon}$ vanish. Therefore, on the right side of equation (2.41) only the divergence of the liquid stress tensor depicted by $\nabla \mathbf{\Gamma}$ remains. For master molds with channel structures the Reynolds number Re is given by $\rho P_0 X_{tool}^2 / \eta_{pol}^2$, where ρ is the mass density, P_0 the externally applied pressure, X_{tool} the width of the mold, and η_{pol} the polymer viscosity.

At the interface between liquid polymer and free surface (see figure 2.10 mark 1) the force balance between liquid normal stress tensor and capillary force is given by [84]

$$\vec{n} \mathbf{\Gamma} = \frac{1}{C_{cap}} H_{curv} \vec{n} + \frac{\vec{F}_r}{X_{tool}^4 d_{NIL}^4}, \quad (2.42)$$

where \vec{n} is the normal vector, C_{cap} is the capillary number, H_{curv} is the curvature of the liquid, \vec{F}_r is an arbitrary repulsive force, and d_{NIL} is the distance of the polymer boundary to the solid mold. The capillary number is defined as $P_0 X_{tool} / \gamma_{sur}$, where γ_{sur} again depicts the surface tension. In equation (2.42) the surface tension force due to the curvature of the polymer surface balances the normal stress from the liquid and the arbitrary contact force.

At the second possible interface, where liquid polymer touches the solid mold (see figure 2.10 mark 2), a stress balance between the forces in the liquid polymer and the ones in the solid material must be maintained

$$\frac{P_0}{\mu_L} \vec{n} \mathbf{\Gamma} = \vec{n} \mathbf{\Gamma}_{el}. \quad (2.43)$$

In this equation the elastic tensor $\mathbf{\Gamma}_{el}$ characterizes the fluidized polymer

$$\mathbf{\Gamma}_{el} = 2\mu_L \mathbf{E}_D + \lambda_L \vec{V}_D, \quad (2.44)$$

where μ_L and λ_L are the Lamé elastic coefficients, \mathbf{E}_D is the small deformation strain tensor and \vec{V}_D is the small deformation strain. The applied pressure is transferred from the solid master to the liquid polymer considering the conservation of momentum, which is given by

$$\frac{\mu_L}{X_{tool}} \nabla \Gamma_{el} + P_0 \Upsilon_P = 0, \quad (2.45)$$

where Υ_P is the general body force of the applied embossing load.

Up to now, an additional important aspect for the polymer deformation has been excluded: the flow behavior of the polymer. In most cases a Newtonian liquid flow is assumed, which only includes a shear-thinning behavior but no elastic properties. Such a Newtonian model is characterized by a linear stress-strain curve with its viscosity as proportionality constant.[85] However, depending on the applied polymer, other non-Newtonian models might be more suited to describing the polymer flow during NIL. As an example, in the Carreau-Yasuda model the polymer viscosity η_{pol} is given by [86]

$$\eta_{pol} = \eta_{pol,0} (1 + (\lambda_{CY} \mathbf{I})^{a_{CY}})^{(n_{CY}-1)/a_{CY}}, \quad (2.46)$$

where \mathbf{I} is the second invariant of the shear rate tensor. In this model the additional zero-shear viscosity $\eta_{pol,0}$, the time constant λ_{CY} , the power law index n_{CY} , and the numerical parameter a_{CY} are adjustable variables.

The different physical correlations and force balances, which are described in this section, were already applied to theoretically simulate the polymer flow during NIL.[84, 87] Interestingly, the results of these finite volume based simulations have shown that often viscosities according to the simple Newtonian model lead to a polymer flow, which can be compared well to experiments.[88]

2.4 X-ray techniques

For the characterization of nanoscopic surface and inner film structures and for the determination of the chemical composition of polymer films, X-ray scattering and X-ray absorption measurements build a crucial part of this thesis. Therefore, in this section the basic principles of X-ray scattering on nanoscopic structures and of near edge X-ray absorption fine structure (NEXAFS) measurements are introduced. First, the scattering on ordered structures is explained (section 2.4.1). In section 2.4.2 the theories of specular X-ray scattering at total reflection and in section 2.4.3 of diffuse scattering close to total reflection are illustrated. The investigated three-dimensional periodic structures result in the formation of a prominent scattering feature: the so-called Ewald sphere, which is discussed in section 2.4.4. Finally, a short introduction to X-ray absorption in the near edge region is given (section 2.4.5).

2.4.1 Basic principles

In general, X-rays are electromagnetic waves in the wavelength regime between 0.01 and 10 nm and they are mathematically given by

$$\vec{E}(\vec{r}) = \vec{E}_0 \exp(i\vec{k}\vec{r}) . \quad (2.47)$$

They are described as periodic oscillations of an electric field \vec{E} at the position \vec{r} , which also depend on the maximum amplitude \vec{E}_0 and the direction of propagation \vec{k} .

In principle, an atom gets excited if hit by an X-ray resulting in dipole oscillations. If accelerated charges of multiple excited atoms emit secondary waves, interference effects occur, which can be determined experimentally. This is especially interesting for the investigated periodically structured polymer films, which have a perfect long range order and are hence ideal for constructive and destructive interferences. In figure 2.11 a schematic illustration of a scattering process at periodic channel structures is shown. Monochromatic X-rays with a wave vector \vec{k}_i hit two scattering targets A_S and B_S , which are located on neighboring periodic structures.

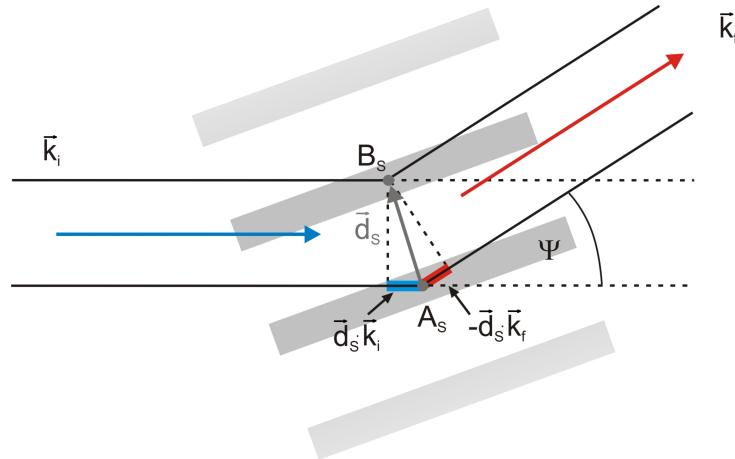


Figure 2.11: Schematic illustration of scattering processes at periodic structures. The X-rays impinge with a wave vector \vec{k}_i and are scattered at two atoms A_S and B_S under an angle ψ . The scattered X-rays propagate with a wave vector \vec{k}_f .

The scattering targets A_S and B_S are separated by a vector \vec{d}_s . As a result, the impinging waves \vec{k}_i are deflected under an angle Ψ and their new direction is given by \vec{k}_f . The difference between the wave vectors \vec{k}_i and \vec{k}_f is defined as the scattering vector \vec{q}

$$\vec{q} = \vec{k}_f - \vec{k}_i . \quad (2.48)$$

In case of elastic scattering, the energy of the incoming X-rays is conserved ($|\vec{k}_i| = |\vec{k}_f|$). Therefore, the absolute value q of the scattering vector is derived as

$$q = |\vec{q}| = \frac{4\pi}{\lambda} \sin \frac{\Psi}{2} . \quad (2.49)$$

From an atomic point of view, the scattering intensity mainly depends on the electron density distribution $\rho_{el}(\vec{r})$ of the scattering object. The amplitude of the scattered intensity $A(\vec{q})$ is given by

$$A(\vec{q}) = A_0 \int \rho_{el}(\vec{r}) \exp(i\vec{q}\vec{r}) d\vec{r} , \quad (2.50)$$

where A_0 corresponds to the scattering amplitude of a single electron. The resulting scattering intensity $I(\vec{q})$ is calculated as the square of the scattering amplitude. For a symmetric ordering of the scattering particles the structure factor $S(\vec{q})$ is introduced to calculate the intensity $I(\vec{q})$ [89]

$$I(\vec{q}) = I_0(\vec{q})S(\vec{q})^2 , \quad (2.51)$$

where $I_0(\vec{q})$ is the scattering intensity proportional to A_0^2 . The structure factor is a measure for the scattering ability of the investigated material. It takes into account the scattering power and the lateral distance between the scattering centers.

In general, for very small incident and scattering angles α_i and α_f , the diffraction effects at ordered structures are negligible and the scattering can be described according to optical laws. Therefore, the material under investigation is described by the complex refractive index n which is in addition material and wavelength λ specific [90]

$$n(\vec{r}, \lambda) = 1 - \delta(\vec{r}, \lambda) + i\beta(\vec{r}, \lambda) . \quad (2.52)$$

In equation (2.52) the dispersion (real part) and the absorption (imaginary part) of the X-rays is included. For polymeric materials the dispersion δ is typically in the order of $\approx 10^{-6}$ and the real part of the refractive index is hence slightly smaller than one. As a result, the investigated material is optically thinner than its surroundings (in this thesis vacuum or air). Therefore, total reflection at the polymer surface occurs for X-rays, which impinge the sample under incident angles smaller than the critical angle α_{crit} . Under the assumption of no absorption, the critical angle is located at $\alpha_{crit} \approx \sqrt{2\delta}$. Within this work, all incident angles are given in respect to the sample surface.

In figure 2.12 a schematic illustration of a specularly reflected X-ray beam is shown, for which the exit angle α_f is equal to the incident angle α_i . The transmitted beam is included as well and its angle α_t depends on the refractive index of the material.

For X-ray investigations, which are performed under a glancing angle (see experimental geometry in figure 2.12), the penetration length Λ_p is important. This value is crucial in

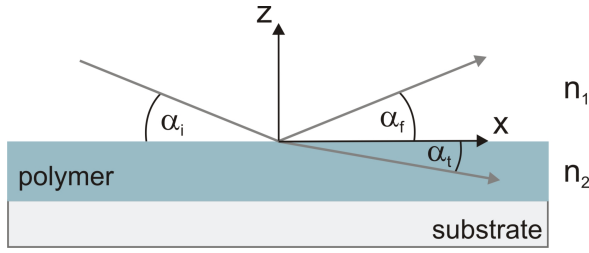


Figure 2.12: X-ray reflection at a polymer surface: The X-ray beam impinges the sample under an angle α_i and is partially reflected (α_f) and partially transmitted (α_t). The refractive indices of the surrounding material and the polymer are depicted by n_1 and n_2 .

order to probe the full film thickness and it is defined as the length at which the strength of the propagating electromagnetic field has fallen by a factor $1/e$ [90]

$$\Lambda_p = \frac{\lambda}{2\sqrt{2}\pi} \left(\sqrt{(\alpha_i^2 - \alpha_c^2) + 4\beta^2} - (\alpha_i^2 - \alpha_c^2) \right)^{-1/2}. \quad (2.53)$$

As it is shown in section 2.4.5, the penetration length Λ_p is also a crucial parameter for X-ray absorption measurements performed in transmission geometry.

2.4.2 Specular scattering

Since for very small incident and exit angles the diffraction effects are negligible (see section 2.4.1), only the thin film characteristics are probed. In case of specular reflection, the scattering vector \vec{q} has only a component normal to the sample surface (in z -direction). This q_z -component is given by

$$q_z = \left(\vec{k}_f - \vec{k}_i \right)_z = \frac{4\pi}{\lambda} \sin \alpha_i. \quad (2.54)$$

Therefore, the measured reflectivities are averaged over the x - y -plane and only contain information about sample characteristics along the sample normal, e.g. film thickness, film roughness, and density profile.

In figure 2.13 the simulated X-ray reflectivity data of a polymer film with a thickness d of 30 nm on a silicon support are shown. In this exemplary system the critical angle of the silicon substrate $\alpha_{crit}(si)$ is larger than the critical angle of the polymer layer $\alpha_{crit}(pol)$. For very small incident angles $0 < \alpha_i < \alpha_{crit}(pol)$ the impinging intensity is reflected completely at the polymer:air interface. At the critical angle of the polymer a dip in the intensity plateau is observed due to transmittance of the X-rays in the polymer film. However, for $\alpha_{crit}(pol) < \alpha_i < \alpha_{crit}(si)$ the X-rays are still reflected at the polymer:substrate interface. The reflected intensity starts to drop for incident angles larger than the critical angle of the substrate. For a simplified vacuum:medium interface this intensity drop follows a power law ($I \propto q^{-4}$). From the additional intensity modulations in figure 2.13 it is seen that additional interference effects play an important role for layered systems.

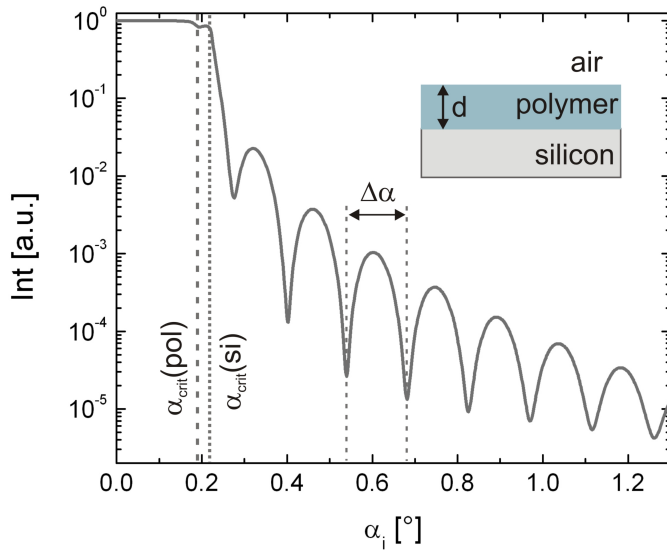


Figure 2.13: Simulated X-ray reflectivity data of a polymer film with a thickness d of 30 nm on a silicon support. The critical angle of the polymer $\alpha_{crit}(pol)$ is seen as a dip in the reflectivity plateau. For incident angles α_i larger than the critical angle of the silicon $\alpha_{crit}(si)$ the reflected intensity drops. The observed modulations have a constant width $\Delta\alpha$ and are correlated to the polymer film thickness d .

The impinging X-rays are reflected at the different interfaces and interfere depending on the angle of incidence α_i and the corresponding differences in optical path length. The observed oscillations are called Kiessig-fringes and in reciprocal space their period length Δq_z is connected to the film thickness d [91]

$$d = \frac{2\pi}{\Delta q_z} \approx \frac{\lambda}{2 \sin \Delta\alpha} . \quad (2.55)$$

For the discussed example of a single layer on a substrate the Kiessig-fringes appear equidistant, whereas for multilayer systems superimposed and more complex reflectivity curves are observed.[92, 93] However, for simple homopolymer films as well, such multilayer approaches are often necessary due to varying polymer densities, which result from polymer enrichment layers at the polymer:substrate or the polymer:air interface. At any present interface with a change in refractive index, absorption, reflection, and refraction have to be taken into account.[90] In order to calculate the reflectivity of such multilayer systems Parrat developed a numerical recursive algorithm.[94] According to the z -axis, the position of each interface is given by z_j , where the sample surface is located at $z_1 = 0$ and the interface to the substrate is at z_N (N total amount of layers). Each layer is described by its thickness $d_j = z_{j-1} - z_j$ and its refractive index $n_j = 1 - \delta_j + i\beta_j$. For the substrate the refractive index is $n_{N+1} = 1 - \delta_{N+1} + i\beta_{N+1}$ and its thickness is assumed to be infinite ($z_{N+1} = -\infty$). In figure 2.14 a single layer is illustrated, which is sandwiched within such a multilayer system. At each interface (position z_j) the transmitted beam is reflected and transmitted.

The ratio between the amplitudes of the reflected wave R_j and of the transmitted wave T_j is denoted as X_j . Assuming an amplitude of the impinging wave of one, X_j is given by

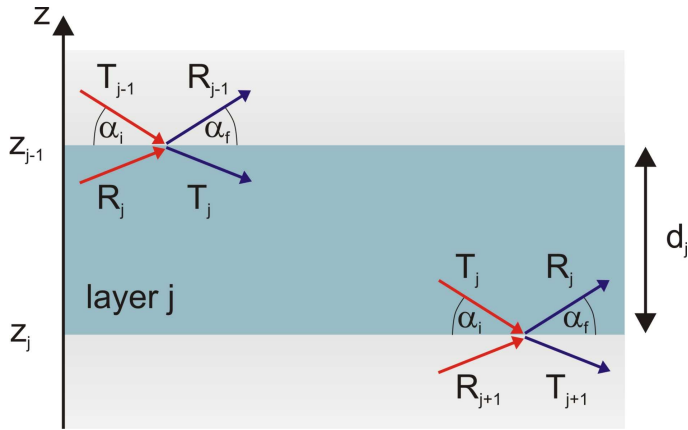


Figure 2.14: Schematic illustration of the transmitted and the reflected X-ray beam on a single layer embedded in a complex multilayer system.

$$X_j = \frac{R_j}{T_j} = \exp(-2ik_{z,j}z_j) \frac{r_{j,j+1} + X_{j+1} \exp(2ik_{z,j}z_j)}{1 + r_{j,j+1}X_{j+1} \exp(ik_{z,j}z_j)}. \quad (2.56)$$

In the equation above, $k_{z,j}$ denotes the z -component of the wave vector in layer j

$$k_{z,j} = k_z \sqrt{n_j^2 - \cos^2 \alpha_i}, \quad (2.57)$$

where k_z is the z -component of the absolute wave vector in vacuum. In equation (2.56) also the Fresnel coefficients $r_{j,j+1}$ for a reflection at a smooth surface are important

$$r_{j,j+1} = \frac{k_{z,j} - k_{z,j+1}}{k_{z,j} + k_{z,j+1}}. \quad (2.58)$$

As a result, the specularly reflected intensity $I_{spec} = |R_1|^2$ is derived after N subsequent iterations of

$$R_{j+1} = \frac{1}{t_{j,j+1}} T_j r_{j+1,j} \exp(-i(k_{z,j+1} + k_{z,j})z_j) + R_j \exp(-i(k_{z,j+1} - k_{z,j})z_j) \quad (2.59)$$

and

$$T_{j+1} = \frac{1}{t_{j,j+1}} \exp(i(k_{z,j+1} + k_{z,j})z_j) + R_j r_{j,j+1} \exp(-i(k_{z,j+1} - k_{z,j})z_j), \quad (2.60)$$

with the second Fresnel coefficient $t_{j+1,j} = 1 + r_{j+1,j}$. [90]

Up to now, only perfectly smooth interfaces have been assumed. However, real multilayer systems also have certain macroscopic surface roughness values, which are measures of the surface texture. The surface roughness is generally quantified by vertical deviations of a real surface in comparison to an ideal one. To have a comparable parameter the film roughness is commonly measured as root mean square roughness R_{rms} , which can be also

extracted from common surface imaging techniques (e.g. atomic force microscopy) as

$$R_{rms} = \sqrt{\frac{1}{N_{points}} \sum_{k=1}^{N_{points}} (z_i - z)^2} . \quad (2.61)$$

In this equation N_{points} denotes the total sampling points, which are illustrated by i , and $|z_i - z|$ is the distance between the individual points z_i on the wavy surface and the nominal mean surface z .

For the X-ray measurements additional surface roughnesses lead to a continuous refractive index transition between two layers. Since only the change of the refractive index n_j in z -direction is important, one-dimensional refractive index profiles are extracted by averaging the interface textures over the x - y -plane:

$$n_j(z) = \int_x \int_y n_j(x, y, z) dx dy . \quad (2.62)$$

A common model for the transition of the refractive index from layer j to layer $j + 1$ was introduced by Névot and Croce, who assumed a symmetric error function [95]

$$n_j(z) = \frac{n_j + n_{j+1}}{2} - \frac{n_j - n_{j+1}}{2} \operatorname{erf} \left(\frac{z - z_j}{\sqrt{2} R_{rms}} \right) . \quad (2.63)$$

The error function is given by $\operatorname{erf}(z) = \int_0^z \exp(-t^2) dt$. As a result, the Fresnel coefficients change to

$$\tilde{r}_{j,j+1} = r_{j,j+1} \exp \left(-2k_{z,j} k_{z,j+1} R_{rms}^2 \right) \quad (2.64)$$

and can be directly applied to calculate the reflectivity according to equation (2.56). However, this fundamental equation remains valid only for absolute surface roughnesses, which are small in comparison to the film thickness.

2.4.3 Diffuse scattering close to total reflection

Besides the already described specular scattering, often the diffuse scattering component is taken into account for sample analysis, as well. However, for this type of measurement a point-like detector, as it is suited for specular scattering, has to be replaced by a two-dimensional area detector for convenient experiments.

Especially increased surface roughnesses have a strong impact on the lateral diffuse scattering. Among other examples, this influence has already been studied for dewetted polymer thin films.[96] In general, the diffuse scattering vector can be split in three perpendicular components along the x -, y -, and z -axis. Typically, the coordinate system is

chosen in such a way, that the x - y -plane corresponds to the sample surface and the X-rays impinge the sample along the x -axis. Hence, the diffuse scattering vector is given by [97]

$$\begin{aligned} q_x &= \frac{2\pi}{\lambda} (\cos \alpha_f \cos \psi - \cos \alpha_i) , \\ q_y &= \frac{2\pi}{\lambda} (\cos \alpha_f \sin \psi) , \text{ and} \\ q_z &= \frac{2\pi}{\lambda} (\sin \alpha_f + \sin \alpha_i) . \end{aligned} \quad (2.65)$$

In figure 2.15 all important parameters for the diffuse scattering are shown: α_i depicts the incident angle between X-rays and sample surface and the scattering angles α_f and ψ correspond to the exit angle in the x - z -plane and to the out-of-plane angle parallel to the sample surface.

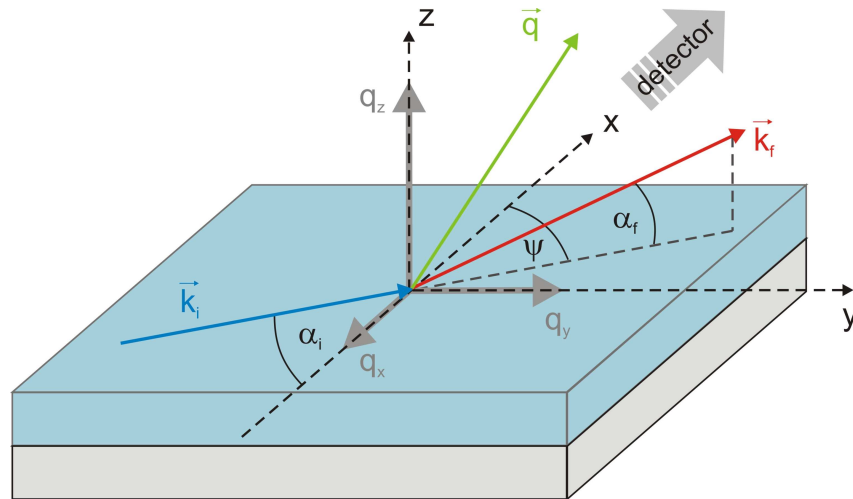


Figure 2.15: Schematic illustration of the diffuse scattering geometry. The X-ray beam impinges the sample in the x - z -plane under the incident angle α_i . It is scattered by ψ in the x - y -plane and has a modified exit angle α_f ($\alpha_i \neq \alpha_f$).

After the diffuse scattering has been recorded, the next step is to analyze the two-dimensional data. A full theoretical simulation of the measured data is the most complex part of the experiment. The distorted-wave Born approximation (DWBA) provides a suitable theoretical framework for this task.[97, 98] In 1988, Sinha et al. were the first to calculate the scattering cross section of a rough surface in DWBA.[99] In scattering theory this quantum-mechanical approach includes first order perturbations in the scattering process, which are induced by particle roughness and contrast variation. The unperturbed case is generally taken as the Fresnel wave field, which is in multilayer systems analytically equivalent to flat interfaces.[100] It is an accurate method as long as the scattered field

is small, if compared to the incident field. The differential cross section $d\sigma_{scat}/d\Omega_{scat}$ in DWBA depends on the total illuminated sample area A_{ill} [99]

$$\frac{d\sigma_{scat}}{d\Omega_{scat}} = \frac{A_{ill}\pi^2}{\lambda^4} (1 - n^2)^2 |r_{F,i}|^2 |r_{F,f}|^2 P_{diff}(\vec{q}), \quad (2.66)$$

where $r_{F,i}$ and $r_{F,f}$ are the Fresnel coefficients of the incident and the scattered beam.[90] These coefficients strongly depend on the angle of incidence α_i and the exit angle α_f . While, due to total reflection, the reflection coefficient is equal to one below the critical angle α_{crit} , the transmission coefficient exhibits a pronounced maximum at α_{crit} . [101] This maximum in intensity is also called Yoneda peak.[102] In equation (2.66) P_{diff} is the diffuse scattering factor, which is a direct measure for the scattered intensity.

For the samples, which are investigated in this thesis, two different models are chosen to simulate the scattered intensity: (i) for polymer blend films with a self-driven phase-separation, cylindrical objects of one component are embedded in a surrounding matrix of the other component and (ii) for imprinted films anisotropic pyramids, which are located on a homogeneous polymer support, mimic the channel structures. Both object types (cylinders and pyramids) are defined by their size and their distance distribution. The measured scattered intensity consists of a coherent I_{coh} and an incoherent I_{inc} scattering term. The latter is due to scattering at objects with monodisperse size distributions. The coherent component I_{coh} is denoted as

$$I_{coh}(\vec{q}) \propto N_{obj} S(\vec{q}) |F_{obj}(\vec{q})|^2, \quad (2.67)$$

where N_{obj} is the number of identical objects, $S(\vec{q})$ the structure factor (also called interference function), and $F_{obj}(\vec{q})$ the form factor. The latter is directly derived as the Fourier transformation of the electron density distribution $\rho_{el}(\vec{r})$ of the applied object

$$F_{obj}(\vec{q}) = \int_V \rho_{el}(\vec{r}) \exp(-i\vec{q}\vec{r}) dV. \quad (2.68)$$

(i) Polymer blend films: For the cylindrical objects, which are given by their radius R_{cyl} and height H_{cyl} , the form factor F_{cyl} is

$$F_{cyl}(\vec{q}, R_{cyl}, H_{cyl}) = 2\pi R_{cyl} \frac{J_1(\sqrt{q_x^2 + q_y^2} R_{cyl})}{\sqrt{q_x^2 + q_y^2}} \sin\left(\frac{1}{2} q_z H_{cyl}\right) \exp\left(\frac{1}{2} q_z H_{cyl}\right), \quad (2.69)$$

where J_1 again corresponds to the first order Bessel function. For the interference function, a regular 1D lattice with a loss of long-range order was used. In this paracrystal model

[103, 104] the long-range order is destroyed gradually, and hence, it acts as a link between a regular lattice and a fully disordered system. The corresponding inter-particle distance D_{int} is therefore approximated by a Gaussian distribution

$$p(D_{int}) = \frac{1}{\omega_D \sqrt{2\pi}} \exp\left(\frac{-(D_{int} - D_{int,c})^2}{2\omega_D^2}\right), \quad (2.70)$$

where ω_D is the width of the distribution and $D_{int,c}$ its central value. First published by Hosemann and Bagchi, the interference function of the commonly applied one-dimensional Hosemann paracrystal appears as [103, 104]

$$S(\vec{q}) = \frac{1 - \Phi_H^2(q)}{1 + \Phi_H^2(q) - 2\Phi_H(q) \cos(qD_{int,c})}, \quad (2.71)$$

where $\Phi_H(q) = \exp(\pi q^2 \omega_D^2)$ and q corresponds to the absolute value of the scattering vector \vec{q} .

Up to this point, only the coherent scattering component has been considered, which results from scattering on identical objects. In order to also account for different object dimensions, the so-called decoupling approximation (DA) is applied.[105] This hypothesis supposes that the kind of the scatterers and their positions are not correlated and that the partial pair correlations functions depend only on the relative positions of the homogeneous scatterers.[106] The genuine random substitutional mixture leads to a scattering cross section, which consists of a diffuse and a coherent scattering term

$$\frac{d\sigma_{scat}}{d\Omega_{scat}}(\vec{q}) = I_d(\vec{q}) + \left| \overline{F(\vec{q})} \right|^2 S(\vec{q}), \quad (2.72)$$

with

$$I_d(\vec{q}) = \overline{|F(\vec{q})|^2} - \left| \overline{F(\vec{q})} \right|^2 \quad (2.73)$$

and

$$S(\vec{q}) = 1 + \rho_{par} \int g_{par}(\vec{R}_{par}) \exp(i\vec{q} \cdot \vec{R}_{par}) d^2 R_{par}. \quad (2.74)$$

Equation (2.73) corresponds to the diffuse component of the scattering and solely depends on the form factor. The total interference function S is depicted in equation 2.74 and it describes the lateral correlation of the objects on the surface depending on the position \vec{R}_{par} , the pair correlation function g_{par} , and the scattering density ρ_{par} .

(ii) Imprinted polymer structures: On the contrary, for the data analysis of the artificially textured polymer films anisotropic pyramids are applied to model the fabricated

channel structures. Such structures have a form factor F_{py} as follows [106]

$$\begin{aligned}
F_{py}(\vec{q}, R_{py}, w_{rid}, d_{cha}, \phi_{cha}) &= \int_0^{d_{cha}} 4 \left(R_{py} - \frac{z}{\tan \phi_{cha}} \right) \left(w_{rid} - \frac{z}{\tan \phi_{cha}} \right) \\
&\quad \sin \left(q_x \left(R_{py} - \frac{z}{\tan \phi_{cha}} \right) \right) \sin \left(q_y \left(w_{rid} - \frac{z}{\tan \phi_{cha}} \right) \right) \\
&\quad \exp(iq_z z) dz . \tag{2.75}
\end{aligned}$$

In the equation above, R_{py} illustrates the length of the pyramid, w_{rid} the width, d_{cha} the height, and ϕ_{cha} the base angle of the inclined side walls (a sketch of the pyramid structure can be found in section 6.1).

However, in order to mimic highly ordered and perfectly oriented channel structures, a regular lattice model with a perfect long range order is necessary. The applied lattice is defined by its basis vectors \vec{a}_{la} , \vec{b}_{la} and their intermediate angle γ_{la} , which is $\pi/2$ for a quadratic lattice. A pattern consisting of N_i particles is attached to each node of the lattice. By again using the DA hypothesis of a full decorrelation between the position of the unit cell and its content, the structure factor is derived to be

$$S(\vec{q}) = \frac{1}{N_i} \left| \sum_k F \left(\vec{q} \exp \left(iq_{|xy|} (x\vec{a} + y\vec{b}) \right) \exp \left(-\frac{q_{|xy|} \mathbf{B}_k q_{|xy|}}{2} \right) \right) \right|^2 , \tag{2.76}$$

where \mathbf{B}_k is the symmetric tensor of the standard deviations of the k -th particle and $q_{|xy|} = \sqrt{q_x^2 + q_y^2}$.

Up to now, only direct scattering events at the objects are considered and any reflection attributed components are neglected. However, for satisfying data modeling, the reflections before and after scattering must also be taken into account. In the framework of the DWBA four different scattering scenarios are possible, which are illustrated in figure 2.16.

In consequence, the form factors of the applied objects have to be modified by additional correction terms, which correspond to the single scattering scenarios. In general, the corrected form factor F_{obj}^{DWBA} comes as follows [98]

$$\begin{aligned}
F_{obj}^{DWBA} \left(q_x, q_y, (\vec{k}_i)_z, (\vec{k}_f)_z \right) &= F_{obj} \left(q_x, q_y, (\vec{k}_f - \vec{k}_i)_z \right) + r_{sub}(\alpha_i) F_{obj} \left(q_x, q_y, (\vec{k}_f + \vec{k}_i)_z \right) \\
&\quad + r_{sub}(\alpha_f) F_{obj} \left(q_x, q_y, (-\vec{k}_f - \vec{k}_i)_z \right) + \tag{2.77} \\
&\quad + r_{sub}(\alpha_i) r_{sub}(\alpha_f) F_{obj} \left(q_x, q_y, (-\vec{k}_f + \vec{k}_i)_z \right) .
\end{aligned}$$

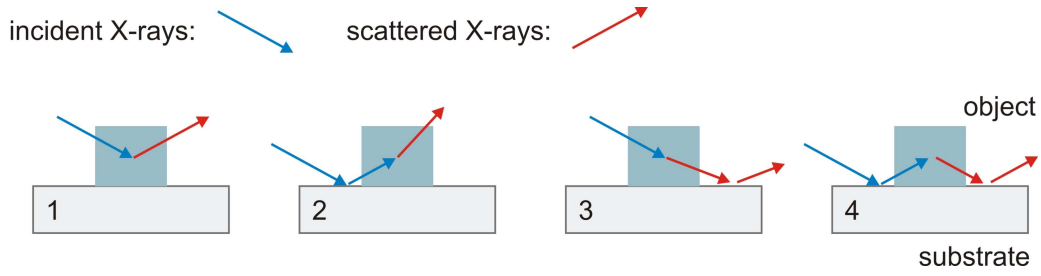


Figure 2.16: Schematic illustration of the four different scattering scenarios as introduced within the distorted-wave Born approximation. The scenarios 2 to 4 result in modified form factors of the applied objects.

In equation (2.78) the Fresnel reflection coefficients r_{sub} depict the substrate material and include roughness corrections. However, for both given examples slight modifications due to the multilayer stack design are necessary. In case of the self-driven polymer blend films, the cylindrical objects are embedded in a surrounding polymer matrix, which sits on a homogeneous homopolymer layer. A similar supporting homogeneous polymer layer is included as well for the artificially textured polymer films.[106]

2.4.4 Ewald sphere - scattering on three-dimensional lattice structures

In contrast to the scattering data of disordered objects, the reciprocal scattering measurements on periodic structures under grazing incident angles show additional prominent scattering features: grating truncation rods (GTR) [107] and the presence of the Ewald sphere.[108] The latter is a common geometric construct in X-ray scattering which illustrates the dependence between the incident and the diffracted wave, the diffraction angle, and the reciprocal lattice constant. As a result, if the grating is parallel to the impinging X-ray beam, diffraction spots are located on a semicircle at the intersection of the GTRs with the Ewald sphere.[109] In figure 2.17 an illustration of the Ewald sphere for X-rays scattered on a grating structure is shown.

For incident X-rays with a constant wavelength λ the equation of the Ewald sphere is given by

$$\left(q_x + \frac{2\pi}{\lambda}\right)^2 + q_y^2 + q_z^2 = \left(\frac{2\pi}{\lambda}\right)^2. \quad (2.78)$$

In addition, at a fixed incident angle α_i the equation of a specular GTR is $q_x = -q_z \tan \alpha_i$. For periodic gratings with a periodicity p_{cha} (see section 6.1) multiple GTRs are located next to the specular reflection. The reciprocal distance between two neighboring truncation rods is $q_y = 2\pi/p_{cha}$. [110] Hence, the location of the intersection of the GTRs with

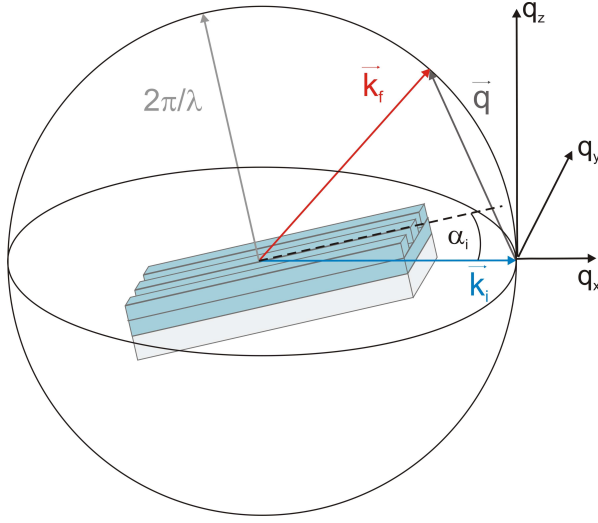


Figure 2.17: Schematic representation of the Ewald sphere including the wave vector of the incident \vec{k}_i and the diffracted wave \vec{k}_f . The axis of the coordinate system are chosen as before.

the Ewald sphere is mathematically resolved by the combination of both relations

$$\left(-q_z \tan \alpha_i + \frac{2\pi}{\lambda}\right)^2 + \left(\frac{2\pi m_{GTR}}{p_{cha}}\right)^2 + q_z^2 = \left(\frac{2\pi}{\lambda}\right)^2, \quad (2.79)$$

where m_{GTR} corresponds to the order of the GTRs on both sides of the specular reflection. Equation (2.79) is now solved for the q_z -component [107]

$$q_z = \frac{2\pi}{\lambda} \cos \alpha_i \sin \alpha_i \left(1 + \left(1 - \left(\frac{m_{GTR} \lambda}{p_{cha} \sin \alpha_i}\right)^2\right)^{1/2}\right). \quad (2.80)$$

The second possible solution of equation (2.79) has a negative q_z -value, which corresponds to reflections below the sample horizon and are therefore not observable in a GISAXS experiment. Real q_z -values are mathematically only possible for $1 - (m_{GTR} \lambda / p_{cha} \sin \alpha_i) \geq 0$. This condition also sets the limit of the observable scattering order m_{GTR} [107]

$$-\frac{p_{cha} \sin \alpha_i}{\lambda} \leq m_{GTR} \leq \frac{p_{cha} \sin \alpha_i}{\lambda}. \quad (2.81)$$

Since all GISAXS measurements were performed at an incident angle above the critical angle, the specific cases of an evanescent wave parallel to the sample surface ($\alpha_i = \alpha_{crit}$) and a total reflection ($\alpha_i < \alpha_{crit}$) are not discussed in the framework of this thesis.

2.4.5 X-ray absorption

Up to this point, X-rays have only been applied for scattering experiments. However, polymers also have a wavelength dependent absorption coefficient $\beta(\lambda)$. Hence, X-rays are also absorbed in soft matter films - similarly to optical light, as described in section

2.1.1. By applying soft X-rays, which typically have a photon energy between 50 and 2000 eV, the probability of X-ray absorption is much higher than of X-ray scattering. Furthermore, only coherent scattering (equivalent to elastic scattering) has to be taken into account, since inelastic scattering events (e.g. Compton scattering) are negligible for soft X-rays. In figure 2.18 the different absorption and relaxation processes are shown which are the origin for the characteristic and material specific NEXFAS spectra. By absorbing an incident X-ray beam (figure 2.18(a)) an electron from the core state is excited into an unoccupied electronic state (figure 2.18(b)). Subsequently, the excited molecule relaxes under the ejection of either an Auger electron or an energetic photon (fluorescence, figure 2.18(c)).

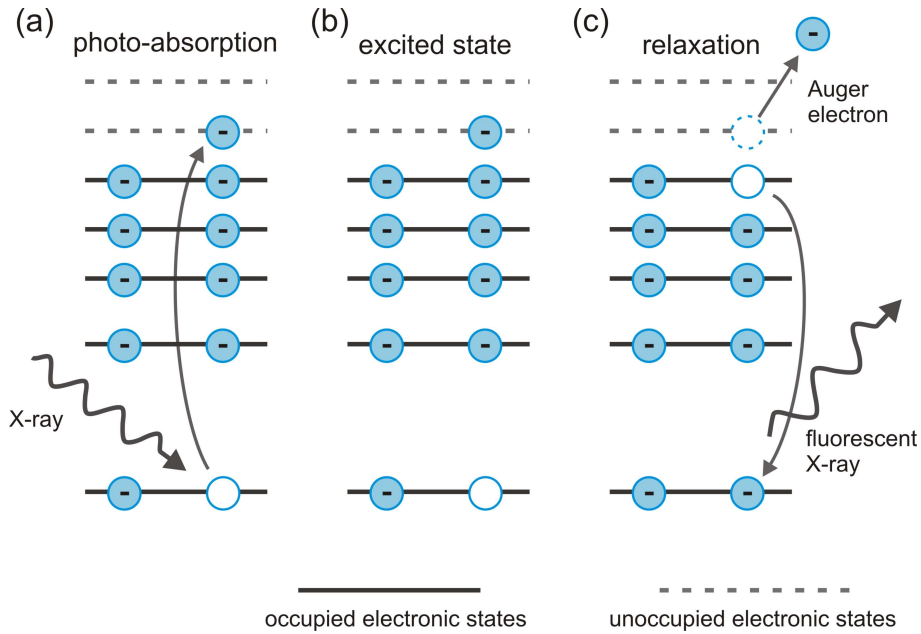


Figure 2.18: Schematic illustration of soft X-ray photo-absorption and subsequent relaxation processes: An incident photon excites an electron from a core level into an unoccupied anti-bonding level. This excited state relaxes under the emission of a fluorescent photon or an Auger electron.

The corresponding X-ray absorption cross section σ_{abs} is defined as the number of electrons excited per unit time divided by the number of incident photons per unit time and unit area. It can be calculated from Fermi's Golden Rule for the transition probability P_{op} from a state $|o\rangle$ to a state $|p\rangle$ [111]

$$P_{op} = \frac{2\pi}{\hbar} |\langle o | \bar{V}_{abs} | p \rangle| \rho_f(E), \quad (2.82)$$

where $\rho_f(E)$ is the energy density of the final states and $V_{abs}(t) = V_{abs,0} \exp(-i\omega t)$ is a harmonic time-dependent perturbation. For the calculation of the X-ray absorption cross section σ_{abs} , the electrons of all shells with an energy below the photon energy have to be

included. If the contribution of the outer shells is ignored and a dipole approximation is assumed the X-ray absorption cross section σ_{abs} is given by

$$\sigma_{abs} = \frac{4\pi^2 \hbar^2 e^2}{m^2} \frac{1}{\hbar c \hbar \omega} |\langle o | \vec{e} \cdot \vec{p} | p \rangle| \rho_f(E), \quad (2.83)$$

where \vec{e} is the unit vector and \vec{p} is the sum of the linear momentum operators of the electron.

Since the binding energies of the core are specific for each element, these absorption measurements are inherently element sensitive. As a consequence, the refractive index of materials, which consist of various different elements (e.g. polymers), is approximated by the scattering factors of each element. This happens in analogy to the atomic scattering factors, which were described by Henke et al.[112] The scattering factor of a material, which is composed of j different atom types, is a wavelength dependent complex value and it is defined in respect to the refractive index (equation (2.52)) as [113]

$$n(\lambda) = 1 - \frac{1}{2\pi} r_0 \lambda^2 \sum_j \tilde{N}_j f_j(\lambda), \quad (2.84)$$

where r_0 is the classical electron radius, \tilde{N}_j is the number density for each element j per unit volume, and $f_j(\lambda)$ is the corresponding atomic scattering factor. However, near-edge resonances depend strongly on the interactions between neighboring atoms. Therefore, the atomic scattering factor f_j has to be replaced by the scattering factors for a molecule or a corresponding polymer repeat unit f'_j . For photon energies far away from the absorption edges the molecular scattering factors f'_j are described via simple addition of the atomic scattering factors f_j proportional to the stoichiometry

$$f'_j = \sum_j N_j f_j(\lambda). \quad (2.85)$$

A similar transition from the atomic to the molecular level can be performed for the photoabsorption cross-section of a molecule $\sigma_{abs,m}$

$$\sigma_{abs,m} = 2r_0 \lambda f'(\lambda). \quad (2.86)$$

Soft X-rays can also be utilized in a focused beam for scanning transmission X-ray microscopy.[114] These measurements are also based on the material specific X-ray absorption cross section and allow a laterally resolved compositional mapping of the investigated polymer blend films.

Chapter 3

Experimental Methods

Historic milestone 1905: Albert Einstein published the most comprehensive theoretical work about the photoelectric effect, for which he was awarded the Nobel Prize in 1921.[115]

For a full characterization of polymer blend and artificially structured thin films, different characterization techniques must be applied. In general, the various methods address five main aspects: direct surface imaging, electrical characterization, analysis of optical properties, and the determination of film morphology and film composition.

As the first characterization step, optical microscopy (section 3.1) is a fast method to analyze the sample surface. It was also used to image large structures on a micrometer scale and to probe the large area quality of the fabricated structures. On the contrary, atomic force microscopy (AFM, section 3.2) is well suited for the investigation of surface structures on a nanometer scale and it provides three-dimensional surface maps. In addition, it reveals the surface composition of polymer blend films. Hence, a combination of both imaging methods allows a full surface analysis on all important length scales.

For the electrical characterization, current-voltage (IV) measurements (section 3.3) were performed under simulation of sunlight to measure the power conversion efficiency of the fabricated organic solar cells. A main influence on the solar cell performance originates from the light harvesting properties of the films, which were investigated with UV/Vis spectroscopy (section 3.4). This method was also applied to determine the light reflection at the film surface, which is especially interesting for the part of the light which is reflected back at the top-electrode in OSCs.

The film thickness of the investigated polymer samples was determined with optical ellipsometry (section 3.5). Besides being a fast method, optical ellipsometry not only provides the film thickness d , but also the corresponding optical refractive index n and the extinc-

tion coefficient k .

In order to characterize the inner film morphology of e.g. polymer blend samples, X-ray scattering methods yielded information about the whole polymer film volume. Besides the determination of the film thickness d and its surface roughness R_{rms} , X-ray reflectivity (XRR, section 3.6) also detects the film composition along the sample normal (see theory section 2.4.2). Grazing incidence small angle X-ray scattering (GISAXS, section 3.7) was used to determine the mean lateral size of the phase separation domains in polymer blend films and to reconstruct the surface structure dimensions of imprinted films. Soft X-rays were used for near edge X-ray absorption spectra (NEXAFS, section 3.8), which reveal the chemical composition of polymer films. In addition, focused soft X-rays allow for two-dimensional chemical composition maps of polymer blend films (scanning transmission X-ray microscopy, STXM, section 3.9).

3.1 Optical microscopy

Optical microscopy (OM) was applied on a routine basis to quickly investigate all spin coated and structured polymer films before further characterization. OM images have the potential to reveal any processing inconsistencies during film preparation, e.g. remaining polymer agglomerates in the films as a result of not fully dissolved polymer solution. In the case of structured polymer films, OM was essential to assess the structure quality on a large scale. For all measurements a Zeiss Axiolab A instrument was used, which was equipped with an objective nosepiece. Different magnifications of 1.25x, 2.5x, 10x, 50x, and 100x were possible and the corresponding resolutions per pixel are given in table 3.1. The microscopy images were recorded with a CCD camera (PixeLink, type PL-S621CU) and directly transferred to a computer, where they were handled with the PixeLink Capture BE plus software. Finally, the brightness and contrast of all the OM images was optimized with ImageJ 1.42q.

magnification	resolution [$\mu\text{m}/\text{pix}$]
1.25x	10.4
2.5x	5.2
10x	1.3
50x	0.26
100x	0.13

Table 3.1: Optical resolution per pixel for the different magnifications.

3.2 Atomic force microscopy

For the fabricated structured inorganic and organic substrates, a detailed knowledge of the height properties is crucial. Therefore, atomic force microscopy (AFM) is very well suited to reveal the full three-dimensional surface topology and it has already proven its application possibility for structure sizes down to the atomic scale.[116, 117] If in multicomponent systems the different materials have modified mechanical or chemical properties (e.g. softness), this method also allows for a detailed analysis of the surface composition.[118]

The fundamental working principle of AFM is based on the interaction between a high precision tip, which has a typical tip radius of a few nanometers, and the surface atoms of the sample. For such small dimensions the tip has to be brought very close to the sample surface in order to be able to detect the interatomic potential. The tip is mounted on a cantilever with a defined spring constant and it is deflected due to the attraction present. By moving the tip laterally over the sample, the cantilever deflection changes depending on the sample surface. This effect is finally used to reconstruct the three-dimensional surface topology.

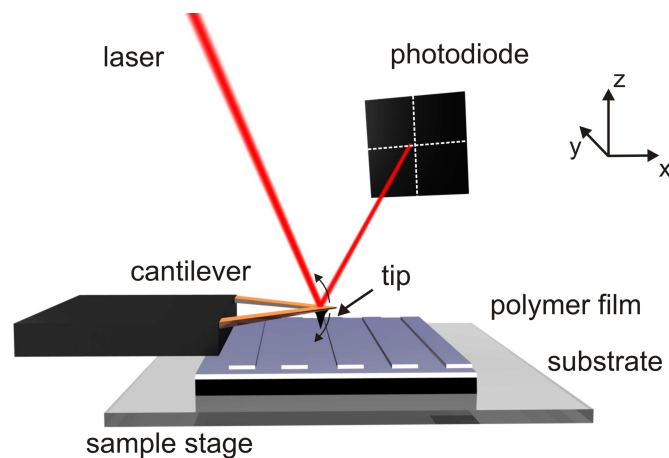


Figure 3.1: Experimental set-up of an atomic force microscope. While the tip, which is mounted on an oscillating cantilever, constantly probes the surface, the sample is scanned on a piezocontrolled stage. The deflection of the cantilever is detected via the reflection of a laser beam, which is monitored with a photodiode.

In figure 3.1 the principal set-up of an atomic force microscope is illustrated. The sample of interest is fixed on a sample stage, which can be adjusted in all three directions in space by high-resolution piezomotors. By movements in the xy -plane the sample surface is laterally scanned, whereas in z -direction only the distance between tip and sample is

adjusted. At the end of the spring-loaded cantilever the tip is fixed and the deflection of the cantilever is detected via the reflection of an impinging laser beam. The position of the reflected laser beam is recorded with a position sensitive photodiode and it is used to automatically calculate the actual sample surface height. Depending on the current x - and y -position, the height information is included in the final three-dimensional output information, which hence depicts the full topographic sample surface.

In order not to harm or to modify the investigated soft matter samples, the non-contact or intermitted contact mode was used for all AFM measurements. Three different atomic force microscopes were applied in this thesis, which all had identical working principles:

AFM-1: One instrument was an AutoProbe CP-R from TM Microscopes (Veeco, Plainview, USA), which was equipped with Ultralever ULNC-B cantilevers. They had a resonance frequency between 70 and 80 kHz and a spring constant of 0.40 N/m.

AFM-2: The second instrument was a Joel JSPM-5200 AFM (Tokyo, Japan). For this instrument ULTRASHARP NSC35/ALBS cantilevers (MikroMasch, Tallinn, Estonia) were used, which had a typical spring constant of 7.5 N/m and were driven at the eigen-frequency of 210 kHz.

AFM-3: In addition, an ULTRAObjective AFM from Surface Imaging Systems GmbH (Herzogenrath, Germany, now Bruker Nano GmbH) was used. For this instrument the laser beam was impinging the cantilever vertically and the necessary height information was calculated from the interference effects of the impinging and the reflected laser beam (this set-up is also called tube AFM). For this instrument PR-NC20 cantilevers were suited, which had a frequency range between 146 and 236 kHz and a typical spring constant between 21 - 98 N/m.

For AFM-1 to AFM-3 all applied cantilevers had tip radii below 15 nm, which was small in comparison to the investigated structure sizes. For AFM-1 and AFM-2 the recorded AFM data consisted of 256 lines with 256 datapoints each. For AFM-3 a resolution of 512 x 512 pixel was chosen. For improved sampling statistics, multiple positions on each sample were probed and the scan size was varied between 0.5 x 0.5 μm^2 and 10 x 10 μm^2 . The AFM data recorded were analyzed with the Gwyddion AFM software v2.22. By default, obvious measurement induced artifacts, which e.g. could result from drifting piezomotors, were corrected by a polynomial background subtraction and a median line height matching. If necessary, also a low pass filter (back and forward fast fourier transformation) was applied to the three-dimensional AFM data in order to remove artificial structure features below

a critical size.

3.3 Current-voltage characterization

The power conversion efficiencies of the fabricated organic solar cells was calculated from electrical current-voltage (IV) measurements, which were performed under dark and light conditions. For the simulation of the solar spectrum a SolarConstant 1200 solar simulator from K. H. Steuernagel Lichttechnik GmbH (Mörfelden-Walldorf, Germany) was used. A schematic illustration of the solar simulator is shown in figure 3.2(a). This device was equipped with a metal halogenide lamp, which was based on different rare earth elements. Its quasi continuous spectrum matched well with the global radiation detected on earth. The parabolic reflector of the solar simulator guaranteed a homogeneous sample illumination and an additional borosilicate diffusor cut of wavelengths below 290 nm. The light intensity was calibrated with a silicon based calibration solar cell (WPVS-ID 3, ISE, Freiburg, Germany) to a power density of 1000 W/m^2 , which corresponds to an AM 1.5 spectrum.

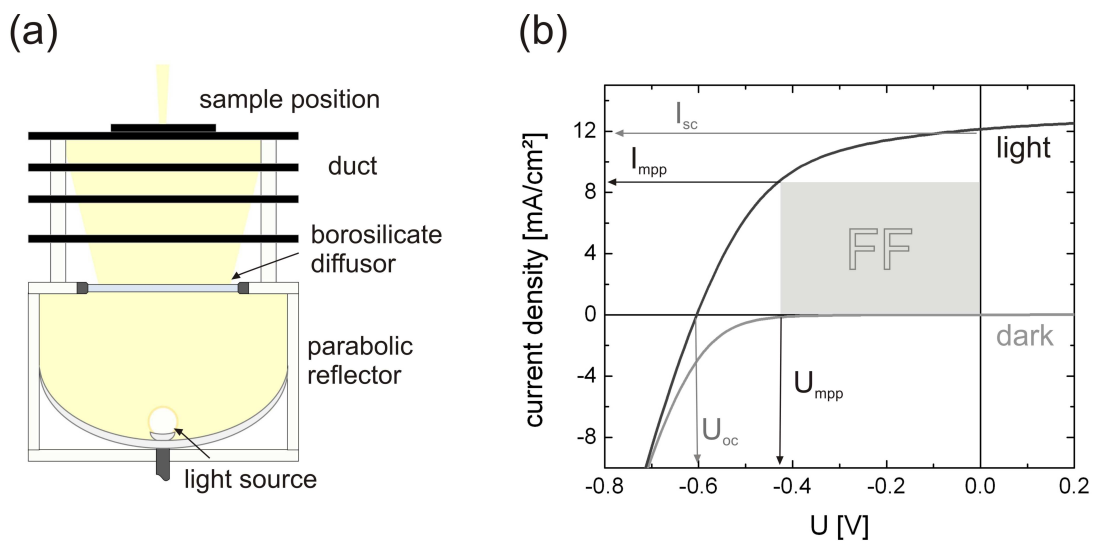


Figure 3.2: In (a) a schematic illustration of the applied solar simulator is shown. An exemplary IV -measurement of an organic solar is plotted in (b) and the measured values, which are necessary for the calculation of the power conversion efficiency, are included as well.

For the IV -measurements the samples were placed at a distance of 320 mm above the borosilicate diffusor of the solar simulator (see figure 3.2(a)). In order to avoid possible experimental errors, the sample was thermally shielded and only the important part of the solar cell was illuminated. The electrical measurements were performed with a Keithley

2400 sourcemeter and the voltage, which was applied between the bottom and the top electrode, was swept from -1 V to 1 V in 0.01 V steps. A delay time of 100 ms was used between each voltage step, which led to a very low current noise level around 10 pA. The IV -spectra were automatically recorded with a self-written program based on Testpoint v6 (Measurement Computing Corporation, Billerica, USA).

In figure 3.2(b) typical IV -curves of an organic solar cell performed in dark conditions (bottom gray line) and under simulated sunlight (upper black line) are shown. The power conversion efficiency η was calculated as the ratio between the input and the output power

$$\eta = \frac{P_{out}}{P_{in}} = \frac{U_{oc}I_{sc}FF}{P_{in}}, \quad (3.1)$$

where U_{oc} is the open-circuit voltage and I_{sc} the short-circuit current. Very important for the power conversion efficiency is also the fill factor FF , which is a measure for the recombination and resistive losses inside the solar cell. The FF is given by

$$FF = \frac{U_{mpp}I_{mpp}}{U_{oc}I_{sc}}, \quad (3.2)$$

with U_{mpp} denoting the voltage at the maximum power point and I_{mpp} the corresponding current value.

3.4 UV/Vis spectroscopy

UV/Vis spectroscopy was used to determine the optical absorption properties of the photoactive polymer films and to probe the grating efficiency of the structured films. Therefore, the sample of interest was illuminated with monochromatic light in the visible and the ultraviolet range and the corresponding absorption spectrum was recorded in dependence on the wavelength. In order to extract the characteristic transmittance T_{opt} and the reflectance R_{opt} , the measurements were performed in transmission and in reflection geometry. However, it had to be taken into account that the recorded transmitted intensity was given by the intensity of the impinging light (normalized to one) minus the absorption of the polymer film and the substrate, and also minus the intensity of the light, which is reflected at the sample and the substrate surface. The absorption of the substrate, which was always glass for this measurement technique (see section 4.3), was eliminated by referring to a reference spectrum, which was recorded simultaneously on an uncoated substrate. The reflectance of the sample $R_{opt,p}$ and of the substrate $R_{opt,s}$ was determined from independent measurements (more information below) and the actual absorption A_{opt} of the polymer film was finally derived as

$$A_{opt} = 1 - T_{opt} - (R_{opt,p} - R_{opt,s}) . \quad (3.3)$$

The corresponding absorbance *abs* which is often used in the context of thin films, is calculated as

$$abs = \log \left(\frac{I_{opt,0}}{I_{opt,t}} \right) = \alpha_{abs} d , \quad (3.4)$$

where $I_{opt,0}$ corresponds to the total incoming light intensity and $I_{opt,t}$ to the transmitted one. The absorbance *abs* is directly given by the product of absorption coefficient α_{abs} and film thickness d .

For the UV/Vis measurements on homogeneous polymer films a Lambda 35 UV/Vis-spectrometer from PerkinElmer (Waltham, USA) was used. This instrument was equipped with two light sources, which cover complementary wavelength spectra: a deuterium lamp produces UV-radiation with wavelengths between 190 nm and 326 nm and a second tungsten halogen bulb covers the visible spectrum up to a wavelength of 1100 nm. A monochromator, which was based on an optical grating, dispersed the white light and a slit system was used to select the specific wavelength. Afterwards, the monochromatic beam passed a beam splitter and was divided into the sample and the reference beam. After penetrating the sample and the reference, respectively, the transmitted intensities were measured with two individual photodiodes. For precise measurements, the intensity spectra of the lamps were calibrated before each measurement. These calibration measurements were also applied to normalize the recorded sample spectra to the photodiode efficiencies. For the measurements in reflectivity geometry a double prism deflected the sample beam by 90° and the beam reflected at the sample surface was conducted to the detector. Since the transmitted light, which was diffracted by an angle larger than 2.5° in respect to the sample normal, was not detected by the finite photodiode, these standard UV/Vis measurements also act as a probe for the spectral grating diffraction efficiency of the fabricated polymer structures (see section 6.3).

The instrument was controlled via the provided software UV-Winlab (PerkinElmer) and a wavelength region between 300 and 1100 nm was appropriate for the applied glass substrates, which strongly absorbed light below 290 nm. A measurement speed of 120 nm/min was chosen with a resolution of 0.1 nm. The effective bandwidth was determined by the widths of the slits to 2 nm.

However, in equation (3.3) A_{opt} does not include any light scattering contribution, which can be an important factor for the fabricated grating structures. For investigations concerning the absorption of strongly scattering samples, the scattered intensity had to be recorded in the complete three-dimensional space with an integrating sphere instead of

only in the direction of direct transmission. Therefore, the measurements on the total optical absorption of structured organic solar cells in section 6.3 were performed using a Lambda 900 spectrometer from PerkinElmer (Waltham, USA), which was equipped with an integrating sphere with a diameter of 60 mm. For these experiments the fabricated solar cells were measured in reflection geometry using the aluminum electrodes as back reflecting material.

3.5 Optical ellipsometry

For photoactive polymer thin films optical ellipsometry was used to determine the film thickness d and the optical parameters n and k . This method is especially useful for very thin films with thicknesses down to single atomic layers.[119] In this thesis, a scanning probe ellipsometric microscope (SPEM) from Accurion (former Nanofilm, Göttingen, Germany) was used, which was based on the combination of an EP3 imaging ellipsometer with an atomic force microscope (further details to this AFM see AFM-3 in section 3.2). The ellipsometric measurements were based on the phenomenon that the polarization of an electromagnetic wave is modified if it penetrates a polymer film and/or if it is reflected from a substrate surface. In accordance with equation (2.47), the polarization of light is given by the direction of the electric field \vec{E} of the photons. Linearly polarized light consists of photons with identical orientations of the electric field. It is common practice to denote waves with an orientation of polarization in the plane of incidence as p -waves and the ones with a perpendicular orientation as s -waves. If the maxima of p - and s -waves are out of phase, elliptically polarized light is generated. For a phase difference of 90° the light is circularly polarized.

The fundamental equation of ellipsometry is based on the Fresnel reflection coefficients for p - and s -waves (r^p and r^s) [120]

$$\tan \Psi_{OE} \exp(i\Delta_{OE}) = \frac{r^p}{r^s} . \quad (3.5)$$

In the equation above, Δ_{OE} depicts the phase difference and it is given by

$$\Delta_{OE} = \delta_{in} - \delta_{out} , \quad (3.6)$$

where δ_{in} and δ_{out} are the phase difference between the parallel and the perpendicular component of the incoming wave and the corresponding outgoing wave, respectively. In equation (3.5), Ψ_{OE} is the angle, whose tangent is the ratio of the magnitudes of the total reflection coefficients

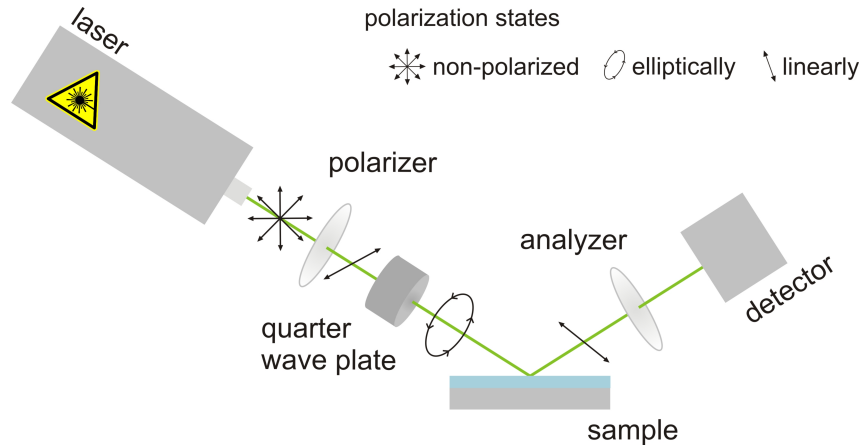


Figure 3.3: Schematic illustration of the optical ellipsometry set-up working in nulling condition: Non-polarized light from the laser is first linearly polarized by passing a polarizer and then elliptically polarized after the quarter wave plate. The position of the polarizer is chosen in such a way that the reflected light is again linearly polarized. The analyzer and the detector are used to determine the polarization angle of reflected light.

$$\tan \Psi_{OE} = \frac{|r^p|}{|r^s|}, \quad (3.7)$$

which are for a single interface defined as

$$r_{12}^p = \frac{\tilde{n}_2 \cos \phi_1 - \tilde{n}_1 \cos \phi_2}{\tilde{n}_2 \cos \phi_1 + \tilde{n}_1 \cos \phi_2} \quad \text{and} \quad r_{12}^s = \frac{\tilde{n}_1 \cos \phi_1 - \tilde{n}_2 \cos \phi_2}{\tilde{n}_1 \cos \phi_1 + \tilde{n}_2 \cos \phi_2}. \quad (3.8)$$

In the upper equation \tilde{n} is the complex optical refractive index of the two materials, ϕ_1 is the angle of incidence and ϕ_2 of the refracted light.

In figure 3.3 the actual instrumentation is shown, as it was used for the applied nulling ellipsometry method. A laser source generated non-polarized light with a wavelength of 532 nm. After passing through a polarizer the laser beam was linearly polarized and a fixed quarter wave plate transferred the light into a elliptically polarized state. Such quarter wave plates are commonly based on anisotropic optical materials, which have a fast and a slow axis for the light propagation. Depending on the orientation of the elliptically polarized light, again a linear polarization after the reflection at the substrate could be achieved. The orientation of this linearly polarized light was detected by an analyzer and a detector, which in nulling-condition measured a minimum in intensity. In practice, the polarizer and the analyzer were rotated iteratively to find the actual null condition. After the measurement, the characteristic ellipsometric values were calculated from the polarizer and the analyzer settings for multiple angles of incidence. In addition, the EP3 ellipsometer used was equipped with an optical focusing unit, which allowed for

two-dimensional ellipsometer images with a lateral resolution down to 1 $\mu\text{m}/\text{pix}$.

3.6 X-ray reflectivity

X-ray reflectivity (XRR) measurements were carried out to probe the film thickness and the vertical film composition of the investigated polymer films. A generalized theoretical description is given in section 2.4.2. The XRR experiments were performed on a Siemens D 5000 Diffraktometer (Munich, Germany) under ambient conditions. For the production of the X-rays, free electrons were generated by a heating coil ($I_{heat} = 30 \text{ mA}$) and accelerated towards a bulk copper block by an electric field of 40 kV. X-rays, which were produced by electron transitions from the $n = 2$ to the $n = 1$ level (K_α -radiation) were used in the present set-up and for copper anodes, such X-rays had a wavelength λ_{K_α} of 0.154 nm.[121]

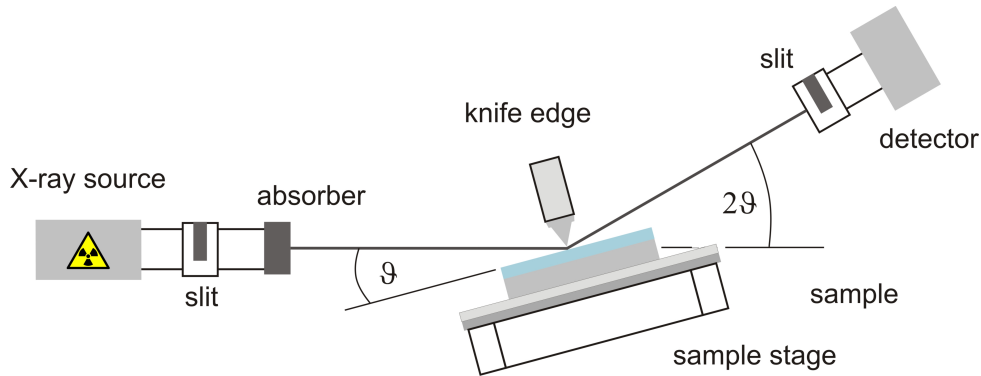


Figure 3.4: X-ray reflectivity set-up: The X-ray beam is collimated by a slit system and an optional absorber is used to shield the detector. The X-ray beam impinges the sample, which is fixed on a rotatable sample stage with a vacuum chuck, under a defined angle ϑ and an additional knife edge further collimates the beam and reduces the diffuse scattering. The detector follows the angle of incidence in $\vartheta/2\vartheta$ -condition.

In figure 3.4 a schematic illustration of the experimental set-up is illustrated. The samples were fixed on a rotatable sample stage by a vacuum chuck. The generated X-ray beam was collimated with a slit system and impinged the sample under an angle ϑ . An additional knife edge made of tantalum defined the beam size on the sample and reduced the diffuse scattering, which would lead to increased background noise. The reflected beam was detected with a scintillation counter, which was placed behind a graphite monochromator in order to filter the $\text{Cu-}K_\beta$ line. For small incident angles an additional absorber was used in order to avoid detector saturation.

Before each measurement the sample had to be aligned to the X-ray source and the detector by performing a so-called rocking scan. Therefore, the X-ray source and the detector were placed in $\vartheta/2\vartheta$ -condition (typically $0.2^\circ/0.4^\circ$) and the sample was rotated while the reflected intensity was continuously recorded. The actual reflectivity curves were finally

obtained by measuring the intensity of the specular reflection for incident angles ϑ between 0° and 6° . The data analysis was performed with the reflectivity simulation software Parratt32.[122] Therefore, the incident angles ϑ were transformed to the corresponding z -components of the scattering vector q -values, which were given by

$$q_z = \frac{4\pi}{\lambda} \sin \vartheta . \quad (3.9)$$

The Parrat32 software calculated the reflectivity of an assumed refractive index profile via the layer based Parratt algorithm [94] and compared it to the measured data (see also section 2.4.2). In an iterative process, the best fit to the data was generated and the correct refractive index profile obtained.

3.7 Grazing incidence (ultra-)small angle X-ray scattering

In this thesis, grazing incidence small angle X-ray scattering (GISAXS) experiments were essential for the structural characterization of the investigated polymer samples [123] and their theoretical background was already discussed in great detail in section 2.4.3. In comparison to the already illustrated XRR measurements, GISAXS measures the specular and the diffuse scattering. As a result, the vertical film morphology and the in-plane structures were detected. Thus, GISAXS was very well suited for a surface analysis of the artificially structured polymer films (section 6.1). Moreover, GISAXS was used to probe the degree of filling, when an additional polymer was cast on top of such structures (section 6.3).

A schematic illustration of the GISAXS experiment is shown in figure 3.5. The sample was illuminated with a collimated X-ray beam with a wave vector \vec{k}_i under an incident angle α_i , which was chosen to be slightly above the critical angle for total reflection α_{crit} . The part of the X-ray beam, which was reflected at the polymer surface, resulted in strong specular scattering. The remaining intensity penetrated the polymer film and the scattered intensity (given by wave vector \vec{k}_f) was recorded with a two-dimensional detector in dependence on the scattering angles α_f and ψ . In this context, α_f was the exit angle in respect to the sample plane and ψ the one in respect to the scattering plane, which was defined by the incoming beam and the sample normal. Besides the high scattering intensity at the specular reflection, also an additional maximum at the critical angle for total reflection of the investigated material was observed ($\alpha_f = \alpha_{crit}$ and $\psi = 0$). This feature is called Yoneda maximum [102] and it is given by the refractive index of the investigated material.

For polymers the penetration depth of the impinging X-rays is on the order of tens of micrometers if incident angles α_i larger than the critical angle α_{crit} are chosen. Therefore, for the investigated thin films ($d < 200$ nm) this method probed the complete sample volume. The sample-to-detector distance (SDD) defined the range of the observable scattering angles and hence of the resolvable structure sizes. For a standard GISAXS set-up with an SDD of around 2 m, structures between a few and up to one thousand nanometers were addressed. However, by increasing the SDD to around 12 m, ultra-small scattering angles were also observed and structures up to several micrometers were resolved.[124] The GISAXS-configuration with such high SDD values is generally referred to as grazing incidence ultra-small angle X-ray scattering (GIUSAXS). An additional advantage of GISAXS lies in the large macroscopic size of the X-ray beam footprint on the sample. Depending on the angle of incidence, footprint lengths of up to a few millimeters were typical. As a consequence, very good sampling statistics of nanoscopic structures distributed over a macroscopic sample area were achieved.

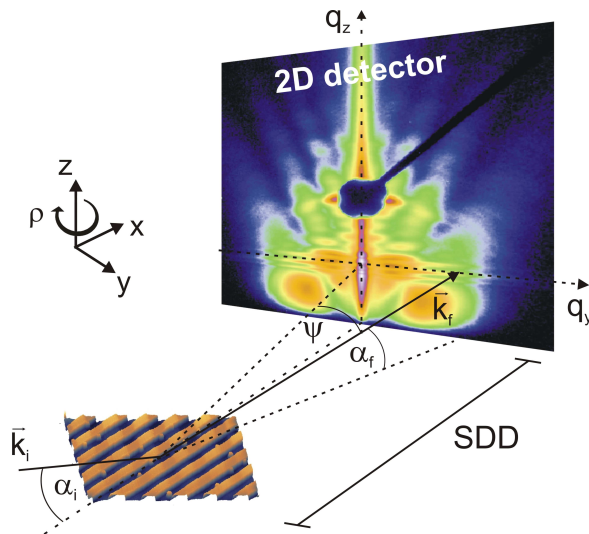


Figure 3.5: Schematic illustration of the GISAXS set-up: X-rays impinge the sample under a grazing angle α_i and the scattered intensity is recorded in dependence on the scattering angles α_f and ψ . The rotational angle between the channel structure and the impinging X-rays is denoted as ρ .

The GISAXS experiments were mainly performed at the beamline BW4 at HASYLAB (DESY, Hamburg, Germany).[125, 126] The applied X-ray beam had a wavelength λ of 0.138 nm and it was focused to a size of $40 \times 80 \mu\text{m}^2$ (width x height) using two entrance slits and a set of beryllium lenses. The scattering data were recorded with a CCD-type MarCCD 165 detector (Marresearch GmbH, Norderstedt, Germany) and consisted of 2048×2048 pixels with a pixel size of $79.1 \times 79.1 \mu\text{m}^2$. For the in-situ thermal annealing GISAXS measurements in section 6.1.4 the beamline was equipped with an additional sample heating stage. In a temperature range between 0 and 100 °C the temperature of the hot plate was increased with a rate of 100 K min^{-1} . For temperatures above 100 °C the heating rate was reduced to 100 K min^{-1} . The hot plate was also equipped with an

air pressure cooling system which allowed the sample to be cooled down to 60 °C at a rate of -50 K min^{-1} . For a further temperature decrease to room temperature the rate was reduced to 100 K min^{-1} .

The GISAXS experiments in section 6.3 were carried out at the new P03 MINAXS (micro- and nanofocus X-ray scattering) beamline, which is located at the PETRA III storage ring (DESY, Hamburg). However, the measurement principles correspond to the given explanation from above. Only the wavelength was changed to 0.0941 nm and the beam size was reduced to $40 \times 20 \text{ }\mu\text{m}^2$. For these experiments a Pilatus 300k detector was applied, which recorded the scattering data at a resolution of 487×619 pixels (pixel size: $172 \times 172 \text{ }\mu\text{m}^2$).

The most detailed analysis of the scattering data concerning the lateral and the vertical distribution of the film structures was based on the simulation of the two-dimensional scattering data. For this complex mathematical modelling approach the IsGISAXS software by Lazzari was applied.[106] This simulation software allowed a full reconstruction of the two-dimensional GISAXS data based on theoretical models of the film morphology. Their fundamental mathematical equations were already discussed in section 2.4.3 and more detailed descriptions on the simulation models are given separately for each polymer system in the corresponding sections. In a first instance, the IsGISAXS software was used to fit the scattering intensity along two prominent line cuts in order to avoid unnecessary computing time.

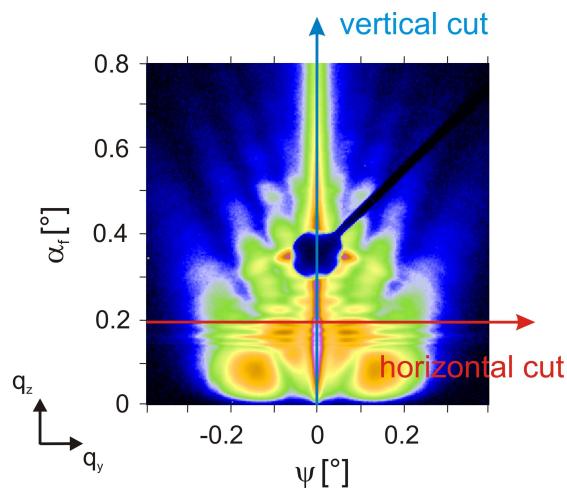


Figure 3.6: Horizontal and vertical line cuts of the scattering data were taken along ψ - and α_f -direction to determine the sample morphology.

In figure 3.6 the positions of the vertical and the horizontal line cuts are depicted, which are also commonly referred to as detector and out-of-plane cut, respectively. The vertical cuts contain information about morphology structures and film composition vertical to the sample surface and were taken at $\psi = 0^\circ$. The horizontal cuts were extracted at the critical angle of the material ($\alpha_f = \alpha_{crit}$) and revealed lateral film structures.[97] For improved statistics, the scattering signal was integrated over three neighboring detector

pixels.

Besides the full IsGISAXS simulations, preliminary structural information was extracted from the out-of-plane cuts by applying a mathematical model, which was based on a resolution function and two structural contributions. This so-called effective surface approximation of the distorted wave Born approximation assumed polydisperse objects with well-defined nearest neighbor distances and a possible domain structure.[127, 128] In this simple model, the characteristic structural lengths were assumed to follow Lorentzian distributions and an additional resolution function was embedded as well.

3.8 Near edge X-ray absorption fine structure spectroscopy

Making use of the element-specific X-ray absorption edges, the film composition of the different polymer films was also determined with near edge X-ray absorption fine structure spectroscopy (NEXAFS, the corresponding theory is discussed in section 2.4.5).

The measurements were performed at the PolLux beamline, which is located at the Swiss Light Source (SLS) of the Paul Scherrer Institute (Villigen, Switzerland).[129] A schematic sketch of the beamline instrumentation is shown in figure 3.7. In comparison to wiggler or undulator magnets, which produce high flux X-ray beams with narrow energy bands, at PolLux a bending magnet with a critical energy of 5.5 keV was installed to generate X-rays with a larger wavelength spectrum ($E = 200 - 1400$ eV). This was necessary for polymer samples to cover the dominant carbon and oxygen K -edges. A monochromator based on two spherical gratings was used to select the desired photon energies.[130] In order to avoid higher order photons (i.e. photons with two or three times the principal photon energy), a higher order suppressor (HOS) was introduced to the X-ray beam after the monochromator.[131] The HOS was based on three fused silica mirrors with a MgF_2 coating and led to a monochromatic X-ray beam with a high energy resolution, but also a reduced intensity.

Finally, the photon beam was focused on the sample by a Fresnel zone plate (FZP). Such devices use diffraction instead of refraction in order to focus X-rays to a point focus. Therefore, the applied zone plate consisted of a set of radially symmetric rings, which alternate between opaque and transparent and their difference in radii was decreasing from the center towards the outer border (see also figure 3.7(b)). As a result, the X-rays, which were diffracted at the rings of the FZP, interfered and the dimensions of the FZP were chosen in such a way that a narrow beam spot of constructive interference occurred in the center. Furthermore, an additional order sorting aperture (OSA) had to be installed to remove interference rings of higher orders. Since the experiments were performed

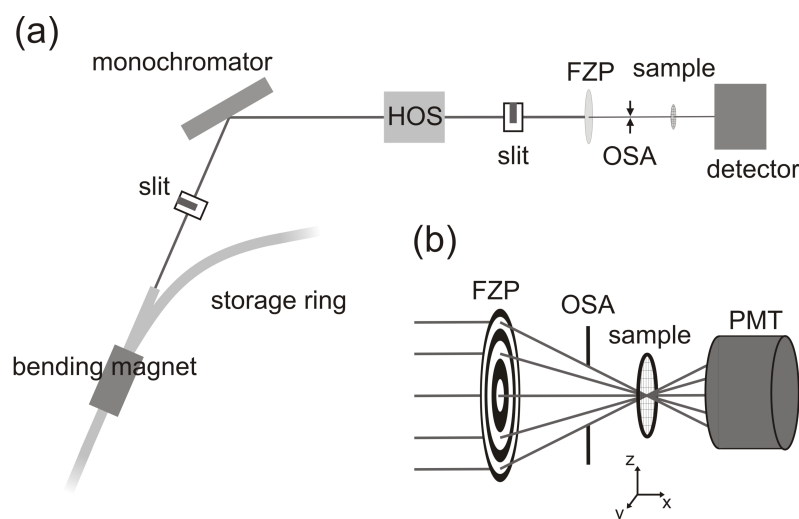


Figure 3.7: Schematic illustration of the NEXAFS set-up: (a) X-rays with a broad wavelength range are generated by a bending magnet and a monochromator is used to select the desired photon energies. A higher order suppressor (HOS) is installed to avoid higher harmonics of the X-rays. The beam is focused on the sample by a Fresnel zone plate (FZP) and an optical aperture (OSA). In (b) a close-up sketch is shown including FZP, OSA, sample, and the photomultiplier tube (PMT), which is used to record the transmitted intensity. In order to achieve a high lateral resolution, the sample is installed on a piezo-driven and interferometrically controlled holder.

in transmission geometry, the polymer films were cast on silicon nitride membranes or transferred to copper transmission electron microscopy (TEM) grids (see also section 4.3). Finally, the substrates were placed on a sample stage, which was movable in three dimensions.

In order to prevent absorption from the surrounding atmosphere, the measurements were performed at a chamber pressure of $9.0 \cdot 10^{-3}$ mbar. The spectra around the oxygen *K*-edge were recorded between 510 and 590 eV at a step size of 0.5 eV and each data point was integrated over 50 ms. For the carbon *K*-edge the measured energy range was shifted from 280 to 320 eV with the experimental conditions from above. The NEXAFS measurements regarding residual solvent content in conducting polymer films (section 5.3) were recorded without FZP and the photon beam was only collimated by the OSA, which had a radius of 70 μm . A photomultiplier tube coupled to a scintillator (phosphor screen), which converted the X-rays to visible light, was used as a detector.

3.9 Scanning transmission X-ray microscopy

Scanning transmission X-ray microscopy (STXM) has been already widely used to chemically map conducting polymer blend films.[132, 133, 134] The same method was utilized in this thesis to investigate the amount of residual solvent molecules - however, now al-

lowing for a high lateral resolution. The STXM measurements were carried at the PolLux beamline (see section 3.8). Recently, a lateral resolution down to 15 nm was achieved at this beamline.[135] In principal, the same measurement set-up, as it was applied for the NEXAFS spectra, was also used for STXM. However, the STXM data were recorded at defined photon energies and the samples were scanned for each energy with respect to the X-ray beam. A resolution of 100 x 100 data points was appropriate for all STXM images and an integration time of 200 ms per pixel guaranteed sufficient sampling statistics. Depending on the total size of the STXM image, this corresponds to pixel sizes between 50 x 50 nm² and 200 x 200 nm². To allow for such high-precision lateral sample movements, the sample stage was piezo-driven and interferometrically controlled (figure 3.7(b)).

For the calculation of the two-dimensional compositional images the raw STXM data were treated using the IDL (Interactive Data Language) widget aXis 2000 by the following process: At the beginning, the lateral drift between images at different energies was corrected by automatically aligning the images in respect to each other. The NEXAFS spectra of all pristine components were taken and normalized to the film thickness. Since each data point of the STXM image was taken at multiple energies, a sum of the pristine spectra was fitted to the resulting spectra at each data point. The coefficients for each component were finally used to calculate the film composition. The same routine was adopted to calculate two-dimensional solvent distribution maps (see section 5.3).

Chapter 4

Materials and Thin Film Preparation

Historic milestone 1954: The Bells Laboratories announce the invention of the first modern silicon solar cells based on p-n-junctions.[136] Still the most common solar cell type to this day.

In this chapter, the investigated conducting polymers are introduced - divided into the classes of hole and electron conducting materials. In addition, the utilized mold materials and their mechanical properties are discussed. Finally, this section ends with the illustration of the basic principles of the spin coating technique, which was applied to fabricate the homogeneous polymer thin films.

4.1 Photoactive conducting polymers

4.1.1 Hole conducting polymers

For the majority of conducting polymers the mobility of induced holes is higher than the mobility of the corresponding electrons (see also section 2.1.4). Such polymers are thus referred to as hole-conductors or p-type polymers. For the actual applications, the difference in hole and electron conductivity is often critical for the performance of organic optoelectronic devices.[137] As a consequence, organic light emitting and photovoltaic devices often have to be equipped with additional electron and hole transport layers which lead to rather complex layer structures.[138]

Figure 4.1 illustrates the chemical structures of the applied hole conducting polymers and for each material more detailed characteristics are given below:

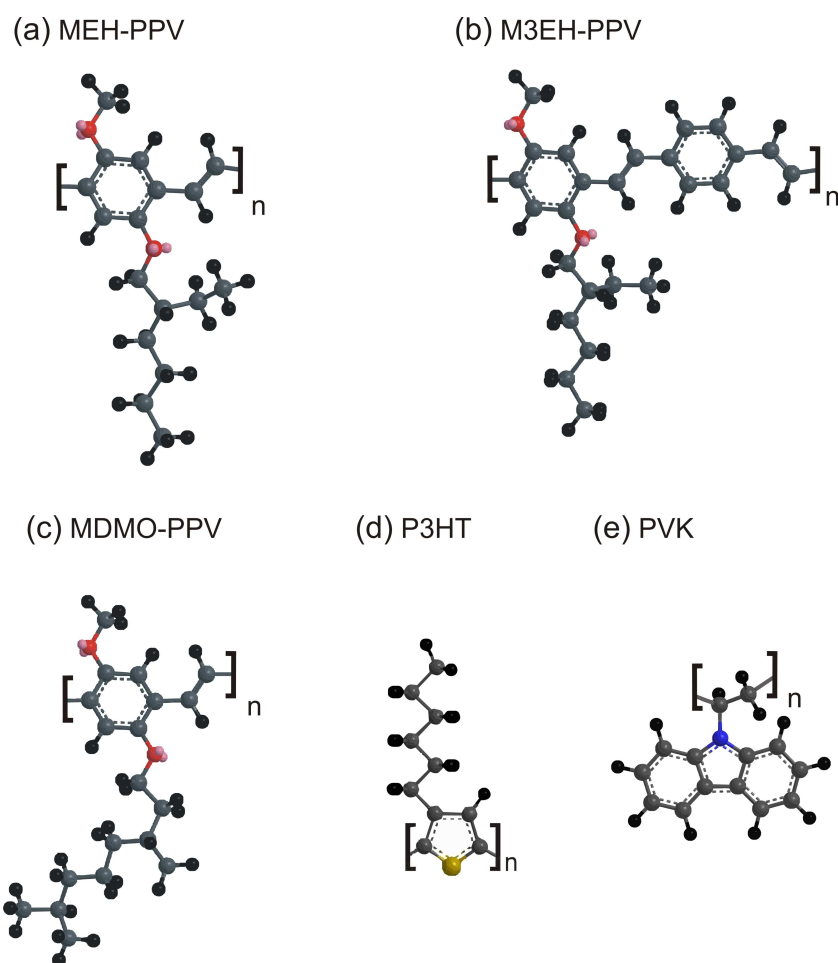


Figure 4.1: 3-dimensional chemical drawings of the molecular structures of the investigated p-type polymers: (a) MEH-PPV, (b) M3EH-PPV, (c) MDMO-PPV, (d) P3HT, and (e) PVK. Carbon atoms are shown in gray, hydrogen atoms in black, sulfur atoms in yellow, nitrogen atoms in blue, and oxygen atoms in red. The hydrogen atoms bond to oxygen are shown in light red in order to depict the highly polar character.

MEH-PPV: In 1990 Burroughes et al. presented the first light-emitting diode based on a conjugated polymer.[139] They used plain poly(p-phenylene vinylene), which was synthesized via a solution-processable precursor. Shortly afterwards, Braun and Heeger confirmed this observation for poly[(1-methoxy)-4-(2-ethylhexyloxy)-p-phenylene vinylene] (MEH-PPV), which has the main advantage of being soluble in conjugated form in organic solvents.[140] The good solubility of MEH-PPV in organic solvents comes from the long side groups (see molecular structure in figure 4.1(a)). MEH-PPV has an average energy level of the highest occupied molecular orbital (HOMO) of -5.0 eV and of the lowest unoccupied molecular orbital (LUMO) of -2.7 eV. As all other polymers inves-

tigated, MEH-PPV is commercially available too. The applied polymer was purchased from Polymer Source (Montreal, Canada). Its molecular weight was $2.9 \cdot 10^6 \text{ g mol}^{-1}$ and its polydispersity (*PDI*, polydispersity index) was 1.5. The *PDI* is a measure of the distribution of the polymer chain length, which is given by the ratio of the weight average molecular weight M_w and the number average molecular weight M_n .

M3EH-PPV: The novel poly[2,5-dimethoxy-1,4-phenylene-1,2-ethenylene-2-methoxy-5-(2-ethylhexyloxy)-(1,4-phenylenevinylene-1,2-ethenylene)] (M3EH-PPV) has also been used in this thesis. M3EH-PPV is an alternating copolymer, which has been already successfully applied for the fabrication of efficient all-polymeric solar cells based on a blend with a cyano-substituted PPV.[141] In case of M3EH-PPV the monomer units consist of covalently bound alternating PPV units with modified side groups. The corresponding molecular structure is found in figure 4.1(b). M3EH-PPV has its HOMO energy level also at -5.3 eV and its LUMO energy level is located at -2.9 eV. The polymer was ordered from Sigma-Aldrich (Steinheim, Germany). Unfortunately, for this polymer the manufacturer could not provide any details on its molecular weight and its polydispersity.

MDMO-PPV: Another interesting polymer from the group of PPVs is the poly[2-methoxy-5-(3-7-dimethyloctyloxy)-1,4-phenylene vinylene] (MDMO-PPV). In 2001, bulk heterojunction solar cells based on a combination of MDMO-PPV with a fullerene material were the first to break the symbolic power conversion efficiency hurdle of 1%. [142] The molecular structure of MDMO-PPV is plotted in figure 4.1(c) and it reveals a polymer backbone configuration identical to the MEH-PPV. For MDMO-PPV the HOMO and the LUMO energy levels are located at -5.3 eV and -3.0 eV, respectively. The polymer was ordered from American Dye Source (Baie d'Urfe, Canada) and it had a molecular weight greater than $1 \cdot 10^6 \text{ g mol}^{-1}$. Its polydispersity index was defined by the supplier only roughly ($PDI(\text{MDMO-PPV}) > 25$). During polymerization the polymer was end capped with DMP (dimethyl benzene-1,2-dicarboxylate).

P3HT: Besides the mentioned PPVs, also the hole conducting poly[3-hexylthiophene] (P3HT) is investigated in this work. From the molecular structure of P3HT in figure 4.1(d) it is seen that the polymer backbone consists of sulfur containing thiophene units. From the different types of polythiophenes with modified sidechains, P3HT is most commonly applied due its high electrical conductivity. For application in organic solar cells, especially thin blend films based on P3HT and various fullerene derivatives are very well studied and the resulting efficiencies have been pushed above 6 %.[143] Until the recent synthetization of novel low-band gap polymers [11], P3HT:fullerene solar cells have been

the pushing system in the field of organic photovoltaics. In this thesis, the P3HT had an average molecular weight of $50 \cdot 10^3 \text{ g mol}^{-1}$ and a regioregularity greater than 98 %. The regioregularity depicts the symmetry of the coupling between the repeating thiophene units which is crucial for a good electrical conductivity. The P3HT was purchased from Rieke Metals Inc (Lincoln, USA) and its HOMO and LUMO energy levels lie at -4.8 eV and -3.0 eV, respectively.

PVK: Poly[vinyl carbazole] (PVK) is a glassy thermoplastic, which is synthesized by reacting acetylene with carbazole. The molecular structure of PVK with its characteristic carbazole units attached to the polymer backbone is found in figure 4.1(e). Back in 1957, Hoegl et al. observed that PVK behaves like a photoconductor, which was the first evidence of a polymer with photoconductive properties.[144, 145] Even today, PVK is still a crucial component for the fabrication of state-of-the-art organic white light emitting devices (OWLEDs).[146] The PVK was ordered from Sigma Aldrich (Seelze, Germany) and had a molecular weight of $1.1 \cdot 10^6 \text{ g mol}^{-1}$ and a *PDI* of 3.8. It has a HOMO energy level of -5.6 eV and its LUMO energy is located at -2.2 eV. The low energy level of the HOMO makes PVK not only interesting for organic solar cells with high open circuit voltages, but it also leads to a low redox potential, which makes it stable against oxidation.[147]

4.1.2 Electron conducting materials

Conducting polymers, which favor an electron instead of a hole transport, are still rare. The electron current is typically severely reduced due to the presence of trap states as it was e.g. shown by Blom et al. for standard conducting PPV derivatives.[148] From a molecular point of view, it is also easier to design electron-rich (p-type) than electron-poor (n-type) polymers. Regarding the synthesis of such n-type polymers, one approach is to introduce additional functional cyano- or nitro-groups in the polymer chain (e.g. MEH-CN-PPV) or to apply polyfluorenes, which often have better solubility parameters.

F8BT: Poly[dioctylfluorene-co-benzothiadiazole] (F8BT) is the most common conducting polyfluorene and it has been already investigated in great detail not only in homopolymer films [149], but also in combination with other polymers.[133] Organic solar cells based on the blend of a similar polyfluorene (F8TBT) and P3HT have the highest observed power conversion efficiencies of 1.2 % for all-polymeric devices.[150] Figure 4.2 illustrates the molecular structure of F8BT with its functional benzothiadiazole groups. It has a large band gap energy of 2.6 eV and the energy level of its HOMO level is at -5.9 eV and of its LUMO at -3.3 eV. The polymer was ordered from American Dye Source (Baie d'Urfe,

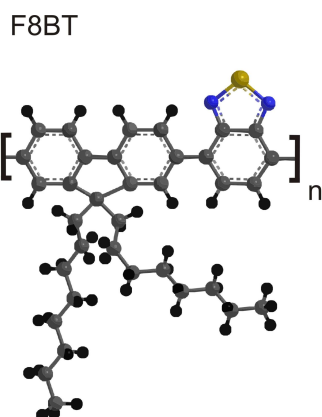


Figure 4.2: 3-dimensional chemical drawing of the molecular structure of the investigated n-type F8BT polymer. The same color coding scheme has been used as in figure 4.1.

Canada) and different batches with varying molecular weights M_w and polydispersity indices PDI were used in the framework of this thesis. Their values are given in table 4.1.

To overcome the limitations in electron accepting polymers, additional material types as well have proven their potential for application in organic optoelectronics. Among them are the different types of fullerenes, which are especially interesting for organic solar cells in a spherical shape (also called buckyballs).

PCBM: The phenyl-C61-butyric acid methyl ester (PCBM) combines a buckminsterfullerene (C_{60}) with an additional acid methyl ester sidegroup, which guarantees good solubility in versatile solvents. For clearer presentation purposes, the molecular structure is plotted in figure 4.3. Due to the large electron attracting potential of PCBM, very short electron transfer times below 1 ps have been observed for fullerene:polymer systems.[151] Standard P3HT:PCBM blends have already been used to fabricate single junction devices with efficiencies of up to 5 % in case of fully optimized fabrication conditions.[152] For P3HT:PCBM solar cells with very small active areas of $1.5 \times 1.5 \text{ mm}^2$ even efficiencies of over 6.5 % have been reported.[153] PCBM has its HOMO energy level at -6.1 eV and its LUMO energy level at -3.7 eV, which results in a band gap of 2.4 eV. In this thesis, the PCBM was purchased from Nano-C Inc (Westwood, USA).

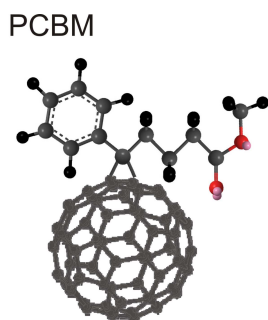


Figure 4.3: Chemical structure of PCBM, which combines a spherical C_{60} fullerene with an acid methyl ester sidegroup. The same color coding scheme has been used as in figure 4.1.

4.1.3 PEDOT:PSS

Up to this point, only polymers suitable as active materials in organic solar cells were discussed. However, in order to improve the overall power conversion efficiency of such devices, thin functional intermediate layers are often introduced. Most commonly, layers based on poly[3,4-alkylenedioxythiophene]:polystyrene sulfuric acid (PEDOT:PSS) are applied as electron blocking and hole injecting layers in OSCs and OLEDs.[154] In addition, such PEDOT:PSS layers also planarize the rough surface of the commonly used transparent indium tin oxide (ITO) electrodes by smoothing surface imperfections. This is important to prevent electrical shorts from local spikes in the ITO. The work function E_{work} of PEDOT:PSS is on the order of 5.0 to 5.2 eV [155] and therefore leads to a built-in potential of 0.8 - 1.0 eV if combined with an aluminum top electrode ($E_{work} = 4.2$ eV). In figure 4.4(a) the molecular structure of PEDOT is shown, which belongs to the group of 3,4-dialkoxythiophene containing polymers. An EDOT monomer consists of an aromatic ring of four carbon atoms with a supplementary sulfuric component. The additionally substituted 3,4-alkylenedioxy-groups are bridged to the thiophene ring and hence build a second ring with a fixed six-fold geometry. Similar mono- and dialkoxy-substituted thiophene derivatives were first developed by Leclerc et al. [156] and later produced on a large scale by Heywang and Jonas at the Bayer AG Corporate Research Laboratories (Leverkusen, Germany).[157] For the synthesis, polystyrene sulfuric acid (PSS) is used to polymerize EDOT by oxidation with a balancing counterion. The molecular structure of PSS is illustrated in figure 4.4(b). As a result of this synthesis, commercial PEDOT is normally available as a well dispersed aqueous solution of PEDOT:PSS. Due to its high density of free positively charged carriers, PEDOT:PSS has a conductive cationic behavior.[158] However, PEDOT:PSS thin films revealed a highly anisotropic conductivity, which strongly depends on the film morphology of the PEDOT and the PSS component.[159]

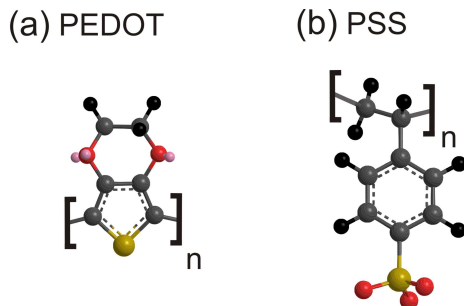


Figure 4.4: 3-dimensional chemical drawings of the molecular structures of the investigated electron blocking PEDOT:PSS polymer. The same color coding scheme has been used as in figure 4.1.

Already in aqueous solution, single PEDOT:PSS particles are formed consisting of high molecular weight PSS, which is physically cross-linked by PEDOT oligomers. Due to its water insolubility, the PEDOT component is mainly located in the center of the particles

and the outer part is rich in PSS, which is strongly hydrophilic. During coating as well, these differences in PEDOT-concentration remain and lead to a spatially distributed conductivity in the final polymer film. As a consequence, a reduced charge carrier mobility due to energy barriers at the PSS-rich surfaces is observed, which also hinders the charge transport between the PEDOT-rich cores.[160] The surrounding PSS-rich shell was measured to have a thickness of about 5 - 10 nm.[161] In addition, an enrichment of PSS at the polymer-air surface was found, which results in a lower conductivity perpendicular to the surface. As a further result of PSS addition, the orientation of the polymer chains within the pure PEDOT cores is also altered. Whereas in pure PEDOT films the polymer chains are π -stacked with a characteristic repeat distance of 0.34 nm, films made of PEDOT:PSS appear completely amorphous.[162, 163] As a consequence, a lot of experimental effort is necessary to fully optimize the PEDOT:PSS layer in actual organic devices.

In this thesis, the PEDOT:PSS was purchased from Sigma Aldrich (Steinheim, Germany) and it is composed of 0.5 wt% PEDOT and 0.8 wt% PSS dispersed in H₂O. It has a conductivity of 1 S/cm and it hence belongs to the conductive grade polymers. For the future fabrication of low-cost optoelectronic devices, high-conductive PEDOT:PSS has the potential to fully replace transparent conductive oxides (TCOs) as electrode material.[164] For this application, its conductivity can be easily enhanced by doping with e.g. N-methylpyrrolidone (NMP) or glycerine, which is discussed in more detail in section 6.3.[165] For this doping approach, glycerine with a purity of $\geq 99.5\%$ was ordered from Carl Roth (Karlsruhe, Germany).

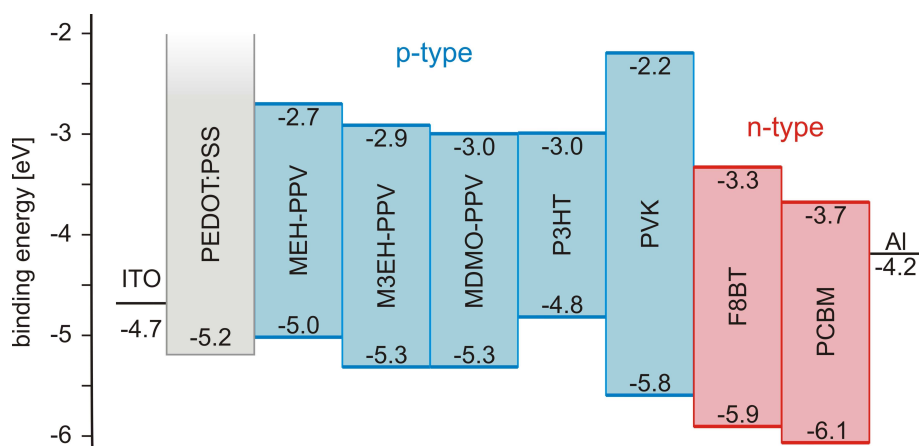


Figure 4.5: Overview of the energetic alignment of the HOMO and LUMO energy levels for the applied photoactive polymers. The working function of the electrode materials - PEDOT:PSS, ITO, aluminum - are included as well. For clarity, the electron conducting materials are depicted in red and the hole conducting polymers in blue.

Since in an actual optoelectronic device, the energetic alignment of the HOMO and LUMO energy levels from the electron donor and acceptor materials is crucial for a successful

charge carrier separation, the energy bands for all investigated materials are compared in figure 4.5. For clarity, in a BHJ organic solar the generated negative electrons have to be extracted to the aluminum electrode, whereas the corresponding positive holes have to be transported to the PEDOT:PSS/ITO electrode. In order to avoid charge accumulation in one material, an efficient ladder alignment of the energy levels must be guaranteed. To conclude this section, the molecular weights M_w and the polydispersity indices of the applied conducting polymers are given in table 4.1.

	M_w [g mol ⁻¹]	PDI
MEH-PPV	$2.9 \cdot 10^6$	1.5
M3EH-PPV	n/a	n.a.
MDMO-PPV	$>1 \cdot 10^6$	>25
P3HT	$50 \cdot 10^3$	n.a.
PVK	$1.1 \cdot 10^6$	3.8
F8BT type-I	$16 \cdot 10^3$	5.6
F8BT type-II	$157 \cdot 10^3$	3.0
F8BT type-III	$42 \cdot 10^3$	3.0

Table 4.1: Molecular weights M_w and polydispersities PDI of the applied conducting polymers.

4.2 Mold materials

For the preparation of the micro- and nano-structured polymer films, two different mold materials were applied: In the course of the inverted MIMIC approach (see sections 2.3.1 and 6.2) molds based on bisphenol-A polycarbonate (BPA-PC) were used and for the temperature sensitive NIL method (see sections 2.3.2 and 6.3) polydimethylsiloxane (PDMS) was the material of choice. Their chemical and mechanical characteristics are discussed below.

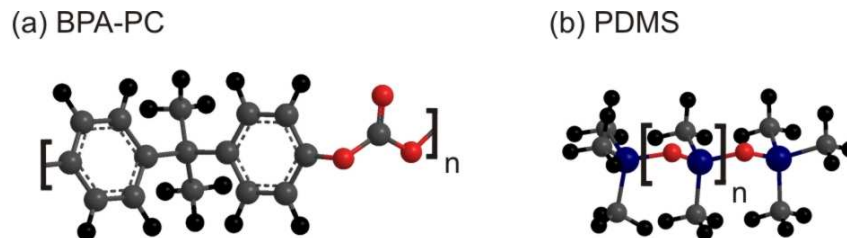


Figure 4.6: Molecular structures of the applied mold materials: (a) BPA-PC and (b) PDMS. The same color coding scheme has been used as in figure 4.1.

BPA-PC: For the solution based fabrication of PEDOT:PSS channels (see section 6.2)

master structures made of bisphenol-A polycarbonate (BPA-PC or PC for short) were applied. On the one hand, such structures are commercially available on a large scale, e.g. as part of blank compact discs (Platinum 700 MB, 4M Systems SA), and on the other hand, more complex polycarbonate structures can also be ordered custom-made depending on the individual requirements (e.g. from CSEM, Centre Suisse d'Électronique et de Microtechnique, Switzerland). The molecular structure of BPA-PC in figure 4.6(a) shows a polymer backbone, which consists of interconnected carbonate groups. Polycarbonate belongs to the group of thermoplastics and, due to the excellent structure transfer from hard master structures to PC at high replication fidelities, it is a standard material for thermal nanoimprinting of nanoscopic structures.[166] In comparison to other mold materials PC has a relatively high Young's modulus of 2 - 2.4 GPa. Its glass transition temperature T_g is located at 150 °C and it shows good chemical resistance against diluted acids. PC is also known to resist high tensile strengths σ_t of up to 60 MPa. As a consequence, the high stiffness of PC in combination with its known capability of undergoing plastic deformations by recovering its original shape makes polycarbonate an ideal candidate also for lithographic approaches. The good flexibility of the PC molds (flexural modulus of 2200 MPa [167]) is also important for homogeneous and reproducible lift-off conditions during the imprint (more details in section 6.2).

PDMS: For the fabrication of polymer structures via nanoimprint lithography (NIL) master molds made of polydimethylsiloxane (PDMS) were used in this thesis. PDMS is an elastomer and it therefore adapts the surface of the imprinting target homogeneously over large areas. Nanoimprinted structures with sizes around 30 - 40 nm have already been reported based on PDMS molds.[168] Nevertheless, such PDMS master structures struggle with the disadvantage of being elastic under pressure ($\sigma_t(\text{PDMS}) \approx 2 - 4 \text{ MPa}$). As a restriction, nanoscopic structures can only be fabricated with relatively low aspect ratios. The chemical structure of PDMS is shown in figure 4.6(b). It has a glass transition temperature of -120 °C and PDMS surfaces are typically hydrophilic, which is important for the fabrication of PEDOT:PSS structures from an aqueous solution. In this work, the PDMS master molds were developed from the two-component Dow Corning product Sylgard 184 (Midland, USA).

4.3 Thin film preparation

In this section, the single processes for the fabrication of homogeneous polymer thin films are introduced. Therefore, it begins with the preparation of the polymer solution, followed by the pre-treatment of the applied substrates, and the actual coating via spinning. The

different structuring approaches are individually described in sections 6.1 to 6.3.

4.3.1 Polymer solution

One main advantage of organic electronics results from the easy solution processability of conducting polymers, which fulfills the needs of low-cost fabrication on large scales. All applied photoactive polymers came as solids and were dissolved for further processing. For this step, the desired amount of polymer was measured by weight using a high precision balance (Sartorius BP 210D) and put into a wetted glass. Afterwards, the desired amount of solvent was added with a microliter pipette. In this thesis, the polymer concentrations in solution are always given in „mg/ml“. For the different polymers, different solvents with varying polarities had to be chosen for homogeneous polymer solutions. In this thesis, the following solvents were applied, listed with increasing polarities (the corresponding purification grades are given in brackets): cyclohexanone ($\geq 99.5\%$), toluene ($\geq 99.9\%$), chloroform (CF, $\geq 99.9\%$), 1,2-dichlorobenzene (DCB, $\geq 99\%$), and tetrahydrofuran (THF, $\geq 99.9\%$). All solvents were ordered from Carl Roth (Karlsruhe, Germany), except DCB, which was purchased from Sigma Aldrich (Steinheim, Germany), and have been used as is. In order to guarantee perfect solution conditions, all polymer solutions were constantly stirred for a minimum of 24 hrs using a magnetic stirrer or an orbital shaker. The preparation of the polymer solution was carried out straight forward and the final polymer solutions were shielded against direct sunlight to avoid an unnecessary oxidation of the conducting polymers. Before casting, all homopolymer and polymer blend solutions - except the ones containing PCBM - were filtered using a polytetrafluorethylene (PTFE) filter with a pore size of $0.45\ \mu\text{m}$. For the aqueous PEDOT:PSS solutions PTFE filters with a pore size of $5\ \mu\text{m}$ were applied.

4.3.2 Substrate preparation

Depending on the characterization method of choice, different substrates have to be applied as support for the polymeric thin films. The following substrate types were used in this thesis: silicon wafers (Si-Mat, Kaufering, Germany), standard glass substrates (Lathi Optifloat/Microfloat from Pilkington, Gelsenkirchen, Germany), conductive transparent indium tin oxide (ITO) substrates (ITOSOL from Solems S. A., Palaiseau France), silicon nitride (SiN) membranes (Silson, Blisworth, England), and copper TEM grids (Plano, Wetzlar, Germany). In order to guarantee reproducible experimental conditions, all substrates were chemically treated before coating according to the following cleaning proce-

dures [169]:

Acidic cleaning: All silicon and glass substrates were cleaned in an acidic hot bath at 80 °C for 15 min before coating. The acidic bath was composed of deionized water, 30 % hydrogen peroxide, and 96 % sulfuric acid. Additional information is found in the literature.[169] Subsequently, the substrates are rinsed with deionized water and dried under constant and oil-free nitrogen flow. It has been reported that this cleaning procedure not only exhibits a very high particle removal efficiency due to its strong oxidizing force [170], but that it also decreases the surface energy of the substrates.

Organic cleaning: Since the acidic cleaning procedure from above leads to a severe damage of conducting oxide layers, the ITO substrates were cleaned according to a more sensitive multi-step process based on different organic solvents. Therefore, the substrates were put subsequently in an ultrasonic bath for 15 min in four different solvents (purification grades are again given in brackets): high precision aqueous Alconox cleaning solution (with a concentration of 16 g/l, from Alconox Inc., White Plains, USA), ethanol ($\geq 99.8\%$), acetone ($\geq 99.9\%$), and 2-propanol ($\geq 99.8\%$). Except for Alconox, all cleaning solvents were ordered from Carl Roth (Karlsruhe, Germany). Between all steps, the substrates were rinsed with the following solvent and directly transferred to the next bath. Finally, all substrates were dried under constant nitrogen flow.

Due to their fragility and their miniature size, the copper TEM grids and the SiN membranes were only gently blown off with nitrogen before usage.

4.3.3 Spin coating

For the fabrication of the homogeneous polymer thin films, spin coating was chosen as the preparation technique. This processing routine is widely used in the semiconductor industry [171] and for fundamental research.[172] A SÜSS MicroTec Delta 6 RC TT spin coater (Garching, Germany) was applied for all homogeneous polymer films. Only the thin films discussed in chapter 5.3 were prepared with a WS-400-6NPP spin coater from Laurell Technologies Corporation (North Wales, USA), which was installed in a glove box. The schematic procedure of this coating process is depicted in figure 4.7. The substrate is fixed with a vacuum chuck and it is covered with polymer solution using a pipette. Immediately afterwards, the top cover of the spin coater is closed and the rotation of the sample is started with a defined acceleration acc . After a spinning time t_{spin} the process stops automatically.

The coating process is a complex interplay between removal of excess solution at the

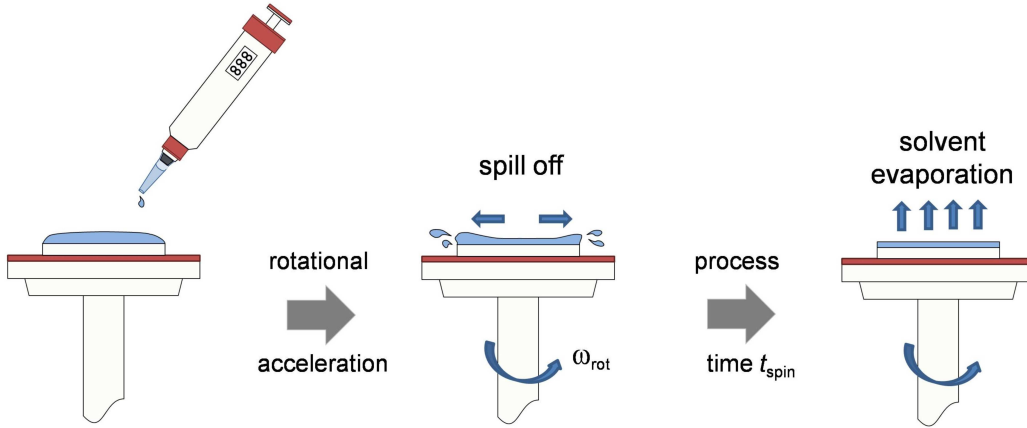


Figure 4.7: Schematic illustration of the spin coating procedure as it was applied for the fabrication of homogeneous polymer thin films.

beginning of the spinning and constant solvent evaporation. In a first theoretical approach, Meyerhofer described the resulting polymer film thickness by accounting only for the continuity equation of the polymer solution.[173] Different and more detailed ideas based on modified solvent evaporation rates followed, but did not lead to fully satisfying and general applicable film thickness predictions. Finally, Schubert et al. have shown that the solvent evaporation only increases the polymer concentration and hence the viscosity of the polymer solution.[174] As a result, the final film thickness d is given by an empirical relationship [175]

$$d = c_{pol} A_{spin} \omega^{-0.5} M_w^{0.25}, \quad (4.1)$$

where c_{pol} is the solution concentration, ω_{rot} the rotational frequency, and M_w the molecular weight of the polymer. A_{spin} is an additional parameter which depends on the applied equipment and the external conditions. Equation (4.1) shows that the final polymer thickness can be easily tuned via the polymer concentration in solution c_{pol} and the rotational speed given by ω_{rot} .

In the case of the conducting F8BT, figure 4.8(a) indeed reveals a linear dependence of the film thickness d on the polymer concentration c_{pol} . However, Schubert and Dunkel have also observed that this dependency is typically not linear over a large concentration range.[174] They have shown that below a critical polymer concentration c_{min} single polymer chains do not overlap completely and hence no homogeneous polymer film is formed. For concentrations higher than c_{min} film formation starts and the film thickness is then proportional to c_{pol} . In addition, above a critical concentration c_{vic} the viscosity of the solution starts to increase disproportionately due to an enhanced entanglement of

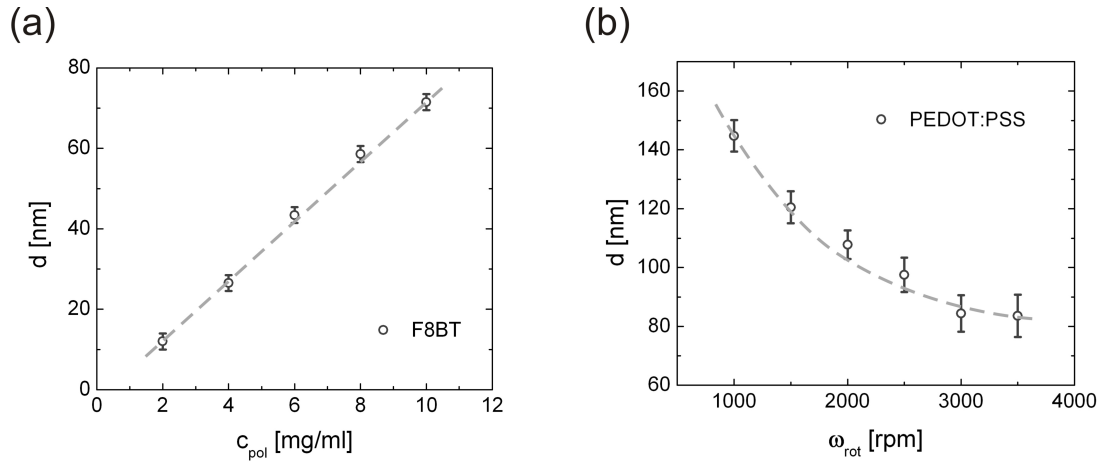


Figure 4.8: Film thickness control of (a) F8BT via the polymer concentration in solution and of (b) PEDOT:PSS via the rotational speed.

the polymer chains. This behavior leads to an excessive increase in film thickness for concentrations above c_{vic} .

Since PEDOT:PSS already comes in a premixed aqueous solution, a better control of the film thickness d is possible via the rotational velocity ω_{rot} . Therefore, in figure 4.8(b) the $\omega_{rot}^{-0.5}$ -dependency of the final film thickness d is shown as it was derived by Schubert (see equation (4.1)).

Unless stated otherwise, table 4.2 illustrates the standard spin coating parameters, which were applied for the listed polymers.

material	ω_{rot} [rpm]	t_{spin} [s]	acc
photoactive polymer	2000	30	9
PEDOT:PSS	2500	60	9
G-PEDOT:PSS	1500	60	9

Table 4.2: Spin coating parameters for the different applied materials.

The *acc* value for the acceleration of 9 corresponds to a time of 6 s which is necessary to reach the desired rotational velocity w_{rot} .

Chapter 5

Self Organized Structuring in Polymer Blend Films

*Historic milestone 1958: D. Kearns and M. Calvin were the first to describe the photovoltaic effect in organic materials.[176]
In 1961 Calvin was awarded the Nobel Prize.*

As it was theoretically discussed in section 2.2, the miscibility behavior between two polymeric materials is often the limiting factor for applications based on polymer blends. Nevertheless, blending two conducting homopolymers boosted not only the efficiency of OSCs [177], but also allowed for the fabrication of white organic light emitting diodes (WOLED), for example.[146, 178, 179] For blends based on standard coiled polymers, namely, polystyrene (PS) and poly(methyl methacrylate) (PMMA), Walheim et al. already studied the influence of various sample preparation parameters on the phase separation in the final films.[180] On the contrary, in this section the phase separation of novel conducting polymers is investigated, which show a modified phase separation due to the rodlike polymer chains and the enhanced tendency to crystallize (see section 2.2). In more detail, the relation between the film thickness and the resulting polymer domain sizes is revealed using the example of MEH-PPV:PVK films (see section 5.1). The influence of different blending ratios on the film morphology is illustrated based on MDMO-PPV:F8BT films (see section 5.2). These films are also used to probe the impact of blend morphology on the photochemical degradation of conducting polymers. Finally, a novel method is introduced to detect retained solvent molecules in conducting blend films and the impact on organic solar cells is discussed (section 5.3).

5.1 Phase separation tuning in polymer blend films

For non-conducting polymer blends Walheim et al. [180] and Böltau et al. [181] have shown that different adsorption energies of the components to the substrate and to the air interface lead to tunable phase separation morphologies. Such different preferential attractions of individual polymeric components have also been observed for conducting polymer blends resulting in complex stacking structures with buried layers at the substrate interface or encapsulating layers at the air interface.[182] In general, the presence of such substrate and air interfaces also increase the likelihood of phase separation that is correlated with the absolute film thickness. Since such polymer depletion layers are important for electronic devices, this correlation is investigated in the current section for a conducting polymer blend system.

5.1.1 Sample preparation

MEH-PPV and PVK have been chosen as the polymeric materials. Both polymers are well understood and have already been widely applied for various optoelectronic applications.[183, 184] More details on the homopolymer characteristics are given in section 4. For example, Zou et al. were able to improve the luminous efficiency of a complex pure polymeric WPLED based on MEH-PPV and two additional polymers by inserting a hole transporting PVK layer.[185] Their achieved luminous efficiency is still considered as one of the highest reported values for WPLEDs based on fluorescent polymer emitters. In addition, blended solutions of MEH-PPV and PVK have also shown potential for the preparation of composite nanoparticles via a precipitation method.[186] However in this section, the MEH-PPV:PVK blend system is chosen for more fundamental reasons: The diverging chemical properties of the two polymers make this sample system unique for investigations concerning the phase separation of rod-like polymers. The two materials have separated optical absorption maxima which allow the determination of the overall film composition (section 5.1.2). In addition, the high contrast in refractive index for MEH-PPV and PVK (contrast is 1/1.16) allows an adequate utilization of various X-ray scattering techniques on such thin films, which are necessary for a full in-film structure analysis (sections 5.1.4 and 5.1.5).

For the following investigations a series of samples consisting of five different film thicknesses was prepared by changing the polymer concentration in solution. For the polymer blends, both homopolymers were separately dissolved in the corresponding solvents. For MEH-PPV pure toluene was used and the polymer concentrations in solution for the thickness series were 1, 1.5, 2, 2.5, and 3 mg/ml. The PVK was dissolved in a blend of toluene and cyclohexanon at a volume ratio of 9:1 and the following concentrations

were applied: 3, 4.5, 6, 7.5, and 9 mg/ml. Subsequently, the solutions were blended at a volume ratio of 3 MEH-PPV : 2 PVK using the polymer solutions of each component starting from the smallest concentration upwards. The blended solutions were finally spin coated on acidic pre-cleaned silicon or glass substrates.

The film thickness d was directly probed with optical ellipsometric measurements (section 3.5). Figure 5.1(a) shows the characteristic Δ_{OE} - and Ψ_{OE} -values (open symbols) for the different film thicknesses plotted against the varying angle of incidence (AOI) and the corresponding optical fits (solid lines).

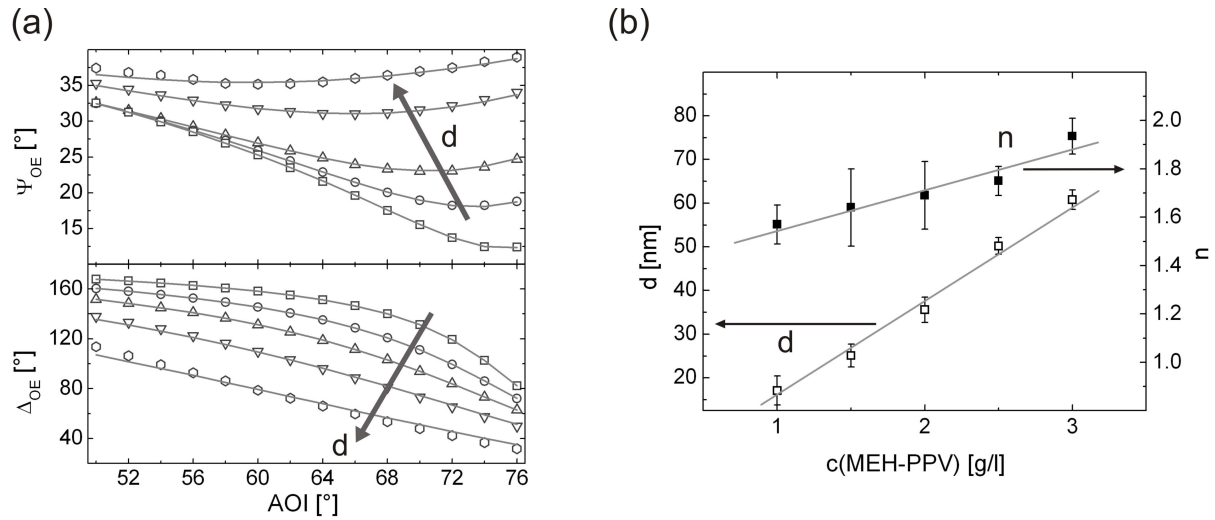


Figure 5.1: Optical ellipsometer measurements on MEH-PPV:PVK polymer blend films with increasing film thicknesses d . In (a) the characteristic Δ_{OE} - and Ψ_{OE} -values are plotted against the angle of incidence (AOI). The solid lines depict the corresponding optical model fits and the added arrows indicate the increasing film thicknesses d . In (b) the film thickness d and the optical refractive index n from the optical modeling are plotted against the polymer concentration of MEH-PPV. The solid lines are drawn as guides to the eyes.

From the optical models in figure 5.1(a) the film thickness d and the optical refractive index n are extracted for all film thicknesses. In figure 5.1(b) both values are plotted versus the concentration of MEH-PPV. Since the concentration of PVK is directly linked to the concentration of MEH-PPV during sample preparation, the PVK concentration could have been chosen as well. The film thickness of the blend films shows a linear dependence on the MEH-PPV concentration in solution $c(\text{MEH-PPV})$, which is in good agreement with the results from Schubert on homopolymer samples (see equation (4.1)).[175] The extracted film thickness values are 16.1, 25.1, 35.6, 52.4, and 60.8 nm for increasing polymer concentrations.

The optical refractive indices n measured for the pristine homopolymer films are 1.70 for PVK and 1.79 for MEH-PPV. Both values were obtained using plain PVK and MEH-PPV polymer films spin cast on silicon substrates. In general, the refractive index of a polymer

film does not depend on its thickness. As a consequence, the increasing refractive index values for thicker blend films would on a first sight indicate a dominating MEH-PPV component. Based on the theoretical studies by Fenstermaker et al. on the influence of increased surface roughnesses on the complex optical refractive index [187], the refractive index of films with small surface roughnesses is given by the combination of the material and the surrounding medium. Since the measurements were performed in air, this effect can only explain the reduced refractive index of the thinnest blend film. However, for ellipsometric measurements on very rough surfaces appreciable light scattering can lead to further modifications of the optical constants and hence account for the optical refractive index value of the thickest film, which even exceeds the pristine values of the pure components. As a consequence, the obtained thickness values have to be confirmed by a complementary method and the microscopic surfaces of the blend films have to be studied as well (see sections 5.1.4 and 5.1.3).

5.1.2 Film composition

The total film composition of the photoactive MEH-PPV:PVK samples was investigated with optical absorption measurements. Due to the fact that both pristine polymers have prominent absorption maxima settled at different optical wavelength bands, UV/Vis spectroscopy measurements reveal the actual amount of each component in the final film. The corresponding absorption spectra for wavelengths between 270 nm and 900 nm are shown in figure 5.2. A pure PVK film has a strong absorption for photons from the ultraviolet wavelength regime (dotted line), whereas a plain MEH-PPV film is a good absorber for photons with longer wavelengths (dashed line).

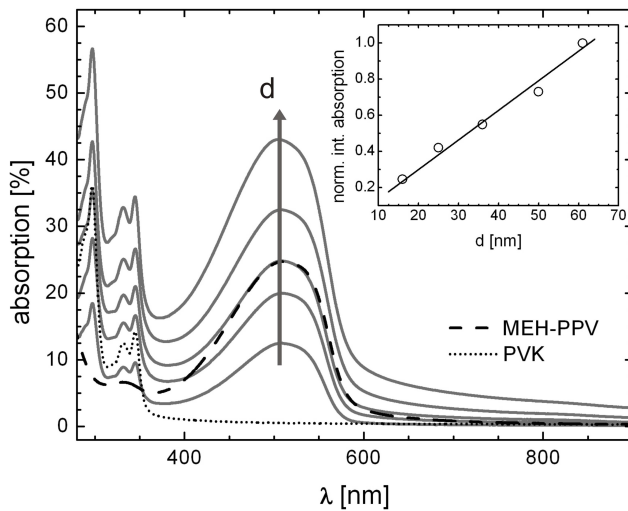


Figure 5.2: Spectral absorption of MEH-PPV:PVK blend films for increasing film thicknesses of 16, 25, 36, 52, and 61 nm (solid lines). The additional dashed line shows the absorption of a pure MEH-PPV- and the dotted line of a pure PVK-film. The arrow indicates the increasing film thicknesses d . The inset shows the integrated absorption from 270 to 900 nm (the error bars are smaller than the symbol size). The solid line is drawn as a guide to the eyes.

For PVK the absorption maxima are located at 295, 330, and 345 nm and MEH-PPV

shows a strong absorption over a broad wavelength spectrum around 500 nm, while it has only a relatively weak absorption at 300 nm. Based on the absorption of the homopolymer films, the chosen volume blending ratio of 3 MEH-PPV : 2 PVK results in almost equally strong optical absorption maxima of the two components. The simultaneous increase of the absorption maxima of PVK and MEH-PPV indicates a constant film composition for increasing polymer concentrations. In more detail, the ratio of the maximum absorption peaks from PVK and MEH-PPV $A_{max}(\text{PVK})/A_{max}(\text{MEH-PPV})$ remains unchanged at 0.82 ± 0.02 for the different film thicknesses between 16 and 61 nm. This ratio is calculated based on the absorption peak at 340 nm, which is almost entirely due to the presence of PVK, and the MEH-PPV absorption maximum at 500 nm. In addition, the inset in figure 5.2 shows the integrated absorption over a range from 270 to 900 nm. The solid line between the calculated points is intended as a visual guide and reveals a linear increase with the polymer concentration as well.

5.1.3 Lateral film morphology

The surfaces of the different polymer blend films were visualized using AFM and the three-dimensional topography data are shown in figure 5.3.

The topography images clearly reveal a strong dependence of the average phase separation size and structure on the overall film thickness. For thin polymer films ($d = 16$ and 25 nm) circular shaped domains with a rather small deviation in size are detected, whereas for samples with a thickness between 36 and 61 nm the average polymer domain size is increased and the typical circular shape is lost. The color coding in figure 5.3 illustrates relative high sample roughness values. The corresponding R_{rms} -values are 3.3, 4.6, 5.7, 9.2, and 11.0 nm for increasing film thicknesses. Hence, the variations in optical refractive index can be indeed explained by roughened film surfaces (see section 5.1.1). Similar roughness values have been reported for other polymer blend systems as well and are typically attributed to a strong tendency of the two components to phase separate.[188]

For a more sophisticated analysis of the lateral surface structures, the power spectrum densities (PSD) of the AFM data are taken via Fourier transformation and radial averaging. The corresponding reciprocal information from the averaged structure sizes of all investigated samples are shown in figure 5.4 (open symbols). For clarity all intensities are normalized and shifted along the y -axis.

In figure 5.4 mathematical fits are added to the data in order to extract the correct values for the mean surface structure sizes Λ_1 and Λ_2 which appear as prominent peaks and shoulders in the PSD plots (indicated by the arrows in figure 5.4). In accordance with the effective surface approximation (see section 3.7) the mathematical fits are based on

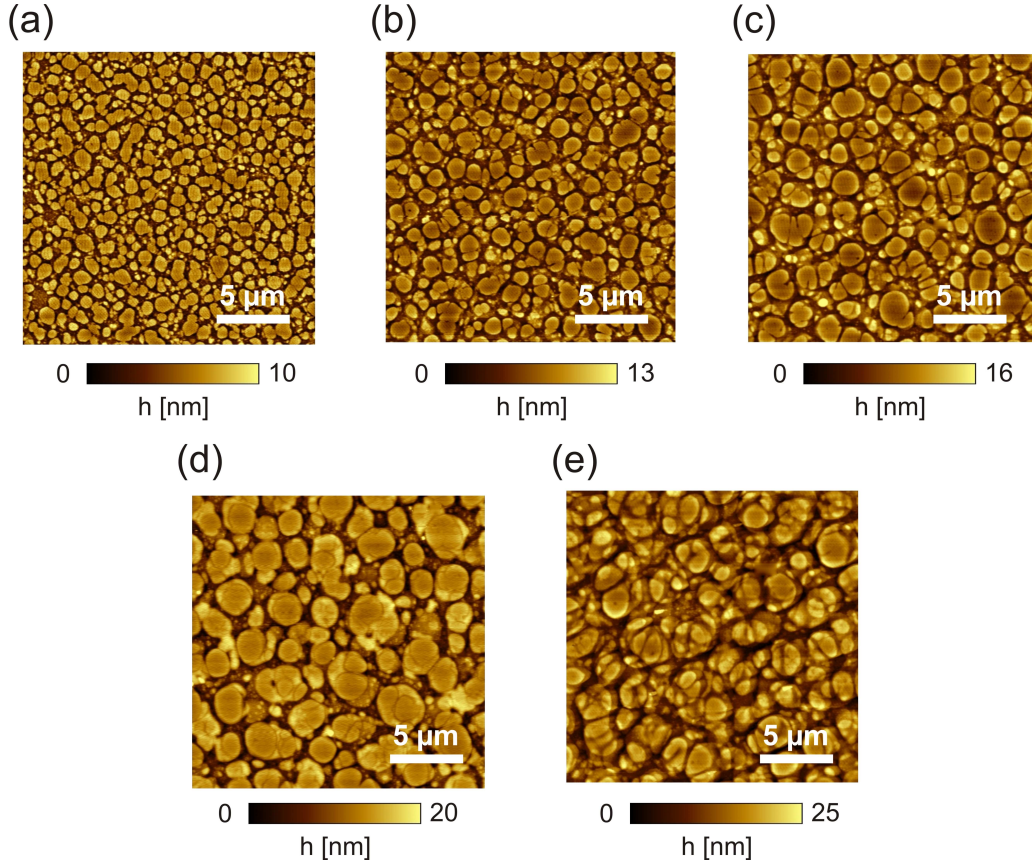


Figure 5.3: AFM topography images of samples with different film thicknesses d : (a) 16, (b) 25, (c) 36, (d) 52, and (e) 61 nm. The measurements were performed with the AFM-3 (see section 3.2).

the sum of two Lorentzian functions and a minor background u_{psd}

$$f_{psd}(x) = g_{psd,1}(x) + g_{psd,2}(x) + u_{psd} , \quad (5.1)$$

where $g_{psd,1}(x)$ and $g_{psd,2}(x)$ are given by

$$g_{psd,1}(x) = \frac{h_{psd,1}}{1 + 4\left(\frac{x-\Lambda_1}{b_{psd,1}}\right)^{2+\beta_{psd,1}}} \quad \text{and} \quad g_{psd,2}(x) = \frac{h_{psd,2}}{1 + 4\left(\frac{x-\Lambda_2}{b_{psd,2}}\right)^{2+\beta_{psd,2}}} . \quad (5.2)$$

In the upper equations, the Lorentzian distributions are described by the position of the maxima $\Lambda_{1/2}$, the width $b_{psd,1/2}$, the slope $\beta_{psd,1/2}$, and the height $h_{psd,1/2}$. The arrows in figure 5.4 illustrate the shift of the two mean structure sizes Λ_1 and Λ_2 to smaller q -values for increasing polymer film thicknesses d , which corresponds to larger structure sizes. The detailed values for the position of the two maxima Λ_1 and Λ_2 are summed up in table 5.1. The errors for the structure size Λ_1 , which result from the mathematical fitting, are found to be smaller than ± 15 nm, whereas for the structure size Λ_2 they are within a range of ± 30 nm.

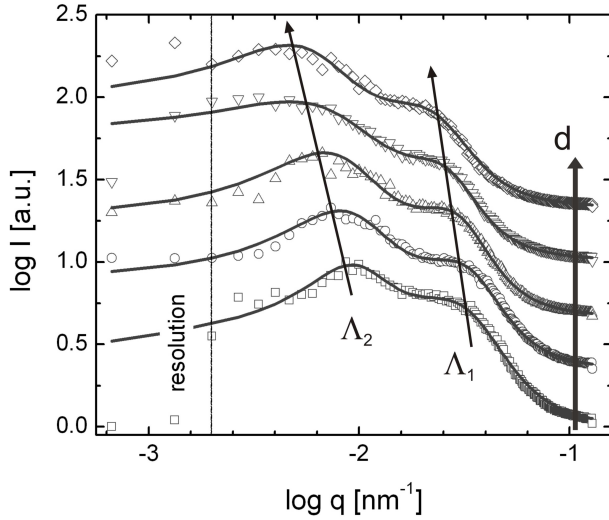


Figure 5.4: Power spectral density functions (open symbols) of the AFM data from MEH-PPV:PVK blend films with the following film thicknesses d : 16, 25, 36, 52, and 61 nm (see figure 5.3). The solid lines correspond to the applied mathematical fits. All data are normalized and shifted along the y -axis for clarity.

d [nm]	16	25	36	52	61
Λ_1 [nm]	236	215	235	262	320
Λ_2 [nm]	740	840	1000	1500	1500

Table 5.1: Fitted mean structure sizes Λ_1 and Λ_2 of the power spectral density functions from MEH-PPV:PVK films in dependence on their film thickness. For Λ_1 the error is found to be smaller than ± 15 nm and for Λ_2 it is within a range of ± 30 nm.

The topographic AFM analysis reveals that the phase separation of the surface morphology strongly depends on the polymer concentration in solution and hence the overall film thickness. The AFM data also change with thickness from circularly shaped surface morphologies to more complex geometries. This is also seen from the increasing widths of the prominent peaks for small q -values (see figure 5.4) which as well prove a broadened spectrum of the typical structure sizes.

Whereas the power density spectra show the presence of larger and smaller polymer domain distances, the later ones are not easily revealed by the two dimensional AFM data in figure 5.3. Therefore, figure 5.5 shows the two dimensional AFM data of the MEH-PPV:PVK film with a thickness of 16 nm taken at a higher lateral resolution.

It is seen that smaller polymer domains are embedded within the framework of the dominating larger phase separation structures. These structures have typical diameters between 100 and 300 nm and therefore match well with the results given in table 5.1. On the contrary to the larger phase segregation domains, which increase with film thickness, the size of the smaller domains does not show such a clear dependency.

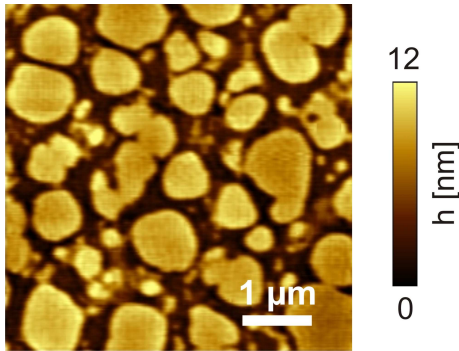


Figure 5.5: Close-up AFM topography data of an MEH-PPV:PVK blend film with a thickness d of 16 nm. The measurement was performed with AFM-3 (see section 3.2).

5.1.4 Vertical film composition

Up to this point, the polymer blend films are only characterized concerning their phase separation at the film surface. To access the inner film structure, e.g. lamellar phase separation domains, X-ray reflectivity measurements are suitable. Due to the observed microscopic phase separation at the film surface on the length scale of several hundred nanometers in comparison to the tens of nanometer thick films, no prominent vertical ordering is to be expected. However, it was already reported for other polymer blends that polymer enrichment layers at the substrate-polymer interface are possible and have very interesting properties for future device applications.[189, 190] The X-ray reflectivity data for the different films with a total film thickness between 16 and 61 nm are plotted as open symbols in figure 5.6.

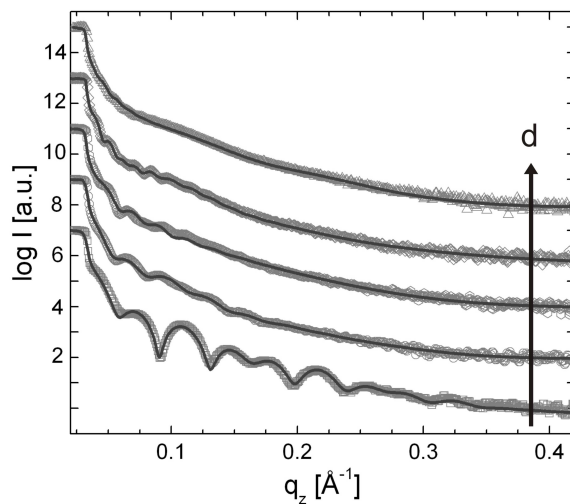


Figure 5.6: X-ray reflectivity data (open symbols) and the corresponding fitted curves (solid lines) for samples with different overall film thicknesses d : 16, 25, 36, 52, and 61 nm (depicted by arrow). For clarity in presentation, the curves are normalized and shifted along the y -axis.

The included solid lines correspond to the fits based on the Parrat algorithm (see also section 2.4.5). All measured data show a prominent superposition of multiple equidistant Kiessig fringe patterns. In addition, the reciprocal distance between the fringes decreases for increasing film thicknesses (as depicted by the arrow in figure 5.6). The overall film

thicknesses from the complex multilayer fits of the XRR data are 17, 22, 32, 52, and 62 nm for increasing polymer concentrations. For all investigated samples, these values confirm the results that were already obtained by the ellipsometric measurements (see figure 5.1). In order to avoid any confusion, only the thickness values from the ellipsometric measurements are used to address the different MEH-PPV:PVK films. Depending on the sample thickness, complex multilayer fit models have to be applied which consist of up to four simulated single layers. In figure 5.7 the resulting refractive index profiles from the applied models are shown (see also equation (2.52)). For clarity, the profiles are plotted as dispersion component δ of the complex refractive index versus film thickness d . The δ -profiles of the different samples are shifted along the y -axis and for each sample the corresponding baselines, which illustrate $d = 0$ nm, are plotted horizontally as dashed lines. As a reference, the refractive index of MEH-PPV ($\delta(\text{MEH-PPV}) = 3.53 \cdot 10^{-6}$) and PVK ($\delta(\text{PVK}) = 4.08 \cdot 10^{-6}$) are included as two vertical lines.

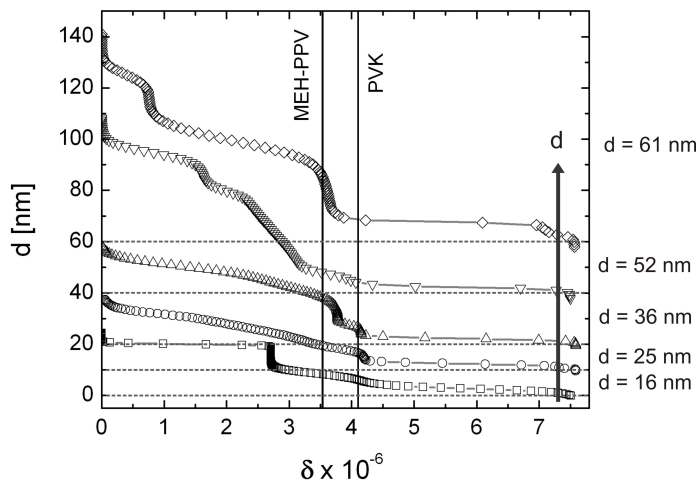


Figure 5.7: Refractive index δ profiles for MEH-PPV:PVK blend films with different film thicknesses: 16, 25, 36, 52, and 61 nm. The perpendicular solid lines depict the δ -values of PVK and MEH-PPV homopolymer films. For clarity, the profiles are shifted along the y -axis. The dashed horizontal lines depict the position of the substrate and hence the film thickness zero of the profiles.

For blend films with a film thickness between 16 and 52 nm the simulated refractive index of the polymer layer at the substrate interface is close to the value of pure PVK. This is clear evidence of a PVK enrichment layer on the silicon substrate. It is found that the thickness d_{enrich} of this PVK dominated film, which is located directly on top of the substrate, is constant for increasing film thicknesses: 5.9, 5.8, 4.9, and 5.4 nm. Such a self-driven formation of polymer enrichment layers is not only interesting for application in organic photovoltaics [189], but such intermediate PVK layers have already facilitated hole injection in organic photodiodes too, leading to higher efficiencies.[185] However, for the thickest sample a pure enrichment layer of PVK is missing. Moreover, a MEH-PPV:PVK blend layer with a simulated refractive index between the values of both homopolymers is formed at the substrate interface. The intermixing of the two components at the

polymer-polymer interfaces results in a smooth profile, which is simulated by large surface roughness values of each layer from the multiple stack system. This is also indicated by the high surface roughnesses of the AFM data in figure 5.3, which imply a homogeneous layer transition at the polymer-air interface as well.

5.1.5 Overall film morphology

The morphology investigations along the sample normal are completed with GIUSAXS measurements (see section 3.7), which allow a complete analysis of the phase separation structures not only at the surface, but also within the blended thin films. In figure 5.8(a) the two dimensional GIUSAXS scattering images are shown for films with thicknesses of 16, 25, 36, and 61 nm.

The reciprocal scattering images of the two thinnest polymer blend films ($d = 16$ and 25 nm) have a strong corset-like shape with a pronounced intensity fringe along the α_f -direction. This modulation in intensity is due to a waveguiding effect within the polymer film which is related to the film thickness.[191] In the scattering data of the films with a thickness of 36 and 61 nm this feature is lost due to a rough and complex film surface. Similar behavior was observed for thin polystyrene films, which were probed with GISAXS before and after dewetting.[123] In comparison to smooth plain PS films, the rough dewetted ones lost the prominent fringe pattern in direction perpendicular to the sample surface as well. This effect is also called correlated roughness. A second prominent scattering feature of the two thinnest films is the split of the Yoneda peak. This characteristic is due to a well pronounced phase separation structure of the two polymers, which vanishes for increasing film thicknesses.

In order to gain full insight into the film structure, figure 5.8(b) shows the IsGISAXS simulations which correspond to the GIUSAXS data of the blend films with a thickness of 16 and 25 nm. A model was applied, which is based on cylinders made of MEH-PPV embedded in a PVK matrix in combination with an underlying plane PVK layer of constant thickness. More theoretical information is found in section 2.4.3. This model is also in good agreement with the results obtained from XRR. For the thin blend films the obtained simulations match very well with the actual scattering data. However, for the thicker films ($d = 36$ and 61 nm) the agreement between simulated and measured data in α_f -direction is not satisfactory due to the high surface roughness which cannot be described well by the available simulation models of the IsGISAXS software. Thus, figure 5.8(c) focuses on the out-of-plane cuts along the Ψ -, respectively the q_y -direction, which contain the essential information of the buried in-plane structures. The out-of-plane cuts for all samples are taken at the critical angle of the MEH-PPV ($\alpha_{crit}(\text{MEH-PPV}) = 0.135^\circ$). In figure 5.8(c) not only the measured data (open symbols) are plotted, but also the corresponding

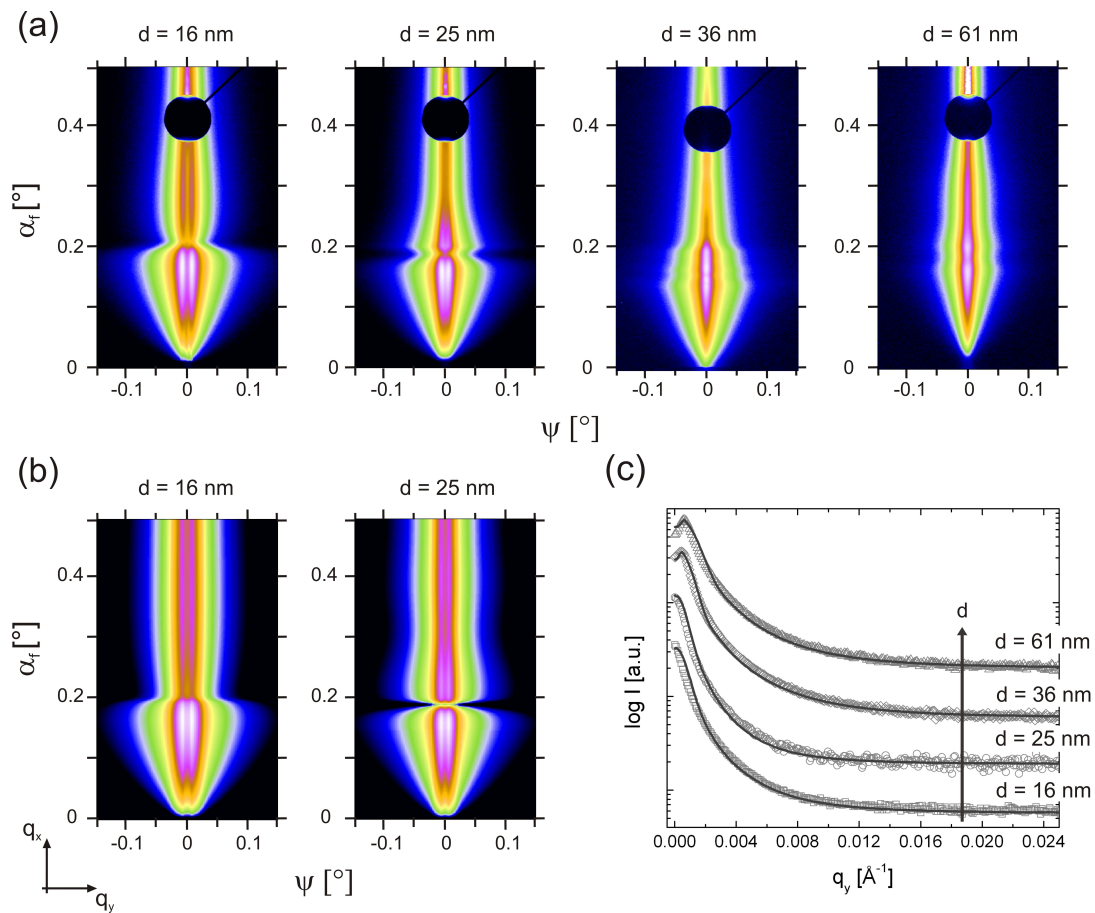


Figure 5.8: (a) Two-dimensional GIUSAXS scattering data of MEH-PPV:PVK films with the following film thicknesses d : 16, 25, 36, and 61 nm. In (b) the IsGISAXS simulations corresponding to the two samples with a film thickness of 16 and 25 nm are shown. As a summary, in (c) the out-of-plane cuts of the four investigated films are plotted as intensity versus q_y -component (open symbols) and the theoretical model fits (solid lines) are included as well. The intensities are normalized for all different film thicknesses and shifted along the y -axis. The corresponding thicknesses are denoted to each curve and indicated by the arrow.

IsGISAXS fits (solid lines). For the simulations, the cylindrical MEH-PPV particles are distributed on a disordered lattice, and the spacing to the first next neighbor is given by a Gaussian distribution (see also section 2.4.3). The simulations have shown that the next neighbor distances depict the positions of the maxima in the out-of-plane cut, whereas the radii of the applied cylinders mainly influence their slope. As a result, on the one hand, the simulations reveal a clearly increasing mean interparticle distance for thicker films (0.75, 0.98, 1.3, and 3.0 μm), whereas on the other hand, the size of the cylinders - given by their radii - does not follow a specific trend (97, 135, 74, and 80 nm). Taking also into account the AFM images from figure 5.3 it is obvious that for samples with a film thickness above 36 nm primarily the small structures between the bigger domains contribute to the out-of-plane scattering. The bigger domains, which are mainly visible

with AFM, are not resolved in the GIUSAXS data. The weak influence of these polymer domains on the scattering data is attributed to the large size in combination with the lack in distinct structure shape and the random lateral distribution. The transition to larger domain structures is also seen in the out-of-plane cuts for small q_y -values (figure 5.8(c)). For samples with a thickness of 16 and 25 nm they reveal concise maxima, but only slight shoulders are found for the thicker blend films. In comparison to the AFM surface analysis, the structure sizes from the power spectral density functions show the averaged next neighbor distances between all surface structures (see table 5.1), whereas the reciprocal scattering measurements allow the knowledge of the film composition and the size of the smaller scattering particles.

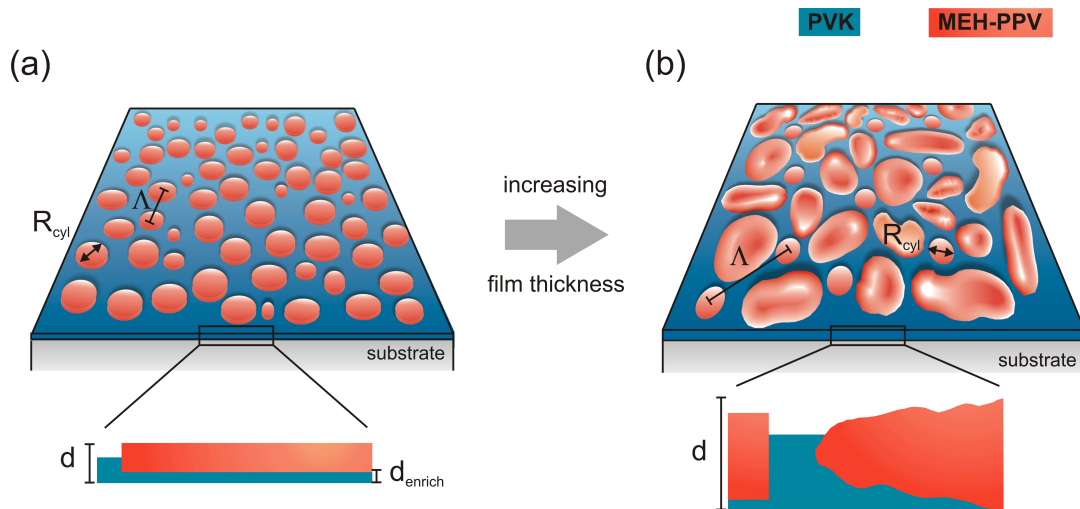


Figure 5.9: Topological and morphological sketches for (a) the sample with a film thickness d of 16 nm and (b) of 61 nm. Λ depicts the mean structure factors and R_{cyl} the radii of the determined cylinders, as they are extracted from the GIUSAXS experiments. The overall film thickness is depicted by d and d_{enrich} gives the thickness of the PVK-enrichment layer at the substrate interface as it is seen in the XRR data.

Combining now the results of the various measurements, the transition in topology and morphology from the ultra-thin film with a thickness d of 16 nm to the one which is 61 nm thick can be sketched (see figure 5.9). The most prominent morphology changes, which depend on the overall thickness increase, are the transition from a cylindrical to a random phase separation, the expansion of the large MEH-PPV domains, the conservation of the small, but ordered cylinders with increasing next neighbor distances, and the disappearance of the pure PVK enrichment layer.

Referring to the theoretical models for the phase separation in polymer blends (see section 2.2), different explanations for the rather large polymer domains in the MEH-PPV:PVK films are feasible. Binder has already calculated that the influence of the substrate- and the air-interface has to be included in an additional chemical potential

term.[61] Especially for the investigated ultra-thin polymer films, these preferential interfaces might contribute to the large domains as the dominant factor. As already discussed in section 2.2.2, in conducting polymer blends the crystalline ordering and the rodlike character (increased stiffness of the polymer backbone) also lead to additional energy terms to the Gibbs free energy of mixing and hence favor phase separation as well.

5.1.6 Evolution of film morphology during spin-coating

Beyond the detailed reconstruction of the final film morphology presented above, the combination of all achieved experimental results also makes it possible to sketch out the evolution of the film morphology during the spin-coating process in dependence on the polymer concentration in solution.

As it was already observed by Walheim et al. for a coiled polymer blend (PS:PMMA), also in case of the investigated conducting MEH-PPV:PVK films the phase separation is influenced by the two interfaces to the substrate and to the air.[180] In general, the phase separation process is known to start during the spin-coating process. Therefore, light scattering has been applied to investigate the evolution of the film morphology during spin coating.[192] However, the structure formation is still not easily observed in-situ.

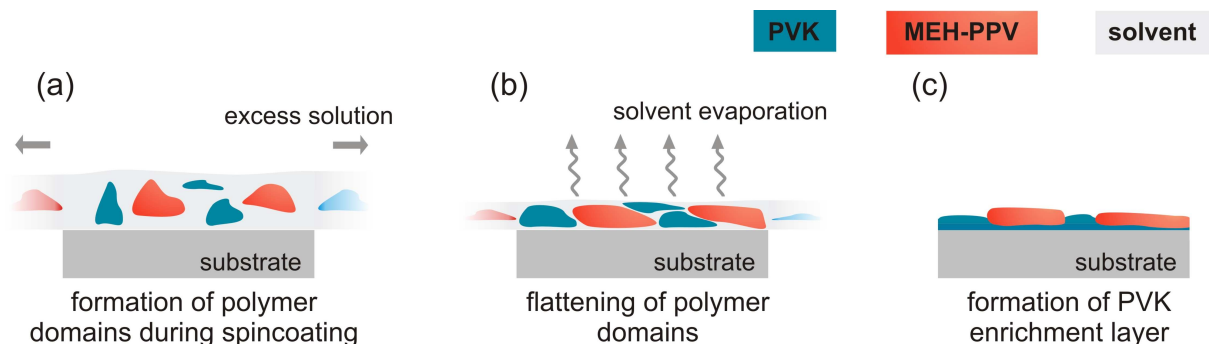


Figure 5.10: Time-resolved illustration of the phase separation of the MEH-PPV:PVK blend during spin-coating: (a) Phase separation already starts in the still wet phase and (b) the polymer domains flatten during the solvent evaporation and the decrease of the film thickness. (c) The PVK enrichment layer forms in the final stages of the film formation.

For more details, the basic principles of spin coating are discussed also in section 4.3.3. At the beginning of the spin-coating process the polymer components are completely dissolved and the phase separation follows a typical bulk-like spinodal decomposition. The polymer micro-phase domains grow in all directions following the same principles as for polymer blends in solution. Up to this point, the phase separation is perfectly described by the Flory-Huggins approach previously discussed and its modifications for conducting polymers (see section 2.2). However, this standard phase separation is finally limited by

the actual film thickness (figure 5.10(a)). Since the film thickness decreases steadily due to solvent evaporation, at one point it reaches the size of the already formed polymer domains in solution. For thinner films this limitation in thickness is the driving force for the flattening of the segregated polymer structures (figure 5.10(b)). For PS:PMMA blends, Walheim et al. also found increasing lateral domain sizes for increasing film thicknesses. They explained this observation by the extended solvent drying times because of their applied slower spin-coating conditions.[180] However, for the MEH-PPV:PVK films the experimental conditions are kept constant and only the polymer concentrations are modified. As a consequence, the final quenched state of the film morphology strongly depends on the evolution of the phase separation in the still wet phase with still present solvent molecules. In addition, the size of the lateral domains in the dry film is given by a flattening of the polymer domains due to solvent evaporation. The detected PVK enrichment layer at the substrate interface shows its preferential orientation to the silicon, whereas the MEH-PPV is in larger contact to the air interface. Since the thickness of the enrichment layer d_{enrich} stays constant with increasing film thicknesses, also the actual surface energies of the layer below the actual blend film, which influence the phase separation most, stay constant. As a consequence, the lateral size of the surface structures as they are seen with AFM and GIUSAXS depend on the size of the polymer domains in the last wet state during spin-coating.

It is known that the shape of the phase separation border between two polymers gives information about their relative solubility. It was seen for coiled PS:PMMA [180] and for conducting P3HT:MEH-PPV systems [193] that the better dissolved polymer normally tends to further collapse during the last stages of solvent evaporation. Thus, the sharp transition from the elevated MEH-PPV phase to the PVK surrounding would imply a better solubility of the PVK. But since the optical absorption measurements clearly revealed a constant composition in the thin films, the PVK has to form the observed enrichment layer at the latest stages of solvent evaporation - slightly before reaching the glassy state (figure 5.10(c)). This observation is crucial and since such PVK layers are often installed on purpose in LEDs, this automatic formation of a PVK enriched substrate coverage is highly interesting for future devices.

To conclude this section, it was found that the phase separation in conducting polymer blend films strongly depends on the final film thickness. Various experimental techniques were applied to fully reconstruct the three-dimensional film morphology of MEH-PPV:PVK blend films with thicknesses between 16 and 61 nm. Besides the dominating larger MEH-PPV polymer domains embedded in a surrounding PVK matrix, also smaller structures were revealed which appear constant in size for modified film thicknesses. In

addition, a PVK enriched layer was installed at the substrate interface due to a preferential surface attraction. Finally, the evolution of the phase separation during spin coating was sketched based on the results of the different measurement techniques.

For the fabrication of devices which require small phase separation structures, the results obtained imply a future potential of layered devices consisting of multiple stacked thin films.

5.2 Photochemical degradation in blend systems

In the previous section 5.1 the influence of film thickness variations on the phase separation of conducting polymer blends was discussed on the basis of MEH-PPV:PVK films. In the following section an additional polymer blend system, namely MDMO-PPV:F8BT, is investigated concerning the influence of compositional changes on the BHJ morphology. This point is of general importance because it is known that the film composition has a strong impact on the performance of similar organic electronic devices.[194, 195] After a brief illustration of the sample preparation (section 5.2.1), the optical absorption is probed for different film compositions (section 5.2.2). In addition to the measurements addressing the phase separation (see section 5.2.3), the influence of UV exposure on the optical absorption of the MDMO-PPV and F8BT homopolymer films and the corresponding BHJ layers is investigated as well (section 5.2.4).

5.2.1 Sample preparation

Although the two chosen polymers MDMO-PPV and F8BT have already been applied widely for the fabrication of OSCs and OLEDs individually, a combination of both materials still has not fully been explored in literature. Recently, ternary OSCs made of P3HT, MDMO-PPV, and F8BT were investigated by Kim et al.[196] However, the extracted efficiencies of such complex devices were low which the authors attributed to the existence of charge blocking resistances in the polymer layer. On the contrary, for blue-light sensitive organic devices based on F8BT the characteristics were improved by an additional doping with MDMO-PPV.[197] More details on the n-type F8BT and the p-type MDMO-PPV homopolymers are given in section 4.

For the following investigation F8BT (type-II, see table 4.1) was dissolved in toluene at a concentration of 4 mg/ml which leads to a homogeneous polymer film with a thickness of 27.4 nm. Since the second component MDMO-PPV shows only a poor solubility in toluene, DCB had to be used instead. However, toluene and DCB are well miscible and show no sign of precipitation. In consequence, a mixture of both solvents is also appropriate for preparing homogeneous thin films. For MDMO-PPV a polymer concentration in solution of 18 mg/ml was used which leads to a film with a thickness of 52.5 nm. As will be discussed in greater detail later, the optical absorption spectra of both polymer concentrations result in photoactive films with comparable maximum absorption values of approximately 40 % (see figure 5.12). To investigate the influence of film composition on film morphology a series of five samples was prepared by varying the blending ratio of the MDMO-PPV- and F8BT-solutions. The amount of MDMO-PPV-solution was changed from 30 to 70 vol% in steps of 10 vol% which corresponds to a F8BT content between 70

and 30 vol%, respectively. For an improved film quality the homopolymer solutions were filtered using a PTFE filter with a pore size of 0.45 μm before blending. Since the optical absorptions of MDMO-PPV and F8BT homopolymer films are influenced only slightly due to the additional filtration step, it can be concluded that both polymer components are very well dissolvable in the chosen solvents and only large agglomerated imperfections are removed. In order to avoid any influence of the filtration on the composition of the polymer blend solution, this step was carried out for each polymer solution separately. In figure 5.11 an optical micrograph of a spin coated blend film with a MDMO-PPV:F8BT ratio of 50:50 vol% is shown.

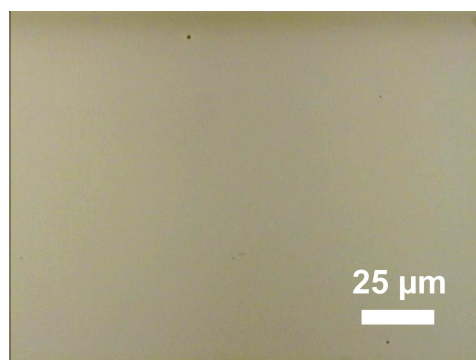


Figure 5.11: Optical micrograph of spin cast MDMO-PPV:F8BT film with a blending ratio of 50:50 vol%.

The resulting polymer films have a very good film quality and in comparison to the already investigated MEH-PPV:PVK blend films, which had a phase separation on the micrometer scale (see section 5.1.3), no distinct phase morphology features are observed for the MDMO-PPV:F8BT films in OM images at any magnification up to 100x.

5.2.2 Film composition dependent optical absorption

In figure 5.12(a) the optical absorption spectra of the applied MDMO-PPV (light line) and F8BT (dark line) homopolymer films are shown. In accordance to MEH-PPV (see figure 5.2) also this PPV-derivate has a broad optical absorption around 490 nm, which corresponds to the characteristic π - π^* transition in the conjugated polymer backbone.[198] On the contrary, F8BT reveals two sharp absorption maxima. One absorption maximum is located at 335 nm, which is already in the UV regime, whereas the second absorption maximum is around 470 nm. Also for the F8BT the two absorption peaks are attributed to π - π^* transitions. In more detail, the absorption peak at 470 nm has a charge transfer character, where one electron is moved from the fluorene to the benzothiadiazole unit.[199] Since typically PPV- and thiophene-derivatives are used for the fabrication of OSCs, which both show a strong absorption around 500 nm, the class of polyfluorenes (e.g. F8BT) is an interesting candidate that also covers the short wavelength regime.

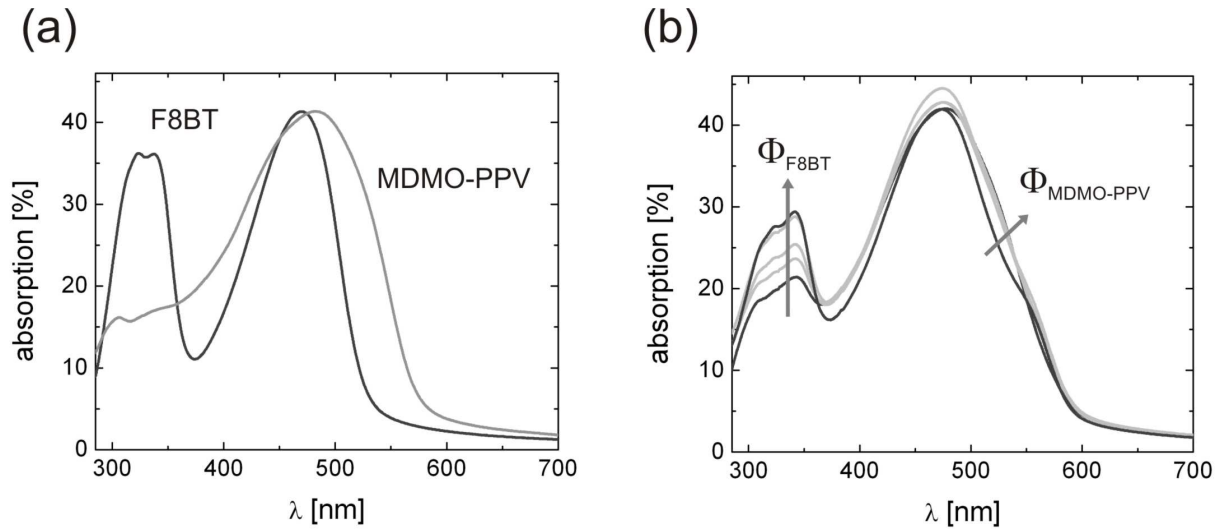


Figure 5.12: Optical absorption of MDMO-PPV and F8BT homopolymers and the corresponding polymer blend films: In (a) the UV/Vis absorption spectrum of the F8BT homopolymer film (dark line) reveals an additional absorption feature in the short wavelength regime in comparison to MDMO-PPV (light line). In (b) the absorption spectra of the MDMO-PPV:F8BT blend films are shown for different blending ratios of 70:30, 60:40, 50:50, 60:40, and 30:70 vol%. For clarity, the spectra of the most asymmetric blending ratios are depicted as dark lines. The arrows included illustrate increasing MDMO-PPV ($\Phi_{\text{MDMO-PPV}}$) and F8BT (Φ_{F8BT}) contents.

The UV/Vis absorption spectra of the MDMO-PPV:F8BT blend films are depicted in figure 5.12(b) for the chosen blending ratios of 70:30, 60:40, 50:50, 40:60, and 30:70 vol%. An increase in F8BT content (depicted by increasing Φ_{F8BT}) results in an increasing absorption of photons with a wavelength below 350 nm. Since both polymers show a similar optical absorption at wavelengths above 400 nm, the dominating absorption maximum at around 480 nm appears only slightly influenced upon modifications in film composition. Only the shoulder at 540 nm indicates an increasing amount of MDMO-PPV in the polymer blend films. To improve clarity in the illustration, the UV/Vis spectra of the polymer blend films with the highest asymmetric MDMO-PPV:F8BT ratios of 70:30 and 30:70 vol% are depicted as dark lines whereas the medium blending ratios are illustrated as light lines.

5.2.3 Film composition dependent film morphology

As previously discussed in the framework of the classic Flory-Huggins approach and the corresponding adapted phase separation models (see section 2.2), the blending ratio and hence the film composition have a crucial impact on the final film morphology. In accordance with the previous investigations on MEH-PPV:PVK blend films, similar X-ray scattering and surface imaging methods are applied to the MDMO-PPV:F8BT films.

However, since the refractive indices of MDMO-PPV and F8BT allow only for a limited contrast of 1/1.02 strong scattering features as observed for the MEH-PPV:PVK films are not expected.

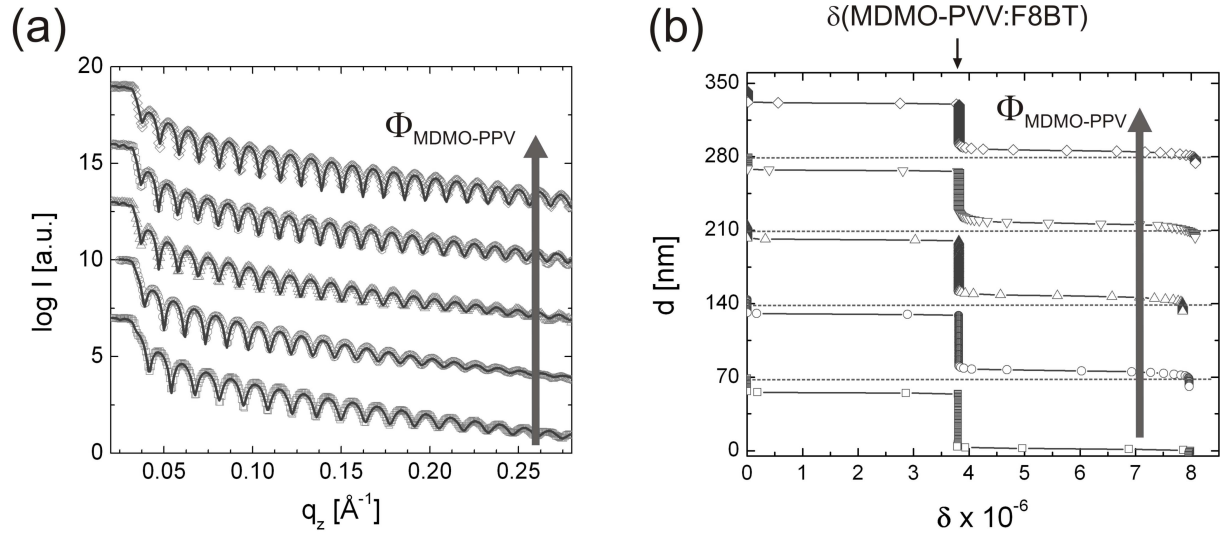


Figure 5.13: X-ray reflectivity measurements and the corresponding refractive index profiles for different blending ratios of 70:30, 60:40, 50:50, 60:40, and 30:70 vol%: In (a) the XRR data (open symbols) and the fits based on the Parrat algorithm (solid lines) are shown. For clarity, the curves are normalized and shifted along the y -axis. In (b) the corresponding refractive index δ profiles are presented which are also shifted along the y -axis. The dashed horizontal lines depict the position of the substrate for each composition.

In figure 5.13(a) the X-ray reflectivity data (open symbols) for MDMO-PPV:F8BT blend films with five different blending ratios and the corresponding mathematical fits (solid lines) based on the Parrat algorithm are shown. The equidistant Kiessig fringe patterns for all investigated MDMO-PPV:F8BT blends imply homogeneous polymer films with smooth film surfaces. A strong vertical layer structuring as typically indicated by the superposition of multiple fringe patterns (see also figure 5.6) is not observed. The overall film thicknesses from the polymer blend films are 45.1, 50.5, 53.4, 53.6, and 53.1 nm for increasing MDMO-PPV volume ratios. The corresponding refractive index δ profiles are shown in figure 5.13(b). For clarity, the profiles of the different samples are shifted along the y -axis and for each sample the corresponding baseline is depicted by the horizontal dashed lines. It is seen that a simple one-layer model is suited for a good fitting of the XRR data from all samples with varying film composition ratios. Hence, no lateral stacking is observed in more detail either. The overall film thicknesses d and the surface roughnesses R_{rms}^{XRR} are extracted from the XRR data and compared in table 5.2 for the different film compositions.

For the MDMO-PPV dominated films ($\Phi_{\text{MDMO-PPV}} \geq 50$ vol%) a homogeneous film thick-

$\Phi_{\text{MDMO-PPV}}$ [vol%]	70	60	50	40	30
d [nm]	53.1	53.6	53.4	50.5	45.1
R_{rms}^{XRR} [nm]	0.34	0.35	0.37	0.41	0.42

Table 5.2: From the X-ray reflectivity measurements extracted film thickness d and surface roughness R_{rms}^{XRR} values.

ness is found which corresponds to the actual film thickness of the MDMO-PPV homopolymer films ($d(\text{MDMO-PPV}) = 52.5$ nm). For higher F8BT contents ($\Phi_{\text{MDMO-PPV}} < 50$ vol%) the thickness of the blend films is reduced due to a stronger contribution of the F8BT, which results in thinner films if spin cast as homopolymer film ($d(\text{F8BT}) = 27.4$ nm). All investigated films have very low surface roughness values R_{rms}^{XRR} which are slightly increasing for higher F8BT contents.

Since the XRR measurements indicate no vertical layering of the two components, a lateral phase segregation has to occur. In order to address the phase separation at the film surface, AFM phase measurements were conducted. In figure 5.14 the two-dimensional AFM phase data for a MDMO-PPV:F8BT blend film with a compositional ratio of 50:50 vol% are shown. These measurements utilize the fact that two different polymers have modified mechanical or chemical properties which result in a phase shift of the cantilever frequency if the probing tip taps onto the sample (see section 3.2).

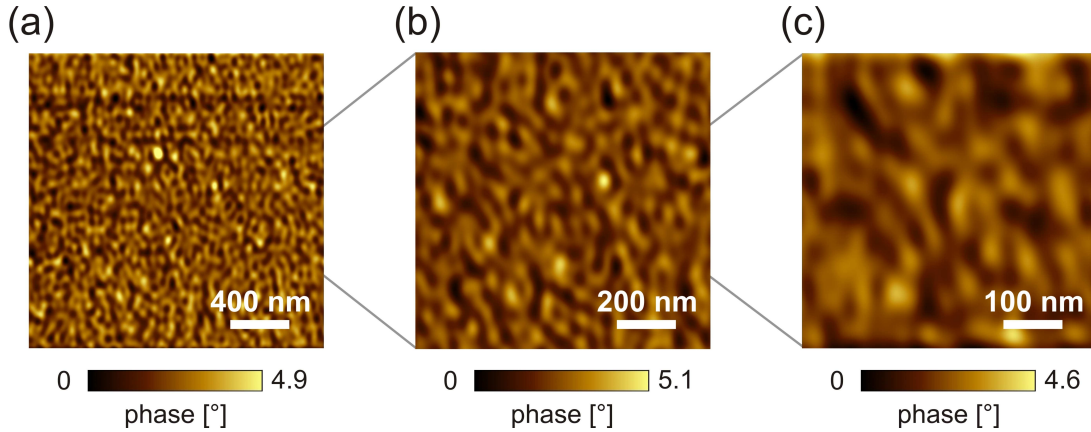


Figure 5.14: Atomic force microscopy phase data of the sample with a MDMO-PPV:F8BT composition of 50:50 vol%. The scan size was varied between 2×2 , 1×1 , and $0.5 \times 0.5 \mu\text{m}^2$.

Since the detected changes in the phase signal are very low, a low pass filter was applied in order to highlight the observed differences in surface composition. From figure 5.14(a) to (c) the phase images of the MDMO-PPV:F8BT blend film are shown with decreasing scan sizes of 2×2 , 1×1 , and $0.5 \times 0.5 \mu\text{m}^2$. The different scan sizes reveal a random polymer

phase segregation at the sample surface with typical domain sizes around 100 nm. The corresponding AFM data for the different blend ratios are shown in the appendix section A.1. Although the two-dimensional AFM phase data show no variations for modified film compositions at a first sight, the corresponding power spectral density analyses reveal differences in the surface composition (see figure 5.15). The same technique was already applied for the MEH-PPV:PVK blend films and more details to the model fits are given in section 5.1.3.

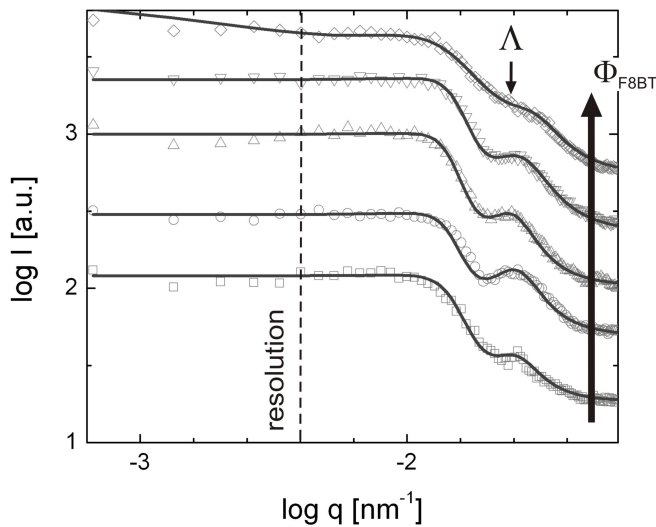


Figure 5.15: Power spectral density functions (open symbols) of the AFM data from MDMO-PPV:F8BT blend films with different blending ratios of 70:30, 60:40, 50:50, 60:40, and 30:70 vol% (arrow highlights increasing F8BT content Φ_{F8BT}). The solid lines correspond to the applied mathematical fits. All data are normalized and shifted along the y -axis for clarity.

For MDMO-PPV:F8BT films with symmetric blending ratios of 60:40, 50:50, and 40:60 vol% prominent in-plane structure lengths are found at 250, 260, and 245 nm. Taking into account the two-dimensional phase data in figure 5.14(c), this value matches most closely the mean distance between the polymer domains. On the contrary, the highest asymmetric blending ratios lead to less defined typical structure lengths of the segregated polymer domains at the film surface.

Combining the results of the optical absorption, the XRR, and the AFM measurements, polymer intermixing with small domains occurs within the active blend layer for all polymer compositions. As a consequence, lateral phase separation domains within the BHJ have to be formed in strong dependence on the film composition. In the following, these embedded structures are probed with GISAXS measurements. In figure 5.16 the out-of-plane cuts (open symbols) from the samples with the different blending ratios are illustrated, taken at the critical angle of the F8BT (more details are found in section 3.7). For clarity, the out-of-plane cuts (open symbols) are shifted along the y -axis and the effective surface approximation (solid lines) is applied to extract the corresponding mean structure sizes. This model was already introduced in section 3.7 and it includes two structural contributions. Whereas the MDMO-PPV:F8BT blend films with F8BT con-

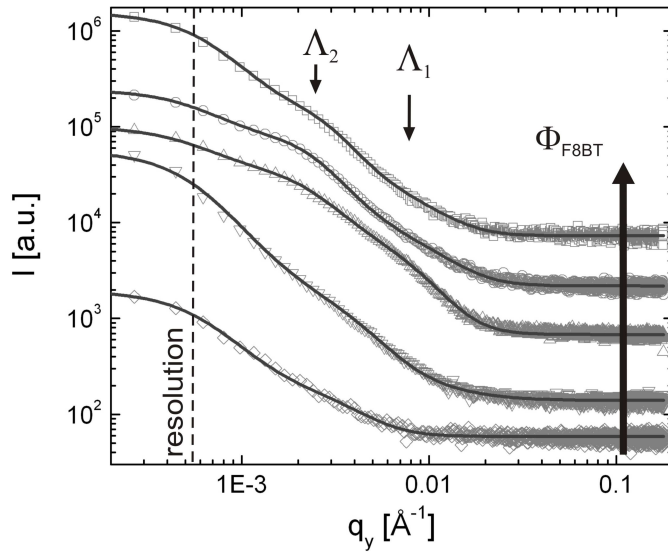


Figure 5.16: GISAXS out-of-plane cuts (open symbols) for MDMO-PPV:F8BT blend films with blending ratios of 70:30, 60:40, 50:50, 40:60, and 30:70 vol%. For clarity, the out-of-plane cuts are shifted along the y -axis with increasing F8BT content (depicted by Φ_{F8BT}) and the solid lines are given by the fits according to the effective surface approximation (see section 3.7).

tents of 30 and 40 vol% (two bottom curves) show only a slight indication for structure peaks at 440 and 550 nm, the out-of-plane cut of the sample with a symmetric blending ratio of 50:50 vol% clearly indicates two structure sizes of 200 (Λ_1) and 560 nm (Λ_2). For higher asymmetric MDMO-PPV:F8BT blending ratios of 40:60 and 30:70 vol%, weak lateral structure features corresponding to structure sizes of 450 and 320 nm are found. However, in comparison to the MEH-PPV:PVK films, which had clear scattering peaks in q_y -direction (see figure 5.8(c)), the GISAXS data on the MDMO-PPV:F8BT films only reveal less-defined scattering features. On the one hand, this effect is attributed to the reduced contrast in refractive index between MDMO-PPV and F8BT, but in addition it also indicates a broad size distribution of the detected polymer domains.

Comparing the results from the AFM and the GISAXS measurements concerning the phase separation, it is found that only in the case of the symmetric blending ratio of 50:50 vol%, similar small polymer domain sizes are found at the film surface and within the film. For asymmetric blending ratios smaller polymer domain sizes are found at the film surface than within the BHJ film. This effect can be due to a preferential surface attraction of one component as it was already observed for other blend systems.[200] For the following investigations on the MDMO-PPV:F8BT system, films with a blending ratio of 50:50 vol% appear most promising due to the small polymer domains within the films.

The results on an additional promising polymer blend system based on M3EH-PPV and F8BT are shown in the appendix section A.2. These blend films reveal a similar dependency of the film morphology on the blending ratio as the MDMO-PPV:F8BT films. In addition, the M3EH-PPV:F8BT are studied in order to address the question of how to harvest the maximum energy of the solar spectrum by varying the film composition (see

also section A.2).

5.2.4 Polymer degradation upon UV exposure

For a successful application of such novel BHJ films in a future large-scale production of organic electronics, the new materials also have to provide a sufficient photochemical and hence device stability.[201] Up to now, the influence of the chemical structure on the photochemical stability is still not fully exploited - in contrast to the relationship between chemical structure and expected device efficiency which is rather well investigated. The main cause for a degradation of the photoactive polymers arises from exposure to sunlight under the presence of oxygen, which leads to reduction or oxidation of the photoactive material. In more detail, two different mechanisms have been observed which influence the stability of the polymers: One influence results from radical oxidation of the side chains which subsequently impact the polymer backbone as e.g. observed for P3HT [202, 203], and a second influence is directly attributed to the nature of the polymer backbone.[204] In order to prevent degradation by external oxygen, OSCs are usually encapsulated, which however limits some of the attractive properties such as flexibility and low-cost fabrication. As will be shown in section 5.3 too, device degradation by internal oxygen sources such as oxygenic residual solvent molecules is still plausible.

Especially for the degradation of photoactive polymer blend films, information can hardly be found in literature. In order to fill this gap, not only the photochemical degradation of MDMO-PPV and F8BT films are studied in this section, but also the degradation of the corresponding blend films. Therefore, UV/Vis measurements are an appropriate tool to probe the optical properties, which provide further insight into the chemical structures. For samples stored at ambient and dark conditions, experiments have shown that the optical absorption of MDMO-PPV changes only slightly over a period of 28 days and the optical properties of F8BT remain even unchanged over a time frame of 90 days. Hence, in order to accelerate the polymer degradation all samples were exposed to UV irradiation with a wavelength of 254 nm. The illumination with UV light was performed with an EPROM-eraser LG-07 which had an intensity of 14 mW/cm².

Figure 5.17(a) shows the absorption spectra of the as-spun MDMO-PPV film (highest absorption) and after 5, 10, 20, 30, and 60 min of exposure to UV light (from top to bottom). For clarity the absorption spectra of the untreated film and the film after 60 min of UV irradiation are highlighted as dark lines. Whereas the pristine MDMO-PPV has a broad absorption band at 480 nm, a decrease in intensity is observed accompanied by a blueshift during UV irradiation (indicated by dashed arrow). This phenomenon corresponds to a loss of the characteristics from the vinylene-units and is due to reduced conjugation lengths that lead to the observed photobleaching of the MDMO-PPV. The results are compliant

with the measurements by Chambon et al. who studied the photooxidation of MDMO-PPV under illumination with UV light and at elevated temperatures.[205] Furthermore, they have shown that the oxidative degradation is explained by a radical process which is induced at the ether moieties and then proceeds to the double bonds. This degradation process yields a loss of conjugation, a chain scission, and hence a decrease in visible absorption as a consequence. The increase in optical absorption for wavelengths below 320 nm can be possibly attributed to the fabricated chemical products upon the photooxidation of the material.[205]

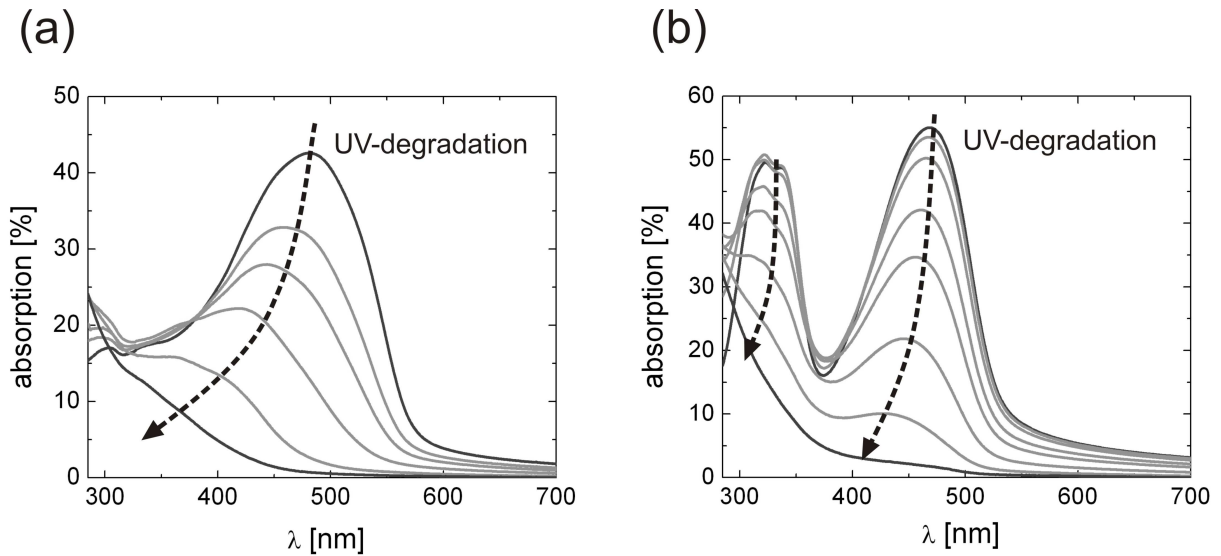


Figure 5.17: UV/Vis absorption spectra of MDMO-PPV and F8BT homopolymer films exposed to UV irradiation: In (a) the absorption spectra of an as-spun MDMO-PPV film and after exposure to UV light for 5, 10, 20, 30, and 60 min are shown (from top to bottom). In (b) the corresponding UV/Vis spectra of an as-spun F8BT film and after exposure to UV light for 60, 180, 300, 360, 420, 480, and 540 min are plotted (from top to bottom). For clarity, in (a) and (b) the absorption spectra of the as-prepared polymer films and after maximum UV exposures are illustrated as dark lines.

Whereas MDMO-PPV is highly sensitive to UV exposure ($t_{UV}^{max} = 60$ min), the optical absorption spectra of F8BT in figure 5.17(b) show a much higher photochemical stability. From top to bottom the UV/Vis spectra of the as-spun F8BT film and after an UV exposure of 60, 180, 300, 360, 420, 480, and 540 min are shown. A similar photobleaching as for MDMO-PPV is found, however happening on a much longer time scale and resulting in only a minor blueshift. Note must be made here that in general further classes of photoactive polymers (e.g. polycarbazoles or polythiophenes) are even more stable than polyfluorenes.[204] Taking into account the molecular structure of F8BT (see figure 4.2), the photochemical instability is a result of the quarternary site in a fluorene unit which is highly oxidizable.[204] Hence, the oxidation process which is induced at this site of the molecular structure leads to a similar chain scission as observed for MDMO-PPV.

Until now, no degradation analysis on semiconducting all-polymer blend films is found in literature. The only investigated blend systems are based on photoactive polymers in combination with fullerenes.[206] In figure 5.18 the absorption spectra of an MDMO-PPV:F8BT blend film which was fabricated with a blending ratio of 50:50 vol% are shown upon UV irradiation. The top spectrum corresponds to the as-prepared film and for the additional spectra the blend film was exposed to UV irradiation for overall accumulation times of 5, 10, 20, 30, 60, 120, 180, and 300 min (from top to bottom).

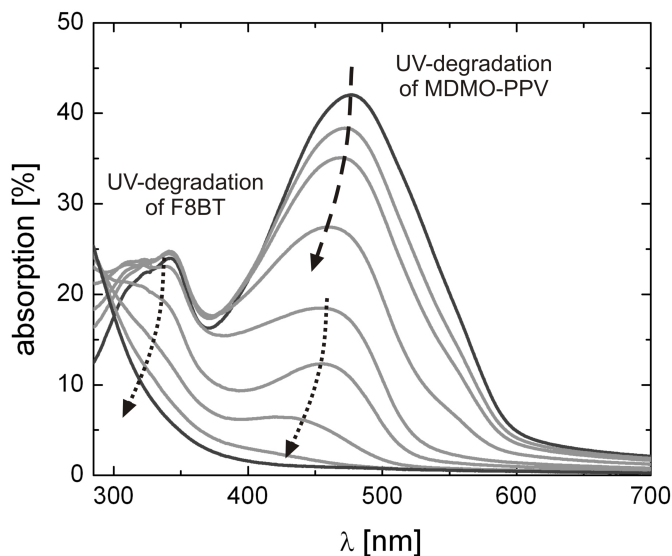


Figure 5.18: UV/Vis absorption spectra of an as-spun MDMO-PPV:F8BT blend film and after UV exposure of 5, 10, 20, 30, 60, 120, 180, and 300 min (from top to bottom). For clarity, the spectra of the as-spun film and after maximum UV exposure are illustrated as dark lines. The dashed arrow depicts the photochemical degradation due to MDMO-PPV and the dotted one the degradation due to F8BT.

For UV exposure times shorter than 30 min the photochemical degradation of the blend film is mainly governed by the impact of the MDMO-PPV component (indicated by dashed arrow). Short illumination times result in a blueshift of the absorption peak of MDMO-PPV at 490 nm, whereas the absorption peak at 335 nm which is mainly attributed to F8BT remains constant. Due to the second absorption maximum of F8BT at 470 nm the observed blueshift is diminished in comparison to the evolution of the spectra for the pure MDMO-PPV film. For total UV exposure times above 30 min, the F8BT also starts to degrade and hence leads to a reduction of the optical absorption at both absorption peaks. In addition, the absorption peak at 455 nm is further shifted to shorter wavelengths. The modifications due to F8BT degradation are depicted by the dotted arrows. However, comparing the total UV exposure times t_{UV}^{max} of the homopolymer (MDMO-PPV: 60 min and F8BT: 540 min) and the blend films (blend: 300 min) it is found that the materials degrade photochemically faster in blend morphology.

For an improved illustration of the relation between the optical absorption and the total UV exposure time t_{UV} , the normalized integrated absorptions for MDMO-PPV (upper graph) and F8BT (lower graph) are shown in figure 5.19(a). In the case of MDMO-PPV, the evolution of the normalized integrated absorption $A_{int}(\text{MDMO-PPV})$ versus

the illumination time t_{UV} is described well by an exponential function

$$A_{int}(\text{MDMO-PPV}) = \exp(-\tau_{UV} t_{UV}) , \quad (5.3)$$

where τ_{UV} corresponds to a decay rate of 0.038 ± 0.003 min. For F8BT the integrated absorption stays constant for approximately 120 min before it drops according to a logistic function

$$A_{int}(\text{F8BT}) = \frac{1}{1 + \exp(k_{UV}(t_{UV} - t_{UV,0}))} , \quad (5.4)$$

where the factor $k_{UV} = 0.014 \pm 0.0008$ min⁻¹ describes the slope of the curve and $t_{UV,0} = 416 \pm 5$ min gives the position of half intensity. Since such logistic functions are used to describe autocatalytic chemical reactions, the observed behavior of F8BT indicates an enhanced photochemical degradation of F8BT due to the resulting reaction products. The most important difference is given by the modified time scales: Whereas MDMO-PPV loses already 80 % of its light absorbing properties in the UV/Vis range within 60 min, F8BT keeps 80 % of the absorption potential for approximately 300 min.

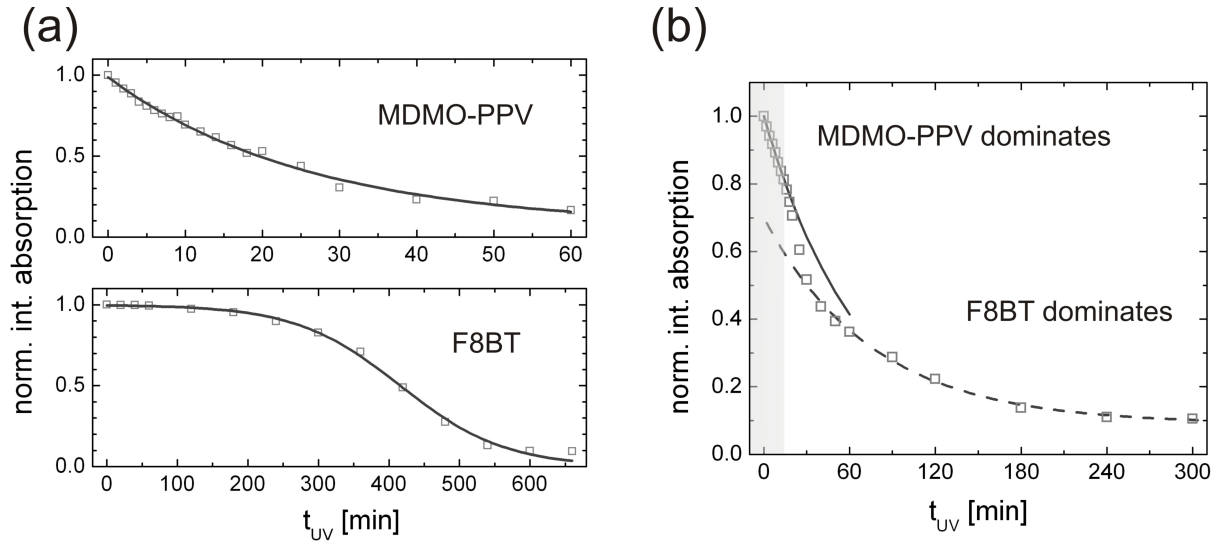


Figure 5.19: Normalized integrated optical absorptions versus UV exposure times t_{UV} : In (a) the integrated optical absorptions are plotted against t_{UV} for MDMO-PPV (upper graph) and F8BT (bottom graph). In (b) the corresponding values are plotted for the MDMO-PPV:F8BT blend film. All shown values are integrated between 300 and 800 nm and the lines correspond to the mathematical fits. The experimental errors are smaller than the symbol sizes.

In figure 5.19(b) the normalized integrated absorptions for the MDMO-PPV:F8BT blend film are shown versus the UV irradiation time t_{UV} . It is found that the extracted values neither follow the exponential decay from the MDMO-PPV nor have a similar logistic shape as the F8BT. Moreover, a two-phase regime is found which is attributed to a

MDMO-PPV dominated region for UV exposure times t_{UV} below 18 min (illustrated by gray background) and an F8BT governed decay for longer irradiation times. The solid line corresponds to an exponential decay (see equation (5.3)) with a decay rate τ_{UV} of $0.015 \pm 0.0002 \text{ min}^{-1}$. Hence, for the MDMO-PPV dominated region the photochemical degradation is retarded due to the presence of the more stable F8BT (illustrated by dashed line). However, for longer illumination times the absorption of F8BT, which was stable in homopolymer films for UV irradiation times of up to 180 min, also shows an exponential decay with a rate of $0.013 \pm 0.001 \text{ min}^{-1}$ if blended with MDMO-PPV (see dashed line). Chambon et al. have shown that the photooxidation of MDMO-PPV includes the formation of radicals at the ether part of the PPV derivatives.[205] Furthermore, under the presence of oxygen additional peroxy radicals are formed. These two radicals are the reason for an enhanced photochemical degradation of F8BT induced at the critical quarternary site of the fluorene unit, which leads to a rapid chain scission of the polyfluorene.

In summary, in this section an additional novel polymer blend based on MDMO-PPV and F8BT was discussed in detail concerning the influence of film composition on the phase separation. By performing GISAXS experiments it was shown that the observed phase separation domains are the smallest for symmetric volume blending ratios. In addition, the photochemical degradation upon UV irradiation was measured for the homopolymer films and a corresponding blend film using UV/Vis absorption measurements. The good photochemical stability of F8BT was drastically reduced in the blend film due to the presence of radicals which are produced during oxidation of MDMO-PPV.

Especially in context with the results from the following section 5.3, which address the presence of oxygenic residual solvent molecules, this section has clearly shown that the photochemical stability of semiconducting polymers is a major concern for future developments in the field of OSC.

5.3 Residual solvent depending on polymer phase separation

As mentioned in the introduction, one main advantage of organic electronic devices results from the ability of conducting polymers to be processed via various simple solution-based casting techniques such as spin coating, doctor blading, solution casting, and spray coating.[201] For many different polymer blend systems the choice of solvent and post-casting annealing steps drastically influence the resulting film morphology and are hence crucial for the final device performance.[207, 200, 208, 209] However, the question whether solvent molecules are retained within the final conducting polymer films is still unanswered, let alone the corresponding lateral distribution. In the following section, soft X-ray absorption measurements are successfully applied to address these open questions. Therefore, the subsequent section is divided into the following parts: A short overview of the results of previous experiments focusing on the solvent retention in non-conducting polymer films is given (section 5.3.1). Subsequently, the absolute solvent content in homopolymer films is revealed (section 5.3.2) and its dependence on the film thickness is probed (section 5.3.3). The lateral distribution of retained solvent molecules in blend films is determined (sections 5.3.4 and 5.3.5), before the impact on organic solar cells is finally discussed (section 5.3.6).

5.3.1 Background

Reduced diffusion rates of solvent molecules through entangled and densely packed polymer chain networks due to chemical interactions, e.g. dipole-dipole interactions or hydrogen bonds between solvent molecules and polymer chains, are the origin of solvent retention in solution cast polymer films. The drying of such films is divided into two subsequent processes: The first phase of drying is limited by solvent evaporation at the air interface, whereas in the second phase the solvent diffusion within the polymer matrix governs the film creation.[210] The same principles also hold for the applied spin coating technique (see section 4.3.3), which facilitates the solvent evaporation at the air interface and therefore leads to an even enhanced stiffening of the polymer chains accompanied by a possible increased solvent trapping. Since polymer chains lose chain mobility at temperatures below glass transition, the material characteristic glass transition temperature T_g plays a crucial role as well. As a result, conducting polymers, which typically have a glass transition at temperatures above room temperature T_{RT} , restrain the solvent diffusion more than polymers with a T_g below T_{RT} . However, conducting polymers not only hamper the diffusion of the solvent molecules, they also provide additional empty space

due to sterical hindrance along the rodlike conducting polymer chains. In thin films of coiled polystyrene this so-called *free volume* already makes up to 11 % of the total sample volume.[211] Therefore, small solvent molecules find an even greater number of volume traps in matrices made of rodlike than in those made of coiled polymer chains.

For non-conducting polymer films the solvent retention has already been determined via different methods, unfortunately all lacking lateral resolution. In previous experiments, gas chromatography was used to determine a residual solvent content of up to 9 vol% in polystyrene films by re-dissolving the already cast polymer film in a different solvent.[212] In addition, laterally unresolved dielectric spectroscopy has proven the presence of solvent molecules in conventional poly[methylmethacrylate] films, as well.[213] Perlich et al. applied neutron reflectometry (NR) to polystyrene films made from deuterated toluene solutions and found a solvent enrichment at the substrate interface.[214] Nevertheless, experiments performed up to now have only focused on standard non-conducting materials and also do not allow any insight into the lateral solvent distribution.

5.3.2 Absolute solvent content in homopolymer films

In order to utilize soft X-ray absorption measurements (see section 2.4.5) specific polymer:solvent systems are investigated based on oxygen free conducting polymers and oxygen containing solvent molecules. The fact that oxygen is found only in the solvent makes it an ideal marker element for X-ray spectroscopy. In addition, the unique carbon *K*-edge spectra of the polymer materials provide a supplementary contrast mechanism that is used to identify and to quantify each of the components in the later investigated polymer blend samples.

In figure 5.20(a) the O *K*-edge NEXAFS spectrum of a 600 nm thick homogeneous PVK film is shown, which was cast from a 40 mg/ml cyclohexanone solution (dark line). The absorption spectrum contains spectral features identical to the electron energy loss spectrum (EELS) of pure cyclohexanone, which is shown in the inset.[215, 216] In the case of the NEXAFS and the EELS spectrum, a prominent absorption maximum at 531.5 eV, which is attributed to O $1s \rightarrow \pi_{C=O}^*$ transitions, is accompanied by a broader and less intense set of absorption peaks between 530 and 560 eV. The latter are due to multiple O $1s \rightarrow \sigma_{C=O}^*$ transitions. In figure 5.20(b) the corresponding absorption spectrum of an F8BT film with a thickness of approximately 550 nm, which was cast from a 16 mg/ml THF solution, is plotted as a dark line (F8BT type-I, see section 4.1.2). The corresponding inset depicts the EELS spectrum of pure THF, which again shows absorption features consistent with the ones from the polymer film. Both spectra have a prominent intensity maximum at 540 eV, which is attributed to O $1s \rightarrow \sigma_{C-O}^*$. [217] The minor variations in

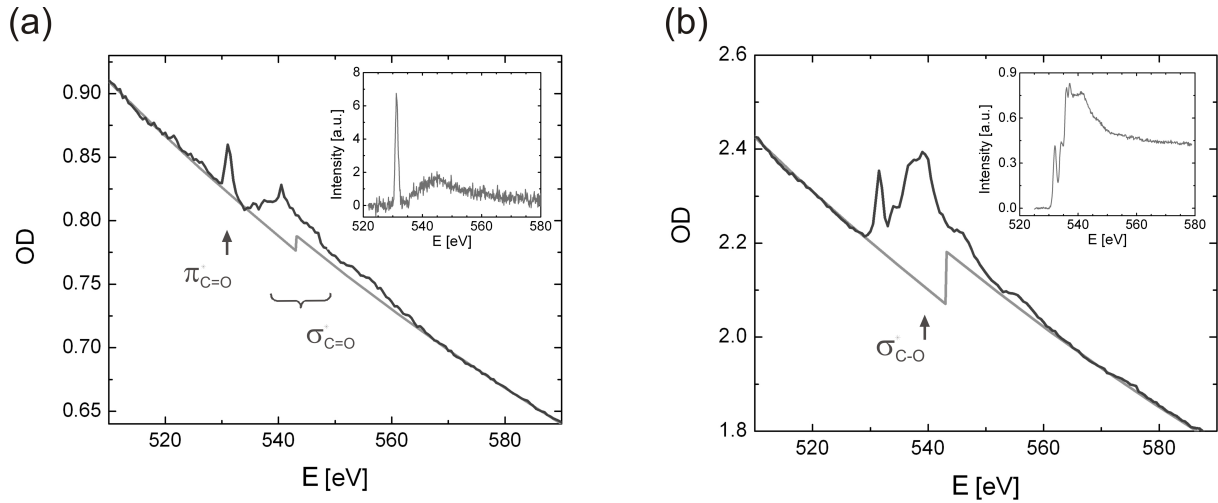


Figure 5.20: NEXAFS spectra probed at the oxygen K -edge (dark lines) of (a) a PVK film prepared from cyclohexanone solution and (b) a F8BT film prepared from THF solution. The spectra are plotted as optical density OD versus energy E of the soft X-rays. The light lines are calculated from theoretical models based on the chemical compositions of the films and they are used to determine the solvent contents in the thin films. The insets show the corresponding EELS converted to oscillator strength per oxygen atom of (a) pure cyclohexanone and (b) pure THF.[215, 216]

intensity around the maximum result from many particle processes (also called *shake-up*) due to molecular resonances. The PVK and the F8BT spectra clearly confirm that the observed oxygen signal is indeed primarily due to retained solvent molecules and is not attributed to the presence of water, air or oxidation of the polymer or substrate, which could occur during sample preparation. In order to avoid such contaminations, the homopolymer films were prepared on SiN-membranes in a glove box and the samples were handled and stored under a nitrogen atmosphere. Moreover, the spectrum of the substrate was eliminated by using measurements on blank nitride membranes for beam intensity corrections at different photon energies.

In addition, the NEXAFS spectra in figure 5.20 show additional step-like increases in absorption, which correspond to transitions to the continuum and indicate the absolute oxygen content. In the framework of this thesis, a theoretical model for the X-ray absorption of the materials was derived based on the chemical composition of the polymer (PVK: $C_{14}H_{11}N$ and F8BT: $C_{35}H_{42}N_2S$) and the solvent (cyclohexanone: $C_6H_{10}O$ and THF: C_4H_8O) and the corresponding atomic scattering factors published by Henke et al.[112] In figure 5.20 the modeled absorption spectra are included as light lines. Fitting the theoretical models for the two polymer:solvent systems to the actual data yields the percentage solvent amount, which is retained within the polymer film. Since the applied Henke atomic scattering factors do not include near-edge resonance effects, the fit of the model to the data is only evaluated by the steps in absorption of the measured intensity

spectra. In practice, the sum of all absorption coefficients of the specific polymer:solvent compositions at a defined ratio was calculated in order to fit the measured optical density (OD) in the pre- and post-edge region

$$OD = -\ln \frac{I_t}{I_0} = \rho^{abs} \mu_{tot}^{abs} d, \quad (5.5)$$

where I_t is again the transmitted and I_0 the total incoming intensity. The total absorption coefficient μ_{tot}^{abs} is given by

$$\mu_{tot}^{abs} = \alpha^{abs} \mu_{pol}^{abs} + \beta^{abs} \mu_{sol}^{abs} = \alpha^{abs} \sum_p n_{q,p} \mu_{a,p}^{abs} + \beta^{abs} \sum_s n_{q,s} \mu_{a,s}^{abs}. \quad (5.6)$$

According to the Lambert-Beer law in equation (5.5) ρ^{abs} depicts the concentration of absorbing species, μ^{abs} the various absorption coefficients, and d the film thickness. In equation (5.6), the percentage polymer and solvent content is described by α^{abs} and β^{abs} and the atomic absorption coefficients of the present atoms are denoted by $\mu_{a,p}$ and $\mu_{a,s}$ depending on the corresponding relative weights $n_{q,p}$ and $n_{q,s}$. By taking into account the mass densities of the polymers ($\rho_{pol} = 1 \text{ g/cm}^3$ for PVK and F8BT) and of the solvents ($\rho_{cyclohexanone} = 0.95 \text{ g/cm}^3$ and $\rho_{THF} = 0.89 \text{ g/cm}^3$) the overall volume content of the solvent is determined. In the case of cyclohexanone in PVK it is found to be 5 vol% and in the F8BT film 14 vol% of THF are retained. These were the first reported values for the solvent retention in solution cast conducting polymer films.[218]

5.3.3 Solvent content depending on film thickness

Bearing in mind the results from previous experiments on the solvent content in non-conducting polymer films (see section 5.3.1), a strong influence of the film thickness on the amount of residual solvent molecules is plausible. In order to investigate the relationship between film thickness d and residual solvent content, the lateral resolution of the STXM set-up was applied to map a thickness gradient sample.

Therefore, an exemplary PVK thickness gradient sample was fabricated via solution casting of a 40 mg/ml PVK:cyclohexanone solution onto a tilted SiN-membrane. The angle of inclination α_{inc} was set to 25° and the casting was performed directly on the thin membrane support with the solution retained by an attached sharp silicon dam. The fabrication method is sketched in figure 5.21.

In the top part of figure 5.22, a two-dimensional STXM image of the transmitted intensity taken from the PVK gradient sample is shown. Since photons with an energy of 520 eV were applied, which is in the oxygen K pre-edge region, this measurement is used as a logarithmic measure of the film thickness d according to the Lambert-Beer law (equation

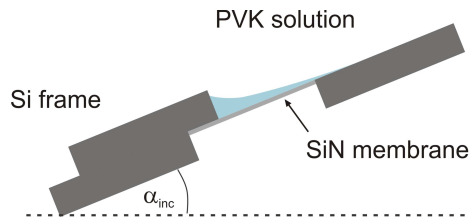


Figure 5.21: Fabrication of PVK thickness gradient: A PVK:cyclohexanone solution ($c = 40 \text{ mg/ml}$) is solution cast on an inclined SiN-membrane ($\alpha_{inc} = 25^\circ$). During solvent evaporation the solution is retained by a sharp silicon dam.

5.5). Since the film thickness gradient is only present along the x -axis, whereas the film thickness is homogeneous in y -direction, an integrated line profile is generated to obtain improved statistics. The calculated film thickness is plotted as a dark line in the graph of figure 5.22. For clarity, the x -axis of the graph in figure 5.22 matches the one of the two-dimensional STXM image above. By an additional intensity map of the same sample area, which was taken at the sharp absorption peak of the cyclohexanone located at 531.5 eV, a spatially resolved optical density map of this oxygen π^* -resonance is calculated. The resulting profile line of the calculated optical density OD of oxygen, which is again obtained by averaging in y -direction, is depicted by the light line in figure 5.22.

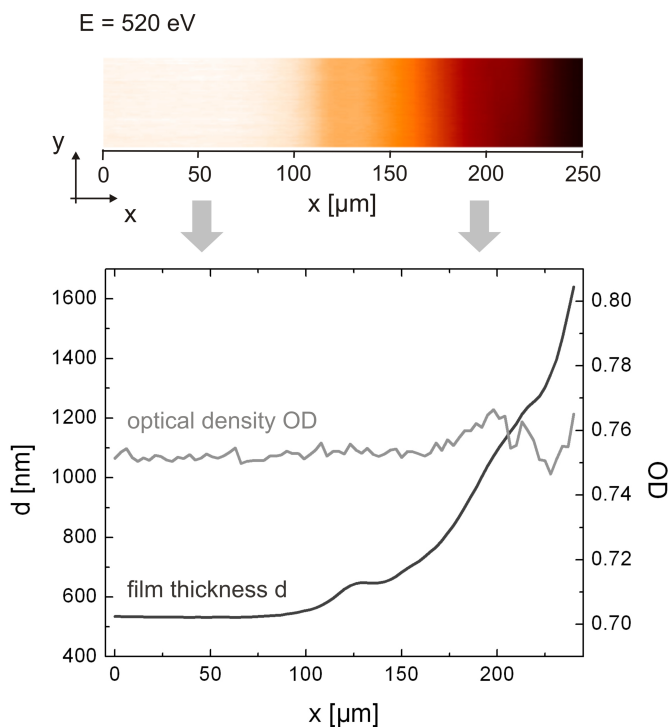


Figure 5.22: In the top part a two-dimensional STXM image of a solution cast PVK thickness gradient is shown recorded at 520 eV. The decreasing transmitted intensity along the x -axis depicts the increasing film thickness d . Below, the calculated film thickness d (dark line) and the optical density OD of oxygen (light line) are plotted as function of the lateral x -position.

In contrast to the PVK thickness d , which is monotonically increasing from 530 to 1630 nm, the measured oxygen OD remains constant at approximately 0.76. This observation indicates that for the PVK film, the solvent molecules are more likely retained at

or near an interface, rather than within the bulk of the polymer film. In addition, this measurement of the film thickness gradient further verifies that the detected oxygen in the film is only due to the embedded solvent, as it was already indicated by the spectral absorption features in the NEXAFS spectra in figure 5.20. An oxidation of the polymer, which could occur between polymer synthesis and coating, would result in a strong thickness dependence.

5.3.4 Compositional mapping of polymer blend films

The surprisingly large difference in solvent uptake for different polymers (e.g. PVK and F8BT in section 5.3.2) implies a similar material correlated solvent distribution in polymer blend films, which can have a previously non-assessable impact on the electrical characteristics of blend devices.

Due to its high lateral resolution, STXM was already applied to image the morphology of conducting blend films, which often show non-equilibrium phase-separation structures on the nano- and micro-scale (see sections 5.1 and 5.2).[133, 219, 220] The key advantage of this method is that it not only reveals the lateral dimensions of non-equilibrium phase-separation structures of polymer blend films, but also the film composition. For investigations on the polymer domain specific solvent uptake, the already discussed PVK was blended with poly[3-hexylthiophene] (P3HT) in THF and thin films were prepared via spin coating. Among other application possibilities, the electroluminescence from such polymer blend thin films has been intensely studied for application in light emitting diodes.[221] Recently, also a novel P3HT-*b*-PVK diblock copolymer was synthesized, which has potential for white light emitting diodes.[222] In figure 5.23 an optical micrograph of a P3HT:PVK blend film is shown, which was spin coated on an acidic pre-cleaned silicon substrate and then transferred to a copper TEM-grid via floating (more details on the floating routine are given in section 6.1.1). P3HT was dissolved at a concentration of 8 mg/ml and PVK at 10 mg/ml, respectively. For both polymers THF was chosen as solvent and a volume ratio of 4:1 (PVK:P3HT) leads to segregated polymer domain sizes, which are appropriate for further investigations with STXM.

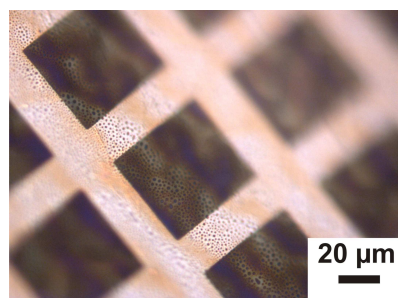


Figure 5.23: Optical microscopy image of a P3HT:PVK polymer blend film: After spin coating on a flat silicon support the film was transferred to a TEM grid via floating.

For a detailed analysis of the surface properties of the P3HT:PVK blend film, AFM data are necessary to address the domain heights. The topography data in figure 5.24(a) reveal a circular shape of the domains with typical diameters between 0.5 and 1.6 μm . As previously observed in the optical microscope image (figure 5.23), the segregated polymer domains are randomly distributed. Profile lines from the close-up topography data in figure 5.24(b) show variations in height of up to 100 nm between the phase separated polymer domains.

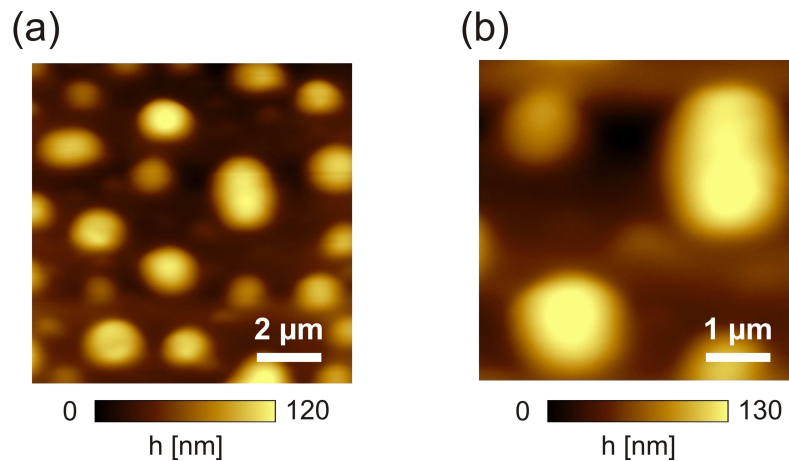


Figure 5.24: AFM data of the surface topology of a P3HT:PVK polymer blend film: In (a) the random lateral distribution of the polymer domains is seen and in (b) a wavy surface topography with deviations of up to 100 nm between the polymer domains is revealed.

In comparison to the investigated MEH-PPV:PVK films, which show sharp transitions at the polymer domain walls (see figure 5.3), the P3HT:PVK films have a wavier surface with smooth height variations at the polymer phase boundary. Such smooth transitions already indicate an intermixing of both polymer components at the phase boundaries. In order to investigate the lateral film composition with STXM in more detail, NEXAFS spectra of the pure components have to be recorded. Since polymeric materials have prominent material specific features at the carbon K -edge, the spectra of P3HT and PVK were recorded at photon energies between 280 and 320 eV. As illustrated in figure 5.25(a), P3HT (dark line) shows a relatively small $1s \rightarrow \pi_{C=C}^*$ transition at 285 eV and a more prominent feature at 288 eV, which is associated with the same π -bond. The broad maximum at 294 eV is attributed to σ_{C-C}^* transitions at the thiophene unit.[223] For the pristine PVK (light line) the first two peaks at 285 and 287 eV result from $1s \rightarrow \pi_{C=C}^*$ resonances of the carbon atoms in the carbazole unit. The third peak at 290 eV is due to $1s \rightarrow \sigma_{C-H}^*$ resonances and at higher photon energies a broad peak from transitions to the quasi state follows ($E = 305$ eV).[224]

From the corresponding NEXAFS spectra in figure 5.25(b), which were recorded within

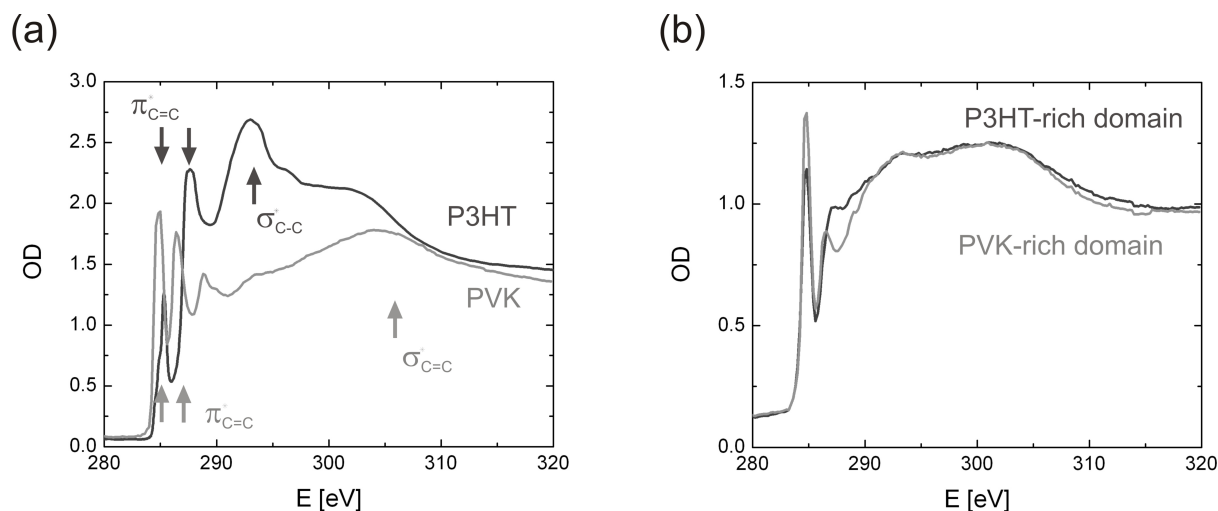


Figure 5.25: Different NEXAFS spectra: In (a) the NEXAFS spectra of the pure P3HT (dark line) and PVK (light line) components are shown, which reveal strong differences in their π -bond structure at the carbon edge. In (b) the NEXAFS spectra from the separated polymer domains show a P3HT enrichment in the elevated polymer domains (dark line) and a PVK governing in the surrounding matrix (light line).

the different polymer domains, an intermixing of both components is obvious. By concentrating on the differences at photon energies of 285 eV and 288 eV the absorption spectrum, which was recorded within the elevated polymer domains (dark line), can be attributed to a P3HT-rich phase, whereas the surrounding polymer matrix appears dominated by PVK (light line).

For a more detailed lateral analysis, two-dimensional compositional maps were already calculated for different polymer blends taking into account multiple STXM images.[225, 226] Therefore, the STXM data must be recorded at energies which match prominent spectral features from the carbon K -edge NEXAFS spectra and finally each data point is modeled to the spectra of the pristine components. In figure 5.26(a) the STXM data taken in the pre-edge region at 280 eV is shown and for figure 5.26(b) the data were recorded at 287.5 eV, a photon energy with a very high contrast between the pristine components. Subsequently, in figure 5.26(c) the actual compositional map is calculated according to section 3.9. The two-dimensional map confirms the result from the local NEXAFS spectra (figure 5.25(b)) that the elevated polymer phase has P3HT as its majority component ($\approx 70\%$), whereas the surrounding polymer matrix is almost entirely composed of PVK. Similar to the AFM data, the compositional map also reveals a smooth transition between the polymer domains with respect to film thickness and composition. In comparison to other conducting polymer blend films - e.g. the common F8BT:PFB [226] or the previously discussed MEH-PPV:PVK system, which typically exhibit distinct polymer domain transitions - the observed smooth transitions are rather uncommon for conducting

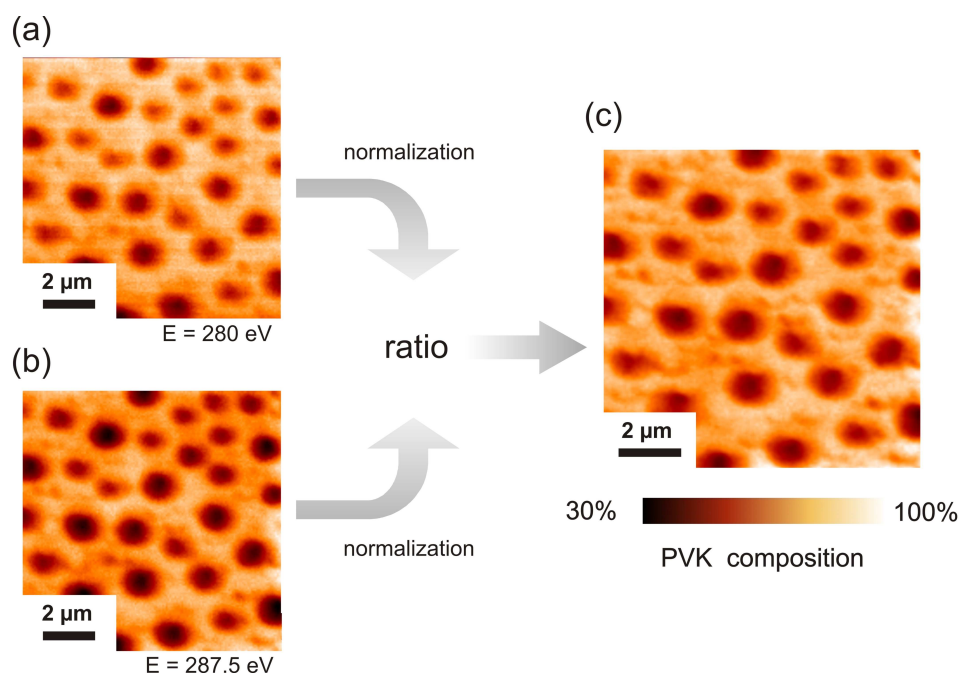


Figure 5.26: STXM data of P3HT:PVK blend film taken at different photon energies of (a) $E = 280$ eV and (b) $E = 287.5$ eV. In (c) the quantitative PVK compositional map is calculated from three STXM images taken at photon energies of 280, 284.5 and 287.5 eV. The color code illustrates the actual PVK content.

polymer blends.

In addition, complementary STXM images with higher resolution were recorded. In figure 5.27 transmission data with a reduced scan size of $4 \times 4 \mu\text{m}^2$ are shown taken at a photon energy of 287.5 eV.

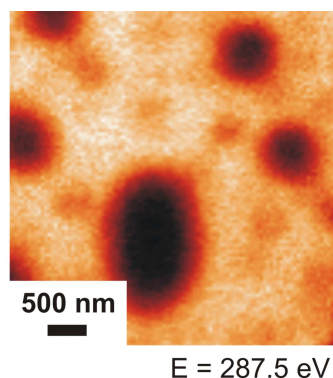


Figure 5.27: High resolution STXM data of P3HT:PVK polymer blend film taken at a photon energy of 287.5 eV: No polymer domains smaller than those already observed in figure 5.26 are detected.

However, within the limit of 35 nm resolution, the high resolution data do not show any structures smaller than those observed in figure 5.26 either.

5.3.5 Lateral solvent distribution in polymer blend films

In the framework of this thesis, the same principles that were successfully applied for the calculation of compositional maps are now adopted for the determination of novel two-dimensional residual solvent maps. For this approach, the contrast between an oxygenic solvent and an oxygen-free polymer blend system is utilized in a way similar to the study on homopolymer films in section 5.3.2.

From a molecular point of view, it is known that the exceptional highly crystalline character of P3HT leads to a more ordered polymer chain arrangement in comparison to PVK. Among other possibilities, this crystallinity effect can result in a preferential trapping of solvent molecules within particular domains of the investigated polymer blend film and hence in an uneven spatial solvent distribution. In order to address the point of a lateral solvent distribution in the P3HT:PVK films, STXM images were taken at photon energies corresponding to the oxygen *K* pre-edge region (525 eV; figure 5.28(a)) and at a prominent spectral feature from THF (531.5 eV; figure 5.28(b)). While both sets of STXM data individually depend strongly on the already observed variations in film thickness (see figure 5.24), this effect is canceled out in their ratio. As a result, a map is derived, which exclusively displays the spatial distribution of THF molecules (figure 5.28(c)).

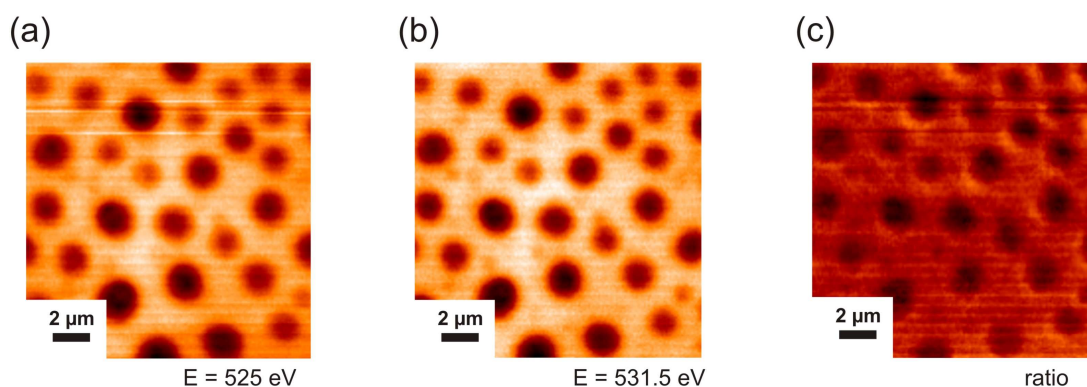


Figure 5.28: STXM microscopy images taken at (a) 525 eV (pre-edge region of oxygen *K*-edge) and (b) 531.5 eV (spectral feature of THF). Calculated from (a) and (b), the data in (c) represent the solvent distribution in the polymer blend, which matches the film composition of the polymer blend (see figure 5.26(c)).

Since the two-dimensional solvent map is calculated from raw transmission images, the contrast of the THF map is such that higher concentrations of THF appear darker. Hence, in figure 5.28(c), a solvent distribution pattern is shown which indeed is similar to the actual phase separation morphology depicted in the separate STXM and AFM data (figure 5.24 and 5.26). The greater amount of residual THF solvent is found in the P3HT-rich domains as compared to the surrounding PVK-rich matrix.

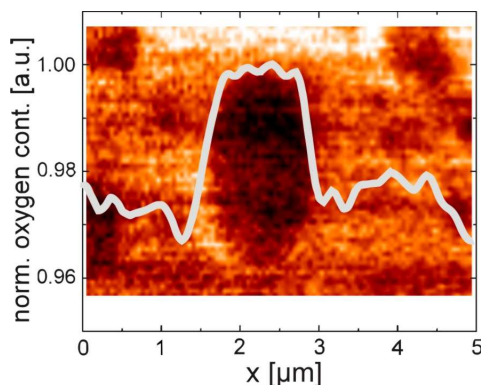


Figure 5.29: Calculated ratio of high-resolution STXM data: A line cut of the absorbance along a P3HT enriched polymer domain reveals a higher solvent content in comparison to the surrounding PVK matrix.

For better clarity, a profile line cut across a P3HT-rich polymer domain is plotted in figure 5.29. The corresponding high resolution STXM image, from which the profile was extracted, is shown in the same graph matching the lateral resolution of the line cut. For convenience, the intensity of the pristine line cut is inverted to better illustrate the actual solvent content and it is normalized to the maximum value of oxygen, which is found in the center of the P3HT domains. In total, the normalized peak-to-valley ratio of the relative oxygen content is approximately 3 % and hence suggests rather small overall deviations from the mean solvent distribution. Nevertheless, the distinct sharp increase in the line cut at the polymer phase boundaries reveals a well-defined preferential residue of THF molecules in the P3HT-rich domains. However, the absolute solvent content values in the two polymer blend domains can only be addressed via similar NEXAFS spectra as they are shown in figure 5.20. Unfortunately, such measurements are only possible using an unfocused set-up due to the low amount of solvent present and are therefore not suited for the small segregated polymer blend domains.

In order to address the observed preferential solvent distribution, it is known from a chemical point of view that H-atoms as present in THF interact with the thienyl backbone bearing π -system of P3HT.[227] In principal, similar weak π -H interactions are also possible between the THF and the carbazole units in the PVK. Nevertheless, in the case of PVK, strong π - π interactions lead to a denser packing of the more flexible PVK chains than in comparison to the rigid P3HT, which is also hindered by its long side chains. Based on these steric restraints, the molecular rearrangements result in a reduced effective surface in the PVK-rich phase, which is necessary for the solvent molecules to attach to the polymer chain. Due to a theoretically predicted increased free volume in the crystalline entanglement of the P3HT-rich domains (see section 5.3.1), the solvent molecules can also be preferentially trapped in such voids.

In figure 5.30 the STXM data of a P3HT:PVK blend film are shown, which was spin cast directly on a SiN membrane. In comparison to figure 5.28, the same polymer solution leads to a polymer phase separation with reduced average domain sizes. This effect is due to the

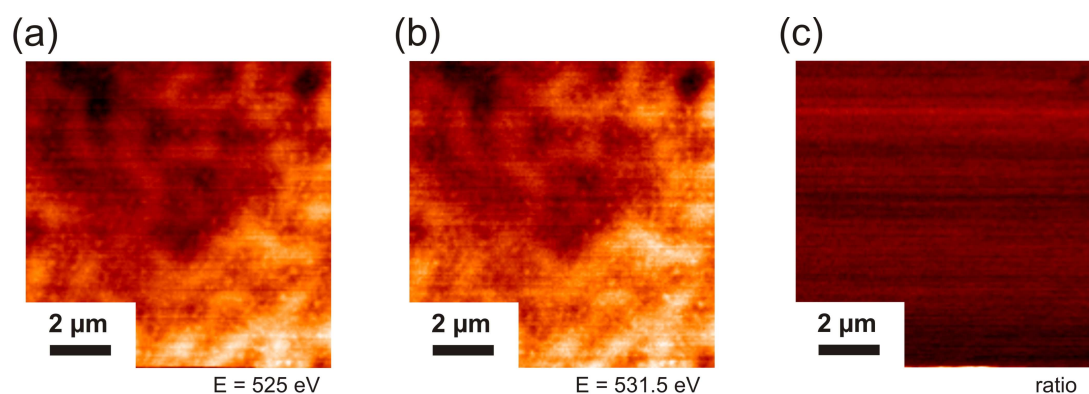


Figure 5.30: STXM data of P3HT:PVK blend film spin cast on a SiN membrane: (a) and (b) are taken at photon energies of 525 eV and 531.5 eV, respectively. The solvent distribution map in (c) does not show any preferential solvent distribution.

thin SiN membranes, which have almost no heat capacity and therefore result in modified film formation conditions with enhanced solvent evaporation rates during the spin coating process. The STXM image in figure 5.28(a) was taken at a photon energy from the pre-edge region of oxygen (525 eV) and for (b) 531.5 eV was chosen, which corresponds to a dominant spectral feature of THF. Surprisingly, the ratio of the two STXM data (figure 5.28(c)) does not show any evidence of a preferential solvent residue in one of the polymer domains as observed in figure 5.28. It was already discussed in section 5.1.6 that especially larger polymer domains are initialized in the early stages of the spin coating process. Hence, for the investigated smaller P3HT:PVK domains the polymer solution appears to be well dissolved at the beginning of the casting. The rapid quenching, which was mainly induced by the temperature sensitive thin SiN membrane, finally results in an accelerated film formation. In comparison to the blend film spin coated on a silicon support, the molecular arrangement of the polymer chains is likely to be perturbed [228] due to the reduced environmental temperature in case of SiN membranes as the substrate material. In consequence, a preferential solvent trapping is not induced.

5.3.6 Impact on organic solar cells

The previous experiments prove an essential amount of residual solvent in thin conducting polymer films, which cannot be ignored for the future development of organic electronic devices. Laterally distributed solvent residues have been unknown until now and their influence in the area of conducting polymer research has therefore hardly been discussed. Very recently Chang et al. used gas chromatography-mass spectrometry (GCMS) to provide general evidence of retained solvent molecules in P3HT:PCBM bulk-heterojunction solar cells and they speculated that the solvent residues lead to an extensive phase separa-

tion in the film.[229] Based on the results from different thermally annealed samples, they also found that non-negligible amounts of excess solvent were retained in the film. Such residual solvent molecules led to higher diffusion rates of the fullerene, which again had a strong impact on the overall power conversion efficiency. Hence, additionally trapped solvent molecules over time alter the film morphology and crystallinity of both homopolymer and blend films due to an energetic shifting of the free enthalpy (so-called *softening effect*). In addition, the results of Chang et al. demonstrate that thermal annealing steps, which are common for the fabrication of organic electronic devices, do not remove residual solvent entirely.[229] Elongated thermal post-production steps did not lead to improved solvent extraction quotes as well. The same behavior was also observed by Perlich et al. for polystyrene films.[214]

Oxygenic solvents play an especially important role for conducting polymers. As pointed out in section 5.2, the optical absorption of photoactive polymer films is gradually reduced due to UV irradiation under the presence of molecular oxygen. As well, the electroluminescence of conducting polymer based light emitting diodes is heavily reduced by oxygen from the surrounding atmosphere.[230] Both degradation effects are attributed to oxygen induced modifications of the chemical structure, e.g. chain scission or ring-opening.[231] Although oxygenic solvent molecules are maybe not as reactive as molecular oxygen, they are often strongly polar as in the case of cyclohexanone and therefore might also lead to chemical modifications of the polymer molecules. As a consequence, the presence of residual oxygenic solvent molecules in an active polymer layer will not only be significant for the efficiency of electronic devices but moreover have a strong influence on the long-time performance - even if the devices are thermally annealed and encapsulated from the surrounding environment.

The results of section 5.3.3 imply the formation of a defined solvent enrichment layer in PVK films. Since this layer is likely to be formed at the air or the substrate interface, they might act as electrical depletion layers and hence can strongly influence the quality of the top or the bottom contact in an actual device.

In a more general perspective, the results on locally distributed solvent molecules also have an impact on the discussed theoretical models for polymer blends based on the Flory-Huggins approach (see section 2.2). For a full description of the polymer blend systems, a local and material specific solvent component needs to be added to the existing models.

5.4 Conclusions - polymer blend films

In this chapter, the complete film morphologies of various conducting polymer blend systems were studied. In-depth knowledge of the phase separation mechanisms in polymer blends is not only crucial for a general understanding in soft-matter physics, but increases in importance for the rapidly developing field of organic electronic device physics.

Therefore, different conducting polymer blend films were discussed regarding the formation of polymer phase segregation domains. On the basis of multiple experimental techniques, the film architectures of samples based on MEH-PPV and PVK were fully revealed for different film thicknesses. These films showed not only thickness-dependent domain sizes, but also a self-driven installation of a PVK enrichment layer at the substrate surface. For MDMO-PPV:F8BT blend films it was shown that the sizes of the polymer domains also depend on the compositional ratio. Moreover keeping in mind the longtime performance of OSCs, an accelerated photochemical degradation of the MDMO-PPV and F8BT components was observed in blend morphology in comparison to the results on the homopolymer films. In general, the photochemical degradation is due to molecular oxygen from the surrounding environment. However, also residual oxygenic solvent molecules in homopolymer films, as they were detected with a novel approach using X-ray absorption measurements, act as possible sources for an enhanced polymer degradation. In addition, a lateral distribution of such solvent molecules embedded in a P3HT:PVK blend film was revealed using the STXM technique which was adopted to specific polymer:solvent systems.

In consequence, three main conclusions can be drawn: (i) In many cases a multi-layer approach proves appealing for optoelectronic devices based on polymer blend films which require a minimum film thickness in combination with a minimum polymer phase separation. (ii) By changing the compositional ratio, modified polymer domain sizes within BHJ films are achievable. (iii) It is not sufficient to simply study the photochemical degradation of conducting homopolymer films, which still limits the wide application possibilities of organic devices. Instead, the complete blend films as actually used in the final devices must be addressed. Due to the presence of retained solvent molecules, a simple encapsulation does not prevent internal oxidation defects.

Chapter 6

Supplemental Structuring Routines for Conducting Polymer Films and Their Application

Historic milestone 1977: A. J. Heeger, A. MacDiarmid, and Hideki Shirakawa reported high electrical conductivities in oxidized iodine-doped polyacetylene.[232] This research earned them the Nobel prize in Chemistry in 2000.

In the previous chapter 5, self-structured polymer blend films were investigated concerning film morphology and different approaches were introduced to tune the related phase separation. However, as previously mentioned, an additional key advantage of polymers is given by the various possibilities to fabricate polymer patterns on the micro- and nanoscale (see sections 2.3.1 and 2.3.2). In this chapter, different novel structuring approaches are introduced which are also suited for the fabrication of textured conducting polymer films. The first imprinting technique is advantageous because all processing steps are individually carried out at room temperature (section 6.1). Polymer films, which were imprinted via this routine, are therefore applied to investigate the influence of a post-treatment thermal annealing step on the structure shape. According to these results, a surface structuring of the intermediate PEDOT:PSS appears more promising for application in organic solar cells than to focus directly on the active layer. For this approach, two additional novel imprinting methods are established: One method is based on an inverted MIMIC approach in combination with a new semi-flexible and reuseable mold material (section 6.2). The other structuring routine makes use of an additional plasticizer, added

temporarily to the PEDOT:PPS, which softens the layer so that it becomes imprintable via NIL (section 6.3). The benefit is that the power conversion of organic solar cells is improved by up to 22 % if such imprinted PEDOT:PSS layers are employed.

6.1 Thermal annealing of structured polymer films

In this section structured polymer films made of F8BT are analyzed concerning the structure evolution upon thermal annealing. Therefore, at the beginning the fabrication routine is illustrated, which has the advantage of being independent on high-temperature or any pressure involved processing steps (section 6.1.1). Subsequently, the influence of polymer film thickness variations on the obtained surface structures is investigated (section 6.1.2). After some general remarks on GISAXS measurements on such polymer structures (section 6.1.3), the surface structure evolution during thermal annealing is probed in-situ with a combination of GISAXS and optical imaging techniques (section 6.1.4).

6.1.1 Fabrication routine

Besides focusing on an efficient polymer phase separation within the active layer as addressed in chapter 5, a second approach to further improve organic optoelectronic devices is based on an additional surface structuring. For example, Na et al. were able to increase the overall power conversion efficiency of P3HT:PCBM solar cells by up to 15 % due to an additional surface imprinting of the photoactive polymer film via the NIL method.[233, 234] A drawback of NIL is that a sample treatment step at elevated temperatures is mandatory to soften the material (see section 2.3.2). As a consequence, for many conducting polymer thin films the potential of tuning the electrical conductivity via defined post-production thermal annealing steps is lost. For example, thin film field-effect transistors based on P3HT showed enhanced electrical characteristics upon thermal annealing.[235] In more detail, this effect was attributed to a higher crystallization of the P3HT polymer chains, which hence leads to an improved electrical conductivity. McNeill et al. reported similar results for all-polymeric OSCs.[150] In their case, thermal annealing of the complete solar cell increased the power conversion efficiency from 0.14 to 1.20 %, whereas annealing of the photoactive films before the deposition of the aluminum top electrode led to only minor improvements in efficiency. Conducting polymer films which are structured via NIL have to undergo thermal treatment steps above the glass transition temperature T_g . Therefore, similar conductivity effects, which are individually regulated by annealing temperature and time, are not possible anymore. In order to avoid such high temperature fabrication steps, the MIMIC approach is in principal better suited for conducting polymers (see section 2.3.1). However, a serious drawback of the MIMIC routine

is that only freestanding polymer structures are fabricated. Hence, a complete polymer coverage of the substrate is not possible, even though it is crucial for any optoelectronic application. The absence of a homogeneous active layer sandwiched between the bottom and the top electrode would result in short-circuit faults. Therefore, new methods have to be found to fabricate application-oriented structured thin films made of conducting polymers.

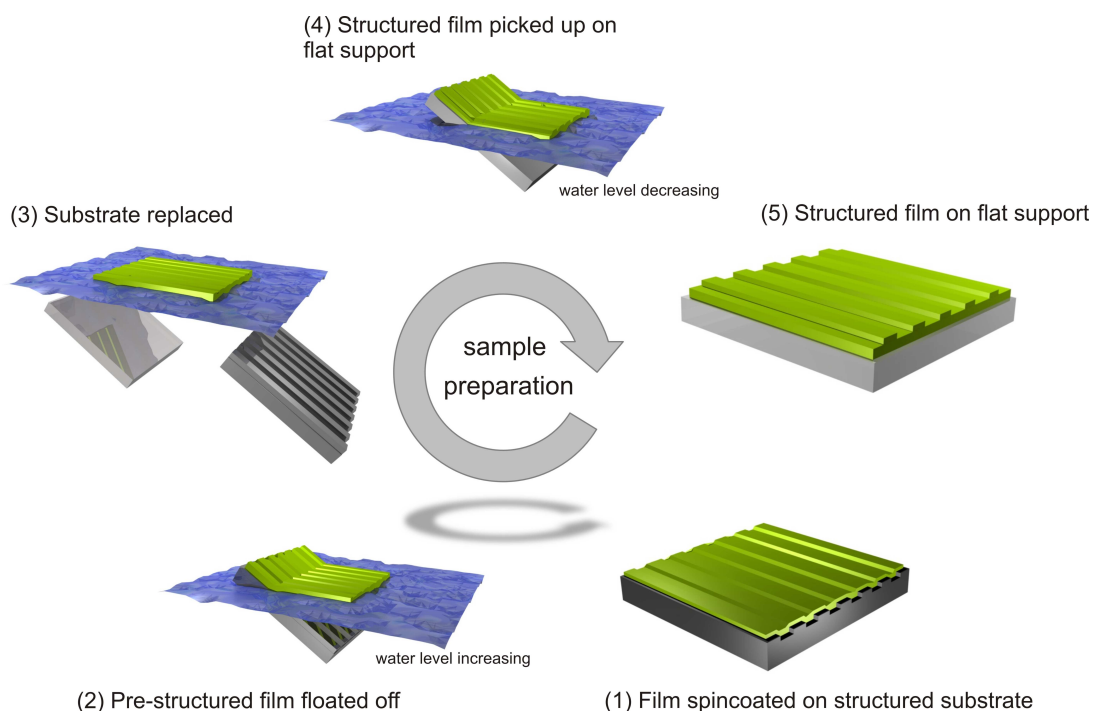


Figure 6.1: Idealized schematic overview of the sample preparation: (1) A thin conducting polymer film is spin coated on a structured silicon substrate. (2) Subsequently, the pre-structured film is floated off using deionized water. In (3) the structured substrate is replaced by a flat solid support and in (4) the water level is decreased. (5) After drying in ambient air, a structured polymer film is left on the flat support.

In figure 6.1 the different steps of an imprinting routine are shown, which allows the fabrication of textured polymer films at ambient conditions. This method is based on the concept of transferring a pre-structured polymer film on a solid support and it is therefore abbreviated as *PSIM* (**P**re-**S**tructured **I**mprinting). In step (1) of figure 6.1 the solid master structure is coated with a thin polymer film. In principal, various different materials are suitable for the master mold. One limitation is given by the resistivity against the solvent of the polymer solution. In this thesis, a silicon master with a 150 nm deep channel structure of 2 μm width and a periodicity of 4 μm was applied. The master was fabricated in-house by photo lithography and reactive ion etching and it had a total structure area of 20 x 20 mm^2 . Due to its strong chemical resistivity the silicon master

was reused multiple times and it was cleaned in an acidic hot bath prior to each usage (see section 4.3.2). Spin coating was used to coat the structured silicon substrates. Also in the case of structured substrates this coating technique allows a good control of the film thickness via the polymer concentration in solution. The influence of the film thickness on the polymer structures is discussed in more detail in section 6.1.2. As it is also illustrated in step (1) of figure 6.1, a wavy surface of the polymer film on top of the structured substrate is observed and its shape is mainly given by the layer thickness. It was found that the absolute peak-to-valley ratio of the wavy surface is reduced for thicker polymer layers. In the following fabrication step (figure 6.1(2)), the floating approach is used to lift off the already pre-structured polymer film from the master mold. For this part of the PSIM routine, the coated master structure is positioned on a sample holder under an inclined angle in a water reservoir, which is slowly filled with water. Since typically adhesion forces between water and substrate are stronger than the ones between polymer and substrate, the water is forced in-between the polymer layer and the silicon substrate. As the water level increases further, the polymer film is gently peeled off the substrate. Given the fact that floatation is very common to transfer polymer films from flat supports on e.g. SiN membranes or copper TEM grids (see section 4.3.2) a large number of polymer-master systems have already proven their abilities to fulfill the floating step. Nevertheless, up to now only flat substrates have been used for floating and it was first shown in the PSIM routine that structured substrates can also be applied. An additional experimental trick is to include an underlying sacrificing layer of a water-soluble polymer. This further increases the abundant application possibilities of the PSIM routine to even more polymer-substrate systems. After the polymer film is completely removed from the substrate (figure 6.1(3)), it floats on the water surface with the main channel structures facing downwards into the water. In the subsequent step (4), the water level decreases steadily and the structured polymer film is picked up by a flat silicon substrate, which was also pre-cleaned in an acidic hot bath to guarantee fully reproducible experimental conditions. Interestingly, for the applied master mold the PSIM routine fabricates similar polymer surface structures whether the floating polymer film is picked up with the structured side facing downwards or if it is transferred to the final substrate flipped around - meaning facing upwards. However, for the applied approach with the channel structures on the water side it is absolutely crucial to dry the polymer film gently after floating. Since the polymer film is still mobile on the substrate and hence fragile if water remains, the trapped water underneath the polymer film has to evaporate slowly. A gentle drying is also necessary to avoid possible voids, which can result from squeezed-out water at the polymer-substrate interface. As shown later in section 6.1.4, GISAXS measurements, which probe the full film thickness, rule out the presence of such interfacial defects. Fi-

nally, the PSIM routine results in structured polymer films on flat silicon substrates as they are illustrated in step (5) of figure 6.1.

To demonstrate the functionality of this structuring protocol, F8BT is chosen as an example material. F8BT has been already widely used for different optoelectronic devices and its properties are well-known (more details are found in section 4.1.2, F8BT type-I).

6.1.2 Structure tuning via film thickness

In this section, the influence of the polymer film thickness on the actual final polymer structures fabricated via PSIM is studied. For this purpose, F8BT was dissolved in toluene at concentrations of 10, 20, and 26 mg/ml, which lead to film thicknesses of 42, 91, and 122 nm, if spin cast on flat silicon supports.

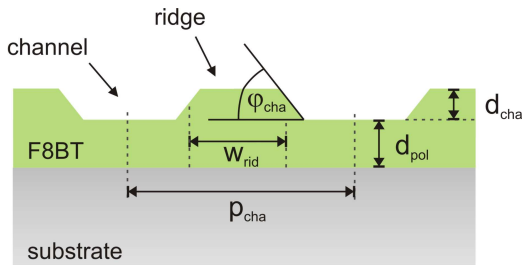


Figure 6.2: Side view sketch of a textured F8BT film perpendicular to the channel structures. All important structural dimensions, such as the width w_{rid} of the polymer ridges, the periodicity p_{cha} , the base angle of the inclined side walls φ_{cha} , the film thickness of the homogeneous polymer underlayer d_{pol} , and the channel depth d_{cha} are included.

For a precise nomenclature of the important structure parameters of the fabricated channels, a schematic illustration of such a structured F8BT film is shown in figure 6.2 including all necessary dimensions. The film thickness of the homogeneous polymer film below the surface structures is given by d_{pol} , the width of the polymer ridge between two channels by w_{rid} , the periodicity by p_{cha} , the depth of the channels by d_{cha} , and φ_{cha} describes the base angle of the inclined side walls of the channels. Keeping in mind that the structure can be considered as infinite along its elongated channels, the illustrated profile view in figure 6.2 depicts all relevant properties to fully describe the investigated structures.

In figure 6.3(a) to (c) the AFM topography data of structured F8BT films are shown made from different polymer solutions with concentrations of (a) 10, (b) 20, and (c) 26 mg/ml. The investigated samples are perfectly homogeneous over the total area of the master mold and do not reveal any cracks on a macroscopic scale either. Additional AFM measurements performed at various scan sizes also reveal a well-defined channel shape which is accompanied by a high long-range order. In order to highlight the perfect channel shape of the F8BT structures, the topography of the F8BT channel structure prepared from a polymer solution with a concentration of 10 mg/ml is shown in figure 6.4(a) at a reduced sampling area of $4 \times 4 \mu\text{m}^2$. Figure 6.4(b) illustrates the sharp edges and the high

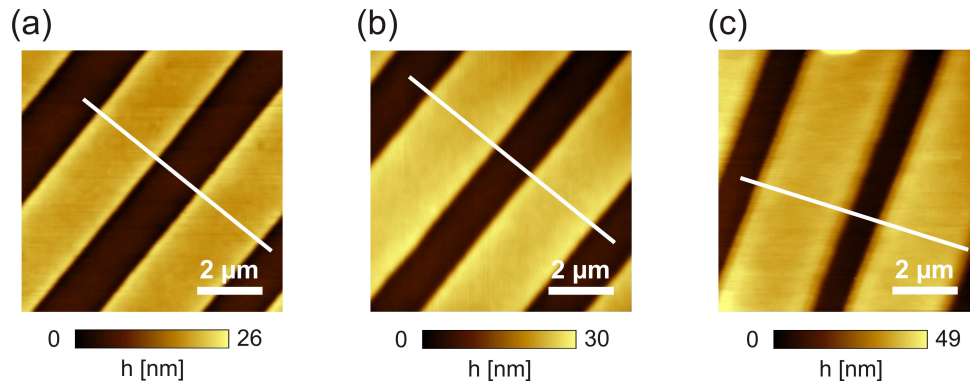


Figure 6.3: Topographic AFM data of the structured F8BT samples with a homogeneous polymer film thickness d_{pol} of (a) 42, (b) 91, and (c) 122 nm. White lines indicate the direction of the profile cuts presented in figure 6.6.

order of the channels on an increased scan size of $12 \times 12 \mu\text{m}^2$. The surface roughness was measured on the polymer ridges and for the different textured polymer films R_{rms} -values of 0.58, 0.55, and 0.79 nm were obtained for increasing polymer concentrations in solution.

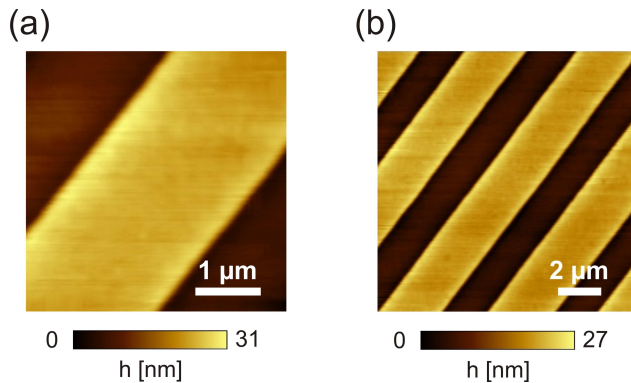
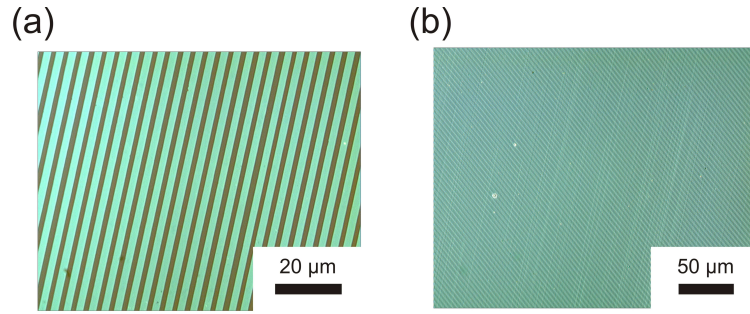


Figure 6.4: Additional AFM topography data of structured F8BT samples with a homogeneous polymer film thickness of 42 nm taken at different scan sizes of (a) $4 \times 4 \mu\text{m}^2$ and (b) $12 \times 12 \mu\text{m}^2$.

The high long range order of the fabricated channel structure is also confirmed with supplementary optical microscopy. In figure 6.5 optical micrographs of F8BT channels are shown, which were fabricated from a polymer solution with a concentration of 20 mg/ml. Whereas the high magnification image reveals a high periodicity over a large area (figure 6.5(a)), no macroscopic cracks and only rare impurities due to dust particles are detected in the micrograph from figure 6.5(b) which was taken with a lower magnification.

As a result, the pre-structured polymer films are stable enough for the critical floating and drying steps during the PSIM routine. For the three different samples, the film thickness d_{pol} of the homogeneous F8BT layer below the surface structure match very well with the film thickness of reference films spin coated on bare silicon supports: (a) 42, (b) 91, and (c) 122 nm. The AFM data in figure 6.3 already indicate that the polymer ridge widths w_{rid} are modifiable via the polymer concentration in solution and hence the film

Figure 6.5: Optical micrographs of structured F8BT film with a polymer film thickness d_{pol} of 91 nm taken at (a) a magnification of 100x and (b) 50x. For both images a polarization filter was used to enhance the contrast.



thicknesses d_{pol} . Also the channel edges become softer for increasing layer thicknesses d_{pol} . In order to investigate the obtained channel structures in more detail, the corresponding profile cuts from the AFM data are shown in figure 6.6. As depicted by the white lines in figure 6.3, the cuts are taken perpendicular to the channel structure. They reveal increasing ridge widths w_{rid} of 2.1, 2.6, and 3.1 μm for increasing polymer film thicknesses d_{pol} . For an exact comparison the corresponding values are extracted at the medium

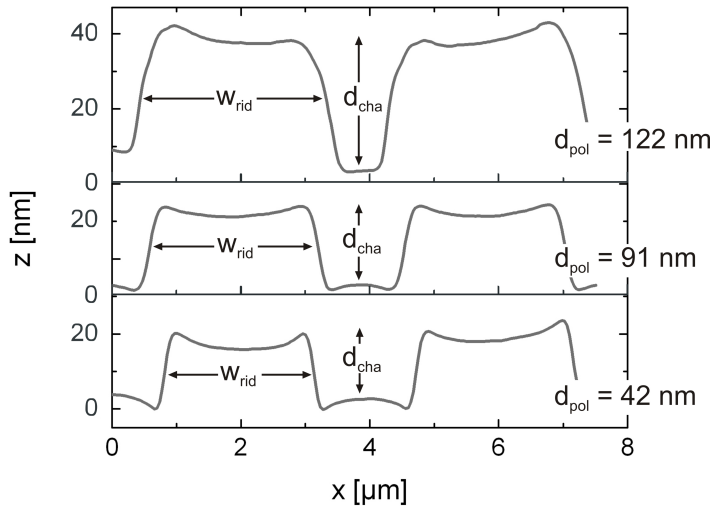


Figure 6.6: Corresponding profile cuts along the illustrated white lines in the AFM data from figure 6.3. A clear trend to an increasing polymer ridge width w_{rid} and an increasing channel depth d_{cha} is observed for thicker films.

channel heights for all samples. However, not only the ridge width, but also the absolute channel depth d_{cha} is tunable via the polymer concentration. In this thesis, the channel depth is always calculated as the difference between medium channel and ridge height. For polymer concentrations of 10, 20, and 26 mg/ml the channel depth increases from 18 to 22 and 33 nm. For all investigated samples, the profile cuts in figure 6.6 also show that the polymer film in the channel structures and on top of the ridges is homogeneous and flattens out almost perfectly with absolute deviations in height below 5 nm. The observed changes in the characteristic ridge width w_{rid} and channel depth d_{cha} make the presented PSIM routine unique. In comparison, the common structuring methods already discussed, NIL (section 2.3.2) and MIMIC (section 2.3.1), result in polymer structures which are given as inverted replica of the applied master structure and therefore require

different structuring stamps for different polymer structures.

6.1.3 GISAXS on structured F8BT films

In addition to the AFM data from figure 6.3, which only provide 3-dimensional sample information restricted to a microscopic sample area, further detailed knowledge of the nano- and microscopic sample structures over larger surface areas is desired. Therefore, again GISAXS was the method of choice (see section 3.7). In the GISAXS experiment, the angle of incidence α_i was set to 0.405° and the impinging X-ray beam had a height of $40\ \mu\text{m}$. In consequence, the total sampling area, which is equal to the footprint of the X-ray beam on the sample, was extended to a distance of almost 6 mm along the x -axis (see also figure 3.5). Thus, the following scattering data allow a real reconstruction of the polymer structures averaged over a macroscopic area. However, a parallel alignment

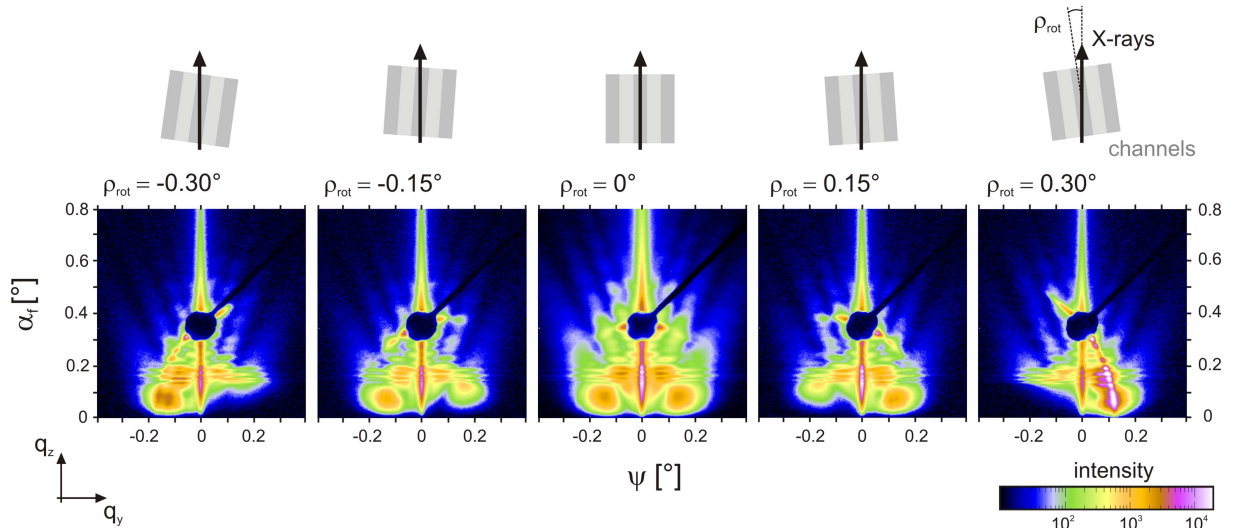


Figure 6.7: GISAXS measurement series of a structured F8BT film ($d_{pol} = 91\ \text{nm}$) probed at different rotation angles ρ_{rot} from -0.30° to 0.30° . For $\rho_{rot} = 0^\circ$ the scattering pattern is perfectly symmetric with respect to the q_z -axis.

of the polymer channels to the incoming X-ray beam is a prerequisite for a symmetric scattering signal, which is hence necessary for an analysis with the IsGISAXS software. In figure 6.7 the GISAXS data of F8BT channels with a film thickness d_{pol} of 91 nm are shown for different channel orientations with respect to the X-ray beam. The rotational angle ρ_{rot} (see figure 3.5) between the channel structure and the impinging X-ray beam is varied in five equidistant steps from -0.30° to 0.30° . For greater clarity of presentation, a sketch of the channel structure and the orientation of the X-ray beam is included on top of each scattering data. It must be pointed out that the sketched rotational angles are illustrated exaggerated in comparison to the actual ρ_{rot} -values added to each GISAXS

measurement. For the center image, the scattering signal appears symmetric and hence the rotational angle ρ_{rot} is set to 0° . Due to the strong influence of only slightly disoriented channel structures on the GISAXS signal, all investigated microstructured samples had to be aligned in ρ_{rot} with an accuracy of 0.01° .

In general, the GISAXS data in figure 6.7 are dominated by three different scattering features: **(i)** inclined truncation rods under various angles, **(ii)** a circular shaped intensity maximum around the specular peak/beamstop, and **(iii)** prominent side maxima at the height of the Yoneda peak.

(i) The preeminent inclined truncation rods result from scattering on inclined surface planes as they are given by the side walls of the F8BT channels (see also AFM profiles in figure 6.6). In general, this feature is independent of the orientation ρ_{rot} of the channels. A closer theoretical interpretation of this feature is given in the following section which focuses on the influence of thermal annealing on such structures.

(ii) The circular intensity maxima around the specular peak is a result of the cut with the Ewald sphere, which was already theoretically discussed in section 2.4.4.[110, 236] Yan et al. have already derived a theoretical prediction for the observed scattering intensity maxima along the Ewald sphere by combining the corresponding mathematical expression with the equation for the maxima of the truncation rods (see equation (2.80)).[109] In addition, they developed a mathematical model to simulate the scattering patterns of slightly misaligned channel structures which also predicted a strong dependence of the scattering image on the channel orientation as observed for the F8BT channels.[109]

(iii) The third prominent feature - the additional side maxima at the position of the Yoneda - is given by the properties of the channel structure. As will be discussed in more detail in the next section, mainly the base angle φ_{cha} , the channel depth d_{cha} , and the ridge width w_{rid} of the channel structure contribute to the diffuse scattering close to the Yoneda maximum. Interestingly, Yan et al. did not observe this feature for channel structures based on silicon - maybe due to a reduced X-ray intensity during their experiment or sharper channel edges.[109]

In consequence it was found that due to the high sensibility of the GISAXS measurements on misalignments in rotational angle ρ_{rot} an accurate sample alignment is absolutely necessary for all GISAXS measurements on structured polymer films (see also figure 6.7).

6.1.4 Thermal treatment of surface structures

As already mentioned, optoelectronic devices based on conducting polymer films generally show improved performances upon thermal annealing. However, for any processing

steps at higher temperatures it has to be taken into account that polymer films undergo plastic deformation if heated above a certain temperature value (section 2.3.2). This actually makes the application of polymer micro- and nanostructures in the field of organic electronics more sophisticated. In order to address the influence of such treatment steps on the fabricated F8BT microstructures, in-situ GISAXS measurements were performed to simultaneously probe the structure evolution during thermal annealing.

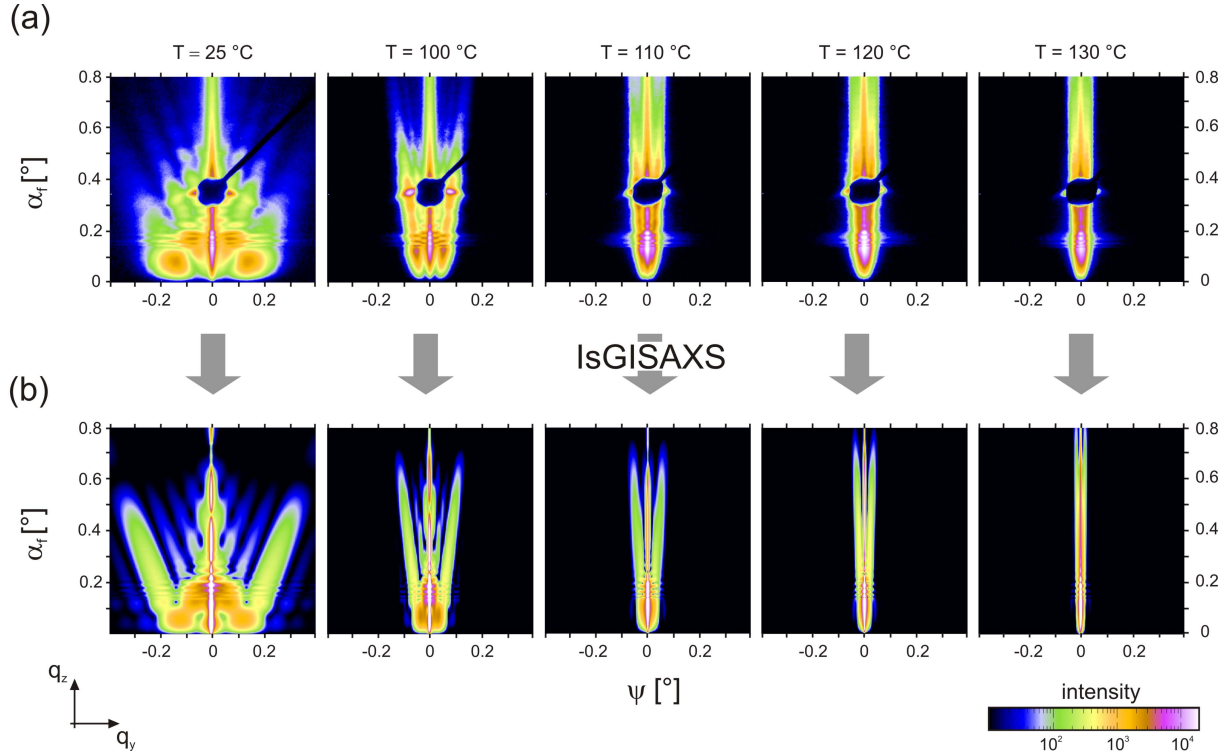


Figure 6.8: GISAXS experimental measurements and the corresponding IsGISAXS simulations: In (a) the GISAXS measurements of a structured F8BT film with a thickness d_{pol} of 91 nm are shown taken at different annealing temperatures (25, 100, 110, 120, and 130 °C). In (b) the corresponding two-dimensional simulations are illustrated. All simulations are based on the DWBA and different models are used, which all consist of anisotropic pyramids with varying base angles and structure heights and widths positioned on the sites of a two-dimensional regular lattice.

In figure 6.8(a) the GISAXS data of a thermally treated structured F8BT film with a film thickness d_{pol} of 91 nm are shown. The sample structures are aligned parallel to the X-ray beam and the annealing temperature is successively increased from 25 to 100, 110, 120 and finally to 130 °C (figure 6.8(a) from left to right). The corresponding IsGISAXS simulations are presented in figure 6.8(b). More experimental details about the annealing routine are given in section 3.7. During thermal annealing, the sample was continuously probed with short-time GISAXS measurements with an integration time of 60 s. These measurements have shown that after an overall waiting time of 30 min at the selected temperatures a constant status of the sample was reached. After 30 min of kinetic sample

evolution, the static GISAXS data from figure 6.8(a) were recorded with an accumulation time of 10 min at each temperature level. Including the short heating times in-between the different selected temperature steps, the sample was kept at each temperature step for 45 min.

For the increasing annealing temperatures the scattering data reveal a clear trend from a broad scattering signal with prominent truncation rods to a more and more featureless scattering intensity image as previously observed for the polymer blend films in chapter 5. The GISAXS data of the F8BT channels at $T = 25\text{ }^\circ\text{C}$ are not only dominated by the three prominent scattering features **(i)** to **(iii)** from the previous section 6.1.3, but also two eye-catching intensity islands are located below the critical angle α_{crit} of the polymer at an out-of-plane angle ψ of -0.12° and 0.12° . The corresponding IsGISAXS simulation from figure 6.8(b) reveal that the position of this scattering feature is mainly given by the base angle φ_{cha} of the simulated channel structure. Since the IsGISAXS simulation software is based on diffuse scattering only, it does not take into account any additional intensity at the specular peak position. As a consequence, all IsGISAXS simulations lack the prominent circular intensity maxima, which are given by the cut of the truncation rods with the Ewald sphere. Despite this lack in scattering intensity, a convincing congruence between the simulated and the measured data is achieved considering the truncation rods and the side maxima. Hence, no further voids due to residual air or water are present either at the polymer-substrate interface after floatation and careful drying of the polymer film (section 6.1.2). The large contrast in refractive index of such interfacial structures would contribute strongly to the scattering pattern. Recently, Rebollar et al. have applied GISAXS to investigate laser-induced periodic surface structures concerning their morphology order over large sample areas.[237] They also used theoretical IsGISAXS simulations to reconstruct their sample topology. However, in the case of Rebollar et al. the gratings miss the high regularity in comparison to the investigated F8BT channels and hence show no prominent truncation rods.

In figure 6.9 the important parameters of the anisotropic pyramids are shown as they were applied in the IsGISAXS simulations for the different annealing temperatures. The base angle φ_{cha} is plotted in respect to the temperature T in figure 6.9(a). For the first temperature step the base angle decreases rapidly from 22 to 6.3° , whereas for the higher temperatures of 110 , 120 , and $130\text{ }^\circ\text{C}$ it only slowly decreases further to 2.6 , 1.8 , and 1.4° . Although taking into account longer time scales, only minor changes in the scattering signal have been observed for temperatures below the critical starting value of $100\text{ }^\circ\text{C}$. In addition, the corresponding values for the channel depth d_{cha} and the ridge width w_{rid} are presented in figure 6.9(b) for the chosen temperatures. For increasing annealing temperatures the simulated channel depths decrease from 38.5 to 25 , 15.1 , 13.3 , and finally to

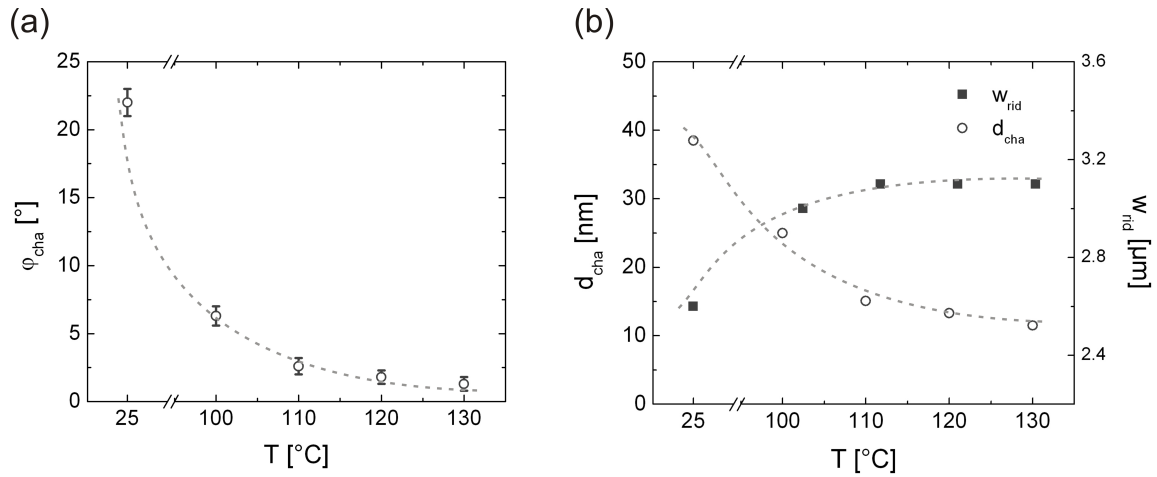


Figure 6.9: Evolution of the channel parameters (see figure 6.2; $d_{pol} = 91$ nm) during thermal annealing extracted from IsGISAXS simulations: In (a) the base angle φ_{cha} of the channel structure is plotted as a function of the annealing temperature T and in (b) the channel depths d_{cha} (open symbols) and the ridge widths w_{rid} (filled symbols) are shown for different temperatures. All values are extracted from the anisotropic pyramids used for the IsGISAXS model systems and the dashed lines act as guides to the eyes.

11.2 nm. Although a flattening of the polymer ridges due to a softening effect at higher temperatures was expected, this dramatic relative change in height of over -70 % definitely surpasses the expectations. On the contrary, the thermal influence on the ridge width w_{rid} is only approximately +19 % if compared to the width of the as-prepared sample. For the temperature increase from 25 to 100 °C the width of the polymer ridges changes from 2.6 to 3.0 μm , before it reaches a constant value of 3.1 μm for higher annealing temperatures. For the untreated structured polymer film the simulated IsGISAXS-value for the ridge width w_{rid} is in good agreement with the results from the AFM data (figure 6.6). However, the simulated values of the channel depth d_{cha} diverge from the topological AFM values, which can be explained by the fact that the actual influence of the channel depth on the simulated scattering signal is minor in comparison to the impact of the base angle and the ridge width. Hence, a larger experimental error in channel depth d_{cha} is likely.

In an additional approach Jones et al. studied the evolution of non-conducting nanoimprinted polymer patterns based on PMMA with critical dimension small-angle X-ray scattering (CD-SAXS).[238] Interestingly, they observed changes in object shape only for temperatures above the bulk glass transition T_g of PMMA. On the contrary, in the case of the investigated F8BT structures the structure evolution already sets in well below the glass transition of F8BT, which is located at 130 °C.[239] Johannsmann and coworkers have also investigated similar imprinted sinusoidal gratings made of PMMA and PS by optical diffraction methods.[240, 241] They have found that the near-surface viscoelastic

behavior of PMMA and PS also depends on the molecular weight of the polymer. As a result, a polymer flow of the investigated channel structures starting at temperatures below bulk T_g is indeed possible. For polymers, structural changes on a molecular level due to annealing temperatures below T_g are generally reversible, whereas modifications at temperatures above T_g are irreversible.

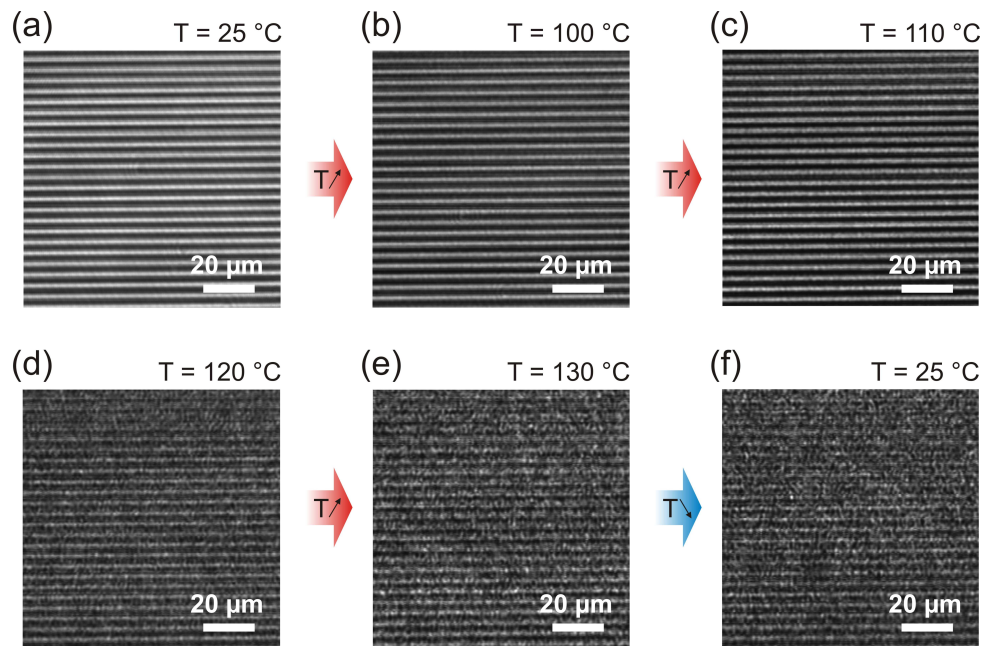


Figure 6.10: In-situ two-dimensional imaging ellipsometry micrographs of a micro-structured F8BT film ($d_{pol} = 91$ nm) during heat treatment: In (a) the as-prepared channel structure is probed and from (b) to (e) the channel structure is measured at different temperature steps: 100, 110, 120, and 130 °C. In (f) the final structure of the annealed sample is measured after cooling down to 25 °C. The imaging ellipsometric measurements shown were performed in-situ with the corresponding GISAXS measurements from figure 6.8.

In comparison to structures made of non-conducting polymers (e.g. PS and PMMA), the investigated surface gratings made of photoactive F8BT have the tendency to additionally form small crystallites upon thermal annealing. Therefore, imaging ellipsometry was used to in-situ probe the development of the F8BT crystals during the temperature treatment (experimental details given in section 3.5). From figure 6.10(a) to (e) the imaging ellipsometry micrographs are shown recorded at the different temperature levels shortly before the next temperature step. Already at 110 °C the F8BT channels start to lose their well-defined structure shape. The observed grainy surface morphology is a good indication for the initiation of the temperature-induced crystal formation. The smoothening and washing out of the channel structure is even accelerated at higher temperatures of 120 and 130 °C. In accordance with the GISAXS measurements, not only the polymer chains crystallize, but also the superimposed artificial microscopic channel structures vanish.

As a consequence, a complex interplay between a polymer flow on the microscale and a molecular rearrangement on the nanoscale takes place during thermal annealing. Only possible due to the combination of both measurement techniques - GISAXS and imaging ellipsometry - it is found that at temperatures below 100 °C mainly polymer flow occurs, whereas at higher temperatures polymer crystallization hampers the polymer flow. In addition, both techniques show no further topological changes during cooling of the sample down to room temperature (figure 6.10(f)).

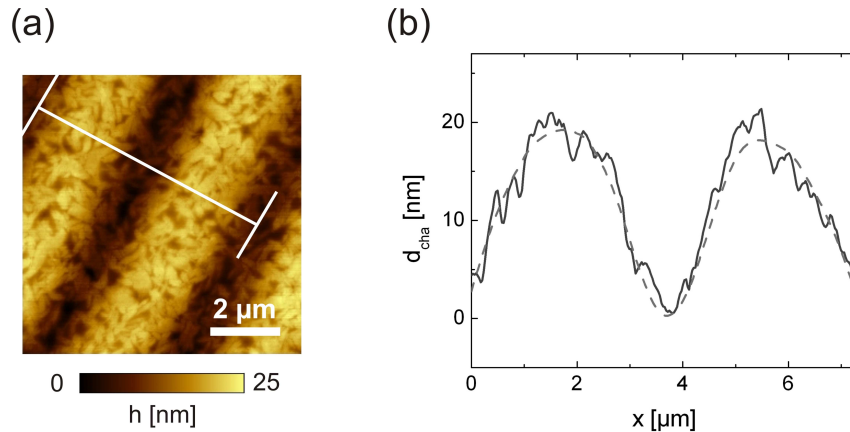
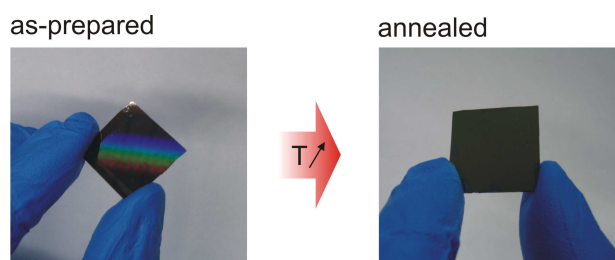


Figure 6.11: Surface topography analysis of an annealed structured F8BT film with a film thickness d_{pol} of 91 nm: In (a) the AFM topography data are shown and the white line illustrates the direction of the profile plot, which is plotted in (b). The solid line depicts the line profile cut of the annealed channel structure and the dashed line illustrates the channel shape integrated over 2 μm implying a sinusoidal surface of the annealed sample.

Nevertheless, within the optical resolution of the applied imaging ellipsometry set-up (section 3.5) a closer investigation of the spatial properties of the polymeric crystals is not possible. Therefore, the topographical AFM data of a thermally annealed structured sample with a polymer film thickness d_{pol} of 91 nm are shown in figure 6.11. The topography data clearly indicate a strong formation of F8BT crystals, which are homogeneously distributed over the sample surface and show no preferential crystallization between or on top of the channel structure. The actual size of the crystals is on a mesoscopic length scale and hence small in comparison to the fabricated channel size. For an enhanced illustration, the corresponding line profile cut taken along the illustrated white line from figure 6.11(a) is plotted as a solid line in figure 6.11(b). The included dashed line corresponds to a smoothed profile, which is integrated over 2 μm perpendicular to the direction of the line cut. The profile cuts reveal surface depressions of up to 6 nm due to the crystal formation. Coming back to the GISAXS experiments from above, it is known that high surface roughness values increase the diffuse scattering (see also section 5.1). [242] Unfortunately, such high roughness values as observed in the AFM data could

not be implemented successfully to the applied IsGISAXS models. Hence, the differences in actual and simulated surface roughness explain the lack of scattering intensity around the Yoneda peak in the IsGISAXS simulations from figure 6.8. However, a tangential fit to the obtained integrated profile cut in figure 6.11(b) reveals a gradient angle of around 1.1° , which is in good agreement with the equivalent base angle φ_{cha} of the simulated channel structure (shown in figure 6.9(a)). Since the formation of the mesoscopic crystallites turned out to reduce the polymer flow, still slight channel superstructures are present after annealing at temperatures around glass transition.

Figure 6.12: Picture of as-prepared and thermally annealed F8BT channels: Due to the post-production heat treatment the optical grating effect is lost. Both pictures were taken under comparable conditions.



From a macroscopic point of view the fabricated channel structures are also interesting for optical gratings. In figure 6.12, pictures of the as-prepared F8BT channels with a polymer thickness d_{pol} of 91 nm (left) and the corresponding thermally annealed sample (right) are presented. Both pictures were taken under similar conditions (angle of observation approximately 30° in respect to the sample normal). The as-prepared channel sample shows a strong optical grating effect, which results in the prominent rainbow spectrum due to wavelength dependent constructive light reflections at varying angles of incidence. On the contrary, thermal annealing leads to a flattening of the F8BT channels and hence to a complete loss of the optical grating properties. Nevertheless, this optical property always acts a quick and easy macroscopic measure of the imprinting success - also for the following structuring routines.

To briefly summarize the results of this section, a new structuring routine was introduced which allows for the fabrication of polymer structures on top of a homogeneous polymer support without requiring any high temperature steps. The thickness d_{pol} of the homogeneous underlayer can be easily controlled via the polymer concentration in solution and the properties of the surface structures can be modified without changing the master structures. Moreover, GISAXS measurements have shown that channel structures have to be aligned in parallel to the X-ray beam at a high precision in order to achieve analyzable symmetric scattering data. However, the most important result for the following sections is that a structuring of the active layer is not appropriate to introduce additional optical and/or electrical benefits to organic solar cells. Due to the softening properties of the polymer at elevated annealing temperatures, the structure shape is not preserved.

As a consequence, for application in organic solar cells, an additional structuring routine has to be found in order to fabricate structured devices which persist thermal annealing steps.

6.2 Film thickness controllable wet embossing

The results discussed in the previous section 6.1 have clearly shown that structuring the photoactive layer in an optoelectronic device is not appropriate, since such textured layers do not persist in shape upon thermal annealing. In consequence, a different idea which is novel in the field of OSCs will be put into focus in this section. Instead of directly structuring the active layer, the intermediate PEDOT:PSS layer is addressed by applying a new imprinting technique. For an improved understanding, figure 6.13 shows an illustrative sketch of possible optical light diffraction effects as they occur in an OSC with (a) an imprinted active layer and (b) a textured PEDOT:PSS interface.

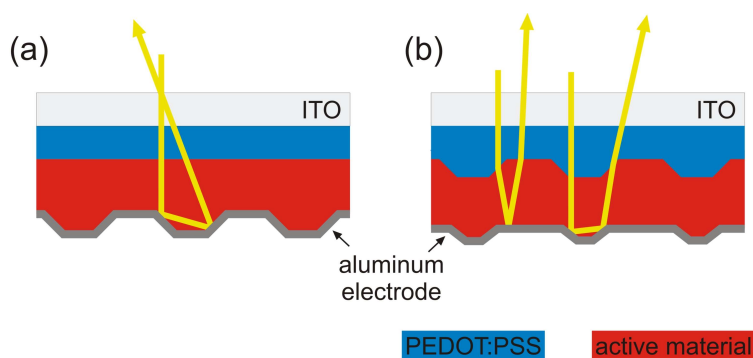


Figure 6.13: Illustration of light trapping effects in structured organic solar cells with (a) a textured active layer and (b) an imprinted PEDOT:PSS electrode.

In both cases presented in figure 6.13, the modified surface of the aluminum electrode leads to a reflection of the incoming light at varying angles and hence results in longer optical pathways within the photoactive layer. Since typically PEDOT:PSS and conducting polymers have different optical refractive indices, an additional part of the impinging light is also refracted at the textured interface between PEDOT:PSS and active material. In comparison to the prior approach of structuring the active layer, the key improvement of this idea is that PEDOT:PSS has no specific glass transition temperature T_g . PEDOT:PSS structures are therefore stable upon thermal annealing at temperatures commonly applied to organic devices (between 100 and 200 °C). However, this also means that standard imprinting methods such as NIL cannot be used due to the absent thermal softening effect for PEDOT:PSS. In consequence, the fabrication of structured PEDOT:PSS layers, especially in combination with a homogeneous substrate coverage, is complex and has not been investigated yet.

In this section, a structuring routine (section 6.2.1) based on a novel mold material (section 6.2.2) is introduced and its application possibilities for structured PEDOT:PSS films (section 6.2.3) are illustrated. The influence of such structured PEDOT:PSS films on the optical properties of spin cast F8BT:P3HT polymer blend films is investigated in section 6.2.4. Finally, the impact of the structured PEDOT:PSS electrodes on the performance of P3HT:PCBM solar cells is discussed in section 6.2.5. Since in this thesis for all OSCs

ITO substrates have been used, the transparent electrodes consist in a correct way of PEDOT:PSS and ITO. However, in the following sections the electrode is simplified as PEDOT:PSS electrode.

6.2.1 Structuring routine

In order to fulfill the demand of large area polymeric microstructures at low costs and under reproducible conditions, new and simple ways to fabricate microstructures have to be developed. One possible approach is the MIMIC method, which has already been discussed (see section 2.3.1).[78] This routine belongs to the group of soft lithography, along with other methods like microcontact-printing [243] or replica-molding [244], and it has great advantages: no exposure to high-energy radiation, fabrication at low-costs, and a direct replication of the master structures. Since many novel conducting polymers are sensitive to temperature and pressure, this method, based on solution casting principles, is also very well suited for organic microstructured devices. As previously mentioned in section 6.1, for such devices a homogeneous substrate coverage by the polymer is absolutely crucial in order to fully utilize the material properties. However, the standard MIMIC approach does not allow for polymer structures on top of a continuous polymer layer.

Therefore, in the framework of this thesis the following imprinting routine is introduced, which combines the principles of MIMIC with the advantages of a semi-flexible mold as a cost effective alternative to other imprinting techniques. It is based on wet embossing principles and therefore abbreviated as *WEMB* (**W**et **E**mbossing). The material of choice is a commercially available mold made from bisphenol-A-polycarbonate (PC), whose advantages are discussed in more detail in section 6.2.2. In figure 6.14 the schematic procedure of the WEMB routine is illustrated. The PC mold has to be leveled out accurately (figure 6.14(1)) and a defined amount of polymer solution, which depends on the solvent type, the polymer concentration, and the substrate material, is spread on the master (figure 6.14(2); specific values for the following examples are given in each section). In the following step (3), a solid substrate is gently put on top of the solution so that a homogeneous layer of solution is sandwiched between substrate and mold. During the solvent evaporation step (figure 6.14(4)), an external pressure P_{wet} is applied to control the total polymer film thickness d_{wet}^{tot} , which is given by the height of the polymer structures and the homogeneous polymer layer underneath (more details are found in section 6.2.3). For this step, additional weights with a size larger than the actual substrate are used to guarantee uniform imprints. Mechanical weights have the advantage of regulating the changing substrate height during solvent evaporation automatically and hence result in a constant pressure. The time necessary for the imprinting process can be controlled

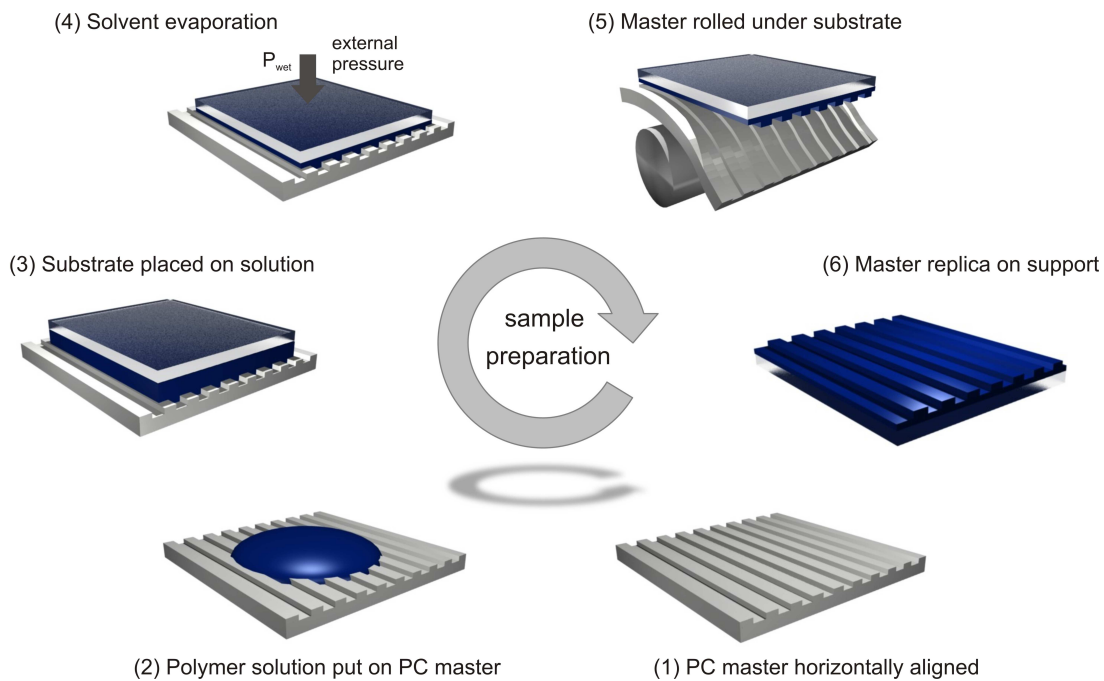


Figure 6.14: Schematic overview of the WEMB routine: (1) The master mold is positioned horizontally and (2) coated with polymer solution. (3) The substrate is gently put on top and (4) an additional pressure is applied during solvent evaporation. (5) For the lift-off, the master is bent beneath the substrate and leaves a structured polymer film on the substrate.

by different environmental conditions such as the surrounding solvent vapor pressure or a change in temperature. For the following examples, the imprinting was performed in a leveled out closed container (relative humidity of $RH = 70\%$) for 48 to 96 hours. After the solvent completely evaporated and the mold structures were filled perfectly with solid polymer, the lift-off takes place. Therefore, in step (5) the master is bent beneath the substrate and leaves a uniformly structured polymer film on the solid support (illustrated in final step (6) of figure 6.14). For the lift-off it is important to mention that a perfect structure transfer from master to polymer is only possible for systems which allow a stronger surface adhesion of the dry polymer film to the applied substrate than to the master mold. In the framework of this thesis, different polymers have shown that PC in combination with standard silicon or glass substrates typically fulfill this restriction.

Besides applying PC as the mold material, the main novelty of this wet embossing routine is the inverted design orientation in comparison to the standard MIMIC-process, in which the master is put on a support and the polymer solution is spread around its edges. In this approach, the mold with the desirable inverted structure is covered with polymer solution and the substrate is placed upside-down on the solution covered mold. By actually changing the order of the mold and the support - support on mold instead of mold on support - a continuous polymer layer underneath the microstructures is installed and in

addition, its thickness can be tuned (see also section 6.2.3). Moreover, the gravitational force of the substrate supports the capillary forces so that the mold channels completely fill with solution. This is necessary for the polymer structures so that they develop during solvent evaporation. The inverted experimental set-up also guarantees a steady material support from the underlying solution layer, which also facilitates a thorough filling of the mold structures and hence a perfect replication of the master structure. However, especially for molds with nanoscopic structure features, good wetting properties and a low viscosity of the polymer solution are desired to assure a complete filling of the mold structures. An inverted approach based on a novel stamp material was already applied to inorganic oxide structures which always required a posterior high temperature annealing step to convert the oxides into their respective crystalline forms.[245]

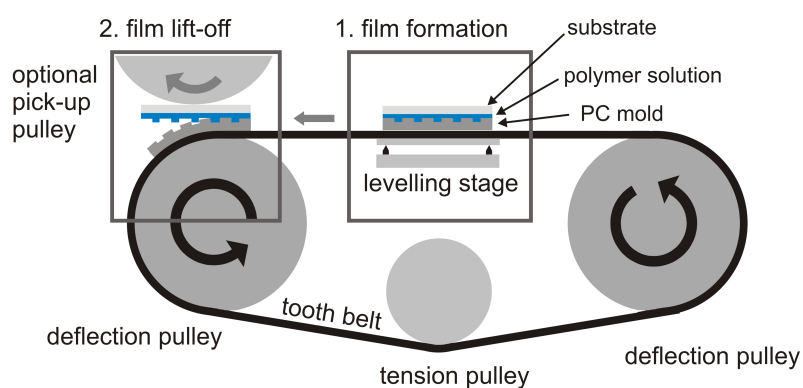


Figure 6.15: Schematic illustration of a batch-processing device for structured polymer films according to the WEMB routine: During the film formation (see box 1) the sample is supported by an additional leveling stage. For the actual sample lift-off (see box 2) the master structure is bent along the curvature of the deflection pulley.

The straight fabrication procedure from figure 6.14 makes this approach also appropriate for a possible application in roll-to-roll fabrication of structured organic materials [246] as it has been already realized on flexible PET substrates by nanoimprint lithography.[247] Therefore, figure 6.15 shows a schematic illustration of a lab-scale fabrication device as it was used for the WEMB routine. The set-up includes two identical deflection pulleys with a diameter of 130 mm and an additional tension pulley, which is needed for a strong tension of the tooth belt and hence a good alignment of the master mold. The PC master structure is mounted on the metal-reinforced rubber tooth belt simply by sticking or screwing. To accurately level out the master structure, the set-up is equipped with a leveling stage, on which the sample remains during the solvent evaporation process (figure 6.15, box 1). For the actual sample lift-off, the master is moved towards the deflection pulley by rotation and due to the bending of the master structure along the curvature of the deflection pulley the sample substrate is automatically separated from

the mold. In this thesis, a rotational speed of the deflection pulley of around 10 deg s^{-1} was appropriate for a successful substrate lift-off. This corresponds to a processing speed of 40 m h^{-1} for this fabrication step. Afterwards the sample could be easily picked up, for example with an optional pick-up pulley and transported to a following production step (figure 6.15, box 2). An additional advantage of this self-made set-up is that it guarantees constant and homogeneous peel-off conditions. Besides a precise control of the environmental conditions (temperature and humidity) and the applied external pressure, constant lift-off conditions are mandatory to achieve high reproducibility rates.

6.2.2 PC master molds

For the already existing different imprinting techniques, generally molds based on PDMS are state-of-the-art. However, PDMS stamps struggle with the disadvantage of being elastic under pressure (see section 4.2). Due to this, stiff inorganic molds produced from silicon, fused silica or amorphous metals still allow for the smallest imprint patterns with sizes down to approximately 10 nm .^[248] However, such hard master molds usually lack homogeneous imprints over large areas if applied via NIL. As a consequence, a new class of rigiflex lithography was introduced in order to bridge the gap between hard and soft lithography, combining the advantages of both methods: high resolution and good flexibility.^[249] Unfortunately, the fabrication of such rigiflex bilayer master structures is rather complicated and hence does not meet the desire for a low-cost sample production. Therefore, in this thesis bisphenol-A-polycarbonate (PC) is used as the mold material. In comparison to PDMS, PC has a higher Young's modulus and a higher T_g (the precise values are given in section 4.2). Since the polymeric structures develop from solution, it is important that PC shows a good resistance against various chemicals such as diluted acids, alcohols, halogenated hydrocarbons, and water. The high stiffness of PC in combination with its known capability of undergoing plastic deformations by keeping its original shape, further supports the idea of using PC as a mold material for lithographic approaches. Since PC is a standard material for thermal nanoimprinting of nanoscopic structures with an excellent structure transfer and at high replication fidelities, structure molds made of PC can be easily fabricated.^[166] Concerning the longtime stability of such PC master molds, it was recently reported that a high elastic modulus of the master structures also increases their reusability for multiple imprinting processes.^[250] Although the following examples are based on PC molds with a total thickness of 1.2 mm , thinner master structures with a thickness of only 0.2 mm have been applied successfully as well.

In figure 6.16(a) the topological AFM data of such an applied PC mold are shown and in (b) the corresponding profile cut is illustrated, which was taken perpendicular to the channel structures and averaged over a width of $1 \text{ }\mu\text{m}$ (according to the white line in

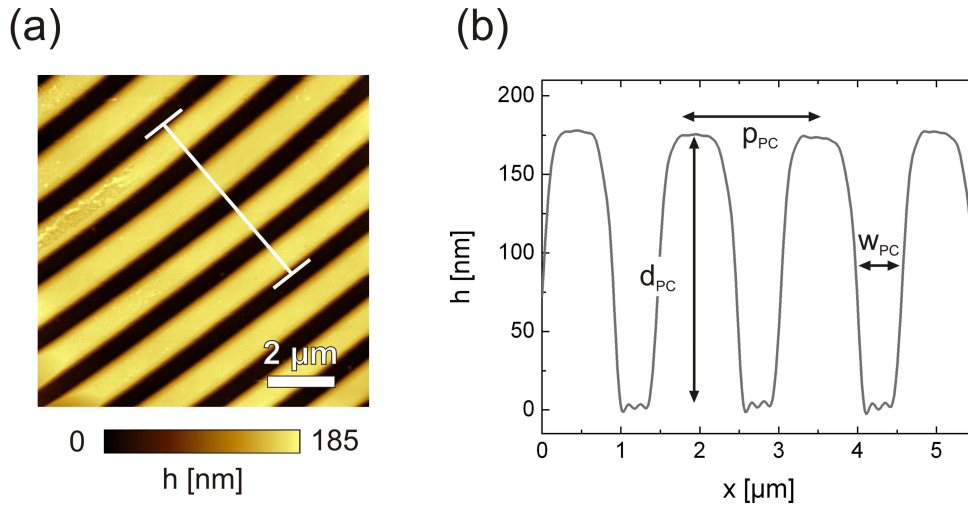


Figure 6.16: (a) AFM topography data of a PC master mold and (b) the corresponding profile cut, which was taken perpendicular to the channel structure (see white line in (a)) and averaged over a width of $1 \mu\text{m}$. The PC mold is characterized by the channel depth d_{PC} , the channel width w_{PC} , and the periodicity p_{PC} . The measurement was performed with AFM-2 (see section 3.2).

figure 6.16(a)). The PC molds reveal periodic channels with an average channel width w_{PC} of $0.6 \mu\text{m}$ and a periodicity p_{PC} of $1.6 \mu\text{m}$. The channel depth d_{PC} is found to be 175 nm . For the imprinting process the master mold was cut to a size of at least $30 \times 30 \text{ mm}^2$, which is larger than the actual substrate size of $20 \times 20 \text{ mm}^2$. Additional AFM measurements in combination with supplementary optical microscopy data show a high grating quality over a large mold area.

6.2.3 Structured PEDOT:PSS films

Patterned PEDOT:PSS anodes with very large channel structures of $100 \mu\text{m}$ have been already fabricated via a wet embossing technique based on a PDMS mold and have been used for polymer light emitting diodes.[251] In a complex and time consuming multi-step photolithography approach, which utilized novel and non-commercially available photoresists, Taylor et al. managed to fabricate textured PEDOT:PSS electrodes with submicron structure sizes.[252]

As mentioned above, the surface adhesion of the polymer to the substrate is a key parameter for homogeneous imprints according to the WEMB routine. Also, the wetting properties of the polymer solution to both interfaces are important to guarantee a full coverage of the substrate and a sufficient filling of the mold structures. Therefore, the contact angles θ_{con} between the PEDOT:PSS solution and the different substrates are an appropriate measure: $\theta_{con}(\text{glass}) = 8^\circ$, $\theta_{con}(\text{PC}) = 91^\circ$, and $\theta_{con}(\text{PC}_{mold}) = 92^\circ$. The contact angles were measured on a dataphysics Contact Angle System OCA (Filderstadt,

Germany). The small contact angle between the PEDOT:PSS solution and the acidic pre-cleaned solid support proves a complete substrate coverage that hence favors a uniform polymer layer underneath the imprinted structures. On the contrary, the high contact angle of the PEDOT:PSS solution on the PC mold implies only small capillary forces. Therefore, a full channel filling is not likely without any additional pressure.

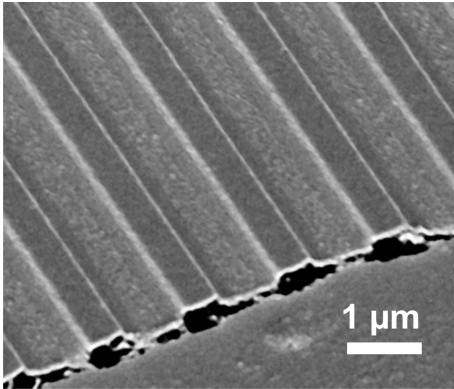


Figure 6.17: Side view SEM image of gold coated PEDOT:PSS channels: Underneath the surface structures a homogeneous polymer layer with a film thickness around 75 nm is revealed.

In organic electronics the intermediate PEDOT:PSS is irreplaceable as an electron blocking or hole injecting layer. In addition, it prevents short-circuit faults between the bottom and the top electrode. Thus, for the investigated PEDOT:PSS, good wetting properties to the substrate and hence a full surface coverage are especially crucial. In figure 6.17 a scanning electron microscopy (SEM) image of a fabricated PEDOT:PSS channel structure with an overall film thickness of 250 nm is shown, which was tilted by 50° during imaging. To enhance the contrast, a thin gold layer was evaporated vertically on the PEDOT:PSS structures and clearly reveals a homogeneous polymer coverage. For all wet embossed PEDOT:PSS films discussed in this section, the polymer solution was directly filtered on the PC mold (PTFE-filter, pore size = 5 μm) and a volume of approximately 0.25 ml was used for a standard substrate size of 20 x 20 mm². From additional AFM data (presented later in figure 6.20(a)), it is known that the imprinted channels have a height of 175 nm and therefore the homogeneous layer thickness is found to be around 75 nm (figure 6.17). It is important to note that also the area between the fabricated structures is coated with a smooth PEDOT:PSS film.

In any organic optoelectronic application, a distinct control of the PEDOT:PSS film thickness is crucial in order to e.g. induce possible thin film interference effects.[253] In figure 6.18(a) the total film thickness d_{wet}^{tot} of the structured films (given by the sum of structure height and homogeneous polymer underlayer) is plotted with respect to the externally applied pressure P_{wet} during the solvent evaporation step (see step (4) in figure 6.14). Interestingly, an increasing film thickness d_{wet}^{tot} is observed for an increasing pressure P_{wet} . A possible explanation for this counterintuitive dependence can be drawn upon a higher and pressure induced degree of entanglement between the polymer chains. Therefore, it

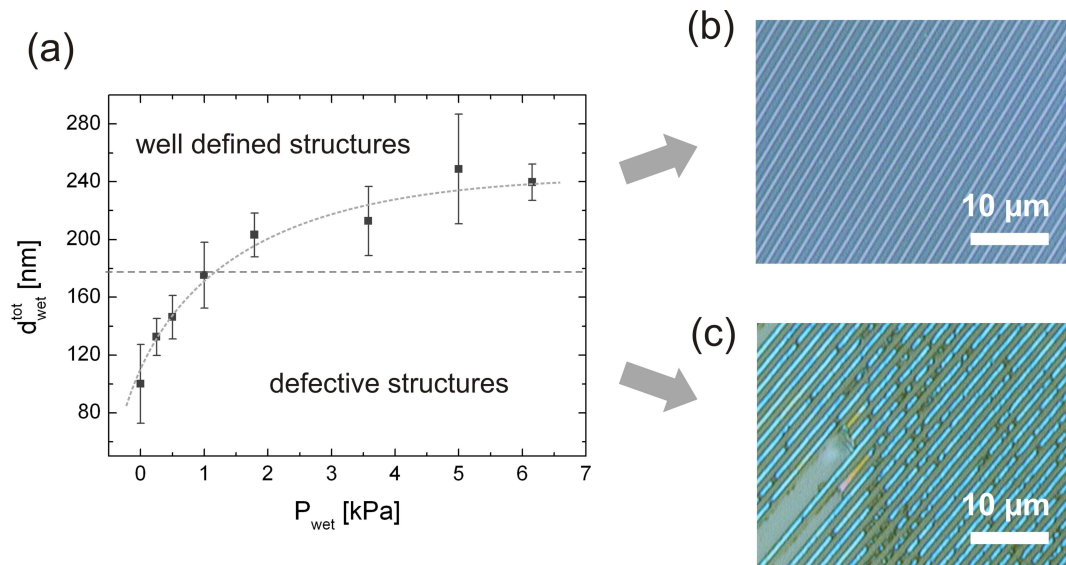


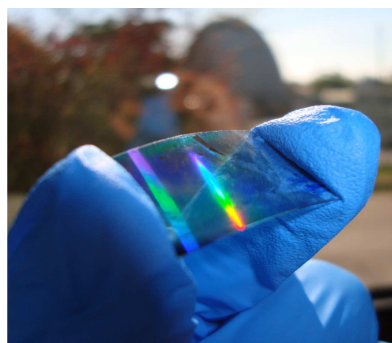
Figure 6.18: In (a) the overall film thickness is plotted in respect to the applied external pressure P_{wet} during wet embossing. The optical microscopy image in (b) reveals perfect channel structures for $d_{wet}^{tot} > 175$ nm and in (c) incomplete channel structures for thinner films. For all samples the aqueous PEDOT:PSS concentration was constant at 0.5 wt% PEDOT and 0.8 wt% PSS.

can be speculated that during the elongated evaporation step a more entangled and denser polymer network might hinder the diffusion of polymer chains to the substrate edge. In consequence, only the smaller solvent molecules can diffuse and the bulky rodlike polymer chains remain trapped within substrate and mold. For higher pressures this effect appears to be increased and hence results in thicker polymer films up to a saturation at around 240 nm.

For the fabrication of actual structured devices, it is more relevant that also the quality of the imprinted channel structures is directly linked to the total film thickness. It has been observed that for PEDOT:PSS films with d_{wet}^{tot} below 175 nm, which actually corresponds to the depth d_{PC} of the mold structures, the imprinted structures are incomplete, whereas for thicker films the imprints are homogeneous. Whereas in figure 6.18(b) an optical micrograph image of a successful structure transfer is shown, a defective film is illustrated in figure 6.18(c). Thin films reveal fractured channel structures, which only partially cover the substrate. A homogeneous polymer film in between the imprinted structures (as observed in figure 6.17) is not present and the obtained channel structures are freestanding. The missing parts of the polymer channels remain attached to the master mold during the lift-off. Besides the given film thicknesses from figure 6.18, PEDOT:PSS films with a further increased overall film thickness of up to 1 μm were also fabricated with modified polymer concentrations.

Always keeping in mind that one of the key advantages of organic electronics lies in

Figure 6.19: The wet embossing routine is also applicable to flexible PET substrates covered with ITO and the fabricated PEDOT:PSS grating shows an optical grating effect (see also figure 6.12).



their mechanical flexibility, figure 6.19 proves that the WEMB approach is not limited to solid supports but can also be applied on flexible PET foils covered with ITO. A similar rainbow spectrum due to the optical grating effect, which was already observed for the F8BT channels in figure 6.12, is also seen for the PEDOT:PSS channels.

In general, PEDOT:PSS channel structures were successfully imprinted up to an overall size of $20 \times 30 \text{ mm}^2$ according to the wet embossing method. Since for all experiments the sample area was only limited by the mold size, larger substrates can be imprinted as well using the same technique with large-area molds.

6.2.4 P3HT:F8BT films on wet embossed PEDOT:PSS

For the application of such structured PEDOT:PSS films in actual devices the impact of the PEDOT:PSS channels on the photoactive layer regarding its surface morphology is important.

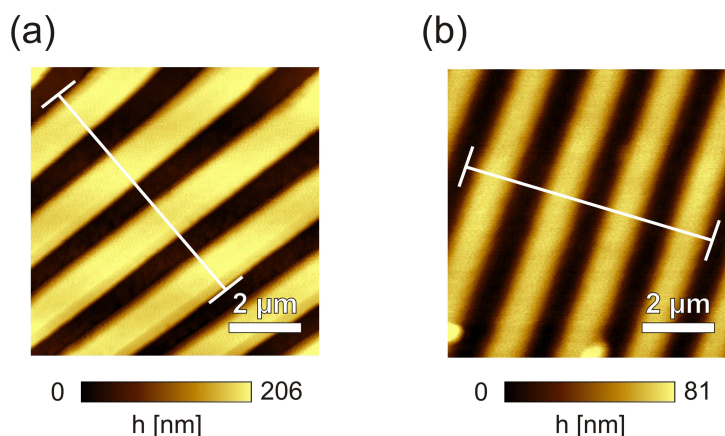


Figure 6.20: AFM data of (a) pure wet embossed PEDOT:PSS grating and (b) coated with a photoactive P3HT:F8BT blend. The white lines correspond to the profile lines which are shown in figure 6.21. The measurements were performed with AFM-3 (section 3.2).

In figure 6.20(a) the AFM data of a wet embossed PEDOT:PSS grating are shown, which

was made from a similar master mold as depicted in figure 6.16 with slightly different parameters in periodicity ($p_{PC} = 2 \mu\text{m}$) and channel width ($w_{PC} \approx 1 \mu\text{m}$). The shape of the channel structure is characterized by a width of the PEDOT:PSS ridges of $1.2 \mu\text{m}$, a periodicity of $2 \mu\text{m}$, and a total height of 175 nm . The shape of the channels is well-defined and the surface of the PEDOT:PSS in the channels and on top of the ridges appears flat. However, the wet embossed PEDOT:PSS films have a relatively high R_{rms} surface roughness value of 4.4 nm , which is due to the imprinting with the PC mold. In figure 6.20(b) the PEDOT:PSS grating is coated with a polymer blend consisting of P3HT and F8BT (type-II, more details in table 4.1 from section 4.1.2). For this sample, both polymers were dissolved in chloroform at a concentration of 7 mg/ml and blended at a ratio of 1:1. The blend film has a thickness of approximately 75 nm if spin cast on an acidic pre-cleaned silicon substrate. It is clearly visible that in comparison to the pure PEDOT:PSS channels, which show a well-defined surface morphology, the photoactive layer on top exhibits a more sinusoidal topology.

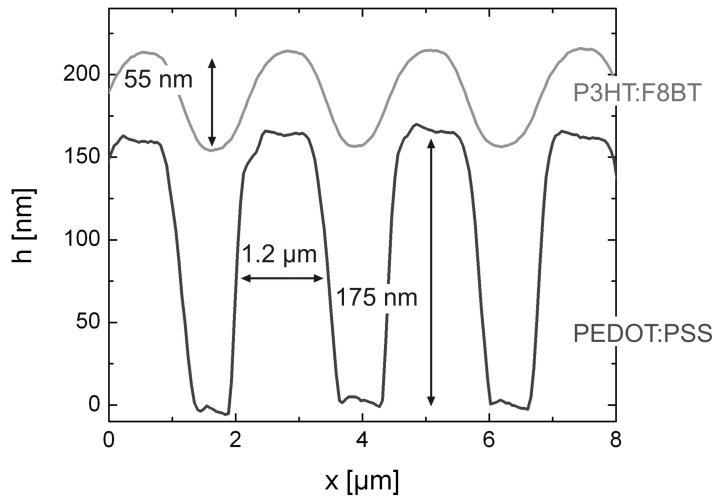
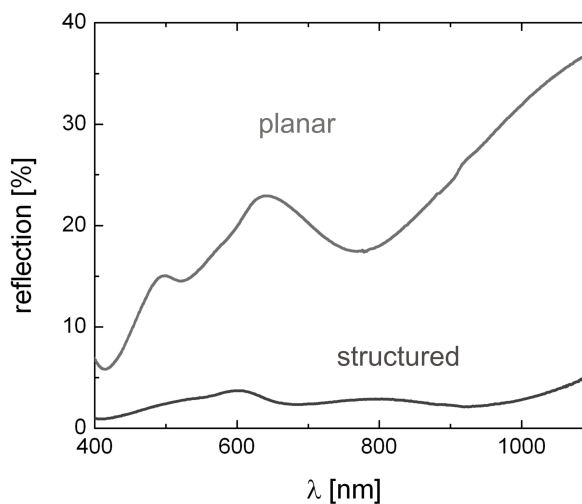


Figure 6.21: Topography profile lines to the corresponding AFM data in figure 6.20 taken perpendicular to the channel structure and averaged over $1 \mu\text{m}$. The profile of the pure channels is depicted as the dark line and the surface of the coated sample as the light line. For clarity in presentation, the profile of the coated PEDOT:PSS channels (light line) is shifted along the y - and x -axis in order to match the actual film architecture.

For an improved illustration of the surface properties, figure 6.21 depicts the corresponding profile cuts of the uncoated and the coated PEDOT:PSS channels from figure 6.20. Both profile lines are taken perpendicular to the channel structure and averaged over a width of $1 \mu\text{m}$ (according to the white lines in figure 6.20). Whereas the pure PEDOT:PSS ridges have a mean height of 175 nm (dark line), the peak-to-valley distance is reduced to 55 nm for the active layer (light line). The periodicities of both surface morphologies are identical, and the shape and the height of the photoactive polymer structures are tunable via the polymer concentration. In order to illustrate the actual film architecture, the distance between the two profile lines was extracted from different optical absorption measurements (more details on this approach are given in the following section). Similar wavy surface modifications, which were achieved by Na et al. via directly applying

NIL, already led to an improved overall power conversion efficiency of polymer:fullerene OSCs.[233] Also the structured F8BT films according to the PSIM routine (see figure 6.12) and the uncoated wet embossed PEDOT:PSS gratings (figure 6.19) have already shown prominent optical grating effects, which are interesting for photoactive applications as indicated by the sketch in figure 6.13. Concerning organic solar cells, mainly light diffraction at the different interfaces is favorable since it elongates the optical path length within the active layer.

Figure 6.22: Optical reflection spectra of P3HT:F8BT polymer blend films spin cast on planar (light line) and structured (dark line) PEDOT:PSS films.



Therefore, the optical reflection of a P3HT:F8BT blend film spin cast on a planar (light line) and a wet-embossed PEDOT:PSS electrode (dark line) was investigated (figure 6.22). In both cases, the reflection was measured along the sample normal. It is found that the overall reflectivity is strongly reduced, which is a reliable indication for a strong light diffraction, since only the light which is reflected along the sample normal is detected (see section 3.4). Besides the overall reduction in reflected intensity, also additional spectral reflection characteristics are introduced due to the defined wavy surface morphology. In order to investigate the impact of such wet embossed PEDOT:PSS electrodes on the performance of OSCs, devices based on P3HT:F8BT have been fabricated. However, the prepared solar cells showed too low overall power conversion efficiencies in order to allow for concrete conclusions ($\eta(\text{P3HT:F8BT}) \approx 10^{-7} \%$). In consequence, this open question is addressed in more detail in the following section making use of more efficient polymer:fullerene solar cells.

6.2.5 OSCs based on wet embossed PEDOT:PSS films

Although solar cells made of P3HT and PCBM have become a standard system for organic photovoltaics in the meantime, they are still among the most investigated types and

have already led to power conversion efficiencies of up to 5 % in case of fully optimized fabrication conditions.[152, 254] For an improved understanding of the influence of wet embossed PEDOT:PSS electrodes on the electrical properties of organic solar cells, this widely discussed system is also applied in this section. For the active layers, P3HT was dissolved at a concentration of 33 mg/ml in dichlorobenzene (DCB) before PCBM was added at a concentration of 27 mg/ml. This polymer concentration leads to homogeneous blend films with a thickness of 165 nm if spin cast on acidic pre-cleaned glass substrates.

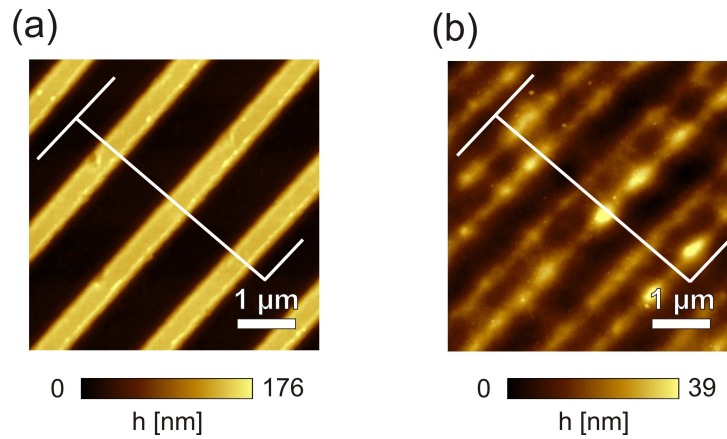


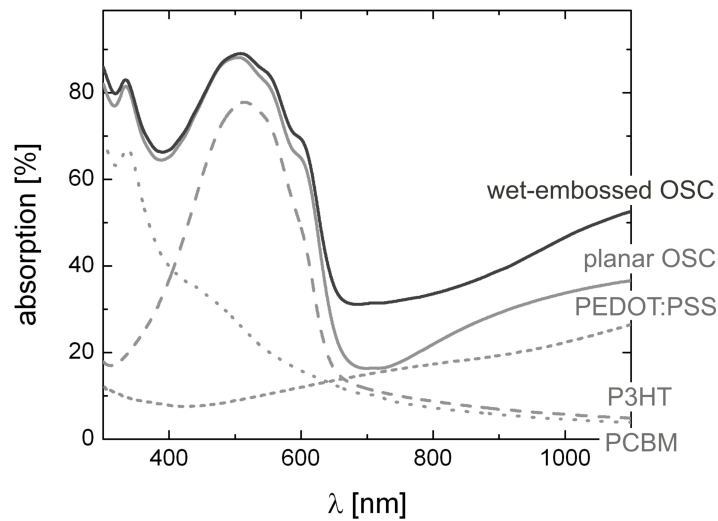
Figure 6.23: AFM topography data of (a) the pure wet embossed PEDOT:PSS grating with a PC mold, as shown in figure 6.16, and (b) coated with a P3HT:PCBM blend film. The white lines correspond to the profile cuts which are shown in figure 6.25. The measurements were performed with AFM-2 (section 3.2).

In figure 6.23(a) the AFM topography data of a wet embossed PEDOT:PSS film with a polymer ridge width of $0.6 \mu\text{m}$, a periodicity of $1.6 \mu\text{m}$, and a maximum structure height of around 175 nm are shown (more details on the surface dimensions are given below). In comparison to the previously investigated P3HT:F8BT film, which revealed a sinusoidal surface morphology (see figure 6.20(b)), the topology of the P3HT:PCBM film has a more complex double peak structure if spin cast on the PEDOT:PSS grating (figure 6.23(b)). It is likely that this effect is attributed to the higher initial film thickness d of the P3HT:PCBM film ($d(\text{P3HT:PCBM}) = 165 \text{ nm}$ vs. $d(\text{P3HT:F8BT}) = 75 \text{ nm}$), which also leads to a better filling of the channel structure during the spin coating process.

However, a crucial point for a later application of the PEDOT:PSS structures is the impact on the optical absorption of the photoactive layer. The UV/Vis spectra of P3HT:PCBM films spin cast on a planar (light solid line) and a wet embossed (dark solid line) PEDOT:PSS film are shown in figure 6.24. For better understanding, the absorption spectra of pure PCBM (light dotted line), pure P3HT (light dashed line), and of planar PEDOT:PSS (light short dashed line) have also been included.

It is found that the absorption at short wavelengths ($\lambda < 400 \text{ nm}$) is mainly attributed

Figure 6.24: UV/Vis absorption spectra of P3HT:PCBM blend films spin coated on wet embossed (dark line) and planar (light line) PEDOT:PSS films. For an improved understanding also the pure absorptions of P3HT (long dashed light line), PCBM (dotted light line), and PEDOT:PSS (short dashed light line) are included.



to PCBM, whereas the main absorption maximum of the blend film at 500 nm is due to the absorption of P3HT. Optical absorption at wavelengths above 700 nm is dominantly assigned to parasitic absorption of PEDOT:PSS that does not contribute to the efficiency of the OSC. However, the most important finding in the UV/Vis spectra is that spin coating of the active P3HT:PCBM layer on wet embossed PEDOT:PSS electrodes results only in a slightly increased optical absorption. Since the ratio of the maximum absorption values of the PCBM- and the P3HT-peak remains unchanged, this measurement also reveals an unmodified film composition if spin coated on a structured PEDOT:PSS film. As a consequence, the overall amount of the material on the textured PEDOT:PSS film is approximately equal to the one on the planar film and the applied wet embossed PEDOT:PSS electrodes do not result in an increased optical absorption if measured in transmission.

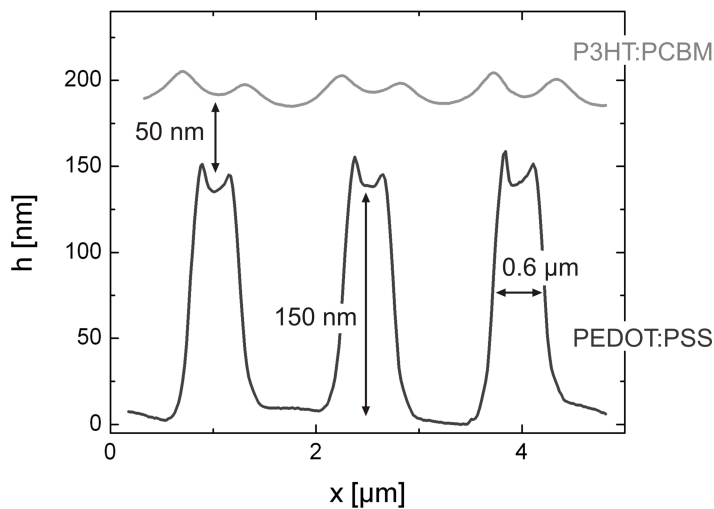


Figure 6.25: Topography profile lines to the corresponding AFM data from figure 6.23 taken perpendicular to the channel structure and averaged over 2 μm . The profile of the active layer (light line) is shifted by a distance of 50 nm above the pure channel profile (dark line), which then corresponds to the actual film architecture.

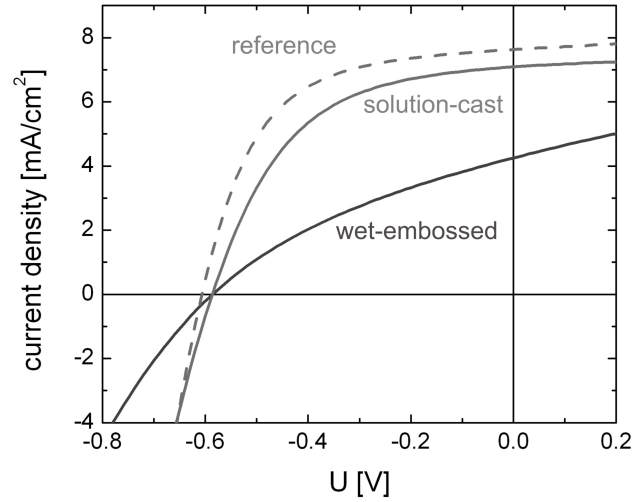
Based on the results from the optical absorption measurements, the profile cuts of the

pure (dark line) and the coated (light line) wet embossed PEDOT:PSS grating from figure 6.23 are plotted in figure 6.25. Both profile cuts are taken perpendicular to the channel structure and averaged over a distance of $2\ \mu\text{m}$ (as indicated by white lines in figure 6.23). In the case of the uncoated channel structure, the already mentioned ridge width of $0.6\ \mu\text{m}$ and the periodicity of $1.6\ \mu\text{m}$ are confirmed and a mean channel height of $150\ \text{nm}$ is found. Since the identical PC mold, which is illustrated in figure 6.16, was used for the PEDOT:PSS grating structure, an inverted replication concerning the width of the channel structure is observed. In contrast to the PEDOT:PSS grating from section 6.2.4, which has a polymer ridge width of $1.2\ \mu\text{m}$ and a height of $175\ \text{nm}$, the reduced channel width results in an incomplete filling of the PC mold and hence in a slightly reduced channel height of $150\ \text{nm}$. Nevertheless, this geometry was chosen in order to minimize the negative influence of thick PEDOT:PSS layers on the charge carrier extraction to the ITO electrode. For the two different PEDOT:PSS gratings, which were used for the F8BT:P3HT (figure 6.21) and the P3HT:PCBM blend (figure 6.25), only the channel width of the PC mold has been modified, whereas the principal fabrication conditions according to section 6.2.1 were the same. As a consequence of the reduced channel width, a small dual peak structure is formed on top of the PEDOT:PSS ridges, as it is typically observed during NIL (already theoretically discussed in section 2.3.2). Most important for the formation of such structures is the force balance between liquid normal stress tensor and the capillary force at the polymer-mold interface.[84] Therefore, the adhesion forces to the PC side walls appear to further attract the polymer for smaller structure domains and hence the prominent bumps on top of the PEDOT:PSS channels are formed. For reduced mold structure dimensions, an additional influence during imprinting results also from air inclusions.[255]

The small peak-to-valley distance of the photoactive layer of only $21\ \text{nm}$ implies that the subsequently spin coated polymer layer fills the PEDOT:PSS channels very well. However, as a result of the dual peak structure of the underlying PEDOT:PSS electrode, the active layer still shows a similar surface topology. Based on the results from the optical absorption measurements and the detailed knowledge of the PEDOT:PSS channel structure and the initial film thickness of the active layer, the mean film thickness of the active layer on top of the PEDOT:PSS channels is calculated to be approximately $50\ \text{nm}$. Therefore, the profile cut of the active layer in figure 6.25 is shifted by the calculated thickness to illustrate the actual film architecture.

In order to finally characterize the impact of the wet embossed PEDOT:PSS electrodes on the OSC performance, *IV*-measurements were conducted on the different device types. In figure 6.26 the characteristic current-voltage-curves of P3HT:PCBM solar cells are shown based on a spin coated (dashed light line), a solution cast (light line), and a wet

Figure 6.26: *IV*-measurements on P3HT:PCBM BHJ OSCs based on wet embossed (dark line), spin coated (dashed light line), and solution cast (light line) PEDOT:PSS electrodes.



embossed PEDOT:PSS electrode (dark line). By comparing the *IV*-curves of the reference OSC (spincoated PEDOT:PSS) and the structured OSC, it is found that the short-circuit current I_{sc} drastically drops from 7.63 to 4.25 mA/cm². This change is also accompanied by a reduction of the fill factor FF from 57.3 to 33.8 %. Both changes are attributed to an increasing series resistance R_S , which increases from 14.5 to 68.0 kΩ/cm². In general, the resistance R_S is given by the slope of the *IV*-curve at the open-circuit voltage U_{oc} and it is a good indication for the presence of depletion layers within the OSC.[177] Besides these conductivity induced effects, also the open-circuit voltage U_{oc} of the solar cells based on wet embossed PEDOT:PSS electrodes is slightly reduced. The exact electrical values are given in table 6.1.

	η [%]	I_{sc} [mA/cm ²]	U_{oc} [V]	FF [%]	R_S [kΩ/cm ²]
reference	2.65	7.63	0.606	57.3	14.5
solution cast	2.14	7.09	0.586	51.4	20.8
wet embossed	0.84	4.25	0.586	33.8	69.0

Table 6.1: Electrical characteristics of different P3HT:PCBM solar cells based on spin coated (reference), solution cast, and wet embossed PEDOT:PSS electrodes.

A main difference in device fabrication results from the elongated solvent evaporation times during the wet embossing of PEDOT:PSS. Therefore, the *IV*-measurement on a P3HT:PCBM solar cell based on a solution cast PEDOT:PSS electrode (light line) is included in figure 6.26 as a second reference as well. This OSC was fabricated under similar conditions as the wet embossed OSC and mimics the influence of longer solvent drying times. The corresponding *IV*-curve also reveals a decreased photocurrent production, which is, however, by far not as strongly reduced as the corresponding values of the wet embossed OSC. Hence, the prolonged fabrication times do not account for the decrease

in efficiency alone. On the contrary, since both cells have identical open-circuit voltages, this shift appears to be solely due to the elongated solvent evaporation. Also, experiments on OSCs based on PEDOT:PSS films, which were intentionally aged in ambient conditions over a period of four days, revealed only a minor influence on the efficiency. Taking into account also the increase in series resistance R_S , it can be speculated that morphological changes, which have already been discussed in great detail in section 4.1.3, lead to a stacking of PEDOT and PSS at the interface to the PC mold and hence result in the formation of PSS enriched depletion layers.[256] Since in general the open-circuit voltage is also slightly influenced by the work functions of the electrodes [257], the observed shift in U_{OC} indicates morphological changes in the PEDOT:PSS as well.[256] The shape of the IV -curve from the wet embossed OSC can also be explained by a layer formation of the two active components at the wrong electrodes.[200] In order to address the phase separation of the P3HT:PCBM BHJ layer on top of the structured PEDOT:PSS, X-ray scattering measurements similar to those applied for the characterization of planar polymer blend films in chapter 5 have been performed. However, up to now no detailed information could be extracted due to the complexity of the film architecture.

In summary, in this section the new WEMB routine was introduced which is very well suited for the fabrication of structured polymer films with defined surface structures and a tunable homogeneous polymer layer thickness. By applying PC as the mold material, an easy and cost-effective way was found to make this wet embossing technique also applicable for a roll-to-roll batch production. The functionality of this routine was illustrated on wet embossed films made of PEDOT:PSS, which were coated with different photoactive polymer blends. In addition, the WEMB approach is also applicable to other polymer types e.g. thermoresponsive polymers.[258] The optical reflectivity of photoactive polymer films was reduced and different additional spectral features induced. As a drawback of this routine, up to now OSCs based on wet embossed PEDOT:PSS electrodes have only shown reduced efficiencies, most certainly due to morphological changes within the PEDOT:PSS, which result in the formation of electrical depletion layers and lead to reduced open-circuit voltages.

As this change is likely due to the extended processing times during the WEMB routine, there is a need to develop a faster imprinting routine. Additionally, more optimized electrode topologies have to be found to finally improve the efficiencies of OSCs.

6.3 Efficiency improved structured organic solar cells

The results from the previous section prove that in general the fabrication of structured PEDOT:PSS electrodes is possible - even in a batch processing approach as it is desired for the future fabrication of organic electronics on a large scale. Nevertheless, for an application of such textured PEDOT:PSS electrodes in OPV, a second imprinting approach needs to be found which is further specialized for the fabrication of efficiency improved structured OSCs. Therefore, in this section a novel imprinting routine is introduced which utilizes the plasticizing properties of chemical compounds blended with PEDOT:PSS (in this context also called *plasticizers*) and combines it with nanoimprint lithography (section 6.3.1). The surface characteristics of such structured PEDOT:PSS films are discussed in section 6.3.2 focusing mainly on the influence of the amount of the added plasticizer. The optical properties of the uncoated PEDOT:PSS structures are investigated in section 6.3.3 concerning the light diffraction properties. Afterwards, the structures are coated with P3HT:PCBM and the impact of the PEDOT:PSS structures on the surface topology is probed (section 6.3.4). Finally, multiple OSCs are made on the basis of such textured PEDOT:PSS electrodes and actually reveal an increase in power conversion efficiency of up to 22 % as compared to the unstructured system (section 6.3.5). By means of various measurements the origin of this enhanced performance is found in an enhanced optical absorption due to diffraction and an improved charge carrier collection efficiency.

6.3.1 Structuring routine

As discussed in section 6.2.1, the most important aspect for the development of new PEDOT:PSS structuring routines for application in organic electronics is to install a homogeneous PEDOT:PSS layer below the surface structures. In principle, the easiest way to fabricate such polymer structures on a continuous support is to use NIL (section 2.3.2). However, since PEDOT:PSS has no distinct glass transition, a typical polymer softening at elevated temperatures is not observed and hence nanoimprint lithography is not possible. A more suitable way is to apply high-energy irradiation with chlorine ions to PEDOT:PSS films, which results in the creation of PEDOT:PSS nano-islands on top of a homogeneous polymer layer.[259] Since this approach is very time- and cost-intensive, it is not suitable for a future large scale production at minimum fabrication costs. In the framework of this thesis, an alternative approach was developed, which is based on plasticizer softened PEDOT:PSS films. It was shown in the literature that films made of glycerol doped PEDOT:PSS (also denoted as *G-PEDOT:PSS*) not only have a sheet resistance, which is reduced by up to two magnitudes in comparison to undoped PEDOT:PSS films [260], but that they are also mechanically softened.[261] Taking advantage of this

for imprinting, figure 6.27 illustrates a fabrication routine for structured OSCs based on plasticizer assisted soft embossed PEDOT:PSS films. The imprinting step is abbreviated as *PASE* (**P**lasticizer **A**ssisted **S**oft **E**mbossing).

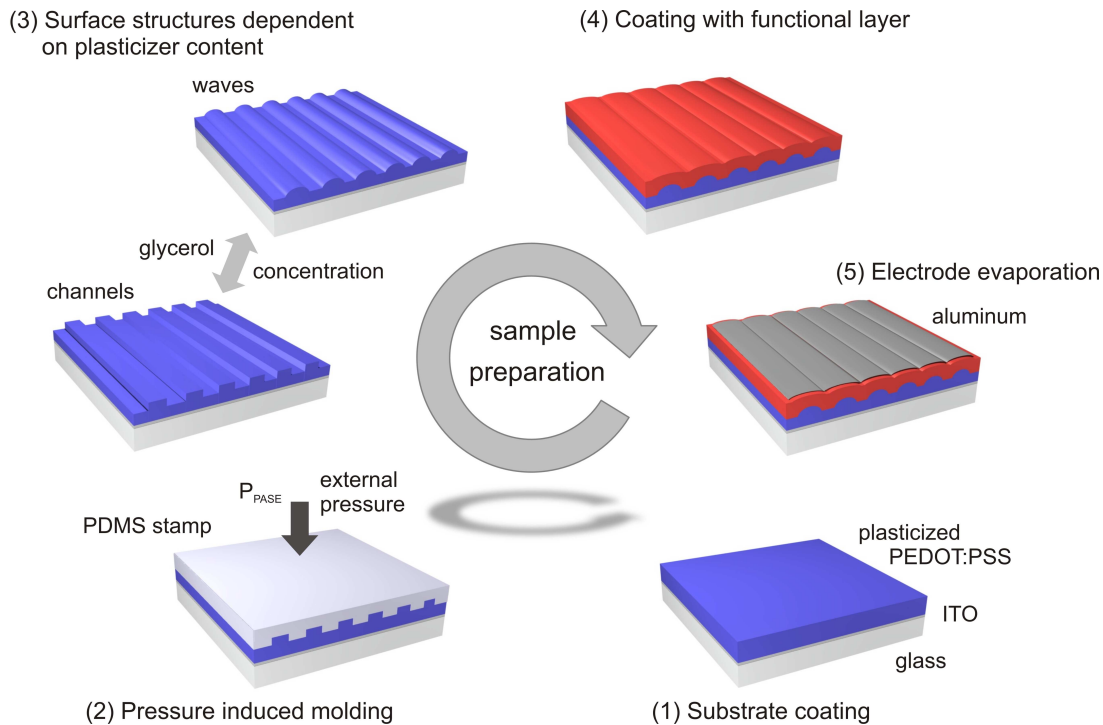


Figure 6.27: Schematic overview of the plasticizer assisted soft embossing routine: (1) A planar substrate is coated with a plasticized PEDOT:PSS layer. (2) A PDMS stamp is used for a pressure induced structure transfer which (3) results in different surface structures depending on the initial plasticizer content. (4) The photoactive layer is spin coated on the structured PEDOT:PSS layer and finally (5) the aluminum electrode is evaporated on top.

Before doping the PEDOT:PSS with the tertiary alcohol glycerol as the plasticizer, the aqueous PEDOT:PSS solution was treated in an ultrasonic bath for 15 min at room temperature and filtered with a 5 μm PTFE filter. Directly following the filtration step, glycerol is added to the polymer solution at different concentrations c_p between 10 and 50 mg/ml. After intense stirring for 20 min with a magnetic stir bar, the G-PEDOT:PSS solution must be used immediately for spin coating. In order to prevent aggregation of the PEDOT:PSS these processing conditions and especially the accurate chronological sequence are crucial to guarantee homogeneous thin films (see step (1) in figure 6.27). The corresponding experimental conditions for the spin coating procedure are given in section 4.3.3. For glycerol concentrations c_p between 10 and 50 mg/ml the initial film thickness of the spin coated PEDOT:PSS films varies between 200 and 450 nm for increasing plasticizer contents (appendix figure A.7(a)). Nevertheless, after thermal annealing, which is described in more detail below, the films have reduced final film thicknesses of approxi-

mately 105 nm which also vary only slightly with the plasticizer concentration (appendix figure A.7(b)). This value also corresponds to the actual film thickness of a spin coated undoped polymer film. In consequence, the previously added glycerol molecules volatilize at elevated temperatures. All thickness values were determined with white light interferometry (Filmetrics F20-UV, San Diego, USA) and more details concerning the dependence of the film thickness on the glycerol content and the spin coating parameters are given in the appendix (section A.3). Also for the G-PEDOT:PSS films the applied substrates (glass and ITO) are pre-cleaned according to the standardized methods described in section 4.3.2. Due to the low vapor pressure of the glycerol at room temperature, the plasticizer remains in the film for several hours and softens the film so that it becomes suitable for imprinting.

The actual structuring process is depicted in step (2) of figure 6.27. The coated substrate is put on a hot plate which is kept at room temperature. An already pre-heated plate results in an immediate hardening of the G-PEDOT:PSS layer. The master structure made of PDMS is impressed at a constant pressure of 30 kPa. The complete imprinting step is performed for three hours at 80 °C on a hot plate with a heating ramp of approximately 15 min at the beginning of the annealing process. However, recent experiments have shown that the total embossing times can be reduced by decreasing the plasticizer concentration and simultaneously increasing the stamping pressure. For optimized imprinting conditions, which also might utilize higher imprinting temperatures, the PASE routine has the potential for a similar roll-to-roll process as already achieved for standard NIL and which is necessary for future large scale and cost-effective device production.[246] Before lifting off the elastomeric PDMS stamp by careful bending, the samples are quenched to room temperature. To conclude the imprinting process, the PEDOT:PSS films undergo an additional thermal annealing step at 140 °C for 10 min, which removes the residual glycerol molecules. More details on the mold material PDMS are given in section 4.2. In combination with the aqueous PEDOT:PSS solution, a more hydrophilic surface of the stamps is established by exposing them to oxygen plasma (200 W, 0.4 mbar) for 30 s directly before imprinting.[262] After cleaning the PDMS stamps in an ultrasonic bath of water for one hour, which is necessary to remove possible polymeric residuals, and fully drying them in an oven at 100 °C for 10 min they can be reused several times. In step (3) of figure 6.27 the obtained PEDOT:PSS surface structures are illustrated. In this sketch it is already anticipated that, depending on the initial glycerol content, the obtained morphologies vary in height and show an additional shape evolution from rectangular to wavy polymer ridges. Subsequently, spin coating is used to homogeneously coat the fabricated structured PEDOT:PSS films with a photoactive polymer layer based on a P3HT:PCBM blend (figure 6.27 step (4)). For the OSCs investigated in this section

the P3HT was dissolved at a concentration of 33 mg/ml in DCB before PCBM was added at a concentration of 27 mg/ml. The same polymer blend solution was already applied to the wet embossed PEDOT:PSS electrodes in section 6.2.5. The sketch in step (4) of figure 6.27 illustrates that also the functional layer adopts the surface structures of the textured PEDOT:PSS electrode. Finally, an aluminum layer with a thickness of approximately 100 nm is thermally evaporated as top electrode (see step (5) in figure 6.27).

6.3.2 Surface morphology control via plasticizer content

For investigations concerning the influence of such structured PEDOT:PSS electrodes on the device performance of OSCs a distinct morphology control over a large sample area is necessary. Since measurements on unstructured PEDOT:PSS layers are always included as a reference, a detailed analysis of the surface properties of planar PEDOT:PSS films is necessary.

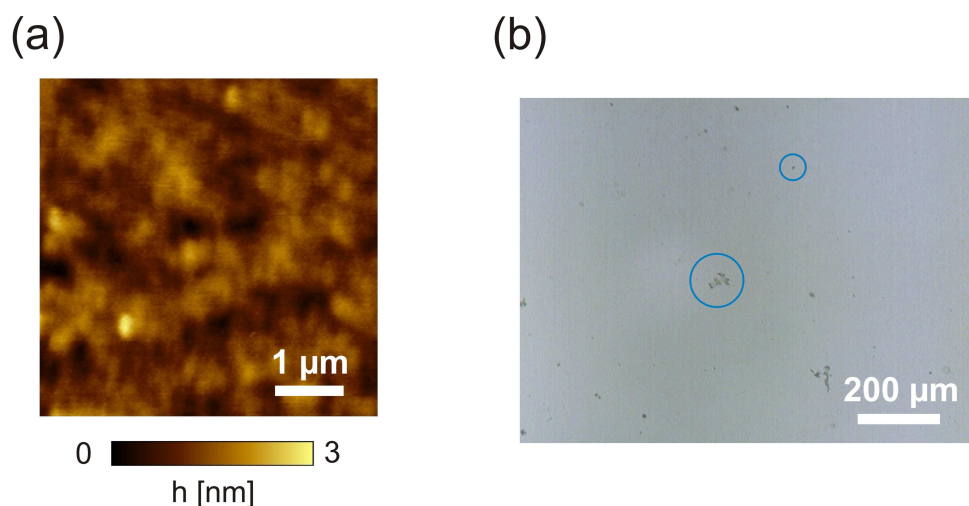


Figure 6.28: Surface morphology of an as-spun PEDOT:PSS film: (a) AFM data reveal a homogeneous flat polymer layer. (b) In the optical micrograph, which images a macroscopic area, larger PEDOT:PSS particles are only rarely found (circled in blue). The AFM measurement was performed with AFM-2 (section 3.2).

In figure 6.28(a) the AFM data of a planar PEDOT:PSS layer are shown. Such as-spun polymer films are perfectly smooth on a microscopic scale and are characterized by a very low surface roughness ($R_{rms} = 0.45$ nm). The optical microscopy image in figure 6.28(b) reveals a good homogeneity of the PEDOT:PSS layer thickness also on a macroscopic sample area (no color gradient observed). However, defects in the surface morphology are also found on rare occasions. Such defects are attributed to local polymer grains of PEDOT:PSS which agglomerate during fabrication of the polymer film [161] or are due to larger completely undissolved polymer parts (highlighted by blue circles). Although

such surface inhomogeneities are typically the reasons for electrical shunts in an OSC, the investigated devices are characterized by a low failure probability ($< 15\%$).

For the structure transfer, PDMS stamps were fabricated using the PC molds from section 6.2 as the master structure. In figure 6.29(a) the AFM topography data of the applied PDMS mold structure are shown and in figure 6.29(b) the corresponding profile cut is illustrated taken perpendicular to the channel structure (depicted by white line in figure 6.29(a)).

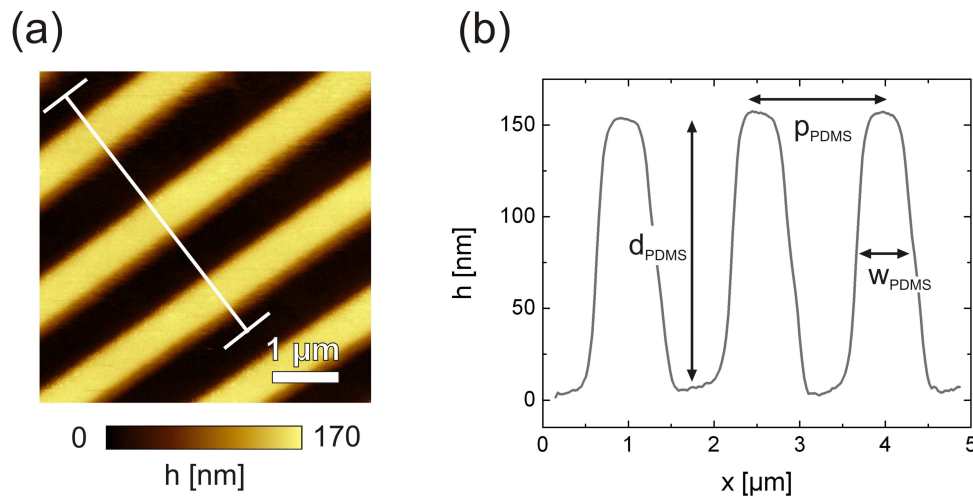


Figure 6.29: Topographical analysis of the applied PDMS mold: In (a) the AFM data of the channel structure are shown and in (b) the corresponding profile cut is depicted including the depth of the channels d_{PDMS} , the periodicity p_{PDMS} , and the width of the PDMS ridge w_{PDMS} . The profile line is taken along the white line and averaged over a width of $1\ \mu\text{m}$. The AFM measurement was performed with AFM-2 (section 3.2).

Taking into account the surface morphology of the original PC master shown in figure 6.16, the PDMS mold has a channel structure which matches perfectly the negative surface it was reproduced from. The applied PDMS channels have a depth d_{PDMS} of $150\ \text{nm}$, a periodicity p_{PDMS} of $1.6\ \mu\text{m}$, and the PDMS ridges have a width of $0.7\ \mu\text{m}$. In general, the channel structure is well-defined and also the top of the PDMS ridges appears smooth and does not show any indication for the formation of a dual peak structure as it was observed for the wet embossed PEDOT:PSS channels in section 6.2.5 (figure 6.25).

In figure 6.30 the two-dimensional AFM topography data of five different plasticizer assisted soft embossed PEDOT:PSS gratings are shown. For these channel structures the glycerol concentration c_p was set to 10, 20, 30, 40, and $50\ \text{mg/ml}$ and the corresponding values are denoted at each sample. In the central part of figure 6.30 not only the profile lines from the illustrated two-dimensional topography are depicted, but also additional profile cuts for intermediate plasticizer concentrations are included. All profile lines are taken perpendicular to the channel structure and are averaged over a width of $1\ \mu\text{m}$ (see

also white lines in the illustrated AFM data). For improved clarity of presentation, the profile cuts are shifted along the y -axis and the two-dimensional AFM data are assigned to the respective profile cuts by arrows. At this point explicit note must be made that for the different fabricated PEDOT:PSS channel structures only the amount of plasticizer was changed, whereas the other experimental conditions remained constant.

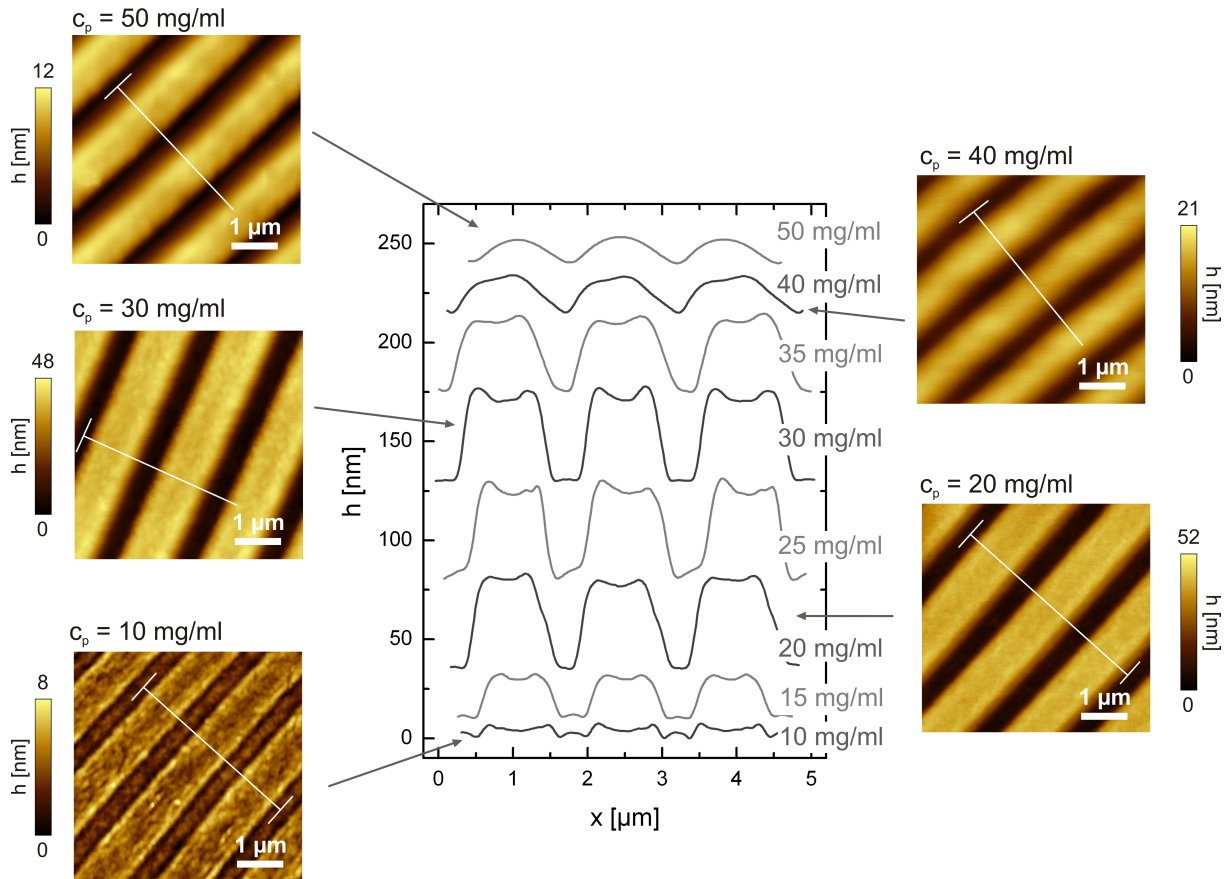


Figure 6.30: Surface analysis of various structured PEDOT:PSS films with different plasticizer concentrations c_p between 10 and 50 mg/ml. In the central part the profile cuts of PEDOT:PSS channels are shown taken perpendicular to the surface structures and averaged over a width of 1 μm (indicated by white lines). The corresponding two-dimensional AFM topography data of the structured PEDOT:PSS films with glycerol contents of 10, 20, 30, 40, and 50 mg/ml are shown as an example and assigned to the profile lines by arrows. The AFM measurements were performed with AFM-2 (see section 3.2)

The AFM data of the sample with the lowest glycerol concentration ($c_p = 10$ mg/ml) reveal an only slightly visible channel structure with an averaged PEDOT:PSS ridge height of 4 nm. However, the surface structures become more prominent for increasing dopant concentrations c_p up to a threshold value of 30 mg/ml. For higher initial glycerol concentrations the defined characteristics of the channel structure vanish again and adapt a more wavy surface morphology. For the illustrated glycerol concentrations of 20, 30, 40, and 50 mg/ml the mean peak-to-valley heights of the PEDOT:PSS ridges are 45, 39,

19, and 11 nm. Also taking into account the profile cuts from the intermediate dopant concentrations ($c_p = 15, 25, \text{ and } 35 \text{ mg/ml}$), detailed knowledge of the on going processes during imprinting is possible. For small amounts of plasticizer ($c_p \leq 10 \text{ mg/ml}$) the PEDOT:PSS film is still too hard so that a defined embossing of the relatively soft PDMS mold into the target film is not possible. However, for an increased glycerol concentration of 15 mg/ml the heights of the PEDOT:PSS ridges rapidly increase to 26 nm. For even higher concentrations ($c_p = 20 - 30 \text{ mg/ml}$) the shape properties of the PEDOT:PSS channels remain roughly constant and have a height of around 40 nm. In general, these medium plasticizer concentrations lead to the most prominent channel structures with the highest aspect ratios. In this case, the aspect ratio is defined as structure height (here $d_{cha} = d_{PEDOT:PSS}$) divided by structure width ($w_{rid} = w_{PEDOT:PSS}$; see also figure 6.2). For these glycerol concentrations the channel structure has a ridge width $w_{PEDOT:PSS}$ of 1.0 μm and a periodicity $p_{PEDOT:PSS}$ of 1.7 μm , which is in good agreement with the negative dimensions of the master mold from figure 6.29. The observed increasing precision in structure shape is due to an enhanced softening of the PEDOT:PSS film. For more plasticized films the PDMS mold is further impressed in the PEDOT:PSS, which in addition is also able to adapt the master structure more precisely. However, glycerol concentrations c_p above 30 mg/ml lead to a counterproductive effect. They have reduced polymer ridge heights and the channel shape changes from rectangular to sinusoidal. In more detail, for a glycerol concentration of 35 mg/ml the height of the PEDOT:PSS ridges is already reduced to 34 nm and the side walls of the channel structure appear more inclined. For further increased plasticizer concentrations c_p of 40 and 50 mg/ml the polymer ridges further collapse to 17 and 9 nm. For the highest plasticizer content, the structured film has an almost perfect sinusoidal topology. This evolution in shape is due to an increasing amount of glycerol residuals, which remain in the PEDOT:PSS matrix during the imprint and might still be present in the films after the lift-off. As a result, the PEDOT:PSS layer is still soft and the channel structures converge. However, since a final thermal annealing step is carried out at 140 °C for 10 min, the residual glycerol molecules are removed completely and hence the surface structures remain constant during further processing towards an OPV device.

The optical microscopy image in figure 6.31 proves that the high macroscopic quality of the applied PDMS molds (see figure 6.29) is transferred successfully to the PEDOT:PSS films via the PASE routine.

Not only a highly oriented channel structure is observed, but also the amount of imperfections due to polymer aggregates is reduced significantly. The latter effect is attributed to the fact that glycerol not only favors the solubility of the polymer, but also results in reduced solvent evaporation rates during spin coating. This additionally hampers the

Figure 6.31: Optical micrograph of a structured PEDOT:PSS film prepared via the PASE routine with a glycerol content c_p of 20 mg/ml: A highly ordered channel structure is also observed on a macroscopic sampling area.



formation of PEDOT:PSS grains.

Similar to the GISAXS analysis of the structured F8BT films (see sections 3.7 and 6.1.4), GISAXS is also used to probe the plasticizer assisted soft embossed PEDOT:PSS films. In case of these films, GISAXS is again advantageous since it allows the reconstruction of the nanoscopic channel structures based on the results from a macroscopic sampling area. For the PASE structures an accurate alignment of the channel structure to the impinging X-ray beam is crucial as well, in order to allow for a final analysis of the scattering data with the IsGISAXS software. In figure 6.32(a) the GISAXS data of PASE-structured PEDOT:PSS films with different glycerol concentrations c_p of 10, 20, 30, 40, and 50 mg/ml are shown.

The most prominent features in the GISAXS data are the truncation rods, which are almost not visible for structures made with the lowest and the highest initial glycerol concentrations ($c_p = 10$ and 50 mg/ml). For medium plasticizer concentrations of 20 and 30 mg/ml truncation rods up to the fifth order are observed. However, the GISAXS data of the sample with a plasticizer content of 40 mg/ml show that this scattering feature starts to disappear for further collapsing channels. In comparison to the scattering data of the pre-structured imprinted F8BT channels, which were perfectly straight and hence resulted in a symmetric scattering (figure 6.8), the results on the PASE gratings reveal a slightly asymmetric scattering intensity. This is due to a minor curvature of the PEDOT:PSS ridges, which is not observable with other nanoscopic measurement techniques. Only the GISAXS method reveals this feature due to its elongated footprint along the channel structure of around 3 mm (angle of incidence α_i was set to 0.43° and more details on the experimental conditions are given in section 3.7). Nevertheless, after a careful alignment of the rotational angle ρ_{rot} (see figure 3.7) the GISAXS data can be exactly fitted with the IsGISAXS software (figure 6.32(b)). It is clearly seen that the IsGISAXS simulations, which are based on a similar theoretical model as applied for the structured F8BT films (further information is also given in the theory section 2.4.3), are in good agreement with

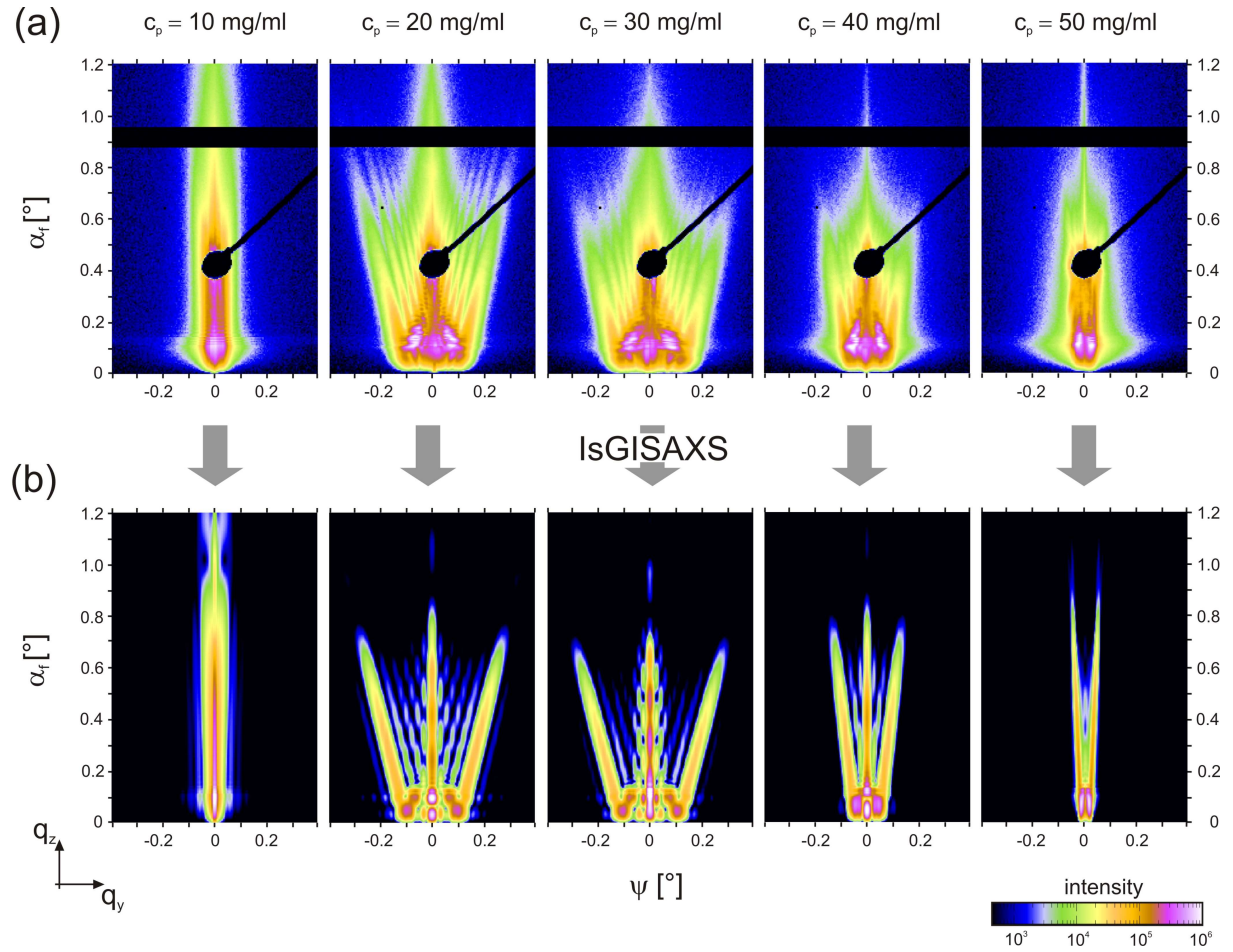


Figure 6.32: Experimental GISAXS data and the corresponding IsGISAXS simulations of PASE-structured PEDOT:PSS gratings with different glycerol concentrations ($c_p = 10, 20, 30, 40,$ and 50 mg/ml): In (a) the GISAXS measurements are shown and in (b) the corresponding two-dimensional simulations are illustrated. All simulations are based on DWBA and different models are used, which all consist of anisotropic pyramids with varying base angles and structure heights and widths positioned on the sites of a regular two-dimensional lattice.

the measured data. Besides the truncation rods, also the scattering intensity around the Yoneda maximum fits well to the data.

c_p [mg/ml]	10	20	30	40	50
φ_{cha}^{GISAXS} [°]	1.5	13.6	14.5	6.5	2.3
φ_{cha}^{AFM} [°]	2.2	14.0	14.0	3.1	2.3

Table 6.2: Base angles of the inclined sidewalls of the PEDOT:PSS channel structure measured with GISAXS φ_{cha}^{GISAXS} and AFM φ_{cha}^{AFM} in dependence on the plasticizer concentration c_p .

The prominent angles under which the truncation rods appear in the scattering data are given by the base angles φ_{cha} of the inclined sidewalls of the channel structure. In table 6.2

a good agreement between the base angle values from the IsGISAXS simulations φ_{cha}^{GISAXS} and the corresponding results from the AFM data φ_{cha}^{AFM} in figure 6.30 is found.

6.3.3 Optical properties of PASE-structured PEDOT:PSS gratings

For application of the PASE-structured PEDOT:PSS layers in organic solar cells the light diffracting properties are most important. Therefore, in figure 6.33 the UV/Vis spectra of structured PEDOT:PSS films made with five different initial glycerol concentrations ($c_p = 10, 20, 30, 40,$ and 50 mg/ml) are shown as dark solid lines, whereas the spectra of planar reference films are included as light dashed lines. For all films the spectra were recorded in transmission (figure 6.33(a)) and in reflection geometry (figure 6.33(b)). For better clarity of presentation, all data are shifted along the y -axis for the different glycerol concentrations.

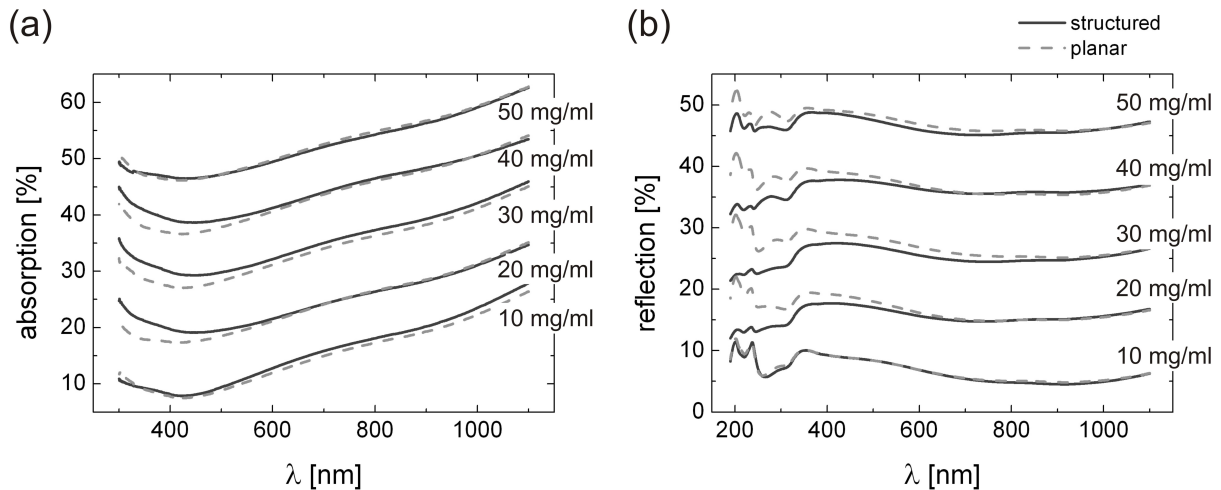


Figure 6.33: Optical characteristics of structured (dark solid lines) and planar (light dashed lines) PEDOT:PSS films: (a) Optical absorption measurements indicate an enhanced grating effect at shorter wavelengths. (b) The same tendency is also observed for the corresponding optical reflection.

In order to exclude any influence of the added glycerol minority component on the optical properties of the measured PEDOT:PSS films, the planar reference samples were doped with the corresponding plasticizer concentrations, as well. For a full imitation of the experimental conditions during the PASE routine, the complete thermal annealing procedure was also applied to the planar reference films (see section 6.3.1). Due to the intrinsic absorption of PEDOT:PSS which was already observed in the case of the wet embossed films (see figure 6.24), figure 6.33(a) also reveals a homogeneous increase in absorption for increasing wavelengths. Although the structured PEDOT:PSS shows no

additional sharp absorption features, the optical absorption appears enhanced for wavelengths below 600 nm. For clarification, it must be pointed out that the measurements were performed on a UV/Vis spectrometer without using an integrating sphere, but rather a narrow photodiode. This detector does not take into account any diffracted light above an angle of 2.5° (see section 3.4). Since also the planar films were fabricated from an initially glycerol doped PEDOT:PSS solution this effect is not due to an additional absorption of the plasticizer, but it is rather attributed to a light diffraction caused by the grating structure. It was already shown by Moharam and Gaylord that the diffraction efficiency of such linearly aligned structures depends strongly on the height and the shape of the objects.[263] For conducting PEDOT diffraction gratings, which were fabricated on gold surfaces via a complex combination of microcontact imprinting and electropolymerization, Marikkar et al. revealed a diffraction efficiency that increases with the depth of the grating.[264] Also the absorption data in figure 6.33(a) imply the highest optical diffraction for channel structures with the deepest trenches as they result from medium glycerol concentrations ($c_p = 20$ to 40 mg/ml). In principle, the reflection measurements in figure 6.33(b) show the same behavior. For low imprinted PEDOT:PSS structures ($c_p = 10$ and 50 mg/ml) the optical reflection, which was only measured along the sample normal, matches well with the results from the planar reference films. More defined imprints lead to a reduced reflection signal which is again attributed to an increased light diffraction. Since the strongest contrast in refractive index between PEDOT:PSS and air is found at short wavelengths, the observed grating effect appears mainly for blue light. It has to be taken into account that the spectra of figure 6.33 only illustrate the grating efficiencies of the uncoated structured PEDOT:PSS electrodes. In case of full organic solar cells, which are investigated in the following sections, the contrast in refractive index at the grating-polymer interface is reduced.

6.3.4 Coated PASE-structured PEDOT:PSS films

For application in OPV the PASE-structured PEDOT:PSS layers were coated with an active layer consisting of a P3HT:PCBM blend (more details in section 6.3.1). In figure 6.34 the surface properties of such an active layer with a thickness of 165 nm are characterized if spin cast on a planar PEDOT:PSS support.

In the AFM topography data in figure 6.34(a) not only a homogeneous surface of the active layer is revealed, but also a typical PCBM crystallite is included. Such microscopic crystallites are depicted by an increased surface height of up to 30 nm and a surrounding PCBM depletion area which is indicated by a slightly reduced film thickness. The latter is a result of PCBM diffusion from the surrounding blend film to the induced nucleation sites at which aggregates of PCBM grow.[134, 265] In comparison to the pure

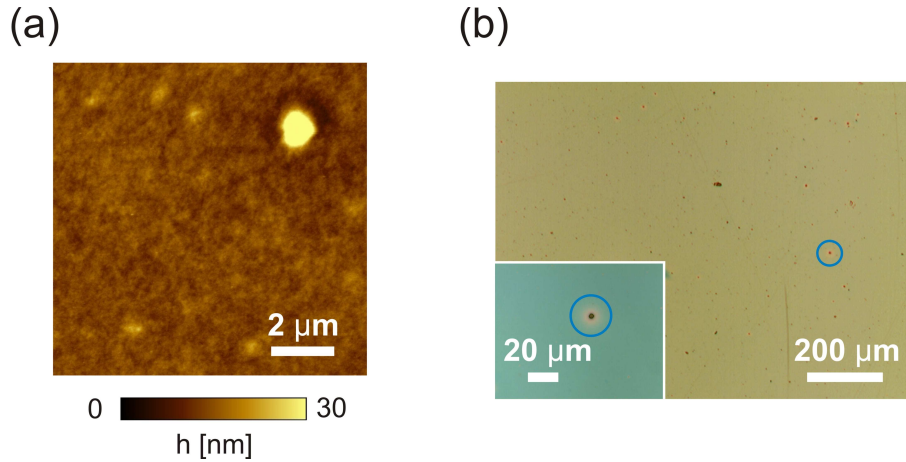


Figure 6.34: Surface characterization of an as-prepared P3HT:PCBM blend film spin cast on a planar PEDOT:PSS layer: (a) AFM data reveal a homogeneous polymer film with local PCBM crystallites. The measurement was performed with AFM-2 (section 3.2). (b) The optical microscopy image shows a homogeneous polymer film with randomly distributed PCBM crystallites (circled in blue). The inset depicts a close-up image of such a PCBM crystallite.

PEDOT:PSS layer the surface roughness of the active layer is increased ($R_{rms} = 1.2$ nm). For P3HT:PCBM blend films increased roughness values are often considered a signature of an enhanced crystallinity of the two components.[266, 267] In the optical microscopy image of figure 6.34(b) a random distribution of the PCBM crystallites is shown on a macroscopic area. In the inset of figure 6.34(b) a close-up image of a PCBM crystallite is depicted and the previously discussed PCBM depletion area is observable due to a change in color (circled in blue).

In figure 6.35 the surface characteristics of P3HT:PCBM films are shown spin cast on PASE-structured PEDOT:PSS films with different initial glycerol concentrations ($c_p = 10, 20, 30, 40,$ and 50 mg/ml). In the center of figure 6.35 the averaged profile cuts of the corresponding AFM data are depicted. The profile lines are taken perpendicular to the channel structures and averaged over a width of $1 \mu\text{m}$ (as indicated by the white lines in the two-dimensional AFM data). For comparison, the corresponding uncoated PEDOT:PSS films were presented in figure 6.30. For the investigated structured P3HT:PCBM films all surface roughnesses are increased in comparison to the planar polymer blend film. For increasing plasticizer amounts the corresponding R_{rms} -values are $3.2, 4.5, 4.6, 6.5,$ and 4.2 nm. However, since the values for medium and high glycerol concentrations are similar, no direct influence of the PEDOT:PSS channel shape on the crystallinity of the two components at the surface of the as-spun films is observed. Nevertheless, sub-micron structures induced by the PEDOT:PSS channels are also visible at the surface of the P3HT:PCBM layer for all glycerol concentrations. As expected, the higher PEDOT:PSS ridges also lead to enhanced surface modulations of the top polymer layer. Whereas for

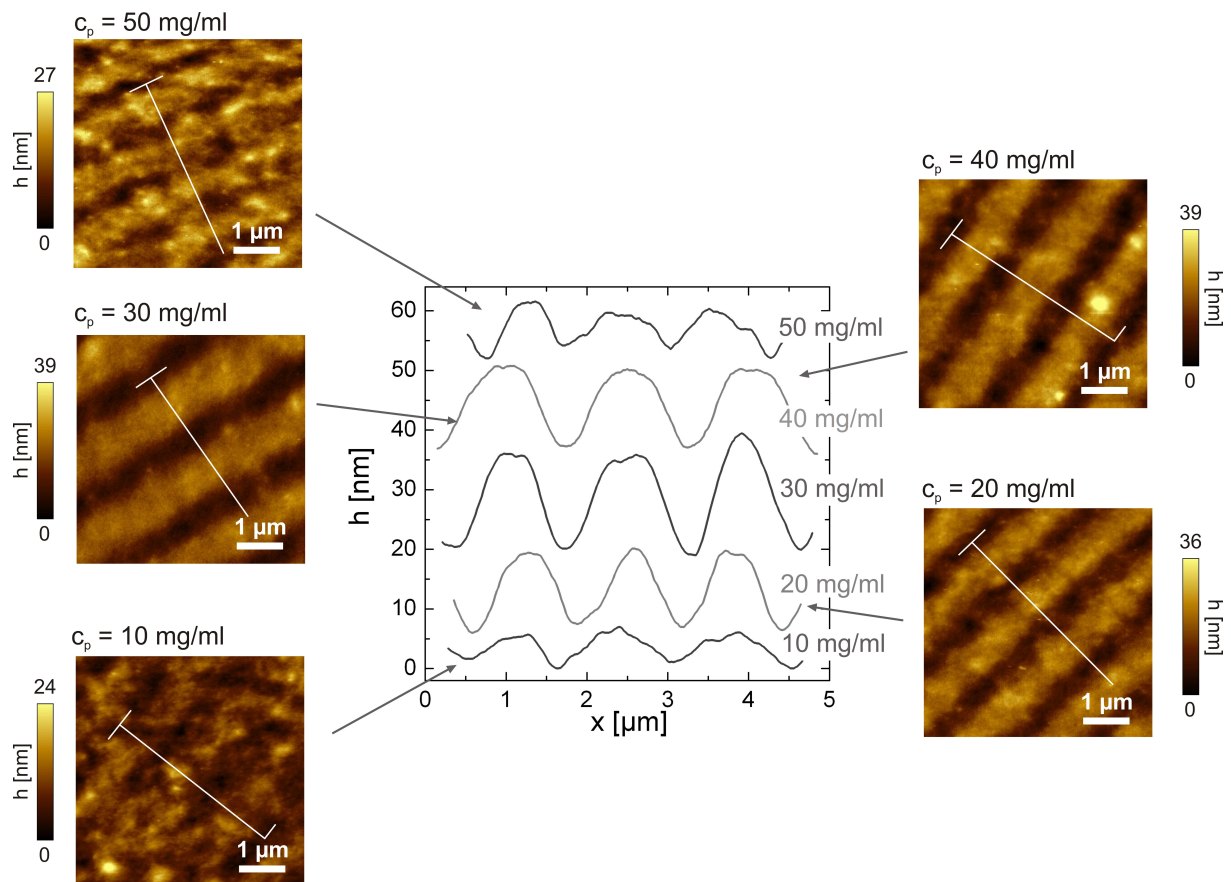


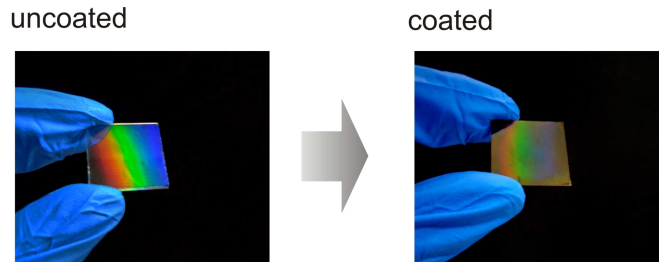
Figure 6.35: Topology analysis of P3HT:PCBM blend films spin cast on different PASE-structured PEDOT:PSS films ($c_p = 10, 20, 30, 40,$ and 50 mg/ml). In the central part the profile cuts, which are taken perpendicular to the surface structures and averaged over a width of $1 \mu\text{m}$ (indicated by white lines in the corresponding AFM data), are shown. For clarity the profile lines are shifted along the y -axis. The corresponding two-dimensional AFM topography data of the structured polymer blend films are linked to each profile cut and the applied glycerol content is noted at each topography image. The measurements were performed on AFM-2 (see section 3.2)

the least pronounced PEDOT:PSS imprints ($c_p = 10$ and 50 mg/ml) only minor topological channel structures are found, they appear much more defined for films spin-cast on PEDOT:PSS structures with higher aspect ratios ($c_p = 20, 30,$ and 40 mg/ml).

In comparison to the topography of the uncoated PEDOT:PSS films (figure 6.30), the P3HT:PCBM layers have a wavy and nearly sinusoidal surface. The photoactive films have the highest peak-to-valley ratios for medium initial glycerol concentrations of the PEDOT:PSS layer and only reduced structure heights for small and high dopant concentrations. For the different plasticizer concentrations of $10, 20, 30, 40,$ and 50 mg/ml the medium heights of the P3HT:PCBM ridges are $6, 13, 14, 17,$ and 8 nm. In consequence, the surface structures of the active layer appear smaller in height than the height of the corresponding uncoated PEDOT:PSS ridges. The impact of the PEDOT:PSS structures

on the surface morphology of the active layer also depends on the overall thickness of this film. Since in this thesis the active layer thickness is set to 165 nm, especially the PEDOT:PSS structures of the lowest and highest glycerol concentrations have only a minor impact on the surface of the active layer. However, the averaged profile lines in figure 6.35 prove that all P3HT:PCBM films mimic the surface topology of the structured PEDOT:PSS electrode underneath.

Figure 6.36: Photographs showing the optical grating effect of (a) an as-prepared PASE-structured PEDOT:PSS layer and (b) coated with a photoactive P3HT:PCBM layer ($c_p = 30$ mg/ml).



In figure 6.36 optical photographs of an uncoated and a coated PASE-structured PEDOT:PSS film are illustrated. Both films are prepared with an initial glycerol concentration of 30 mg/ml and silicon was used as the substrate in order to highlight the optical grating effect, which was already discussed in the framework of the pre-structured F8BT films (see figure 6.12) and the wet embossed PEDOT:PSS samples (figure 6.19). For the smoothed P3HT:PCBM surface structures the reflected intensity from the coated grating is reduced in comparison to the pure PEDOT:PSS structures.

6.3.5 Solar cells based on PASE-structured PEDOT:PSS electrodes

As previously discussed, Na et al. have shown that the power conversion efficiency of P3HT:PCBM solar cells is increased due to additional surface structures of the active layer similar to the ones observed in figure 6.35.[234, 233] To prove that the PASE structuring approach also leads to an increase in efficiency, OSCs were fabricated based on structured and flat PEDOT:PSS layers. In order to avoid any possible effects of the added glycerol component on the electrical performance, the same experimental conditions as used for the structured OSCs were applied to the planar reference cells. Therefore, the corresponding plasticizer concentrations were as well added to the PEDOT:PSS and the planar films also underwent the same thermal annealing as described in section 6.3.1.

In figure 6.37(a) the IV -curves of a PASE-structured (dark solid line) and a planar (light dashed line) organic solar cell are shown, which are both recorded under illumination with AM 1.5 G. Both devices were fabricated with an initial glycerol concentration of 20 mg/ml. Most obvious in this plot is the increase in photocurrent production due to

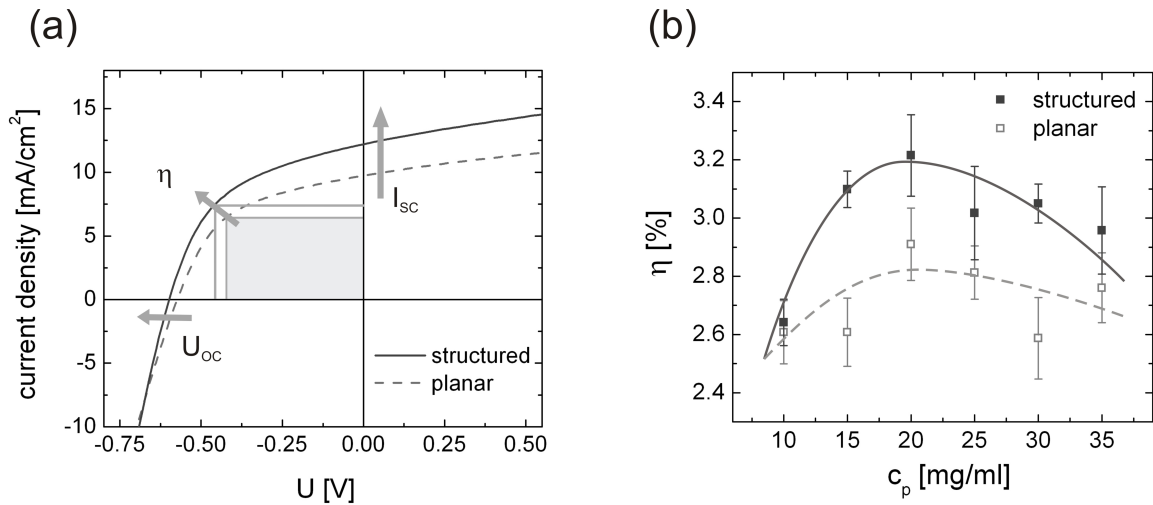


Figure 6.37: Analysis of the device performance of P3HT:PCBM OSCs based on structured and planar PEDOT:PSS electrodes: In (a) the IV -characteristics depict an improved performance of the PASE-structured OSC in comparison to the planar reference OSC. Both devices are based on PEDOT:PSS films with an initial glycerol concentration c_p of 20 mg/ml. In (b) an overview of the averaged efficiencies η of structured (filled symbols) and planar (open symbols) OSCs are plotted as functions of the initial glycerol content c_p . The error bars are given by the corresponding standard deviations and the solid lines act as guides to the eyes.

a structuring of the PEDOT:PSS electrode. For the planar reference cell an open-circuit voltage U_{oc} of -0.57 V, a short-circuit current density I_{sc} of 9.73 mA cm^{-2} , a fill factor FF of 49 %, and a final power conversion efficiency η of 2.74 % are obtained. In contrast, the performance characteristics of the structured cells are enhanced to an open-circuit voltage U_{oc} of -0.59 V, a short-circuit current density I_{sc} of 12.42 mA cm^{-2} , a fill factor FF of 46 %, and an efficiency η of 3.35 %. As a result, for this chosen solar cell the efficiency is increased by 22 % due to an efficient structuring of the PEDOT:PSS electrode. As the IV -curves already reveal, the increase in the energy conversion efficiency, which is calculated according to equation (3.1), is mainly attributed to the increase in short-circuit current I_{sc} .

Utilizing the key advantage of the PASE routine, which is the fabrication of different surface morphologies by simply tuning the plasticizer concentration, in figure 6.37(b) the solar cell efficiencies η of multiple solar cells are shown based on different structured (filled symbols) and planar PEDOT:PSS electrodes (open symbols). For the given examples, the PEDOT:PSS films were doped with initial glycerol concentrations c_p of 10, 15, 20, 25, 30, and 35 mg/ml. For an enhanced statistical relevance, the efficiencies presented in figure 6.37(b) are averaged values of multiple single solar cells and the corresponding standard deviations are included as error bars. In comparison to the OSCs based on PEDOT:PSS electrodes with low structure heights (e.g. $c_p = 10 \text{ mg/ml}$ and $c_p > 35 \text{ mg/ml}$), which

result only in minor improvements in power conversion efficiency, the higher aspect ratio electrode structures lead to OSCs with an increase in mean efficiency by over 18 %. The solid lines are included as a visual guide. It should be pointed out here that in order to only focus on the effect of the electrode structure, the OSCs are not fully optimized regarding the highest possible efficiency. As an example, spacing layers and top blocking layers were not introduced which have already been used to further enhance the efficiency of similar polymer:fullerene solar cells.[268, 269]

For a detailed physical explanation of the enhanced electrical device efficiencies, the impact of the structured PEDOT:PSS electrodes on the photoactive layer has to be addressed. For this purpose additional measurements were performed on OSCs based on a plasticizer concentration c_p of 20 mg/ml, which according to figure 6.37(b) have the highest overall power conversion efficiencies. In order to investigate the impact on the optical absorption, the real absorptions of the structured (solid line) and the planar (dashed line) solar cell are shown in figure 6.38(a). Both measurements were carried out in reflection geometry and the aluminum electrodes of the OSCs were used as reflecting material. In order to avoid any parasitic absorption effect e.g. due to light diffraction, an integrating sphere was used for these UV/Vis measurements (see section 3.4). Recently Burkhard et al. have shown that such measurements are necessary for correct spectral optical measurements on OSCs especially at short wavelengths and in regions with a weak intrinsic polymer absorption.[270] As previously discussed for OSCs based on wet embossed PEDOT:PSS layers (figure 6.24), also in this section the investigated OSCs reveal a strong absorption peak due to P3HT at around 500 nm. The additional maximum at 330 nm attributed to the PCBM is not shown in this measurement due to the strong absorption of the ITO substrate at wavelengths below 350 nm. Besides a slight increase in optical absorption at small wavelengths ($\lambda < 400$ nm), the spectrum of the structured device is characterized by an increased absorption of photons with wavelengths greater than 500 nm in comparison to the planar solar cell. In general, the shoulder at 600 nm is also a good hint for a high crystallinity of P3HT in the blend film which is already indicated by the high surface roughness values.[271] However, photoluminescence measurements show that the increase in absorption for wavelengths above 500 nm is not attributed to an enhanced crystallization of P3HT (more information is given below). As a consequence, the observed broadening can only be due to an enhanced absorption of light reflected at the structured aluminum electrode or of light diffracted at the textured interface between PEDOT:PSS and the active material. For wavelengths above 650 nm the total optical absorption is dominated by parasitic effects within the cell.[270]

Nevertheless, the observed increase in absorption, and hence in charge carrier generation, cannot account for the observed increase in photocurrent alone. In fact, it was

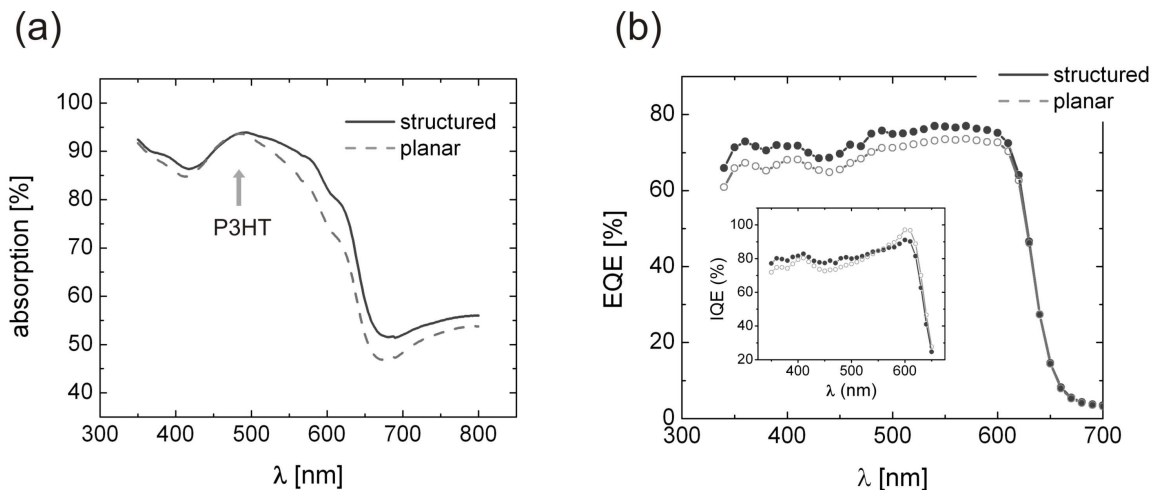


Figure 6.38: Absorption and external and internal quantum efficiency (EQE and IQE) characterization of P3HT:PCBM films on PASE-structured (dark solid lines) and planar (light dashed lines) PEDOT:PSS electrodes. In (a) the actual optical absorptions in the OSCs are measured in reflection geometry with an integrating sphere. In (b) the wavelength dependent EQE spectra are illustrated for OSCs fabricated on structured and planar PEDOT:PSS layers with an initial glycerol concentration c_p of 20 mg/ml. The inset shows the corresponding IQE values.

reported that polymer:fullerene solar cells have typically an almost constant power conversion efficiency for active layers thicknesses above a certain threshold value (typically around 100 nm).[267, 272] In general, OSCs with high active layer thicknesses have reduced charge carrier efficiencies due to an enhanced charge carrier recombination rate that is often indicated by a decreasing fill factor (see also section 2.1.4). In order to rule out a possible influence of variations in active layer thickness on the extracted device efficiencies a high primary active layer thickness of 165 nm was chosen for the investigated samples and additional *IV*-curves have shown that variations in film thickness of ± 55 nm have only a slight impact on the device efficiencies (see appendix section A.3). Similar to variations in active layer thickness also changes concerning the PEDOT:PSS layer thickness influence the performance of organic electronics.[256] However, in the case of the investigated material system, OSCs based on various different planar PEDOT:PSS film thicknesses between 50 and 150 nm have constant power conversion efficiencies (see appendix section A.3).

Besides this optical analysis, additional external quantum efficiency (EQE) measurements were performed to further investigate the influence of structured PEDOT:PSS electrodes on the charge carrier extraction efficiency. In figure 6.38(b) the EQE spectra of high-efficient OSCs ($c_p = 20$ mg/ml) fabricated on structured (dark solid line) and planar (light dashed line) PEDOT:PSS layers are plotted. The shown EQE spectra are mean values of multiple devices. The measurements were recorded with an automated LabView

computer program, which controlled a Keithley 2400 source meter. For the spectrally resolved measurements a xenon white light source was focused into a grating monochromator, which was equipped with a set of necessary edge pass filters. In agreement with the increase in short-circuit current I_{sc} (figure 6.37(a)), the measured EQE spectra also reveal values for the structured solar cells higher than those for the planar solar cells. In the case of the structured device, a slight flattening is observed for shorter wavelengths. Due to the fact that the EQE spectra were recorded in steady-state conditions without a white-light background illumination, the observed values are fairly high. However, similar EQE values ($\text{EQE}_{max}(\text{planar}) = 73\%$ and $\text{EQE}_{max}(\text{structured}) = 77\%$) have already been reported by other groups.[273, 274] Unfortunately, in the case of the investigated devices the high currents drop in forward bias and hence the high values cannot be converted to power conversion efficiency without further device optimization. Comparing the results of the EQE and the IV -measurements, at a first glance the increase in external quantum efficiency implies an enhanced fill factor FF . However, due to an increased charge carrier recombination rate the high current is reduced in forward bias and the fill factors of the planar and the structured devices are not ideal.

In order to fully address the aspect of an improved charge carrier collection efficiency, the corresponding internal quantum efficiency (IQE) spectra are shown in the inset of figure 6.38(b) calculated from the measured EQE data (figure 6.38(b)) and the corresponding total optical absorptions of the full devices (figure 6.38(a)). For wavelengths below 550 nm, where only small improvements in optical absorption are observed, the IQE appears to be enhanced due to the additional PEDOT:PSS surface structures. However, in the wavelength regime, which is dominated by an enhanced optical absorption ($\lambda > 550$ nm), similar charge carrier collection efficiencies are observed for the planar and the structured devices. The IQE data are shown for wavelengths between 350 and 650 nm since only in this regime the assumption holds that the active layer is responsible for the majority of the absorption.[270]

Up to this point, a complete filling of the PASE-structured PEDOT:PSS electrodes with P3HT:PCBM is assumed. Also the measured high power conversion efficiencies of the OSCs and the relatively low aspect ratio of the fabricated channel structures make the presence of any imperfections (e.g. air inclusions) at the PEDOT:PSS interface unlikely. To fully rule out the existence of such voids additional GISAXS measurements were performed (see figure 6.39), which imply a complete filling of the trenches in the PEDOT:PSS film, as well. Recently, we have used the same measurement method to probe the filling of nanostructured P3HT films with a PCBM film floated on top.[275] In comparison to the complex scattering of the uncoated PEDOT:PSS structures shown in figure 6.39(a), which was already described in more detail in section 6.3.2, the GISAXS data of the

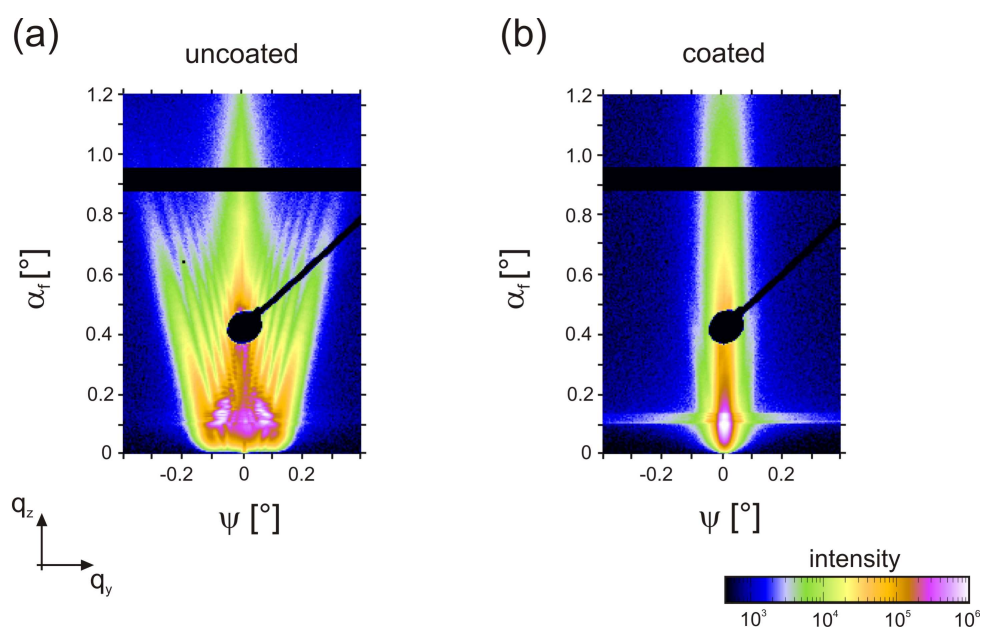


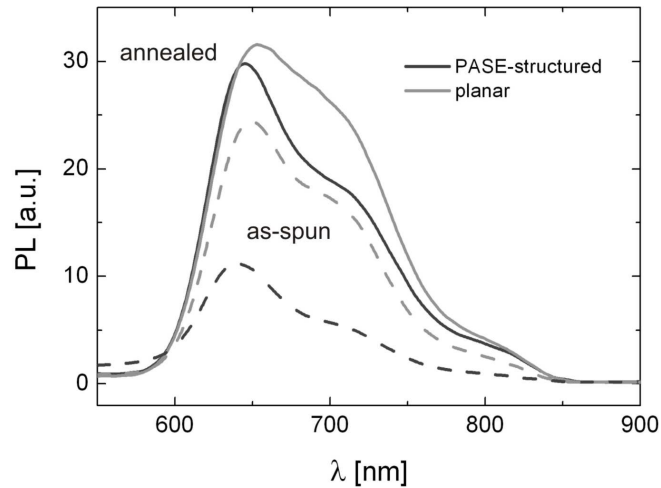
Figure 6.39: GISAXS measurements on (a) uncoated and (b) coated PASE-structured PEDOT:PSS films which were fabricated with an initial glycerol content of 20 mg/ml.

coated structures show no similar prominent scattering features (figure 6.39(b)). Since these measurements probe the full sample volume, this result is a very good indication for a complete filling of the PEDOT:PSS structures with active polymer material. Air inclusions or other defects have a strong contrast in refractive index to the surrounding polymer matrix and would therefore result in a more pronounced scattering.

To complete the analysis on the PASE-structured organic solar cells additional photoluminescence (PL) measurements were performed in order to address the phase separation in the P3HT:PCBM blend film. In figure 6.40 the PL spectra of P3HT:PCBM BHJ films on structured (dark lines) and planar (light lines) PEDOT:PSS films ($c_p = 20$ mg/ml) are shown for the as-spun (dashed lines) and the annealed (solid lines) cases. In accordance with the actual OSCs, the thermal annealing of these investigated samples was also performed at 140 °C for 10 min in an inert nitrogen atmosphere. The photoluminescence was studied with a LS 55 fluorescence spectrometer from Perkin Elmer (Waltham, USA) using a Xenon discharge lamp and the excitation wavelength was set to 485 nm.

After being excited, the PL spectra reveal a more pronounced quenching of the photoluminescence signal of the P3HT:PCBM blend if cast on a structured PEDOT:PSS electrode. In general, a reduced PL yield indicates an intimate mixing of the donor and acceptor phase. Since the PL yield is maximum for pure homopolymer samples, large scale phase separations which are beyond the exciton diffusion length scale result in a recovery of the luminescence yield.[276] It is clearly seen that the PL yield is increased due to the post-

Figure 6.40: Photoluminescence spectra of as-spun (dashed lines) and annealed (solid lines) P3HT:PCBM blend films spin coated on PASE-structured (dark lines) and planar (light lines) PEDOT:PSS films. The PL signal is quenched for as-spun or structured films.



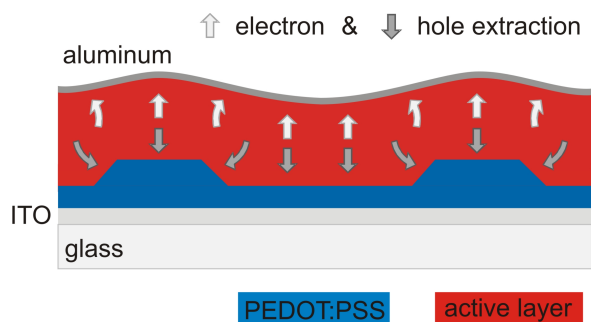
production heat treatment. This effect can only be described by the fact that the phase segregation of both components increases upon annealing.[277] However, in the case of the P3HT:PCBM blend on the PASE-structured electrode the additional shoulder in PL signal at 700 nm, which is attributed to the signal of a pure P3HT film [276], still appears quenched. In consequence, the PL measurements indicate an enhanced intermixing of the P3HT and the PCBM component if spin cast on a structured PEDOT:PSS electrode. However, since PL measurements only probe the small fraction of excitons which decay via fluorescence (in case of pure P3HT around 1 % [278]), absolute implications of the PL data are delicate. Especially since the more generalized absorption data reveal only minor differences in P3HT crystallinity (see figure 6.38(a)). The majority of the generated excitons decay via non-radiating relaxations as e.g. vibrational or rotational processes.

6.3.6 Improved charge carrier collection model

As a result of the various measurement techniques applied to the different sample types, the PASE-structured electrodes mainly lead to an enhanced optical absorption in the complete device due to reflections at the structured aluminum electrodes. This effect is mainly observed for impinging light with wavelengths above 500 nm. However, in the case of absorbed photons with shorter wavelengths the additionally generated charge carriers are also more efficiently extracted to the structured top aluminum and the structured bottom PEDOT:PSS/ITO electrodes.

In figure 6.41 a suitable model for the efficient charge carrier extraction is illustrated, which includes shortened pathways for the charge carriers to the structured electrodes. Due to the elevated PEDOT:PSS electrodes the photogenerated holes are extracted to the side walls of the PEDOT:PSS channels via shortened percolation paths. In order to guarantee electrical neutrality in the device, an unbalanced transport which results in a loss in

Figure 6.41: Model for an efficient charge carrier extraction in organic solar cells based on PASE-structured PEDOT:PSS electrodes. Due to additional surface structures shorter percolation paths for the charge carriers to both electrodes are induced.



efficiency due to increased recombination has to be avoided.[279] However, since also the aluminum electrodes adapt modified surface structures, reduced electron transport paths to the top electrode are found, as well. As a consequence of the closer distances to both electrodes, reduced charge carrier recombination rates are possible, which are the most limiting factors for the photocurrent generation.

In summary, in this section an additional novel structuring routine was presented which allows the fabrication of textured PEDOT:PSS electrodes based on the plasticizing effect of an added glycerol component. OSCs with such modified intermediate PEDOT:PSS layers have an improved power conversion efficiency of up to 22 % as compared with the planar ones. This is a significant jump, especially keeping in mind that the applied electrode topologies have not been fully optimized for the most efficient device performances. By applying various different experimental techniques, the increase in efficiency is mainly attributed to an optical diffraction effect for short wavelengths and a more efficient charge carrier collection at both electrodes.

6.4 Conclusions - structured polymer films

In this chapter three novel structuring routines were introduced and successfully applied for the fabrication of textured conducting polymer thin films.

Thin films of F8BT were structured via the PSIM approach, which has the key advantage that it can be fully performed at ambient conditions. In-situ GISAXS measurements on such structured F8BT films during thermal annealing have shown that a polymer flow already sets in at temperatures below glass transition. As a result, a direct structuring of the active layer appears inappropriate for the development of efficiency improved organic devices. Since the material of choice, F8BT, is widely used and has material characteristics which are common for conducting polymers (e.g. crystallinity), the obtained results can also be transferred to other materials.

For application in OSC a structuring of the intermediate functional PEDOT:PSS layer is more promising, since PEDOT:PSS is mechanically stable upon thermal annealing. However, no common structuring routines can be applied for the fabrication of PEDOT:PSS structures, which are also suited for the fabrication of solar cells. Hence, two structuring routines were developed which both result in PEDOT:PSS structures on top of a homogeneous PEDOT:PSS support.

The WEMB routine, which is based on the combination of an inverted MIMIC approach with a novel mold material, allows for the fabrication of structures from different polymeric materials in a batch process.

However, for application in OSCs the PASE approach is more efficient. Such structured solar cells achieved an improvement in efficiency of up to 22 %, which is attributed to an increase in optical absorption due to light diffraction and an enhanced charge carrier extraction efficiency. Taking into account that the applied structures were not fully optimized for maximum power conversion efficiencies the PASE routine has great potential for future improvements in the field of OPV.

Chapter 7

Conclusions

Organic solar cells already show power conversion efficiencies of 10.0 % and are promising candidates for a future low-cost type of commercial solar cells.[8]

In order to answer the fundamental questions from the introduction, not only different conducting polymer blend systems were studied in the present thesis in regard to film morphology, but also novel imprinting techniques have been established for the fabrication of textured organic solar cells (OSC) with surface structures on the micro- and nanometer scale. The studies performed contribute to an increased understanding of the basic principles in OSCs and they continuously focus on the fabrication of efficiency improved devices as it was finally realized for structured OSCs. For all investigated blend films a full reconstruction of the film architecture was possible based on the combination of multiple different experimental techniques, which were not only surface sensitive but also probed the total sample volume (e.g. X-ray scattering methods).

In a first step it was found that the phase separation in polymer blend films can be modified by tuning the actual active layer thickness. For thinner films, spin cast conducting polymer blends show an increased degree of intermixing (reduced polymer domain sizes) as it is crucial for applications in organic electronics, which require high interfacial areas between the electron donating and accepting polymers. This observation favors device designs based on multiple thin layers in order to guarantee an efficient charge carrier separation at the polymer:polymer interfaces accompanied e.g. by a sufficient optical absorption as in the case of OSCs.

In addition, the film morphology also depends strongly on the compositional ratio of the two polymeric components. Whereas asymmetric blending ratios lead to an unde-

finer intermixing in BHJ films, more pronounced polymer domains with structure sizes on the nanoscale were found for symmetric blending ratios. The long-time stability of photoactive polymers, which is still one of the limiting properties of OSCs on the way to marketability, is even further reduced in the case of blend films with a defined intermixing. In comparison to the photochemical degradation of homopolymer films, the aging of blend films is drastically increased due to the presence of chemical products which act as degradation catalysts.

In general, the presence of oxygen plays a crucial role for the aging of organic photoactive materials. Soft X-ray absorption measurements have been adopted to detect a significant amount of retained oxygenic solvent molecules within such conducting polymer films. These measurements are not only the first directly addressing the absolute solvent content in conducting polymer matrices, but they additionally revealed a lateral solvent distribution depending on the chemical composition of the polymer domains. In consequence, a possible internal degradation source for OSCs was detected which cannot be avoided by applying complex cell encapsulations.

For the investigations concerning the influence of polymer structures on OSCs, first the thermal stability of textured polymer films had to be investigated. Therefore, microstructured polymer channels were fabricated at room temperature using a new approach based on the floating technique. During thermal annealing the polymer structures showed a loss of structure shape already at temperatures below glass transition. Starting from a well-defined channel structure, a wavy surface topology was adopted accompanied by the formation of mesoscopic crystals. Since in organic photovoltaic devices an annealing step at high temperatures is absolutely necessary, a structuring of the transparent ITO/PEDOT:PSS electrodes was more promising.

Therefore, within the framework of this thesis a structuring routine was established based on wet embossing principles in combination with a novel semi-flexible master mold. This approach allowed for the fabrication of polymer structures on top of a homogeneous polymer support which is crucial for electronic applications. By applying an external pressure during the sample preparation, the thickness of this homogeneous polymer support is modifiable, which makes this routine easily adoptable to the requirements of different organic devices. A simple batch-production device was designed to illustrate the potential for a future roll-to-roll application. In addition, optical gratings made of thermoresponsive polymers were produced according to the same routine and furthermore highlight the widespread application possibilities to different polymeric materials.

However, for applications in OSCs this wet embossing technique was not appropriate due to the prolonged processing times, which have a negative influence on the device performance. Therefore, finally an additional novel structuring method, which is based on

nanoimprint lithography (NIL) and involves the addition of a plasticizing component, led to an increase in power conversion efficiency of OSCs. A key benefit of this structuring approach is that the surface structures can be easily modified by changing the plasticizer concentration without requiring different structure molds. Due to the softening effect of the plasticizer, high annealing temperatures and imprinting pressures as they are typically required for standard NIL are also not needed. The results of various experiments have shown that the increase in the power conversion efficiency of the structured OSC in comparison to the planar reference cells is attributed not only to an enhanced optical absorption, but also to a more efficient charge carrier extraction at the textured bottom and top electrodes.

From an experimental point of view the attention was put on the application of X-ray scattering (GISAXS) and X-ray absorption (NEXAFS and STXM) techniques on soft matter blend systems. GISAXS was used not only to determine the inner film morphology in polymer blend systems, but also to characterize the surface of the artificially structured polymer films and to prove the filling of the textured electrodes with photoactive material. Soft X-rays were successfully applied to detect small amounts of residual solvent in conducting polymer films.

Chapter 8

Outlook

Future: Mitsubishi Chemical plans the commercialization of OSCs with 15 % efficiency by 2015.[280]

Aside from the results obtained in the field of organic photovoltaics - especially focusing on structured devices - some questions still remain unanswered and additional experiments appear promising.

Taking into account that in the future the photochemical degradation of organic solar cells will be pushed more and more into the focus of worldwide research, the results of the investigated polymer blend films clearly show that also the aging mechanisms of other commonly applied systems need to be studied in blend geometry and not only for the homopolymer films. However, additional infrared spectroscopy measurements will be necessary to determine the individual reaction products of the photochemically degraded conducting polymers.

In order to answer the basic question of why solvent, which is a possible source for an internal degradation, is at all retained within conducting polymer films, the soft X-ray absorption measurements will be further exploited and additional homopolymer and polymer blend systems will be investigated. Due to the continuous improvements in beamline instrumentation the residual solvent content in blend films as they are currently used in state-of-the-art solar cells with nanoscopic phase segregation domains should soon be detectable as well.

Especially in the new research field of structured organic solar cells, additional experiments will have to be performed in order to achieve even higher power conversion efficiencies. Therefore, different surface structures - e.g. inverted pyramids which have already been successfully applied for silicon based solar cells - also appear interesting for OPV. Since

the structured electrodes also led to an increase in charge carrier extraction efficiency, even thicker photoactive layers with higher optical absorptions might result in further improvements.

Until now, the impact of substrate structures on the phase separation in polymer blend films has also only been discussed to a limited extent. Therefore, we have already performed GIUSAXS measurements on polymer blend films spin cast on structured silicon substrates. In figure 8.1(a) the scattering data of the uncoated silicon substrate are shown, whereas in (b) the substrate has been covered with a conducting polymer blend. The corresponding out-of-plane cuts in figure 8.1(c) highlight the strong influence of the silicon channels. However, due to the complexity of the scattering data, a successful simulation with the IsGISAXS software has not been possible yet.

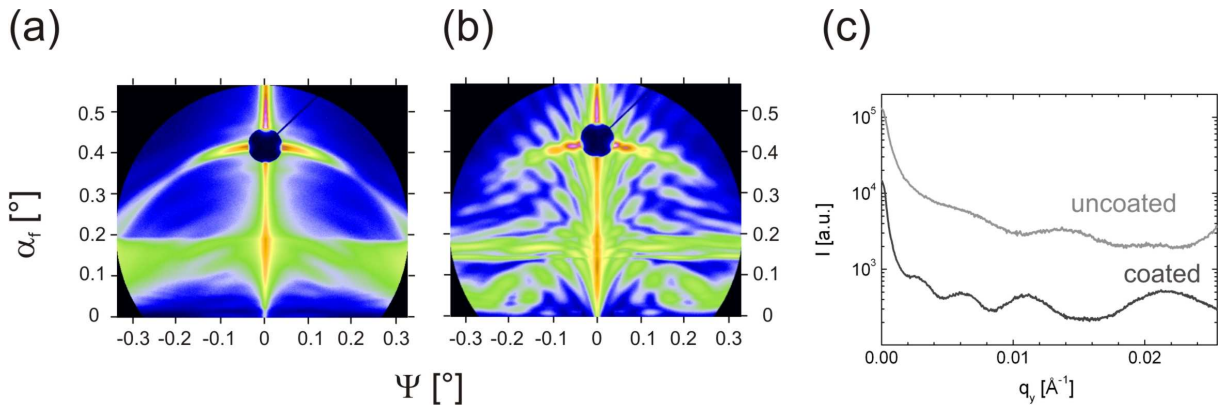


Figure 8.1: Two-dimensional GIUSAXS scattering data of (a) an uncoated structured silicon substrate and (b) coated with a M3EH-PPV:F8BT polymer blend. In (c) the out-of-plane cuts taken at the critical angle of the F8BT reveal maxima in scattering intensity at higher orders for the coated silicon structures (dark line), whereas the uncoated structures show less scattering features (light line). For improved clarity of presentation the out-of-plane cut of the uncoated structures is shifted along the y -axis.

Appendix A

Appendix

A.1 Supplementary AFM data

In figure A.1 the two-dimensional AFM phase data of MDMO-PPV:F8BT blend films with compositional ratios of 70:30, 60:40, 50:50, 40:60, and 30:70 vol% are shown.

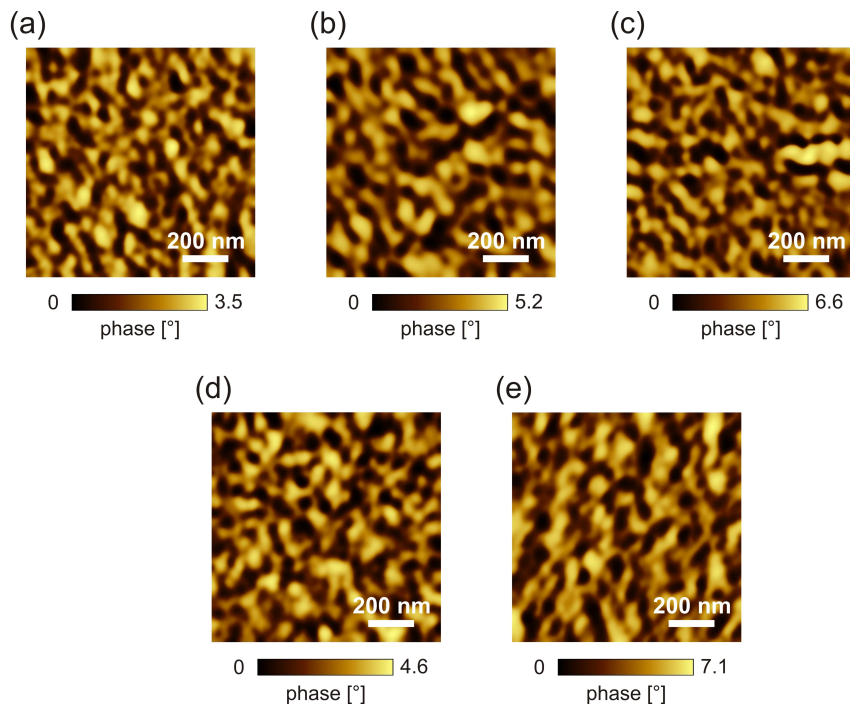


Figure A.1: Atomic force microscopy phase data of MDMO-PPV:F8BT samples with compositional ratios of (a) 70:30, (b) 60:40, (c) 50:50, (d) 40:60, and (e) 30:70 vol%. The scan size is $1 \times 1 \mu\text{m}^2$.

These measurements have been used to calculate the typical structure size of phase separation at the sample surface by fitting the corresponding power spectral density functions (5.15). Whereas the corresponding power spectral density analysis shows clear differences

between symmetric and asymmetric blending ratios, the two-dimensional AFM data are difficult to interpret.

A.2 Additional polymer blend system

In this section the film morphology of M3EH-PPV:F8BT blend films is briefly investigated applying GISAXS measurements. In addition, the influence of different blending ratios on the optical absorption is studied in order to target the solar spectrum.

Sample preparation

For the sample preparation, M3EH-PPV and F8BT have been dissolved in toluene separately. Before the homopolymer solutions are blended, the M3EH-PPV and the F8BT (type-III, see table 4.1) solutions were filtered with a 0.2 μm and a 0.45 μm PTFE filter, respectively. In figure A.2 the thickness values d of the spin cast M3EH-PPV (light squares) and F8BT films (dark triangles) are shown for different polymer concentrations in solution c .

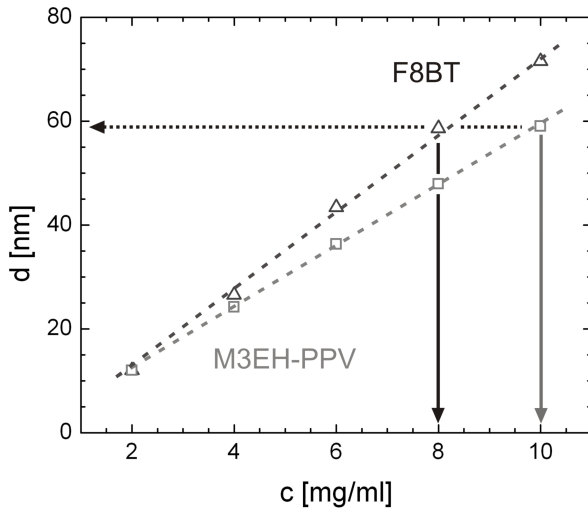


Figure A.2: Film thicknesses d of M3EH-PPV (light squares) and F8BT (dark triangles) homopolymer films for different polymer concentrations in solution c : Both polymers show a linear dependence of the film thickness on the polymer concentration (indicated by dashed lines) and have equivalent film thicknesses of 60 nm for a concentration of 8 mg/ml in case of F8BT and 10 mg/ml for M3EH-PPV.

For both polymers a linear dependence of the film thickness on the polymer concentration in solution was observed within the investigated concentration regime. For the following experiments F8BT was used at a concentration of 8 mg/ml and for M3EH-PPV 10 mg/ml was chosen. Since for both polymers the chosen concentrations result in homogeneous polymer films with thicknesses around 60 nm, also blend films with different compositional ratios have the same thickness.

Optical absorption - targeting the solar spectrum

In figure A.3(a) the optical absorption of a M3EH-PPV (light line) and a F8BT (dark line) homopolymer film is shown. Although both films have a thickness of only 60 nm, they absorb almost 60 % of the incoming photons at the polymer specific maximum absorption peaks.

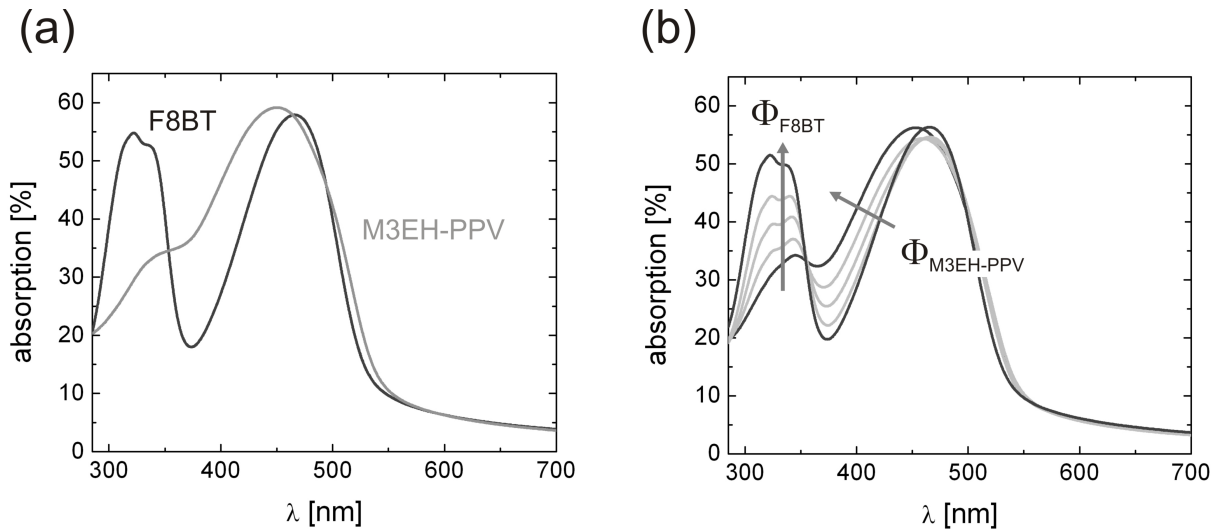


Figure A.3: Optical absorption spectra of M3EH-PPV and F8BT homopolymer and blend films: In (a) the optical absorption of M3EH-PPV and F8BT films with a thickness of 60 nm are shown. In (b) the UV/Vis spectra of M3EH-PPV:F8BT blend films with blending ratios of 10:90, 30:70, 50:50, 70:30, 90:10 vol% are plotted. The arrows indicate the increasing M3EH-PPV ($\Phi_{\text{M3EH-PPV}}$) and F8BT (Φ_{F8BT}) content. For clarity, the absorption of the blend films with the most asymmetric blending ratios are highlighted as dark lines.

In figure A.3(b) the optical absorption spectra of M3EH-PPV:F8BT blend films with compositional ratios of 10:90, 30:70, 50:50, 70:30, 90:10 vol% are plotted. For an increasing F8BT content the optical absorption is mainly increasing for wavelengths below 350 nm. On the contrary, for higher M3EH-PPV contents, the optical absorption between 350 and 450 nm is enhanced.

Since for application of such films in OSCs the optical absorption of the solar spectrum as it is actually available on the surface of the earth is important, the normalized solar spectrum is illustrated in figure A.4(a) (dark line). In addition, the optical absorption of M3EH-PPV (light dashed line) and F8BT films (light dotted line) with a thickness of 60 nm are included as references.

Based on the optical absorption of the blend films, the number of photons available at each wavelength and the corresponding energy of the photons, the total absorbed energy can be calculated. In A.4(b) the total absorbed energy is not only plotted for the different

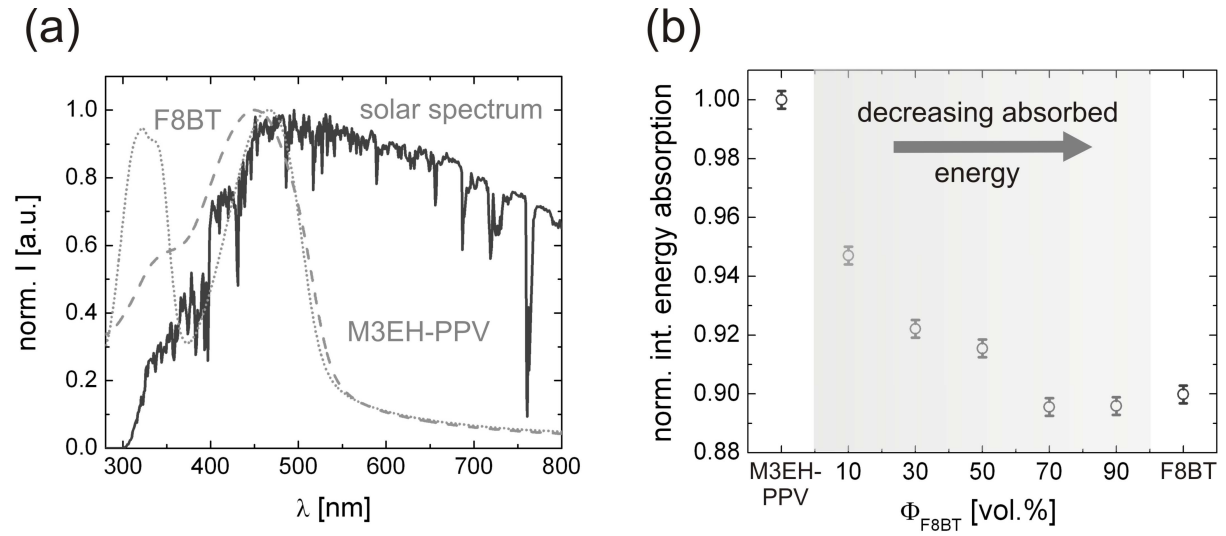


Figure A.4: Optical absorption measurements addressing the harvested solar energy: In (a) the typical solar spectrum is illustrated (dark line) as measured on the surface of the earth. The light dashed line depicts the absorption of M3EH-PPV and the dotted light line of F8BT. All spectra are normalized. In (b) the normalized integrated energy absorption is plotted for the homopolymer and the polymer blend films with M3EH-PPV:F8BT blending ratios of 10:90, 30:70, 50:50, 70:30, and 90:10 vol%.

blend films but also for the M3EH-PPV and the F8BT homopolymer films. It is observed that for increasing F8BT contents the total absorbed energy is reduced. This is attributed to the fact that the number of available photons in the solar spectrum is smaller for shorter wavelengths. However, this is exactly the region in which the second absorption maximum of F8BT is located, which hence cannot contribute to the absorption.

Film composition dependent film morphology

The influence of the morphology in BHJ films has been widely discussed within this thesis. Also for the M3EH-PPV:F8BT films GISAXS experiments have been performed to address the phase separation within the blend film. In figure A.5 the out-of-plane cuts taken at the critical angle of the polymers are shown for the different blending ratios of 10:90, 30:70, 50:50, 70:30, and 90:10 vol%.

In accordance to the investigations on the MDMO-PPV:F8BT blend films, also for the M3EH-PPV:F8BT films a pronounced intermixing of the two components with a characteristic structure length Λ of 350 nm is found for symmetric blending ratios, whereas asymmetric blending ratios lead to a less defined phase separation.

The corresponding detector cuts are illustrated in figure A.6. The critical angle α_{crit} , at which the out-of-plane cuts from figure A.5 are taken, is depicted by the arrow. The investigated blend films show a defined correlated roughness with decreasing fringe pat-

Figure A.5: GISAXS out-of-plane cuts (open symbols) for M3EH-PPV:F8BT blend films with blending ratios of 10:90, 30:70, 50:50, 70:30, and 90:10 vol%. For clarity, the out-of-plane cuts are shifted along the y -axis with increasing F8BT content (depicted by Φ_{F8BT}) and the solid lines are given by the fits according to the effective surface approximation (see section 3.7).

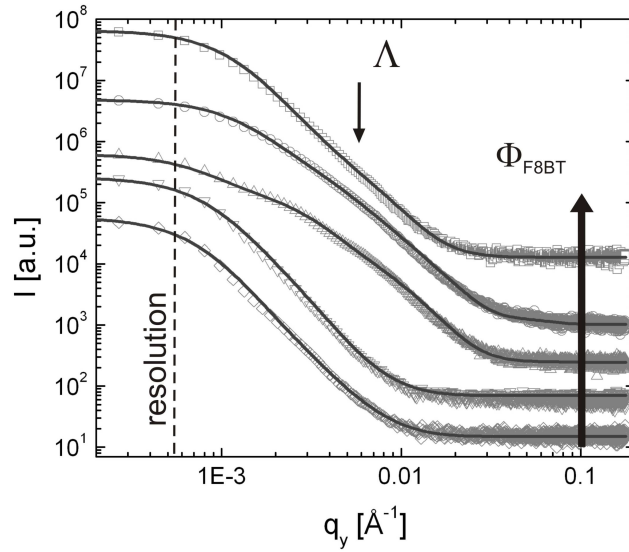
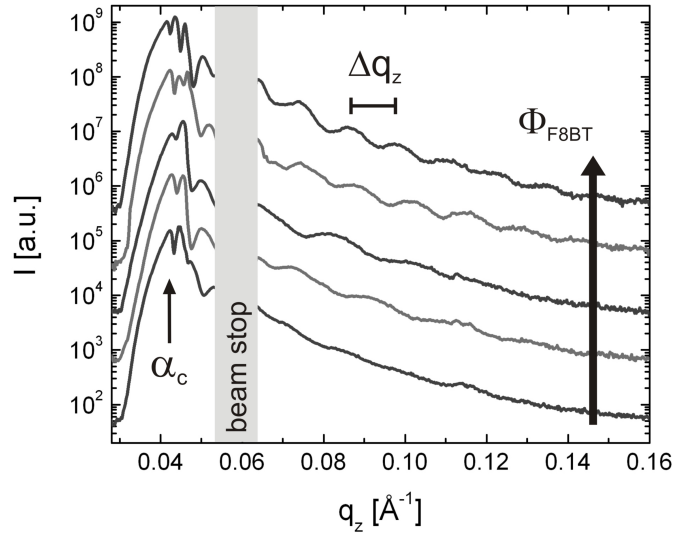


Figure A.6: GISAXS detector cuts (open symbols) for M3EH-PPV:F8BT blend films with blending ratios of 10:90, 30:70, 50:50, 70:30, and 90:10 vol%. For clarity, the detector cuts are shifted along the y -axis with increasing F8BT content (depicted by Φ_{F8BT}). Prominent intensity modulations (Δq_z) indicate the formation of two-layer stacking within the blend morphology.



terns for increasing F8BT contents (indicated by Δq_z). Since for all investigated M3EH-PPV:F8BT samples the film thickness is constant, the increasing Δq_z -values indicate a vertical layering with increasing layer thicknesses.

A.3 Supplementary information: PASE-structured solar cells

PEDOT:PSS film thickness

For the PASE routine the aqueous PEDOT:PSS solutions are doped with glycerol as plasticizing component. However, the plasticizer not only leads to a mechanical softening

of the PEDOT:PSS film, it also results in modified film thicknesses. In figure A.7(a) the thicknesses of the as-spun PEDOT:PSS films are plotted in dependence on the initially added glycerol concentration c_p . The film thicknesses are also shown for different rotational velocities ω_{rot} during the spin coating process ($\omega_{rot} = 1000, 1500, 2000, 2500, 3000,$ and 3500 rpm). The solid lines are linear fits to the experimental data. The dark line illustrates the results for the spinning velocity which was actually applied for the fabrication of the solar cells ($\omega_{rot} = 3000$ rpm).

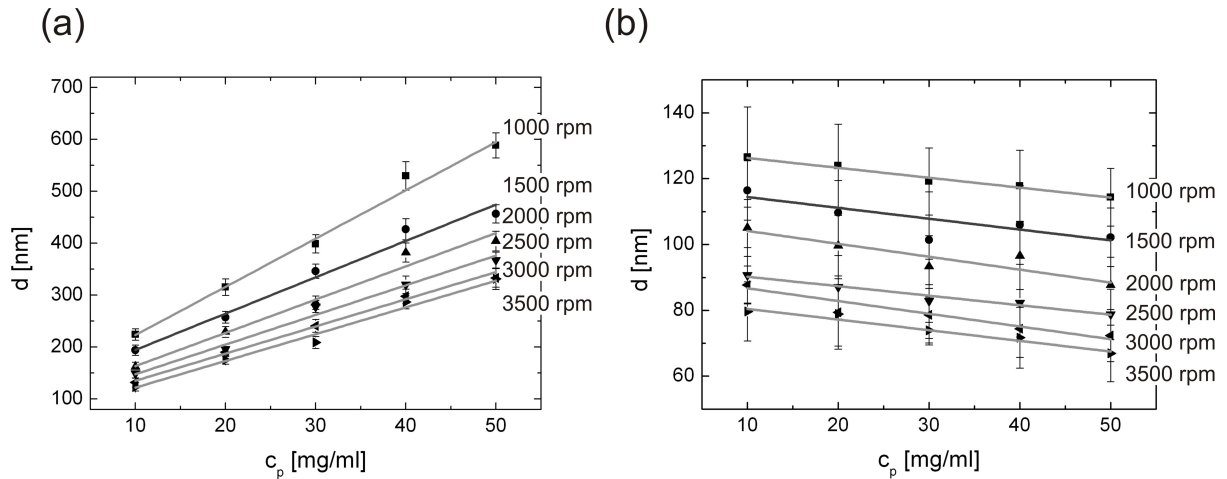


Figure A.7: In (a) the PEDOT:PSS film thickness d is plotted for different initial glycerol concentrations c_p in the as-prepared case and in (b) after thermal annealing on a hot plate at 140 °C for 10 min. For (a) and (b) the results for different rotational velocities are shown.

Whereas the as-prepared films show great variations in film thickness for different glycerol concentrations, the film thickness vary only slightly after thermal annealing at 140 °C for 10 min on a hot plate (figure A.7(b)). In case of a rotational velocity of 3000 rpm the PEDOT:PSS film thickness varies between 190 and 450 nm in the as-prepared case, but only between 117 and 107 nm after thermal annealing.

Influence of thickness variations on device performance

In order to prove, that the efficiency of the PASE-structured organic solar cells is not depending on the film thickness of the PEDOT:PSS layer (see section 6.3), OSCs based on five different PEDOT:PSS layer thicknesses between 50 and 150 nm were fabricated. In figure A.8(a) it is seen that the power conversion efficiencies of the P3HT:PCBM solar cells are constant around 2.8 %.

Also the effect of P3HT:PCBM film thickness variations on the device performance has to be considered. In figure A.8(b) it is shown that the power conversion efficiencies of

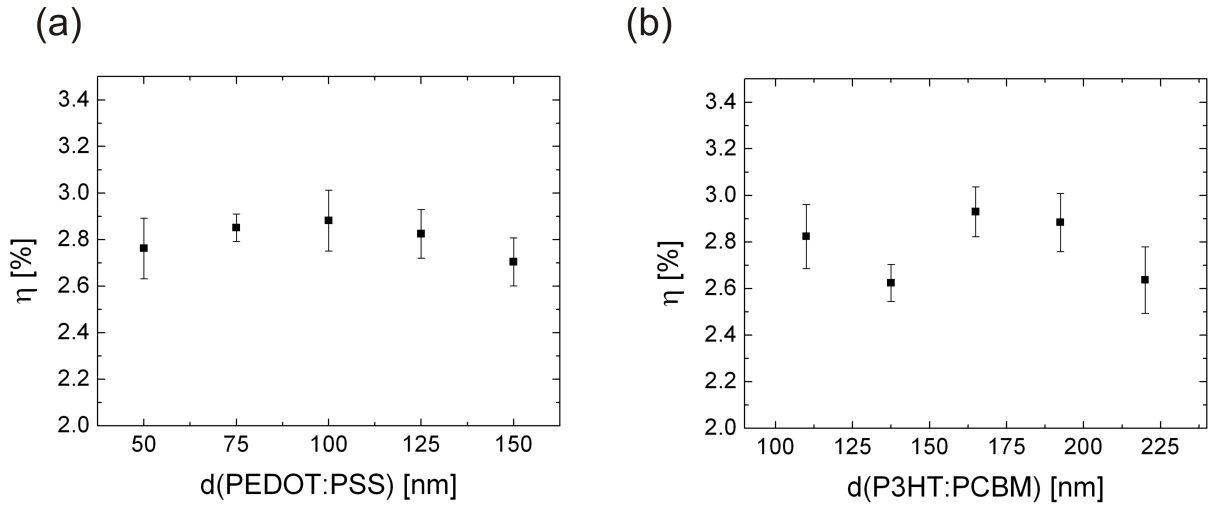


Figure A.8: Power conversion efficiencies of P3HT:PCBM BHJ solar cells for variations in film thickness of (a) the PEDOT:PSS layer and (b) the active layer.

the P3HT:PCBM solar cells vary only slightly between 2.65 and 2.92 % for active layer thicknesses between 110 and 220 nm.

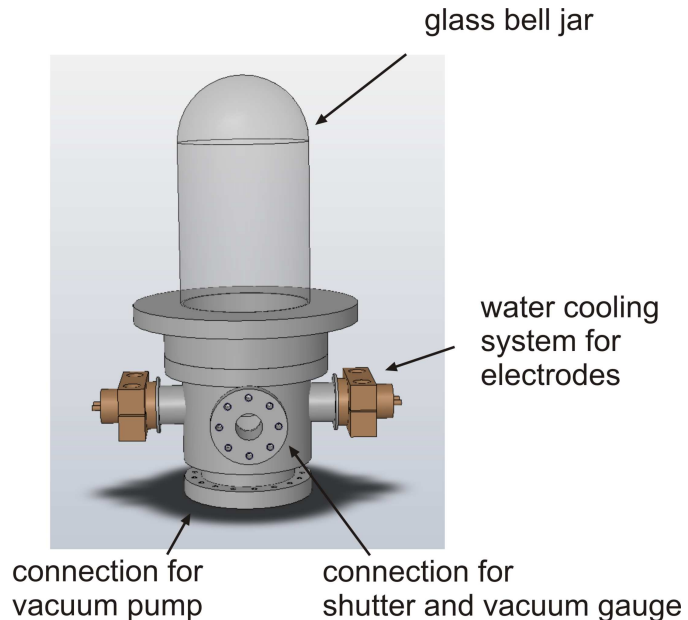
A.4 Design and implementation of thermal evaporation set-up

An additional project within this PhD thesis was the design and the implementation of a thermal evaporation set-up as it is used for the deposition of the metal electrodes in OSCs. Two main aspects were important for the design of the set-up : (i) Fast processing times and (ii) a possible installation in a glove box.

In figure A.9 the three-dimensional AutoCAD drawing of the vacuum recipient and the covering glass bell jar is shown. The recipient has an inner diameter of 150 mm and a depth of 160 mm. A cylindrical glass bell jar allows the continuous monitoring of the evaporation process. In principal, different glass bell jars with a diameter between 145 and 260 mm can be placed on the polished sealing surface of recipient. Currently, two bell jars are available for the set-up: one with a diameter of 160 mm and a height of 250 mm, and the second with a diameter of 250 mm and a height of 170 mm. Besides a standardized sample holder for OSCs, also other samples can be coated by simply fixing them on a flat sample holder. In general, values between 100 and 250 mm are possible for the distance between the sample and the evaporation source. For the materials applied as top electrodes in OSCs - aluminum and gold - a working pressure around $1 - 3 \cdot 10^{-5}$ mbar

is suited. In this pressure range gold evaporates at a temperature around 1300 °C and aluminum around 900 °C, respectively. For the thermal evaporation of gold, boat sources made of tungsten (Kurt J. Lesker, tungsten dimple EVS7005W) are used, which can reach temperatures of 1800 °C if a current of 180 A ($P = 450$ W). In case of aluminum, which is actually the standard electrode material, tungsten boat heaters from Leybold Optics GmbH are applied (BD482000-T). For the high electrical current a power transformer from GETRA (Au/Hallertau, Germany) is connected to the two electrodes. Especially in case of gold elongated evaporation times are necessary to achieve sufficient film thicknesses, which, hence, result in a heating of the copper electrodes. In order to avoid any heating of the recipient, which might lead to a loss of working pressure due to material expansion, an additional water cooling system for the electrodes was designed.

Figure A.9: Three-dimensional AutoCAD drawing of the designed evaporation set-up: For clarity only the vacuum recipient, the glass bell jar, the electrodes including the water cooling system, and the vacuum connections for the vacuum pump and shutter are included.



In order to avoid a high leakage rate mostly high vacuum copper gaskets are used (especially for the large sealing surfaces) and only the bell jar, the two electrodes, and the vacuum gauge are connected to the recipient via viton gaskets. For short evacuation times, the system is equipped with a combination of a nEXT 300 D turbo pump and a XDS 10 scroll pump (both from Edwards, Kirchheim, Germany). For the smaller glass bell jar evacuation times of approximately 15 min are sufficient to reach the necessary vacuum. For an improved control of the total evaporation time a mechanical shutter was installed to shield the samples from the evaporation source.

In figure A.10 an image of the evaporation set-up is shown in operation. On the left control unit the current status of the turbo pump is monitored and the other two displays show the actual pressure in the main chamber and at the turbo pump. According to the Planck's law the boat sources start to emit light at the high temperatures necessary for

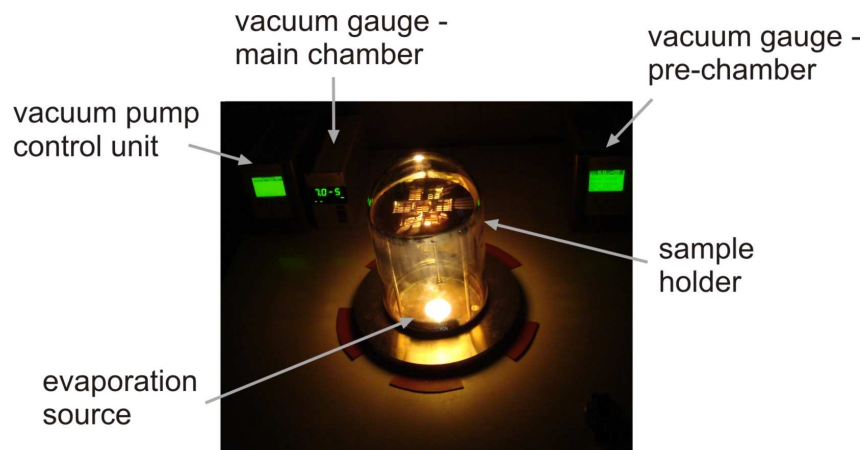


Figure A.10: Image of the evaporation set-up in operation. The status of the turbo pump, the pressure in the main chamber and at the turbo pump are monitored by the different control units. In addition, the sample holder and the evaporation source are seen.

evaporation. In the bell jar the sample holder is seen with the empty slots for the OSCs. In a last update, the evaporation set-up will be equipped with a crystal sensor (SL-A0E40) and the corresponding multi film rate/thickness monitor (SQM-160). Both instruments were purchased from Inficon (New York, USA) and allow for a distinct control of the metal layer thickness and the deposition rate during evaporation.

Bibliography

- [1] E. Becquerel. Mémoire sur les effets électriques produits sous l'influence des rayons solaires. *Comptes rendus*, 9:561–567, 1839.
- [2] S. Carnot. Reflections sur la puissance motrice du feu. *Bachelier*, 1824.
- [3] G. Dennler and C. J. Brabec. *Organic Photovoltaics*. Wiley-VCH, 2008.
- [4] International Energy Agency. Key world energy statistics. *www.iea.org*, January 2012.
- [5] BP. Statistical review of world energy 2009. *www.bp.com/statisticalreview*, January 2012.
- [6] W. P. Su, J. R. Schrieffer, and A. J. Heeger. Soliton excitations in polyacetylene. *Phys. Rev. B*, 22:2099–2111, 1980.
- [7] National Renewable Energy Laboratory. Best-research cell efficiencies 2011. *www.nrel.gov/ncpv/*, January 2012.
- [8] M. A. Green, K. Emery, Y. Hishikawa, W. Warta, and E. D. Dunlop. Solar cell efficiency tables (version 39). *Prog. Photovolt: Res. Appl.*, 20:12–20, 2012.
- [9] M. C. Scharber, D. Mühlbacher, M. Koppe, P. Denk, C. Waldauf, A. J. Heeger, and C. J. Brabec. Design rules for donors in bulk-heterojunction solar cells - towards 10 % energy-conversion efficiency. *Adv. Mater.*, 18:789–794, 2006.
- [10] G. Dennler, M. C. Scharber, T. Ameri, P. Denk, K. Forberich, C. Waldauf, and C. J. Brabec. Design rules for donors in bulk-heterojunction tandem solar cells - towards 15 % energy conversion efficiency. *Adv. Mater.*, 20:579–583, 2008.
- [11] D. Mühlbacher, M. Scharber, M. Morana, Z. Zhu, D. Waller, R. Gaudiana, and C. Brabec. High photovoltaic performance of a low-bandgap polymer. *Adv. Mater.*, 18:2884–2889, 2006.

- [12] G. Yu, J. Gao, J. C. Hummelen, F. Wudl, and A. J. Heeger. Polymer photovoltaic cells: Enhanced efficiencies via a network of internal donor-acceptor heterojunctions. *Science*, 270:1789–1791, 1995.
- [13] G. Yu, C. Zhang, and A. J. Heeger. Dual-function semiconducting polymer devices: Light-emitting and photodetecting diodes. *Appl. Phys. Lett.*, 64:1540–1542, 1994.
- [14] N. S. Sariciftci, D. Braun, C. Zhang, V. I. Srdanov, A. J. Heeger, G. Stucky, and F. Wudl. Semiconducting polymer-buckminsterfullerene heterojunctions: Diodes, photodiodes, and photovoltaic cells. *Appl. Phys. Lett.*, 62:585–587, 1993.
- [15] W. G. Adams and R. E. Day. The action of light on selenium. *Proc. R. Soc. London, Ser. A*, 25:113–117, 1876.
- [16] J.-L. Bredas, J. Cornil, D. Beljonne, D. A. dos Santos, and Z. Shuai. Excited-state electronic structure of conjugated oligomers and polymers: A quantum-chemical approach to optical phenomena. *Acc. Chem. Res.*, 32:267–276, 1999.
- [17] R. E. Peierls. *Quantum Theory of Solids*. Oxford University Press: Oxford, 1955.
- [18] S. Yang and M. Kertesz. Bond length alternation and energy band gap of polyene. *J. Phys. Chem. A*, 110:9771–9774, 2006.
- [19] G. Strobl. *The Physics of Polymers - Concepts for Understanding Their Structure and Behavior*. Springer Verlag, 2007.
- [20] C. Deibel, T. Strobel, and V. Dyakonov. Role of the charge transfer state in organic donor-acceptor solar cells. *Adv. Mater.*, 22:4097–4111, 2010.
- [21] G. Blanchard and J. P. Heritage. Franck-Condon enhancement of $\chi^{(3)}$ in a conjugated polymer under double resonance conditions. *J. Chem. Phys.*, 93:4377–4382, 1990.
- [22] H. D. Burrows, J. S. de Melo, C. Serpa, L. G. Arnaut, A. P. Monkman, I. Hamblett, and S. Navaratnam. S1 \rightarrow T1 intersystem crossing in π -conjugated organic polymers. *J. Chem. Phys.*, 115:9601, 2001.
- [23] G. Lanzani, G. Cerullo, C. Brabec, and N. S. Sariciftci. Time domain investigation of the intrachain vibrational dynamics of a prototypical light-emitting conjugated polymer. *Phys. Rev. Lett.*, 90:047402, 2003.
- [24] R. Kersting, U. Lemmer, R. F. Mahrt, K. Leo, H. Kurz, H. Bässler, and E. O. Göbel. Femtosecond energy relaxation in π -conjugated polymers. *Phys. Rev. Lett.*, 70:3820–3823, 1993.

- [25] V. I. Arkhipov, E. V. Emelianova, and H. Bässler. Hot exciton dissociation in a conjugated polymer. *Phys. Rev. Lett.*, 82:1321–1324, 1999.
- [26] J. G. Müller, M. Anni, U. Scherf, J. M. Lupton, and J. Feldmann. Vibrational spectroscopy of single conjugated polymer molecules. *Phys. Rev. B*, 70:035205, 2004.
- [27] C. Silva. A little energy goes a long way. *Nature Materials*, 9:884–885, 2010.
- [28] L. Lüer, H.-J. Egelhaaf, D. Oelkrug, G. Cerullo, G. Lanzani, B.-H. Huisman, and D. Leeuw. Oxygen-induced quenching of photoexcited states in polythiophene films. *Org. Electron.*, 5:83–89, 2004.
- [29] T. Stübinger and W. Brütting. Exciton diffusion and optical interference in organic donor-acceptor photovoltaic cells. *J. Appl. Phys.*, 90:3632–3641, 2001.
- [30] A. C. Morteani, R. H. Friend, and C. Silva. Exciton trapping at heterojunctions in polymer blends. *J. Chem. Phys.*, 122:244906, 2005.
- [31] J. J. M. Halls, J. Cornil, D. A. dos Santos, R. Silbey, D.-H. Hwang, A. B. Holmes, J. L. Bredas, and R. H. Friend. Charge- and energy transfer processes at polymer/polymer interfaces: A joint experimental and theoretical study. *Phys. Rev. B*, 60:5721–5727, 1999.
- [32] N. S. Sariciftci, L. Smilowitz, A. J. Heeger, and F. Wudl. Photoinduced electron transfer from a conducting polymer to buckminsterfullerene. *Science*, 258:1474–1476, 1992.
- [33] C. J. Brabec, G. Zerza, G. Cerullo, S. De Silvestri, S. Luzzati, J. C. Hummelen, and N. S. Sariciftci. Tracing photoinduced electron transfer process in conjugated polymer/fullerene bulk heterojunctions in real time. *Chem. Phys. Lett.*, 340:232–236, 2001.
- [34] J. P. S. Farinha and J. M. G. Martinho. Resonance energy transfer in polymer nanodomains. *J. Phys. Chem. C*, 112:10591, 2008.
- [35] T. Förster. Experimentelle und theoretische Untersuchungen des zwischenmolekularen Übergangs von Elektronenanregungsenergie. *Z. Naturforsch. Sect. A*, 4:321–327, 1949.
- [36] I. Z. Steinberg. Nonradiative energy transfer in systems in which rotatory brownian motion is frozen. *J. Chem. Phys.*, 48:2411–2413, 1968.

- [37] J. Yang, M. A. Winnik, and T. Pakula. Numerical simulations of fluorescence resonance energy transfer in diblock copolymer lamellae. *Macromolecules*, 38:8882–8890, 2005.
- [38] R. Gelles and C. W. Frank. Effect of molecular weight on polymer blend phase separation kinetics. *Macromolecules*, 16:1448–1456, 1982.
- [39] L. Onsager. Initial recombination of ions. *Phys. Rev.*, 54:554–557, 1938.
- [40] C. L. Braun. Electric field assisted dissociation of charge transfer states as a mechanism of photocarrier production. *J. Chem. Phys.*, 80:4157–4161, 1984.
- [41] V. D. Mihailetschi, L. J. A. Koster, J. C. Hummelen, and P. W. M. Blom. Photocurrent generation in polymer-fullerene bulk heterojunctions. *Phys. Rev. Lett.*, 93:216601, 2004.
- [42] C. Deibel, T. Strobel, and V. Dyakonov. Origin of the efficient polaron pair dissociation in polymer-fullerene blends. *Phys. Rev. Lett.*, 113:036402, 2009.
- [43] H. Ohkita, S. Cook, Y. Astuti, W. Duffy, S. Tierney, W. Zhang, M. Heeney, I. McCulloch, J. Nelson, D. D. C. Bradley, and J. R. Durrant. Charge carrier formation in polythiophene/fullerene blend films studied by transient absorption spectroscopy. *J. Am. Chem. Soc.*, 130:3030–3042, 2008.
- [44] R. A. Marcus. On the theory of oxidation-reduction reactions involving electron transfer. I. *J. Chem. Phys.*, 24:966–978, 1956.
- [45] R. A. Marcus. Electron transfer reactions in chemistry. Theory and experiment. *Rev. Mod. Phys.*, 65:599–610, 1993.
- [46] A. Miller and E. Abrahams. Impurity conduction at low concentrations. *Phys. Rev.*, 120:745–755, 1960.
- [47] H. Bässler. Charge transport in disordered organic photoconductors - a Monte Carlo simulation study. *phys. stat. sol. (b)*, 175:15–56, 1993.
- [48] H. Houli, E. Tutis, I. Batistic, and L. Zuppiroli. Investigation of the charge transport through disordered organic molecular heterojunctions. *J. Appl. Phys.*, 100:033702, 2006.
- [49] T. Offermans, S. C. J. Meskers, and R. A. J. Janssen. Monte-Carlo simulations of geminate electron-hole pair dissociation in a molecular heterojunction: a two-step dissociation mechanism. *Chem. Phys.*, 308:125–133, 2005.

- [50] S. V. Novikov, D. H. Dunlap, V. M. Kenkre, P. E. Parris, and A. V. Vannikov. Essential role of correlations in governing charge transport in disordered organic materials. *Phys. Rev. Lett.*, 81:4472–4475, 1998.
- [51] C. Tanase, E. J. Meijer, P. W. M. Blom, and D. M. de Leeuw. Unification of the hole transport in polymeric field-effect transistors and light-emitting diodes. *Phys. Rev. Lett.*, 91:216601, 2003.
- [52] W. F. Pasveer, J. Cottaar, C. Tanase, R. Coehoorn, P. A. Bobbert, P. W. M. Blom, D. M. de Leeuw, and M. A. J. Michels. Unified description of charge-carrier mobilities in disordered semiconducting polymers. *Phys. Rev. Lett.*, 94:206601, 2005.
- [53] V. I. Arkhipov, E. V. Emelianova, and G. J. Adriaenssens. Effective transport energy versus the energy of most probable jumps in disordered hopping systems. *Phys. Rev. B*, 64:125125, 2001.
- [54] R. J. O. M. Hoofman, M. P. de Haas, L. D. A. Siebbeles, and J. M. Warman. Highly mobile electrons and holes on isolated chains of the semiconducting polymer poly(phenylene vinylene). *Nature*, 392:54–56, 1998.
- [55] P. J. Flory. Thermodynamics of high polymer solutions. *J. Chem. Phys.*, 9:660–661, 1941.
- [56] P. J. Flory. Thermodynamics of high polymer solutions. *J. Chem. Phys.*, 10:51–61, 1942.
- [57] M. L. Huggins. Solutions of long chain compounds. *J. Chem. Phys.*, 9:440, 1941.
- [58] M. L. Huggins. Some properties of solutions of long-chain compounds. *J. Phys. Chem.*, 46:151–158, 1942.
- [59] T. Nishi and T. T. Wang. Melting point depression and kinetic effects of cooling on crystallization in poly(vinylidene fluoride)-poly(methyl methacrylate) mixtures. *Macromolecules*, 8:909–915, 1975.
- [60] C. Koning, M. van Duin, C. Pagnouille, and R. Jerome. Strategy for compatibilization of polymer blends. *Prog. Polym. Sci.*, 23:707–757, 1998.
- [61] K. Binder. Phase transitions of polymer blends and block copolymer melts in thin films. *Adv. Polym. Sci.*, 138:1–89, 1999.
- [62] P. G. de Gennes. Dynamics of fluctuations and spinodal decomposition in polymer blends. *J. Chem. Phys.*, 72:4759–4763, 1980.

- [63] K. Binder. Collective diffusion, nucleation, and spinodal decomposition in polymer mixtures. *J. Chem. Phys.*, 79:6387–6409, 1983.
- [64] I. Schmidt and K. Binder. Model calculations for wetting transitions in polymer mixtures. *J. Phys. France*, 46:1631–1644, 1985.
- [65] T. Flebbe, B. Dünweg, and K. Binder. Phase separation versus wetting: a mean field theory for symmetrical polymer mixtures confined between selectively attractive walls. *J. Phys. II France*, 6:667–695, 1996.
- [66] C. Shen and T. Kyu. Spinodals in a polymer dispersed liquid crystal. *J. Chem. Phys.*, 102:556–562, 1995.
- [67] W. Maier and A. Saupe. Eine einfache molekularstatistische Theorie der nematischen kristallinflüssigen Phase. Teil 1. *Z. Naturforsch., A: Phys. Sci.*, 14:882, 1959.
- [68] W. Maier and A. Saupe. Eine einfache molekularstatistische Theorie der nematischen kristallinflüssigen Phase. Teil 2. *Z. Naturforsch., A: Phys. Sci.*, 15:287, 1960.
- [69] M. Mucha. Polymer as an important component of blends and composites with liquid crystals. *Prog. Polym. Sci.*, 28:837–873, 2003.
- [70] P. G. de Gennes. *The Physics of Liquid Crystals*. Oxford University Press, 1974.
- [71] A. Z. Panagiotopoulos. Direct determination of phase coexistence properties of fluids by Monte Carlo simulation in a new ensemble. *Mol. Phys.*, 61:813–826, 1987.
- [72] H. S. Lee, H. C. Jung, M. S. Han, C. S. Lee, and W. N. Kim. Compatibility studies of blends of a thermotropic liquid crystalline polymer and flexible chain polymers by application of Flory’s lattice theory. *Polymer*, 42:2177–2184, 2001.
- [73] P. J. Flory. Statistical thermodynamics of mixtures of rodlike particles. 6. Rods connected by flexible joints. *Macromolecules*, 11:1141–1144, 1978.
- [74] G. Strobl. From the melt via mesomorphic and granular crystalline layers to lamellar crystallites: A major route followed in polymer crystallization? *Eur. Phys. J. E*, 3:165–183, 2000.
- [75] A. J. Liu and G. H. Fredrickson. Phase separation kinetics of rod/coil mixtures. *Macromolecules*, 29:8000–8009, 1996.

- [76] Z. Akcasu, M. Benmouna, and H. Benoit. Application of random phase approximation to the dynamics of polymer blends and copolymers. *Polymer*, 27:1935–1942, 1986.
- [77] L. Onsager. Reciprocal relations in irreversible processes. 1. *Phys. Rev.*, 37:405–426, 1931.
- [78] E. Kim, Y. Xia, and G. M. Whitesides. Polymer microstructures formed by moulding in capillaries. *Nature*, 376:581–584, 1995.
- [79] E. Kim and G. M. Whitesides. Imbibition and flow of wetting liquids in noncircular capillaries. *J. Phys. Chem. B*, 101:855–863, 1997.
- [80] J. B. Hudson. *Surface Science - An Introduction*. Butterworth-Heinemann, 1990.
- [81] D. Myers. *Surfaces, Interfaces, and Colloids - Principles and Applications*. VCH, 1991.
- [82] S. Y. Chou, P. R. Krauss, and P. J. Renstrom. Imprint of sub-25 nm vias and trenches in polymers. *Appl. Phys. Lett.*, 67:3114–3116, 1995.
- [83] S. Y. Chou, P. R. Krauss, W. Zhang, L. Guo, and L. Zhuang. Sub-10 nm imprint lithography and applications. *J. Vac. Sci. Technol.*, 15:2897–2904, 1997.
- [84] H. D. Rowland, A. C. Sun, P. R. Schunk, and W. P. King. Impact of polymer film thickness and cavity size on polymer flow during embossing: toward process design rules for nanoimprint lithography. *J. Micromech. Microeng.*, 15:2414–2425, 2005.
- [85] R. P. Chhabra and J. F. Richardson. *Non-Newtonian Flow in the Process Industries*. Butterworth-Heinemann, 1999.
- [86] P. Wapperom and R. Keunings. Simulation of linear polymer melts in transient complex flow. *J. Non-Newtonian Fluid Mech.*, 95:67–83, 2000.
- [87] G. A. A. V. Haagh and F. N. van de Vosse. Simulation of three-dimensional polymer mould filling processes using a pseudo-concentration method. *Int. J. Numer. Meth. Fluids*, 28:1355–1369, 1998.
- [88] H. D. Rowland and W. P. King. Polymer deformation and filling modes during microembossing. *J. Micromech. Microeng.*, 14:1625–1632, 2004.
- [89] A. Guinier and G. Fournet. *Small Angle Scattering of X-rays*. Wiley, 1955.
- [90] M. Tolan. *X-Ray Scattering from Soft-Matter Thin Films*. Springer Verlag, 1999.

- [91] H. Kiessig. Interferenz von Röntgenstrahlen an dünnen Schichten. *Ann. Phys.*, 402:769–788, 1931.
- [92] H. Zabel. X-ray and neutron reflectivity analysis of thin films and superlattices. *Appl. Phys. A*, 58:159–168, 1994.
- [93] G. Decher. Fuzzy nanoassemblies: Toward layered polymeric multicomposites. *Science*, 277:1232–1237, 1997.
- [94] L. G. Parratt. Surface studies of solids by total reflection of X-rays. *Phys. Rev.*, 95:359–369, 1954.
- [95] L. Névot and P. Croce. Caractérisation des surfaces par réflexion rasante de rayons x. application à l'étude du polissage de quelques verres silicates. *Phys. Appl.*, 15:761–779, 1980.
- [96] P. Müller-Buschbaum and M. Stamm. Correlated roughness, long-range correlations, and dewetting of thin polymer films. *Macromolecules*, 31:3686–3692, 1998.
- [97] P. Müller-Buschbaum. Grazing incidence small-angle x-ray scattering: an advanced scattering technique for the investigation of nanostructured polymer films. *Anal. Bioanal. Chem.*, 376:3–10, 2003.
- [98] M. Rauscher, T. Salditt, and H. Spohn. Small-angle x-ray scattering under grazing incidence: The cross section in the distorted-wave Born approximation. *Phys. Rev. B*, 52:16855–16863, 1995.
- [99] S. K. Sinha, E. B. Sirota, and S. Garof. X-ray and neutron scattering from rough surfaces. *Phys. Rev. B*, 38:2297–2311, 1988.
- [100] R. Lazzari, F. Leroy, and G. Renaud. Grazing-incidence small-angle x-ray scattering from dense packing of islands on surfaces: Development of distorted wave Born approximation and correlation between particle sizes and spacing. *Phys. Rev. B*, 76:125411, 2007.
- [101] M. Schmidbauer, D. Grigoriev, M. Hanke, P. Schäfer, T. Wiebach, and R. Köhler. Effects of grazing incidence conditions on the x-ray diffuse scattering from self-assembled nanoscale islands. *Phys. Rev. B*, 71:115324, 2005.
- [102] Y. Yoneda. Anomalous surface reflection of X-rays. *Phys. Rev.*, 131:2010–2013, 1963.

- [103] R. Hosemann and S. N. Bagchi. *Direct Analysis of Diffraction by Matter*. Amsterdam: North-Holland, 1962.
- [104] F. Leroy, R. Lazzari, and G. Renaud. Effects of near-neighbor correlations on the diffuse scattering from a one-dimensional paracrystal. *Acta Cryst.*, 60:565–581, 2004.
- [105] M. Kotlarchyk and S.-H. Chen. Analysis of small angle neutron scattering spectra from polydisperse interacting colloids. *J. Chem. Phys.*, 79:2461–2469, 1983.
- [106] R. Lazzari. IsGISAXS: a program for grazing-incidence small-angle X-ray scattering analysis of supported islands. *J. Appl. Cryst.*, 35:406–421, 2002.
- [107] M. Yan and A. Gibaud. On the intersection of grating truncation rods with the Ewald sphere studied by grazing-incidence small-angle x-ray scattering. *J. Appl. Cryst.*, 40:1050–1055, 2007.
- [108] P. P. Ewald. Introduction to the dynamical theory of X-ray diffraction. *Acta Cryst. A*, 25:103–108, 1969.
- [109] M. Yan, J. F. Bardeau, G. Brotons, T. Metzger, and A. Gibaud. Combined studies of gratings by X-ray reflectivity, GISAXS, and AFM. *KEK Proc.*, 3:107–116, 2006.
- [110] M. Jergel, P. Mikulik, E. Majkova, S. Luby, R. Senderak, E. Pincik, M. Brunel, P. Hudek, I. Kostic, and A. Konecnikova. Structural characterization of lamellar multilayer gratings by x-ray reflectivity and scanning electron microscopy. *J. Phys. D: Appl. Phys.*, 32:220–223, 1999.
- [111] J. Stöhr. *NEXAFS Spectroscopy*. Springer Verlag, 1992.
- [112] B. L. Henke, E. M. Gullikson, and J. C. Davis. X-ray interactions: photoabsorption, scattering, transmission, and reflection at $E = 50\text{--}30,000$ eV, $Z = 1\text{--}192$. *At. Data Nucl. Data Tables*, 54:181–342, 1993.
- [113] B. Watts, S. Swaraj, D. Nordlund, J. Lüning, and H. Ade. Calibrated NEXAFS spectra of common conjugated polymers. *J. Chem. Phys.*, 134:024702, 2011.
- [114] H. Ade and H. Stoll. Near-edge x-ray absorption fine-structure microscopy of organic and magnetic materials. *Nature*, 8:281–290, 2009.
- [115] A. Einstein. Über einen die Erzeugung und Verwandlung des Lichtes betreffenden heuristischen Gesichtspunkt. *Ann. Phys.*, 322:132–148, 1905.

- [116] G. Binnig, C. F. Quate, and C. Gerber. Atomic force microscope. *Phys. Rev. Lett.*, 56:930–933, 1986.
- [117] G. Binnig and H. Rohrer. Scanning tunneling microscopy. *Surf. Sci.*, 152-153:17–26, 1985.
- [118] S. Morita, R. Wiesendanger, and E. Meyer, editors. *Noncontact Atomic Force Microscopy*. Springer Verlag, 2002.
- [119] C. D. Bain, E. B. Troughton, Y. T. Tao, J. Evall, G. M. Whitesides, and R. G. Nuzzo. Formation of monolayer films by the spontaneous assembly of organic thiols from solution onto gold. *J. Am. Chem. Soc.*, 111:321–335, 1989.
- [120] H. G. Tompkins. *A user's guide to ellipsometry*. Academic Press, New York, 1993.
- [121] R. D. Deslattes, E. G. Kessler, P. Indelicato, L. de Billy, E. Lindroth, and J. Anton. X-ray transition energies: new approach to a comprehensive evaluation. *Rev. Mod. Phys.*, 75:35–99, 2003.
- [122] C. Braun. *Parratt32*, HMI Berlin, 2002.
- [123] P. Müller-Buschbaum. *Polymer Surfaces and Interfaces: Characterization, Modification and Applications*, chapter Structure Determination in Thin Film Geometry Using Grazing Incidence Small-Angle Scattering, pages 17–46. Springer Verlag, 2008.
- [124] P. Müller-Buschbaum. High-resolution grazing incidence small angle X-ray scattering: Investigation of micrometer sized structured polymer films. *Progr. Colloid. Polym. Sci.*, 132:23–32, 2006.
- [125] S. V. Roth, R. Döhrmann, M. Dommach, M. Kuhlmann, I. Kröger, R. Gehrke, H. Walter, C. Schroer, B. Lengeler, and P. Müller-Buschbaum. Small-angle options of the upgraded ultrasmall-angle x-ray scattering beamline BW4 at HASYLAB. *Rev. Sci. Instrum.*, 77:085106, 2006.
- [126] J. Perlich, J. Rubeck, S. Botta, R. Gehrke, S. V. Roth, M. A. Ruderer, S. M. Prams, M. Rawolle, Q. Zhong, V. Körstgens, and P. Müller-Buschbaum. Grazing incidence wide angle x-ray scattering at the wiggler beamline BW4 of HASYLAB. *Rev. Sci. Instrum.*, 81:105105, 2011.
- [127] C. R. McNeill, A. Abrusci, I. Hwang, M. A. Ruderer, P. Müller-Buschbaum, and N. C. Greenham. Photophysics and photocurrent generation in polythiophene/polyfluorene copolymer blends. *Adv. Funct. Mater.*, 19:3103–3111, 2009.

- [128] P. Müller-Buschbaum. *Applications of Synchrotron Light to Scattering and Diffraction in Materials and Life Sciences*. Springer Verlag, 2009.
- [129] J. Raabe, Tzvetkov, U. Flechsig, M. Böge, A. Jaggi, B. Sarafimov, M. G. C. Ver-nooij, T. Huthwelker, H. Ade, D. Kilcoyne, T. Tyliczszak, R. H. Fink, and C. Quit-mann. PolLux: A new facility for soft x-ray spectromicroscopy at the Swiss Light Source. *Rev. Sci. Instrum.*, 79:113704, 2008.
- [130] J. Kirz and H. Rarback. Soft x-ray microscopes. *Rev. Sci. Instrum.*, 56:1–13, 1985.
- [131] U. Frommherz, J. Raabe, B. Watts, R. Stefani, and U. Ellenberger. Higher order suppressor (HOS) for the PolLux microspectroscopy beamline at the Swiss Light Source SLS. *AIP Conf. Proc.*, 1234:429–432, 2010.
- [132] H. Ade and A. P. Hitchcock. NEXAFS microscopy and resonant scattering: Com-position and orientation probed in real and reciprocal space. *Polymer*, 49:643–675, 2008.
- [133] C. R. McNeill, B. Watts, L. Thomsen, W. J. Belcher, N. C. Greenham, and P. C. Dastoor. Nanoscale quantitative chemical mapping of conjugated polymer blends. *Nano Lett.*, 6:1202–1206, 2006.
- [134] B. Watts, W. J. Belcher, L. Thomsen, H. Ade, and P. C. Dastoor. A quantitative study of PCBM diffusion during annealing of P3HT:PCBM blend films. *Macro-molecules*, 42:8392–8397, 2009.
- [135] K. Jefimovs, J. Vila-Comamala, T. Pilvi, J. Raabe, M. Ritala, and C. David. Zone-doubling technique to produce ultrahigh-resolution X-ray optics. *Phys. Rev. Lett.*, 99:264801, 2007.
- [136] D. M. Chapin, C. S. Fuller, and G. L. Pearson. A new silicon pn junction photocell for converting solar radiation into electrical power. *J. Appl. Phys.*, 25:676, 1954.
- [137] M. H. Harun, E. Saion, A. Kassim, N. Yahya, and E. Mahmud. Conjugated con-ducting polymers: A brief overview. *J. Acoust. Soc. Am.*, 2:63–68, 2007.
- [138] J. Drechsel, B. Männig, F. Kozlowski, M. Pfeiffer, K. Leo, and H. Hoppe. Effi-cient organic solar cells based on a double *p-i-n* architecture using doped wide-gap transport layers. *Appl. Phys. Lett.*, 86:244102, 2005.
- [139] J. H. Burroughes, D. D. C. Bradley, A. R. Brown, R. N. Marks, K. Mackay, R. H. Friend, P. L. Burns, and A. B. Holmes. Light-emitting diodes based on conjugated polymers. *Nature*, 347:539–541, 1990.

- [140] D. Braun and A. J. Heeger. Visible light emission from semiconducting polymer diodes. *Appl. Phys. Lett.*, 58:1982–1984, 1991.
- [141] T. Kietzke, H.-H. Hörhold, and D. Neher. Efficient polymer solar cells based on M3EH-PPV. *Chem. Mater.*, 17:6532–6537, 2005.
- [142] S. E. Shaheen, C. J. Brabec, N. S. Sariciftci, F. Padinger, T. Fromherz, and J. C. Hummelen. 2.5 % efficient organic plastic solar cells. *Appl. Phys. Lett.*, 78:841–843, 2001.
- [143] G. Zhao, Y. He, and Y. Li. 6.5% efficiency of polymer solar cells based on poly(3-hexylthiophene) and indene-C₆₀ bisadduct by device optimization. *Adv. Mater.*, 22:4355–4358, 2010.
- [144] H. Hoegl, O. Süss, and W. Neugebauer. *German Patent*, (1,068,115), 1957.
- [145] H. Hoegl. On photoelectric effects in polymers and their sensitization by dopants. *J. Phys. Chem.*, 69:755–766, 1965.
- [146] H. Wu, G. Zhou, J. Zou, C.-L. Ho, W.-Y. Wong, W. Yang, J. Peng, and Y. Cao. Efficient polymer white-light-emitting devices for solid-state lighting. *Adv. Mater.*, 21:4181–4184, 2009.
- [147] D. M. de Leeuw, M. M. J. Simenon, A. R. Brown, and R. E. F. Einerhand. Stability of n-type doped conducting polymers and consequences for polymeric microelectronic devices. *Synth. Met.*, 87:53–59, 1997.
- [148] P. W. M. Blom, M. J. M. de Jong, and J. J. M. Vleggaar. Electron and hole transport in poly(p-phenylene vinylene) devices. *Appl. Phys. Lett.*, 68:3308–3310, 1996.
- [149] B. Watts, T. Schuettfort, and C. R. McNeill. Mapping of domain orientation and molecular order in polycrystalline semiconducting polymer films with soft X-ray microscopy. *Adv. Funct. Mater.*, 21:1122–1131, 2010.
- [150] C. R. McNeill, J. J. M. Halls, R. Wilson, G. L. Whiting, S. Berkebile, M. G. Ramsey, R. H. Friend, and N. C. Greenham. Efficient polythiophene/polyfluorene copolymer bulk heterojunction photovoltaic devices: Device physics and annealing effects. *Adv. Funct. Mater.*, 18:2309–2321, 2008.
- [151] B. Kraabel, C. H. Lee, D. McBranch, D. Moses, N. S. Sariciftci, and A. J. Heeger. Ultrafast photoinduced electron transfer in conducting polymer-buckminsterfullerene composites. *Chem. Phys. Lett.*, 213:389–394, 1993.

- [152] W. Ma, C. Yang, X. Gong, K. Lee, and A. J. Heeger. Thermally stable, efficient polymer solar cells with nanoscale control of the interpenetrating network morphology. *Adv. Funct. Mater.*, 15:1617–1622, 2005.
- [153] S.-H. Lee, D.-H. Kim, J.-H. Kim, G.-S. Lee, and J.-G. Park. Effect of metal-reflection and surface-roughness properties on power-conversion efficiency for polymer photovoltaic cells. *J. Phys. Chem. C*, 113:21915–21920, 2009.
- [154] S. A. Carter, M. Angelopoulos, S. Karg, P. J. Brock, and J. C. Scott. Polymeric anodes for improved polymer light-emitting diode performance. *Appl. Phys. Lett.*, 70:2067–2069, 1997.
- [155] T. M. Brown, J. S. Kim, R. H. Friend, F. Caciallia, R. Daik, and W. J. Feast. Built-in field electroabsorption spectroscopy of polymer light-emitting diodes incorporating a doped poly(3,4-ethylene dioxythiophene) hole injection layer. *Appl. Phys. Lett.*, 75:1679–1681, 1999.
- [156] G. Daoust and M. Leclerc. Structure-property relationships in alkoxy-substituted polythiophenes. *Macromolecules*, 24:455–459, 1991.
- [157] G. Heywang and F. Jonas. Poly(alkylenedioxythiophene)s - new, very stable conducting polymers. *Adv. Mater.*, 4:116–118, 1992.
- [158] M. Kus and S. Okur. Electrical characterization of PEDOT:PSS beyond humidity saturation. *Sens. Actuators, B*, 143:177–181, 2009.
- [159] S. Kirchmeyer and K. Reuter. Scientific importance, properties and growing applications of poly(3,4-ethylenedioxythiophene). *J. Mater. Chem.*, 15:2077–2088, 2005.
- [160] C. Brabec, V. Dyakonov, and U. Scherf, editors. *Organic Photovoltaics - Materials, Device Physics, and Manufacturing Technologies*. Wiley-VCH, 2008.
- [161] U. Lang, E. Müller, N. Naujoks, and J. Dual. Microscopical investigations of PEDOT:PSS thin films. *Adv. Funct. Mater.*, 19:1215–1220, 2009.
- [162] K. E. Aasmundtveit, E. J. Samuelsen, L. A. A. Pettersson, O. Inganäs, T. Johansson, and R. Feidenhans'l. Structure of thin films of poly(3,4-ethylenedioxythiophene). *Synth. Met.*, 101:561–564, 1999.
- [163] L. Niu, C. Kvarnström, K. Fröberg, and A. Ivaska. Electrochemically controlled surface morphology and crystallinity in poly(3,4-ethylenedioxythiophene) films. *Synth. Met.*, 122:425–429, 2001.

- [164] K. Fehse, K. Walzer, K. Leo, W. Lövenich, and A. Elschner. Highly conductive polymer anodes as replacements for inorganic materials in high-efficiency organic light-emitting diodes. *Adv. Mater.*, 19:441–444, 2007.
- [165] A. Jarkov, S. Bereznev, K. Laes, O. Volobujeva, R. Traksmaa, A. Öpik, and E. Melnikov. Conductive polymer PEDOT:PSS back contact for CdTe solar cell. *Thin Solid Films*, 519:7449–7452, 2011.
- [166] F. Zhang and H. Y. Low. Ordered three-dimensional hierarchical nanostructures by nanoimprint lithography. *Nanotechnology*, 17:1884–1890, 2006.
- [167] C. K.-Y Li, Z.-Y Xia, and H.-J Sue. Simple shear plastic deformation behavior of polycarbonate plate II. Mechanical property characterization. *Polymer*, 41:6285–6293, 2000.
- [168] T. W. Odom, V. R. Thalladi, J. C. Love, and G. M. Whitesides. Generation of 30-50 nm structures using easily fabricated, composite PDMS masks. *J. Am. Chem. Soc.*, 124:12112–12113, 2002.
- [169] P. Müller-Buschbaum. Influence of surface cleaning on dewetting of thin polystyrene films. *Eur. Phys. J. E*, 12:443–448, 2003.
- [170] M. Itano, Jr. F. W. Kern, M. Miyashita, and T. Ohmi. Particle removal from silicon wafer surface in wet cleaning process. *IEEE Trans. Semicond. Manuf.*, 6:258–267, 1993.
- [171] C. Weisbuch and M. J. Kelly, editors. *Physics and Fabrication of Microstructures and Microdevices*. Springer Verlag New York, LLC, 1986.
- [172] P. Müller-Buschbaum, J. S. Gutmann, J. Kraus, H. Walter, and M. Stamm. Suppression of roughness replication in bilayer films prepared by spin coating. *Macromolecules*, 33:569–576, 2000.
- [173] D. Meyerhofer. Characteristics of resist films produced by spinning. *J. Appl. Phys.*, 49:3993–3997, 1978.
- [174] D. W. Schubert and T. Dunkel. Spin coating from a molecular point of view: Its concentration regimes, influence of molar mass and distribution. *Mat. Res. Innovat.*, 7:314–321, 2003.
- [175] D. W. Schubert. Spin coating as a method for polymer molecular weight determination. *Polym. Bull.*, 38:177–184, 1997.

- [176] D. Kearns and M. Calvin. The photovoltaic effect and photoconductivity in laminated organic systems. *J. Chem. Phys.*, 29:950–951, 1958.
- [177] H. Hoppe and N. S. Sariciftci. Organic solar cells: An overview. *J. Mater. Res.*, 19:1924–1945, 2004.
- [178] K. T. Kamtekar, A. P. Monkman, and M. R. Bryce. Recent advances in white organic light-emitting materials and devices (WOLEDs). *Adv. Mater.*, 21:1–11, 2009.
- [179] S. Reineke, F. Lindner, G. Schwartz, N. Seidler, K. Walzer, B. Lüssem, and K. Leo. White organic light-emitting diodes with fluorescent tube efficiency. *Nature*, 459:234–239, 2009.
- [180] S. Walheim, M. Böltau, J. Mlynek, G. Krausch, and U. Steiner. Structure formation via polymer demixing in spin-cast films. *Macromolecules*, 30:4995–5003, 1997.
- [181] M. Böltau, S. Walheim, J. Mlynek, G. Krausch, and U. Steiner. Surface-induced structure formation of polymer blends on patterned substrates. *Nature*, 391:877–879, 1998.
- [182] A. J. Parnell, A. D. F. Dunbar, A. J. Pearson, P. A. Staniec, A. J. C. Dennison, H. Hamamatsu, M. W. A. Skoda, D. G. Lidzey, and R. A. L. Jones. Depletion of PCBM at the cathode interface in P3HT/PCBM thin films as quantified via neutron reflectivity measurements. *Adv. Mater.*, 22:2444–2447, 2010.
- [183] S. Kan, X. Liu, F. Shen, J. Zhang, Y. Ma, G. Zhang, Y. Wang, and J. Shen. Improved efficiency of single-layer polymer light-emitting devices with poly(vinylcarbazole) doubly doped with phosphorescent and fluorescent dyes as the emitting layer. *Adv. Funct. Mater.*, 13:603–608, 2003.
- [184] R. Meier, R. C. Word, A. Nadarajah, and R. Könenkamp. Unipolar transport and interface charge transfer in nanostructured CdTe/polymer hybrid films. *Phys. Rev. B*, 77:195314, 2008.
- [185] J. Zou, J. Liu, H. Wu, W. Yang, J. Peng, and Y. Cao. High-efficiency and good color quality white light-emitting devices based on polymer blend. *Org. Electron.*, 10:843–848, 2009.
- [186] F. Kong, Y. M. Sun, and R. K. Yuan. Enhanced resonance energy transfer from PVK to MEH-PPV in nanoparticles. *Nanotechnology*, 18:265707, 2007.

- [187] C. A. Fenstermaker and F. L. McCrackin. Errors arising from surface roughness in ellipsometric measurement of the refractive index of a surface. *Surf. Sci.*, 16:85–96, 1969.
- [188] M.-C. Wu, H.-C. Liao, Y. Chou, C.-P. Hsu, W.-C. Yen, C.-M. Chuang, Y.-Y. Lin, C.-W. Chen, Y.-F. Chen, and W.-F. Su. Manipulation of nanoscale phase separation and optical properties of P3HT/PMMA polymer blends for photoluminescent electron beam resist. *J. Phys. Chem. B*, 114:10277–10284, 2009.
- [189] S. S. van Bavel, E. Sourty, G. de With, and J. Loos. Three-dimensional nanoscale organization of bulk heterojunction polymer solar cells. *Nano Lett.*, 9:507–513, 2009.
- [190] S. Nilsson, A. Bernasik, A. Budkowski, and E. Moons. Morphology and phase segregation of spin-casted films of polyfluorene/PCBM blends. *Macromolecules*, 40:8291–8301, 2007.
- [191] Z. Jiang, D. R. Lee, S. Narayanan, J. Wang, and S. K. Sinha. Waveguide-enhanced grazing-incidence small-angle x-ray scattering of buried nanostructures in thin films. *Phys. Rev. B*, 84:075440, 2011.
- [192] P. C. Jukes, S. Y. Heriot, J. S. Sharp, and R. A. L. Jones. Time-resolved light scattering studies of phase separation in thin film semiconducting polymer blends during spin-coating. *Macromolecules*, 38:2030–2032, 2005.
- [193] M. A. Ruderer, E. Metwalli, W. Wang, G. Kaune, S. V. Roth, and P. Müller-Buschbaum. Thin films of photoactive polymer blends. *Chem. Phys. Chem.*, 10:664–671, 2009.
- [194] J. K. J. van Duren, X. Yang, J. Loos, C. W. T. Bulle-Lieuwma, A. B. Sieval, J. C. Hummelen, and R. A. J. Janssen. Relating the morphology of poly(p-phenylene vinylene)/methanofullerene blends to solar-cell performance. *Adv. Funct. Mater.*, 14:425–434, 2004.
- [195] J.-S. Kim, P. K. H. Ho, C. E. Murphy, and R. H. Friend. Phase separation in polyfluorene-based conjugated polymer blends: Lateral and vertical analysis of blend spin-cast thin films. *Macromolecules*, 37:2861–2841, 2004.
- [196] Y. Kim, M. Shin, and H. Kim. Polymer solar cells with ternary blend nanolayers. *J. Nanosci. Nanotechnol.*, 8:6247–6252, 2008.
- [197] T. Fukuda, S. Kimura, Z. Honda, and N. Kamata. Blue-sensitive organic photoconductive device with MDMO-PPV doped F8BT layer. *Mol. Cryst. Liq. Cryst.*, 539:202–209, 2011.

- [198] S. C. Veenstra, W. J. H. Verhees, J. M. Kroon, M. M. Koetse, J. Sweelssen, J. J. A. M. Bastiaansen, H. F. M. Schoo, X. Yang, A. Alexeev, J. Loos, U. S. Schubert, and M. M. Wienk. Photovoltaic properties of a conjugated polymer blend of MDMO-PPV and PCNEPV. *Chem. Mater.*, 16:2503–2508, 2004.
- [199] K. G. Jespersen, W. J. D. Beenken, Y. Zaushitsyn, A. Yartsev, M. Andersson, T. Pullerits, and V. Sundström. The electronic states of polyfluorene copolymers with alternating donor-acceptor units. *J. Chem. Phys.*, 121:12613–12617, 2004.
- [200] M. A. Ruderer, S. Guo, R. Meier, H.-Y. Chiang, V. Körstgens, J. Wiedersich, J. Perlich, S. V. Roth, and P. Müller-Buschbaum. Solvent-induced morphology in polymer-based systems for organic photovoltaics. *Adv. Funct. Mater.*, 21:3382–3391, 2011.
- [201] F. C. Krebs. Fabrication and processing of polymer solar cells: A review of printing and coating techniques. *Sol. Energy Mater. Sol. Cells*, 93:394–412, 2009.
- [202] H. Hintz, H.-J. Egelhaaf, H. Peisert, and T. Chassé. Photo-oxidation and ozonization of poly(3-hexylthiophene) thin films as studied by UV/VIS and photoelectron spectroscopy. *Polym. Degrad. Stab.*, 95:818–825, 2010.
- [203] M. Manceau, A. Rivaton, J.-L. Gardette, S. Guillerez, and N. Lemaitre. The mechanism of photo- and thermooxidation of poly(3-hexylthiophene) (P3HT) reconsidered. *Polym. Degrad. Stab.*, 94:898–907, 2009.
- [204] M. Manceau, E. Bundgaard, J. E. Carlé, O. Hagemann, M. Helgesen, R. Sondergaard, M. Jorgensen, and F. C. Krebs. Photochemical stability of π -conjugated polymers for polymer solar cells: a rule of thumb. *J. Mater. Chem.*, 21:4132–4141, 2011.
- [205] S. Chambon, A. Rivaton, J.-L. Gardette, M. Firon, and L. Lutsen. Aging of a donor conjugated polymer: Photochemical studies of the degradation of poly[2-methoxy-5-(30,70-dimethyloctyloxy)-1,4-phenylenevinylene]. *J. Polym. Sci., Part A: Polym. Chem.*, 45:317–331, 2007.
- [206] A. Rivaton, S. Chambon, M. Manceau, J.-L. Gardette, N. Lemaître, and S. Guillerez. Light-induced degradation of the active layer of polymer-based solar cells. *Polym. Degrad. Stab.*, 65:278–284, 2010.
- [207] U. Zhokhavets, T. Erb, H. Hoppe, G. Gobsch, and N. S. Sariciftci. Effect of annealing of poly(3-hexylthiophene)/fullerene bulk heterojunction composites on structural and optical properties. *Thin Solid Films*, 496:679–682, 2006.

- [208] J. W. Kiel, A. P. R. Eberle, and M. E. Mackay. Nanoparticle agglomeration in polymer-based solar cells. *Phys. Rev. Lett.*, 105:168701, 2010.
- [209] T. Kirchartz, J. Mattheis, and U. Rau. Detailed balance theory of excitonic and bulk heterojunction solar cells. *Phys. Rev. B*, 78:235320, 2008.
- [210] C.-M. Hansen. *The Three Dimensional Solubility Parameter and Solvent Diffusion Coefficient*. Danish Technical Press, 1967.
- [211] J. Liu, Q. Deng, and Y. C. Jean. Free-volume distributions of polystyrene probed by positron annihilation: comparison with free-volume theories. *Macromolecules*, 26:7149–7155, 1993.
- [212] J. García-Turiel and B. Jérôme. Solvent retention in thin polymer films studied by gas chromatography. *Colloid. Polym. Sci.*, 285:1617–1625, 2007.
- [213] S. Bistac and J. Schultz. Solvent retention in solution-cast films of PMMA: study by dielectric spectroscopy. *Prog. Org. Coat.*, 31:347–350, 1997.
- [214] J. Perlich, V. Körstgens, E. Metwalli, L. Schulz, R. Georgii, and P. Müller-Buschbaum. Solvent content in thin spin-coated polystyrene homopolymer films. *Macromolecules*, 42:337–344, 2009.
- [215] J. T. Francis and A. P. Hitchcock. Distinguishing keto and enol structures by inner-shell spectroscopy. *J. Phys. Chem.*, 98:3650–3657, 1994.
- [216] A. P. Hitchcock. <http://unicorn.mcmaster.ca/corex/cedb-title.html>.
- [217] T. K. Sham, B. X. Yang, J. Kirz, and J. S. Tse. K-edge near-edge x-ray-absorption fine structure of oxygen- and carbon-containing molecules in the gas phase. *Phys. Rev. A*, 40:652–669, 1989.
- [218] R. Meier, M. Schindler, B. Watts, and P. Müller-Buschbaum. Residual solvent content in conducting polymer-blend films mapped with scanning transmission x-ray microscopy. *Phys. Rev. B*, 84:174205, 2011.
- [219] R. Giridharagopal and D. S. Ginger. Characterizing morphology in bulk heterojunction organic photovoltaic systems. *J. Phys. Chem. Lett.*, 1:1160–1169, 2010.
- [220] M. A. Ruderer and P. Müller-Buschbaum. Morphology of polymer-based bulk heterojunction films for organic photovoltaics. *Soft Matter*, 7:5482–5493, 2011.

- [221] H. Nishino, G. Yu, A. J. Heeger, T.-A. Chen, and R. D. Rieke. Electroluminescence from blend films of poly(3-hexylthiophene) and poly(n-vinylcarbazole). *Synth. Met.*, 68:243–247, 1995.
- [222] M. Heo, J. Kim, J. Y. Kim, and C. Yang. A first approach to white organic electroluminescence device from a single rod-coil poly[thiophene-block-(n-vinylcarbazole)] diblock copolymer. *Macromol. Rapid Commun.*, 31:2047–2052, 2010.
- [223] D. S. Germack, C. K. Chan, B. H. Hamadani, L. J. Richter, D. A. Fischer, D. J. Gundlach, and D. M. DeLongchamp. Substrate-dependent interface composition and charge transport in films for organic photovoltaics. *Appl. Phys. Lett.*, 94:233303, 2009.
- [224] S. J. Naftel, P.-S. G. Kim, T. K. Sham, R. Sammynaiken, B. W. Yates, and Y.-F. Hu. Soft x-ray excited optical luminescence from poly(n-vinylcarbazole). *Appl. Phys. Lett.*, 93:5191, 2003.
- [225] H. Ade, X. Zhang, S. Cameron, C. Costello, J. Kirz, and S. Williams. Chemical contrast in x-ray microscopy and spatially resolved XANES spectroscopy of organic specimens. *Science*, 258:972–975, 1992.
- [226] C. R. McNeill, B. Watts, L. Thomsen, H. Ade, N. C. Greenham, and P. C. Dastoor. X-ray microscopy of photovoltaic polyfluorene blends: Relating nanomorphology to device performance. *Macromolecules*, 40:3263–3270, 2007.
- [227] D. H. Kim, Y. D. Park, Y. Jang, H. Yang, Y. H. Kim, J. I. Han, D. G. Moon, S. Park, T. Chang, C. Chang, M. Joo, C.Y. Ryu, and K. Cho. Enhancement of field-effect mobility due to surface-mediated molecular ordering in regioregular polythiophene thin film transistors. *Adv. Funct. Mater.*, 15:77–82, 2005.
- [228] M. A. Ruderer, S. M. Prams, M. Rawolle, Q. Zhong, J. Perlich, S. V. Roth, and P. Müller-Buschbaum. Influence of annealing and blending of photoactive polymers on their crystalline structure. *J. Phys. Chem. B*, 114:15451–15458, 2010.
- [229] L. Chang, H. W. A. Lademann, J.-B. Bonekamp, K. Meerholz, and A. J. Moulé. Effect of trace solvent on the morphology of P3HT:PCBM bulk heterojunction solar cells. *Adv. Funct. Mater.*, 21:1779–1787, 2011.
- [230] Y. Kaminorz, E. Smela, O. Inganäs, and L. Brehmer. Sensitivity of polythiophene planar light-emitting diodes to oxygen. *Adv. Mater.*, 10:765–768, 1998.

- [231] N. Ljungqvist and T. Hjertberg. Oxidative degradation of poly(3-octylthiophene). *Macromol.*, 28:5993–5999, 1995.
- [232] C. K. Chiang, C. R. Fincher, Y. W. Park, A. J. Heeger, H. Shirakawa, E. J. Louis, S. C. Gau, and A. G. MacDiarmid. Electrical conductivity in doped polyacetylene. *Phys. Rev. Lett.*, 39:1098–1101, 1977.
- [233] S.-I. Na, S.-S. Kim, J. Jo, S.-H. Oh, J. Kim, and D.-Y. Kim. Efficient polymer solar cells with surface relief gratings fabricated by simple soft lithography. *Adv. Funct. Mater.*, 18:3956–3963, 2008.
- [234] S.-I. Na, S.-S. Kim, S.-S. Kwon, J. Jo, J. Kim, T. Lee, and D.-Y. Kim. Surface relief gratings on poly(3-hexylthiophene) and fullerene blends for efficient organic solar cells. *Appl. Phys. Lett.*, 91:173509, 2007.
- [235] Z. Bao, A. Dodabalapur, and A. J. Lovinger. Soluble and processable regioregular poly(3-hexylthiophene) for thin film field-effect transistor applications with high mobility. *Appl. Phys. Lett.*, 69:4108, 1996.
- [236] D. Lübbert, T. Baumbach, S. Ponti, U. Pietsch, L. Leprince, J. Schneck, and A. Talneau. Strain investigation of low strained buried gratings by grazing incidence x-ray diffraction and elasticity theory. *Europhys. Lett.*, 46:479–485, 1999.
- [237] E. Rebollar, S. Perez, J. J. Hernandez, I. Martin-Fabiani, D. R. Rueda, T. A. Ezquerro, and M. Castillejo. Assessment and formation mechanism of laser-induced periodic surface structures on polymer spin-coated films in real and reciprocal space. *Langmuir*, 27:5596–5606, 2011.
- [238] R. L. Jones, T. Hu, C. L. Soles, E. K. Lin, R. M. Reano, S. W. Pang, and D. M. Casa. Real-time shape evolution of nanoimprinted polymer structures during thermal annealing. *Nano Lett.*, 6:1723–1728, 2006.
- [239] H. Kim, M. Shin, and Y. Kim. Distinct annealing temperature in polymer:fullerene:polymer ternary blend solar cells. *J. Phys. Chem. C*, 113:1620–1623, 2009.
- [240] M. Hamdorf and D. Johannsmann. Surface-rheological measurements on glass forming polymers based on the surface tension driven decay of imprinted corrugation gratings. *J. Chem. Phys.*, 112:4262–4270, 2000.
- [241] K. Petersen and D. Johannsmann. Measurements on the surface glass transition of PMMA from the decay of imprinted surface corrugation gratings: the influence of molecular weight. *J. Non-Cryst. Solids*, 307-310:532–537, 2002.

- [242] P. Müller-Buschbaum, N. Hermsdorf, S. V. Roth, J. Wiedersich, S. Cunis, and R. Gehrke. Comparative analysis of nanostructured diblock copolymer films. *Spectrochim. Acta, Part B*, 59:1789–1797, 2004.
- [243] A. Kumar and G. M. Whitesides. Features of gold having micrometer to centimeter dimensions can be formed through a combination of stamping with an elastomeric stamp and an alkanethiol ink followed by chemical etching. *Appl. Phys. Lett.*, 63:2002–2004, 1993.
- [244] Y. Xia, E. Kim, X.-M. Zhao, J. A. Rogers, M. Prentiss, and G. M. Whitesides. Complex optical surfaces formed by replica molding against elastomeric masters. *Science*, 273:347–349, 1996.
- [245] M. J. Hampton, S. S. Williams, Z. Zhou, J. Nunes, D.-H. Ko, J. L. Templeton, E. T. Samulski, and J. M. DeSimone. The patterning of sub-500 nm inorganic oxide structures. *Adv. Mater.*, 20:2667–2673, 2008.
- [246] F. C. Krebs, S. A. Gevorgyan, and J. Alstrup. A roll-to-roll process to flexible polymer solar cells: model studies, manufacture and operational stability studies. *J. Mater. Chem.*, 19:5442–5451, 2009.
- [247] S. H. Ahn and L. J. Guo. High-speed roll-to-roll nanoimprint lithography on flexible plastic substrates. *Adv. Mater.*, 20:2044–2049, 2008.
- [248] G. Kumar, H. X. Tang, and J. Schroers. Nanomoulding with amorphous metals. *Nature*, 457:868–872, 2009.
- [249] D. Suh, S.-J. Choi, and H. H. Lee. Rigiflex lithography for nanostructure transfer. *Adv. Mater.*, 17:1554–1560, 2005.
- [250] D. R. Barbero, M. S. M. Saifullah, P. Hoffmann, H. J. Mathieu, D. Anderson, G. A. C. Jones, M. E. Welland, and U. Steiner. High resolution nanoimprinting with a robust and reusable polymer mold. *Adv. Funct. Mater.*, 17:2419–2425, 2007.
- [251] T. Granlund, T. Nyberg, L. S. Roman, M. Svensson, and O. Inganäs. Patterning of polymer light-emitting diodes with soft lithography. *Adv. Mater.*, 12:267–273, 2000.
- [252] P. G. Taylor, J.-K. Lee, A. A. Zakhidov, M. Chatzichristidi, H. H. Fong, J. A. DeFranco, G. G. Malliaras, and C. K. Ober. Orthogonal patterning of PEDOT:PSS for organic electronics using hydrofluoroether solvents. *Adv. Mater.*, 21:2314–2317, 2009.

- [253] S. H. Park, A. Roy, S. Beaupré, S. Cho, N. Coates, J. S. Moon, D. Moses, M. Leclerc, K. Lee, and A. J. Heeger. Bulk heterojunction solar cells with internal quantum efficiency approaching 100%. *Nature Photonics*, 3:297–302, 2009.
- [254] M. T. Dang, L. Hirsch, and G. Wantz. P3HT:PCBM, best seller in polymer photovoltaic research. *Adv. Mater.*, 23:3597–3602, 2011.
- [255] H. Schiff. Nanoimprint lithography: An old story in modern times? A review. *J. Vac. Sci. Technol. B*, 26:458–480, 2008.
- [256] B. Friedel, P. E. Keivanidis, T. J. K. Brenner, A. Abrusci, C. R. McNeill, R. H. Friend, and N. C. Greenham. Effects of layer thickness and annealing of PEDOT:PSS layers in organic photodetectors. *Macromolecules*, 42:6741–6747, 2009.
- [257] C. J. Brabec, A. Cravino, D. Meissner, N. S. Sariciftci, T. Fromherz, M. T. Rispen, L. Sanchez, and J. C. Hummelen. Origin of the open circuit voltage of plastic solar cells. *Adv. Funct. Mater.*, 11:374–380, 2001.
- [258] R. Meier, F. Markl, C. Birkenstock, and P. Müller-Buschbaum. Film thickness controllable wet-imprinting of nanoscale channels made of conducting or thermoresponsive polymers. *J. Mater. Chem.*, 22:192–198, 2012.
- [259] J. Joo, S.-K. Park, D.-S. Seo, S.-J. Lee, H.-S. Kim, K.-S. Ryu, T.-J. Lee, S.-H. Seo, and C.-J. Lee. Formation of nanoislands on conducting poly(3,4-ethylenedioxythiophene) films by high-energy-ion irradiation: Applications as field emitters and capacitor electrodes. *Adv. Funct. Mater.*, 15:1465–1470, 2005.
- [260] F. Zhang, M. Johansson, M. R. Andersson, J. C. Hummelen, and O. Inganäs. Polymer photovoltaic cells with conducting polymer anodes. *Adv. Mater.*, 14:662–665, 2002.
- [261] L. Tan, Y. P. Kong, S. W. Pang, and A. F. Yee. Imprinting of polymer at low temperature and pressure. *J. Vac. Sci. Technol. B*, 22:2486–2492, 2004.
- [262] D. T. Eddington, J. P. Puccinelli, and D. J. Beebe. Thermal aging and reduced hydrophobic recovery of polydimethylsiloxane. *Sens. Actuators, B*, 114:170–172, 2006.
- [263] M. G. Moharam and T. K. Gaylord. Diffraction analysis of dielectric surface-relief gratings. *J. Opt. Soc. Am.*, 72:1385–1392, 1982.

- [264] F. S. Marikkar, C. Carter, K. Kieltyka, J. W. F. Robertson, C. Williamson, A. Simmonds, R. Zangmeister, T. Fritz, and N. R. Armstrong. Conducting polymer diffraction gratings on gold surfaces created by microcontact printing and electropolymerization at submicron length scales. *Langmuir*, 23:10395–10402, 2007.
- [265] M. Campoy-Quiles, T. Ferenczi, T. Agostinelli, P. G. Etchegoin, Y. Kim, T. D. Anthopoulos, P. N. Stavrinou, D. D. C. Bradley, and J. Nelson. Morphology evolution via self-organization and lateral and vertical diffusion in polymer:fullerene solar cell blends. *Nature Materials*, 7:158–164, 2008.
- [266] G. Li, V. Shrotriya, Y. Yao, J. Huang, and Y. Yang. Manipulating regioregular poly(3-hexylthiophene):[6,6]-phenyl-C61-butyric acid methyl ester blends - route towards high efficiency polymer solar cells. *J. Mater. Chem.*, 17:3126–3140, 2007.
- [267] G. Li, V. Shrotriya, Y. Yao, and Y. Yang. Investigation of annealing effects and film thickness dependence of polymer solar cells based on poly(3-hexylthiophene). *J. Appl. Phys.*, 98:043704, 2005.
- [268] J. Y. Kim, S. H. Kim, H.-H. Lee, K. Lee, W. Ma, X. Gong, and A. J. Heeger. New architecture for high-efficiency polymer photovoltaic cells using solution-based titanium oxide as an optical spacer. *Adv. Mater.*, 18:572–576, 2006.
- [269] C. J. Brabec, S. E. Shaheen, C. Winder, N. S. Sariciftci, and P. Denk. Effect of LiF/metal electrodes on the performance of plastic solar cells. *Appl. Phys. Lett.*, 80:1288–1290, 2002.
- [270] G. F. Burkhard, E. T. Hoke, and M. D. McGehee. Accounting for interference, scattering, and electrode absorption to make accurate internal quantum efficiency measurements in organic and other thin solar cells. *Adv. Mater.*, 22:3293–3297, 2010.
- [271] V. D. Mihailetschi, H. Xie, B. de Boer, L. J. A. Koster, and P. W. M. Blom. Charge transport and photocurrent generation in poly(3-hexylthiophene):methanofullerene bulk-heterojunction solar cells. *Adv. Funct. Mater.*, 16:699–708, 2006.
- [272] K. M. Coakley and M. D. McGehee. Conjugated polymer photovoltaic cells. *Chem. Mater.*, 16:4533–4542, 2004.
- [273] A. Gadisa, W. D. Oosterbaan, K. Vandewal, J.-C. Bolse'e, S. Bertho, J. D'Haen, L. Lutsen, D. Vanderzande, and J. V. Manca. Effect of alkyl side-chain length on photovoltaic properties of poly(3-alkylthiophene)/PCBM bulk heterojunctions. *Adv. Funct. Mater.*, 19:3300–3306, 2009.

- [274] P. Schilinsky, C. Waldauf, and C. J. Brabec. Recombination and loss analysis in polythiophene based bulk heterojunction photodetectors. *Appl. Phys. Lett.*, 81:3885–3887, 2002.
- [275] W. Wiedemann, L. Sims, A. Abdellah, A. Exner, R. Meier, K. P. Musselman, J. L. MacManus-Driscoll, P. Müller-Buschbaum, G. Scarpa, P. Lugli, and L. Schmidt-Mende. Nanostructured interfaces in polymer solar cells. *Appl. Phys. Lett.*, 96:263109, 2010.
- [276] M. Drees, H. Hoppe, C. Winder, H. Neugebauer, N. S. Sariciftci, W. Schwinger, F. Schäßler, C. Topf, M. C. Scharber, Z. Zhu, and R. Gaudiana. Stabilization of the nanomorphology of polymer-fullerene „bulk heterojunction“ blends using a novel polymerizable fullerene derivative. *J. Mater. Chem.*, 15:5158–5163, 2005.
- [277] S. S. van Bavel, M. Bärenklau, G. de With, H. Hoppe, and J. Loos. P3HT/PCBM bulk heterojunction solar cells: Impact of blend composition and 3D morphology on device performance. *Adv. Funct. Mater.*, 20:1458–1463, 2010.
- [278] J. Piris, T. E. Dykstra, A. A. Bakulin, P. H. M. van Loosdrecht, W. Knulst, M. T. Trinh, J. M. Schins, and L. D. A. Siebbeles. Photogeneration and ultrafast dynamics of excitons and charges in P3HT/PCBM blends. *J. Phys. Chem. C*, 113:14500–14506, 2009.
- [279] G. Li, V. Shrotriya, J. Huang, Y. Yao, T. Moriarty, K. Emery, and Y. Yang. High-efficiency solution processable polymer photovoltaic cells by self-organization of polymer blends. *Nature Materials*, 4:864–868, 2005.
- [280] Mitsubishi Chemical. www.mitsubishichem-hd.co.jp/english/group/strategy/major_project/solar_cell.html, January 2012.

List of publications

Publications related to the dissertation

- R. Meier, M. A. Ruderer, A. Diethert, G. Kaune, V. Körstgens, S. V. Roth, and P. Müller-Buschbaum: Influence of film thickness on the phase separation mechanism in ultrathin conducting polymer blend films; *J. Phys. Chem. B* **2011**, *115*, 2899-2909.
- R. Meier, M. Schindler, B. Watts, and P. Müller-Buschbaum: Residual solvent content in conducting polymer-blend films mapped with scanning transmission x-ray microscopy; *Phys. Rev. B* **2011**, *84*, 174205.
- R. Meier, F. Markl, C. Birkenstock, and P. Müller-Buschbaum: Film thickness controllable wet-imprinting of nanoscale channels made of conducting or thermoresponsive polymers; *J. Mater. Chem.* **2012**, *22*, 192-198.
- R. Meier, H.-Y. Chiang, M. A. Ruderer, G. Shuai, V. Körstgens, J. Perlich, and P. Müller-Buschbaum: In-situ film characterization of thermally treated microstructured conducting polymer films; *J. Polym. Sci., Part B: Polym. Phys.* accepted for publication.
- W. Wiedemann, L. Sims, A. Abdellah, A. Exner, R. Meier, K. P. Musselman, J. L. MacManus-Driscoll, P. Müller-Buschbaum, G. Scarpa, P. Lugli, and L. Schmidt-Mende: Nanostructured interfaces in polymer solar cells; *Appl. Phys. Lett.* **2010**, *96*, 263109.
- R. Meier, C. Birkenstock, C. M. Palumbiny, and P. Müller-Buschbaum: Efficiency-improved organic solar cells based on plasticizer assisted soft embossed PEDOT:PSS layers, in revision.

Further publications

- M. A. Ruderer, S. Guo, R. Meier, H.-Y. Chaing, V. Körstgens, J. Wiedersich, J. Perlich, S. V. Roth, and P. Müller-Buschbaum: Solvent induced morphology in polymer-based systems for organic photovoltaics; *Adv. Funct. Mater.* **2011**, *21*, 3382-3391.
- G. Kaune, E. Metwalli, R. Meier, V. Körstgens, K. Schlage, S. Couet, R. Röhlberger, S. V. Roth, P. Müller-Buschbaum: Growth and Morphology of Sputtered Aluminum Thin Films on P3HT Surfaces; *ACS Appl. Mater. Interfaces* **2011**, *3*, 1055-1062.
- A. Buffet, M. M. Abul Kashem, K. Schlage, S. Couet, R. Röhlberger, A. Rothkirch, G. Herzog, E. Metwalli, R. Meier, G. Kaune, M. Rawolle, P. Müller-Buschbaum, R. Gehrke, and S.V. Roth: Cobalt nanoparticle growth on a multiple structured colloidal template; *Langmuir* **2011**, *27*, 343-346.
- V. Körstgens, J. Wiedersich, R. Meier, J. Perlich, S. V. Roth, R. Gehrke, P. Müller-Buschbaum: Combining imaging ellipsometry and grazing incidence small angle x-ray scattering for an in-situ characterization of polymer nanostructures; *Anal. Bioanal. Chem.* **2010**, *396*, 139-149.
- G. Kaune, M. Memesa, R. Meier, M. A. Ruderer, A. Diethert, S. V. Roth, M. D'Acunzi, J. S. Gutmann, P. Müller-Buschbaum: Hierarchically structured titania films prepared by polymer/colloidal templating; *ACS Appl. Mater. Interfaces* **2009**, *1*, 2862-2869.
- R. Meier, R. C. Word, A. Nadarajah, and R. Könenkamp: Unipolar transport and interface charge transfer in nanostructured CdTe/polymer hybrid films; *Phys. Rev. B* **2008**, *77*, 195314.

Scientific reports

- R. Meier, F. Markl, C. Birkenstock, and P. Müller-Buschbaum: Film thickness controllable wet-imprinting of nanoscale channels made of conducting polymers; *Lehrstuhl für Funktionelle Materialien, Annual report 2011*.
- R. Meier, J. Perlich, and P. Müller-Buschbaum: Thermally modified molecular arrangement of P3HT films probed in-situ with a novel combination of optical ellipsometry and GIWAXS; *Lehrstuhl für Funktionelle Materialien, Annual report 2010*.

- R. Meier, V. Körstgens, H.-Y. Chiang, S. Guo, J. Wiedersich, J. Perlich, S. V. Roth, and P. Müller-Buschbaum: In-situ GIWAXS - Ellipsometry Study of Molecular Arrangement of Conducting P3HT Films; *HASYLAB, Annual report 2010*.
- R. Meier, S. V. Roth, and P. Müller-Buschbaum: Thin photoactive polymer blend films on structured substrates: A GISAXS study; *Lehrstuhl für Funktionelle Materialien, Annual report 2009*.
- R. Meier, F. Markl, and P. Müller-Buschbaum: Structuring of an electron-blocking PEDOT:PSS layer in Organic Solar Cells; *Lehrstuhl für Funktionelle Materialien, Annual report 2009*.
- R. Meier, M. A. Ruderer, F. Markl, V. Körstgens, S. V. Roth, and P. Müller-Buschbaum: In-situ Vapour Treatment of Structured Thin Conducting Polymer Films; *HASYLAB, Annual report 2009*.
- R. Meier, M. A. Ruderer, G. Kaune, A. Diethert, S. V. Roth, and P. Müller-Buschbaum: Surface and structure analysis of thin polymer blend films based on MEH-PPV and PVK; *Lehrstuhl für Funktionelle Materialien, Annual report 2008*.
- R. Meier, M. A. Ruderer, G. Kaune, J. Perlich, R. Georgii, and P. Müller-Buschbaum: SLD determination of conducting polymers based on PPV derivatives; *Lehrstuhl für Funktionelle Materialien, Annual report 2008*.
- R. Meier, M. A. Ruderer, G. Kaune, A. Diethert, S. V. Roth, and P. Müller-Buschbaum: Surface and structure analysis of thin polymer blend films based on MEH-PPV and PVK; *HASYLAB, Annual report 2008*.
- R. Meier, G. Kaune, V. Körstgens, E. Metwalli, S. Couet, K. Schlage, G. Herzog, A. Buffet, S. V. Roth, P. Müller-Buschbaum: In-situ comparative GISAXS study on continuous vs. step-wise aluminum growth on a conducting polymer blend template via sputtering; *HASYLAB, Annual report 2008*.
- R. Meier and P. Müller-Buschbaum: Structured Organic Solar Cells; *Lehrstuhl für Funktionelle Materialien, Annual report 2007*

Conference talks

- R. Meier and P. Müller-Buschbaum: Breaking the Wall of Organic Photovoltaics; *Falling Walls Lab, Berlin (Germany), November 2011*.

- R. Meier, H.-Y. Chiang, M. A. Ruderer, S. Guo, J. Wiedersich, V. Körstgens, J. Perlich, S. V. Roth, and P. Müller-Buschbaum: Thermal tuning of micro-structured conducting polymer thin films; *DPG spring meeting*, Dresden (Germany), March 2011.
- R. Meier, M. A. Ruderer, G. Kaune, A. Diethert, F. Markl, V. Körstgens, J. Wiedersich, S. V. Roth, and P. Müller-Buschbaum: Structural analysis of photoactive polymer blend films on textured polymeric and inorganic substrates; *DPG spring meeting*, Regensburg (Germany), March 2010.
- R. Meier, M. A. Ruderer, G. Kaune, A. Diethert, F. Markl, V. Körstgens, J. Wiedersich, S.V. Roth, and P. Müller-Buschbaum: Polymer Blend Thin Films Investigated with GISAXS; *HASYLAB-TUM Colloquium*, Hamburg (Germany), January 2010.
- R. Meier, M. A. Ruderer, G. Kaune, J. Perlich, R. Georgii, and P. Müller-Buschbaum: Neutron Reflectivity on Conducting Polymer Films; *4th FRM-II Workshop on Neutron Scattering*, Burg Rothenfels (Germany), June 2009.

Conference poster presentations

- R. Meier, C. Birkenstock, and P. Müller-Buschbaum: Structured polymer films and their application for organic photovoltaics; *MSE Colloquium*, Garching (Germany), July 2011.
- R. Meier, M. A. Ruderer, M. Haese-Seiller, R. Kampmann, and P. Müller-Buschbaum: GISANS Study on Complex Protonated Polymer Blend Films Probing the Solvent Content; *5th FRM-II Workshop on Neutron Scattering*, Burg Rothenfels (Germany), June 2011.
- R. Meier, M. Schindler, A. Nathan, A. Diethert, R. Georgii, and P. Müller-Buschbaum: Residual Solvent Study in Homopolymer Films utilizing Neutron Reflectivity Measurements; *FRM II User Meeting*, Garching (Germany), October 2010.
- R. Meier, M. A. Ruderer, G. Kaune, A. Diethert, F. Markl, V. Körstgens, S. V. Roth, and P. Müller-Buschbaum: Morphology Analysis of Pretextured Polymer Blend Films for Photovoltaic Application; *3. Joint Nanoworkshop 2010*, Eindhoven (Netherlands), June 2010.
- R. Meier, M. A. Ruderer, G. Kaune, A. Diethert, F. Markl, V. Körstgens, J. Wiedersich, S. V. Roth, and P. Müller-Buschbaum: Thin photoactive polymer films on

textured substrates: A GISAXS study; *HASYLAB User Meeting*, Hamburg (Germany), January 2010.

- R. Meier, M. A. Ruderer, G. Kaune, J. Perlich, R. Georgii, and P. Müller-Buschbaum: Neutron Reflectivity Study addressing the solvent content in thin conducting polymer films; *E-MRS spring meeting*, Strasbourg (France), June 2009.
- R. Meier, M. A. Ruderer, G. Kaune, J. Perlich, R. Georgii, and P. Müller-Buschbaum: Neutron Reflectivity Study addressing the solvent content in thin conducting polymer films; *FRM II User Meeting*, Garching (Germany), May 2009.
- R. Meier, M. A. Ruderer, G. Kaune, A. Diethert, S. V. Roth, and P. Müller-Buschbaum: Surface and structure analysis of thin polymer blend films based on MEH-PPV and PVK; *DPG spring meeting*, Dresden (Germany), March 2009.
- R. Meier, M. Ruderer, J. Perlich, G. Kaune, and P. Müller-Buschbaum: Neutron Reflectivity Measurements on Conducting Polymer Films; *German Neutron Scattering Conference*, Garching (Germany), June 2008.

Acknowledgements

I want to thank Prof. Dr. P. Müller-Buschbaum for giving me the opportunity to work in the highly interesting field of organic photovoltaics. His critical view on my scientific work and his great knowledge in the field of X-ray scattering and polymer science were crucial for my success as a PhD student. Although typically struggling with his busy schedule, the door to his office was always open and he always had time for extended discussions. I really appreciate this.

I also thank Prof. M. Brandt and Prof. M. Zacharias for examining this thesis.

In addition, the financial support by the BMBF in the project 05KS7W01 is gratefully acknowledged.

Since many experiments within this thesis were performed at large scale facilities, I was allowed to experience very interesting and often quite demanding beamtimes with my colleagues. I will especially miss the long nights with M. Schindler at the Swiss Light Source (Villigen, Switzerland). Due to the excellent teamwork, all beamtimes turned out to be a great success. For the very good team work, I want to thank Dr. V. Körstgens, M. Ruderer, M. Schindler, Dr. E. Metwalli, Dr. A. Diethert, Dr. G. Kaune, H.-Y. Chiang, Dr. E. Herzig, S. Guo and Q. Zhong. In addition, I thank M. Rawolle for measuring my samples although I did not join the beamtime.

However, every beamtime can only succeed if the corresponding beamline scientists deliver the best solutions to all arising problems. Thus, I wish every future beamline-user the same great support during their measurements I was allowed to receive. A big thank you goes to Dr. S. Roth, Dr. J. Perlich, and Dr. A. Timmann at the HASYLAB (Desy) and B. Watts and J. Raabe from the PolLux beamline (SLS, Villigen).

I also want to acknowledge the help of the collaborators from the Ludwig Maximilians University, W. Wiedemann and Prof. Dr. L. Schmidt-Mende, for their important advice during the fabrication of the first working organic solar cells at E13. In addition, I thank B. Russ and Prof. Dr. P. Böni for providing the possibility to use the X-ray reflectometer at the Lehrstuhl E21.

A special thank you goes to 'my' former diploma, master, and bachelor students M. Schindler, C. Birkenstock, H.-Y. Chiang, F. Markl, and M. Demharter. Their passion and motivation contributed heavily to this thesis. Good luck with your PhD thesis, your time as a consultant, and your future studies.

Moreover, I am very thankful to the people who read the manuscript and contributed to its improvement: M. Rawolle, Dr. V. Körstgens, Dr. M. Philipp, D. Magerl, Dr. E. Herzig, M. Schindler, Dr. E. Metwalli, M. Niedermeier, and C. Palumbiny. In addition I want to thank A. Gelhar for double-checking the complete thesis for grammar errors. Maybe somebody should have also read these pages...

At this point, the help of S. Prams with the 3-dimensional chemical drawings of the applied polymers needs to be acknowledged as well.

For his help and his advice during the development and the installation of the thermal evaporation set-up, I thank J. Kaplonski. Almost all parts of the set-up were made in our workshop. Therefore, I say thank you to R. Funer, R. Jahrstorfer, L. Hein, and P. Bork.

Besides only doing science, I really enjoyed the many opportunities for presenting and discussing my current research projects. In addition, I want to emphasize the good atmosphere among the complete group. Explicitly, I want to thank M. Ruderer for introducing me to everything at the beginning of my PhD-time and for sharing his deep knowledge during my whole time in the group of Functional Materials.

Although I am definitely not good in soccer (I even tore my ligament without touching the ball), I always enjoyed the soccer matches. In addition, our group-intern conferences and workshops, and of course the intense visits to the Nockherberg or the Oktoberfest have also been very refreshing. Also the team members I did not mention so far, contributed a lot to the very kind atmosphere: J. Adelsberger, S. Ener (thank you for the Raki-supply), A. Golosova, M. He, W. Hefter, T. Hoppe, S. Jaksch, Prof. Dr. C. Papadakis, S. Prams, K. Sarkar, Prof. Dr. W. Schirmacher, A. Sepe, K. Wagenbauer, W. Wang (2x), Dr. J. Wiedersich, A. Akhtar, C. Gebbe, E. Kopperger, S. Lindner, L. Wei, A. Naumann, Dr. N. Paul, S. Roßbauer, F. Schaff, J. Zhang, and Y. Yuan.

I also want to thank my former room mates D. Müller, A. Meier-Koll, and all from the big office at the beginning of my time in the group of Functional Materials.

I thank my cousin C. Schmidgall for welding the experimental set-up for the batch-production of the wet embossed PEDOT:PSS gratings.

Last, but definitely not least, a special thank you goes to our secretary. Their refreshing and happy mood has and will always be an essential part of working in the group of Functional Materials! Just stay as you are, Susanna, Petra, and Marion.

However, the biggest thank-you goes to my family, on which I can always rely. Because of their continuous support during my whole life, I dedicate this thesis to them.

I thank my beloved Melanie for all her support and I am looking forward to our future.